Non-canonical small heat shock protein activity in health and disease of *C. elegans*

DISSERTATION
zur Erlangung des akademischen Grades

Doctor of Philosophy (Ph.D.)

eingereicht an der
Lebenswissenschaftlichen Fakultät der Humboldt-Universität zu Berlin

von
M. Sc. Manuel Iburg

Präsidentin/Präsident
der Humboldt-Universität zu Berlin

Prof. Dr.-Ing. Dr. Sabine Kunst

Dekanin/Dekan der Lebenswissenschaftlichen Fakultät
der Humboldt-Universität zu Berlin

Prof. Dr. Bernhard Grimm

Gutachter/innen

1. Prof. Dr. Adam Lange
2. Prof. Dr. Janine Kirstein
3. Prof. Dr. Christian Freund

Tag der mündlichen Prüfung: 10. Februar, 2021

Table of contents

1. Summary & Zusammenfassung

Summary

Successful synthesis and folding of proteins is a prerequisite for cellular function and failure of protein homeostasis leads to disease or death. Within the cell, molecular chaperones ensure correct protein folding or aid in the disposal of terminally misfolded protein substrates. Among these chaperones, small heat shock proteins (sHsps) are ATP-independent members of the proteostasis network, which are known to inhibit the aggregation of their protein substrates before ATP-dependent chaperones may take over. In the genomes of metazoans like *C. elegans*, a high number of sHsps are encoded and their specific functions that necessitate this variety are not yet understood.

In this work, I analyzed the so far under-researched *C. elegans* sHsp HSP-17. Unlike other sHsps, HSP-17 exhibited only weak activity in preventing aggregation of protein substrates. Instead, I could show *in vitro* that HSP-17 can promote the aggregation of protein substrates, which was previously demonstrated for yeast and bacterial sHsps and is a first demonstration for metazoan sHsps. HSP-17 co-precipitates with substrates and potentially modifies the aggregates. *In vivo*, *C. elegans* reporter strains revealed that HSP-17 is abundant, most expressed in the alimentary system and the excretory tract. HSP-17 colocalizes with aggregates and pro-aggregation activity is present *in vivo*, which I demonstrated for the physiological substrate KIN-19

and heterologously expressed amyloidogenic polyQ peptides. By physiological, biochemical and proteomic analysis I showed that HSP-17 activity is relevant for organismal fitness, reproduction and development and protective under heat, osmotic and biotic stress.

In vivo microscopy, short generation times and a conserved proteostasis network make *C. elegans* a powerful model organism for aging and disease. Humanized *C. elegans* strains allow bridging the gap from insights into *C. elegans* chaperone activity to understanding proteostasis in the human context. The amyloid β peptide can form amyloid fibrils and is associated with the neurodegenerative Alzheimer's disease.

In a second project, I contributed to the development and characterization of a novel model of Aβ pathology in *C. elegans*. This new AD model employs sub-stoichiometric labeling to allow live visualization of Aβ aggregation in distinct cell types such as neurons or body wall muscle. The model mirrors known phenotypes of Aβ proteotoxicity in humans and existing *C. elegans* Aβ strains, including defects in autophagy and the endo-membrane system which were demonstrated by proteomic, biochemical and physiological methods. Interestingly, a subset of neurons, the IL2 neurons, is shown to be more vulnerable to Aβ proteotoxicity and targeted depletion of Aβ in these neurons systemically ameliorates pathology. Thereby, the model presents a new platform to assess the relevance of molecular chaperones such as sHsps in amyloidosis with a perspective on human disease.

Zusammenfassung

Die erfolgreiche Synthese und Faltung von Proteinen ist eine Voraussetzung der Zellfunktion und ein Versagen der Proteinhomöostase führt zu Krankheit oder Tod. In der Zelle sichern molekulare Chaperone die korrekte Faltung der Proteine oder tragen zur Entsorgung unwiederbringlich fehlgefalteter Proteinsubstrate bei. Unter diesen Chaperonen sind kleine Hitzeschockproteine (sHsp) ein ATP-unabhängiger Teil des Proteostasenetzwerks, von denen bekannt ist, dass sie die Aggregation ihrer Proteinsubstrate inhibieren, bevor diese von anderen ATP-abhängigen Chaperonen weiter prozessiert werden. Die Genome von Metazoen wie *C. elegans* kodieren eine Vielzahl von sHsps und deren spezifische Funktionen, die diese Vielfalt erfordern, sind noch nicht bekannt.

In dieser Arbeit habe ich das bisher wenig erforschte sHsp HSP-17 aus *C. elegans* untersucht. Im Gegensatz zu anderen sHsps zeigte HSP-17 nur eine geringe Aktivität beim Verhindern der Aggregation von Proteinsubstraten. Stattdessen konnte ich *in vitro* zeigen, dass HSP-17 die Aggregation von Modellsubstraten fördert, was im Vorfeld für bestimmte sHsps aus Hefe und Bakterien beschrieben und hier für Metazoen-sHsps erstmals gezeigt wurde. HSP-17 kopräzipitiert mit Substraten und modifiziert deren Aggregate möglicherweise. *In vivo* enthüllten *C. elegans*-Reporterstämme, dass HSP-17 ein abundantes Protein ist, welches vorwiegend im Verdauungssystem und dem exkretorischen Kanal exprimiert wird. HSP-17 kolokalisiert mit Aggregaten, und seine aggregationsfördernde Aktivität konnte ich *in vivo* für das physiologische Substrat KIN-19 und heterolog exprimierte polyQ-Peptide validieren. Durch physiologische, biochemische und proteomische Analysen konnte ich zeigen, dass die Aktivität von HSP-17 für die Fitness, Reproduktion und Entwicklung relevant ist und unter Hitze-, osmotischem oder biotischem Stress schützend wirkt.

In vivo Mikroskopie, kurze Generationszeiten und ein konserviertes Proteostasenetzwerk machen *C. elegans* zu einem attraktivem Modellsystem für Forschungsfragen zu Alterung und Krankheit. Humanisierte *C. elegans*-Stämme ermöglichen das Überbrücken der Lücke von Erkenntnissen der Chaperonaktivität in *C. elegans* bis zum Verständnis von Proteostase im menschlichen Kontext. Das Amyloid β ist ein Peptid, welches amyloide Fibrillen ausbilden kann und mit der Entstehung der neurodegenerativen Alzheimerschen Erkrankung assoziiert wird.

In einem zweiten Projekt habe ich zur Entwicklung eines neuen Modelles für Aβ-Pathologie in *C. elegans* beigetragen, welches substöchiometrische Markierungen verwendet, um eine zeitnahe Visualisierung der Aβ-Aggregation in spezifischen Zelltypen wie Neuronen oder Körperwandmuskeln zu ermöglichen. Das Modell spiegelt bekannte Phänotypen der Aβ-Proteotoxizität aus Menschen und bestehenden *C. elegans* Aβ-Stämmen wider, einschließlich Defekten der Autophagie und des Endomembranystems, was hier durch proteomische, biochemische und physiologische Methoden gezeigt wurde. Interessanterweise zeigt eine Untergruppe der Neuronen, die IL2-Neuronen, eine höhere Anfälligkeit für die Aggregation und Proteotoxizität von $A\beta_{1-42}$. Eine gezielte Reduktion von $A\beta_{1-42}$ in IL2 Neuronen führt zu einer systemischen Reduktion der Pathologie. Somit bietet

das Modell eine neue Plattform, um die Bedeutung molekularer Chaperone, wie z. B. der sHsps, für Amyloidosen zu untersuchen, auch im Hinblick auf menschliche Erkrankungen.

2. Authorship Disclaimer

The work I present here was accomplished at the Leibniz-Forschungsinstitut für Molekulare Pharmakologie (FMP), in the research group and under the supervision of Prof. Dr. Janine Kirstein. Parts of my work were done in close collaboration with fellow researchers. Because these data are indispensable to provide a complete context of the experiments carried out, I will present some data prepared by my colleagues in text or graphic form and this will be noted in the respective part of the results section. Colleagues who contributed data presented here are in particular, in order of the first data presented:

Alice Baumann, who provided intact protein QTof-MS analysis (Figure 6).

Dr. Fan Liu and Heike Stephanowitz of the MS core facility, who performed MS/MS experiments and support in their evaluation (Supplementary Tables 1 & 2, Figures 44 & 45).

Dr. Dmytro Puchkov, who provided the preparation and imaging of electron microscopy samples, including TEM and CLEM data (Figures 23, 31, 36, 46).

The generation of a new *C. elegans* model of Aβ pathology (presented as part **3.2**) was carried out in close cooperation with Christian Gallrein. I refer to FLIM data generated by Christian Gallrein and we also shared work in molecular cloning and handling of *C. elegans* as noted in the text of that section. We also cooperated in generating the swim-exhaustion data presented in Figure 52.

Dr. Sara Ayala Mariscal and I worked together to generate the lifespan data presented in Figure 52.

3. Introduction

3.1. Proteostasis

The cell needs to generate proteins to carry out its biological tasks and their variety is enormous – on average, more than 20,000 different proteins in human cells. After synthesis at the ribosome, most proteins need to attain a correct three-dimensional folding state to be functional (1), which is inherent to their primary structure, but not guaranteed (2). Starting at synthesis, proteins are thermodynamically and kinetically challenged and at risk of misfolding with potentially deleterious consequences. Hence, the large protein family of molecular chaperones supports nascent proteins in reaching the correct folding state and maintaining it throughout their lifetime (3). This provides a challenge as proteins face molecular crowding of 200-300 g protein / l within the cell, which causes competition for correct folding and poses the risk of protein aggregation (4,5). Next to this cellular hindrance to protein folding, heat stress is the most common and ubiquitous non-physiological cause of protein misfolding and aggregation. Molecular chaperones, whose expression is induced upon heat shock, have also been labeled “heat shock proteins” (HSPs), although their expression is not exclusive to heat stress and plays a role under constitutive, unstressed conditions (6). Likewise, oxidative stress, osmotic stress and aging (among others) are risk factors of protein aggregation and induce the expression of chaperone proteins (6-8). Finally, spontaneous mutations in protein sequences can destabilize the resulting protein structure and chaperones buffer such proteins to prevent deleterious consequences or enable evolution (9). Proteins that become terminally misfolded or aggregated can be degraded by the cell, another process that is aided by molecular chaperones (1).

The entire process of proteins attaining their correct folding state against intrinsic challenges, maintaining it against external insults and otherwise salvaging or degradation of aggregated proteins is known as protein homeostasis (proteostasis), the machinery behind this mechanism is the proteostasis network (PN). The eventual failure of proteostasis can lead to protein aggregation disease and is not only a consequence, but also a cause of organismal aging (10).

3.1.1. Molecular chaperones

The prominent involvement of molecular chaperones in heat stress which lead to their labeling as heat shock proteins also became the basis for naming chaperone families: Hsp60 or the chaperonins, the Hsp70 family and their co-chaperones, the Hsp40 or J-proteins, Hsp90 and Hsp100 (3). These ATP-dependent chaperones are joined by the family of small heat shock proteins, which range in individual size between 12 and 43 kDa, are ATP-independent (11,12) and will be discussed in section **2.2**.

Notably, the Hsp100 family contains members such as yeast Hsp104 or *E. coli* ClpB, both of which work to resolubilize aggregated protein substrates in cooperation with Hsp70 and Hsp40 members (13,14). These disaggregases belong to the larger AAA+ protein family which also contains AAA+ proteases that target their substrates to degradation (15). The Hsp100 chaperones are strikingly absent from eukaryotic cytosol (besides mitochondria and plastids) and until recently this has led to assumptions that disaggregases are absent from the eukaryotic cell at large (16).

The Hsp70 members, or Hsc70 (“heat shock cognate”), for constitutive, heat shock independent members, are almost universal chaperones that recognize and bind unfolded substrates. In addition, they can also aid in membrane transposition or the assembly of select protein complexes, making them the most versatile molecular chaperones (17). Hsp70 chaperones are monomeric and undergo an ATP-dependent substrate binding cycle that is strongly dependent on nucleotide exchange factors (NEFs) and J-proteins / Hsp40 members as co-chaperones (9). The Hsp40 proteins in particular aid the Hsp70 system by leading Hsp70 members to specific substrates and localizations or binding substrates themselves and delivering them to Hsp70. The J-domain coined the name J-protein for Hsp40 members and interacts with Hsp70, stimulating ATPase activity. ATP-bound Hsp70 is open for substrate binding; interaction with the J-protein and the substrate leads to hydrolysis of ATP and the ADP-bound Hsp70 has a strongly reduced on/off ratio for the protein substrate. Finally, ADP and the substrate are released by binding of the NEF (18). The J-proteins are highly diverse (with 49 different members in humans and 32 in *C. elegans*) and share little common structure outside the J-domain, enabling the high versatility in combination with Hsp70 chaperones (19,20).

3.1.2. Protein disaggregation and degradation

Although in yeast, Hsp70 members can disaggregate and refold aggregated protein substrates with the help of Hsp40 and Hsp100 chaperones (21), the genomes of higher eukaryotes do not encode Hsp100 members (16). Instead, disaggregation in metazoans is enabled by the cooperation of Hsp70 with Hsp40 members and Hsp110 (22). Members of the Hsp110 group are related to the Hsp70 chaperone family (not the Hsp100 family), have a nucleotide binding domain themselves and can act as NEFs for other Hsp70 chaperones (23). Disaggregation by the human triad of Hsc70 (Hsp70 member), Hdj1 (Hsp40 / J-protein) and Apg2 (Hsp110 member) is comparable in efficiency to the yeast system *in vitro* and flexible, i.e., other Hsp110 members can be utilized. Intriguingly, Hsp110 chaperones are present in yeast, but cannot replace Hsp100 members in this function, and the NEF function, but not ATPase activity of Hsp110, is required for disaggregation (24). The metazoan disaggregation machinery was actually demonstrated first in *C. elegans* (24) and involves the sole cytosolic nematode Hsp110 member HSP-110, combined with at least one J-protein (such as DNJ-12 or DNJ-13) and one Hsp70 member (i. e. HSP-1). Interestingly, a tight stoichiometrical combination of type I (also: type A, e. g. DNJ-12 in *C. elegans*) and type II (also: type B, e. g. DNJ-13 in *C. elegans*) J-proteins was shown to enable significantly more effective protein disaggregation in this triad compared to a single J-protein, showcasing the minute control of Hsp70 machinery by its cochaperones (25). Besides amorphous aggregates, disaggregation in metazoans extends to amyloids such as α-synuclein fibrils, which are “pulled apart" by the same machinery (consisting of Hsp70, the type B J-protein DNAJB1 and Hsp110), generating non-toxic monomers (26). The same was demonstrated for fibrils of the polyQ amyloid Huntingtin, where *C. elegans* HSP-1, DNJ-13 and HSP-110 can prevent and revert native or seeded amyloid formation by the huntingtin species $HttEx1Q_{48}$ (Huntingtin exon 1, pathologically elongated polyQ stretch of 48 glutamine residues). In this context it was also demonstrated that amorphous aggregates compete with amyloid fibrils for the disaggregation machinery (27). This machinery, which controls protein aggregation is essential for viability, be it in bacteria, yeast or metazoans and particularly under (heat) stressed conditions (14,24,28).

As an additional layer of protection, proteins that are terminally misfolded and pose a risk for the cell can be targeted to degradation. Soluble protein species can be guided to proteolysis by Hsp70 and its cochaperones (e. g. the NEF BAG1) – in eukaryotes, this happens via ubiquitination and the proteasome (29). As ubiquitin is absent in prokaryotes, AAA+ proteases (e. g. the Clp proteins that Hsp100 members belong to) perform proteolysis aided by their own set of adaptors and cochaperones, using other means of substrate identification (15). In contrast to this targeted degradation of individual proteins, autophagy is a cellular mechanism of bulk self-digestion, to generate nutrients under starvation or to eliminate biotic intrusions. In the context of proteostasis, autophagy is important because misfolded or aggregated proteins can become substrates and be degraded, adding to the proteasomal pathway (30). Hsp70 members, paired with BAG3 as NEF, can induce the ubiquitination of protein substrates that failed to be folded correctly, targeting them for autophagy. This is followed by the binding of autophagic adaptors such as p62/SQSTM-1 (itself a substrate) identify proteins as autophagy substrates. The adaptor recruits LC3 (human) or LGG-1 (*C. elegans*) to induce the formation of an autophagosome which eventually merges with a lysosome to recycle the degraded proteins (31).

3.1.3. Amyloids and neurodegeneration

Mutations in chaperone proteins, consistent expression of aggregation-prone protein substrates, repeated stress and sporadic or programmed effects of aging eventually overpower the PN, leading to the accumulation of aggregated proteotoxic species (32). Unchallenged misfolding and aggregation of proteins can lead to a variety of progressive diseases with common features despite them being caused by various proteins forming distinct aggregate species (33). These protein misfolding diseases are commonly referred to as neurodegenerative diseases, as neurons are most vulnerable to proteostasis failure (34) and consequently include afflictions with cognitive defects, such as Alzheimer's disease (AD) or frontotemporal dementia (FTD), as well as motor dysfunction diseases such as amyotrophic lateral sclerosis (ALS), Huntington's disease (HD) or Parkinson's disease (PD), although these symptoms are not exclusive (35). Among different protein folding states, amyloids, consisting of stacked β-sheets, present a thermodynamic sink and easily self-interact,

first forming oligomers and ultimately aggregating into insoluble amyloid fibrils. The formation of amyloids is a general property of peptides, although some proteins are particularly prone to it and some amyloids are functional within the cell. Proteostasis can be overwhelmed by amyloid accumulation and many amyloidogenic peptides stand at the center of specific neurodegenerative diseases (36,37).

First described over a century ago (38,39), AD has risen to be the most prominent neurodegenerative disease. AD poses a global problem, being the most common cause of dementia (40) and leading to economic and social disturbance for societies and patients (41,42). Although hereditary forms of AD exist and can manifest early in life, sporadic forms dominate (43) and while environmental factors play a role, aging is the primary risk factor (44). In hereditary cases, disease causing mutations mainly appear in the Amyloid Precursor Protein (APP) or Presenilin-1/2 (PSEN-1/2) (45). PSEN specifically affects cleavage of APP by β-&γ-secretases, leading to the release of the amyloidogenic peptide amyloid-β_{1-42} ($A\beta_{1-42}$; the 42 amino acid species is more proteotoxic than $A\beta_{1-40}$), a principal proteotoxic agent in AD (46). The generation of Aβ-peptides by cleavage through secretases from APP is required for neuronal viability and synaptic plasticity (47,48), but the ongoing proteotoxic aggregation of Aβ both challenges the PN and is exacerbated by the PN declining in age (10). In early interpretations, the role of Aβ in AD on a biochemical level is the formation of aggregates that eventually accumulate in extracellular amyloid plaques, which would then cause all downstream symptoms of the disease such as systemic dysfunction and death of neurons. Placing this cumulative, proteotoxic aggregation of Aβ at the basis of AD is the “amyloid cascade hypothesis” (49,50).

Attempts at treatment have fallen short so far and recent findings mandate significant additions to this hypothesis. In particular, the tau-protein (MAPT), forming intracellular neurofibrillary tangles in AD pathology, is believed to be equally important in proteotoxicity (51) and both peptides interact in a proteotoxic feedback loop (52). More so than amyloid plaques, the oligomers of Aβ appear to be proteotoxic and cytotoxic, indicating that insoluble amyloid plaques may be a symptom rather than causative agents (53,54). Following biochemical considerations, the “cellular phase” of Aβ proteotoxicity includes spreading into and dysfunction of the glia, the vascular system or oligodendrocytes coupled to inflammation and inhibited clearance of aggregates (55). Indeed, it could be demonstrated that soluble

Aβ species can cause membrane damage (56), further aggregation in a prion-like manner (57) and spread proteotoxicity systemically to vulnerable cells, causing neurodegeneration (58). All these eventually culminate in the “clinical phase” of AD, where memory dysfunction, loss of spatial orientation and dementia in addition to a multitude of other symptoms become progressively apparent (59). In principle, the PN can target amyloids like Aβ to stave off neurodegeneration by disaggregation or degradation and it remains unclear what makes this mechanism prevail or collapse. Moreover, clearance mechanisms such as autophagy were not only reported to fail in neurodegeneration, but subsequently exacerbate pathology (60). Therefore, modern approaches at therapy not only utilize small molecules to target amyloids, but also aim to activate and direct the PN to ameliorate pathologies like AD (34,36,61).

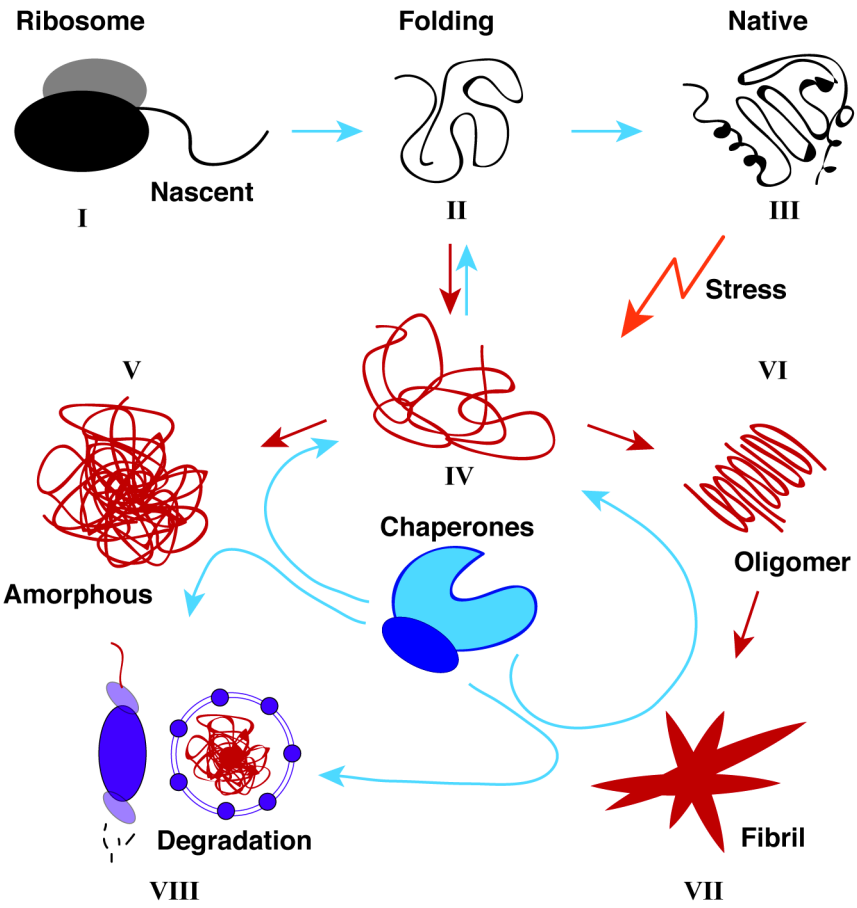

Figure 1: Introduction to proteostasis

Proteostasis is the process of proteins attaining their correct fold (black) while preventing or reversing misfolded and aggregated protein states (red) or else degradation of the off-pathway species (purple), which is aided by molecular chaperones (blue, represented by an Hsp70 member and a cochaperone). Top row, **I**: at the ribosome, a nascent polypeptide is synthesized. **II**: unfolded proteins

have to reach their correct folding state to be functional but are also at risk of misfolding **III**: native proteins can become misfolded under stress conditions (orange). Steps I-III are commonly aided by molecular chaperones. **IV**: a misfolded protein can be rescued by chaperones and return to the native folding pathway. If this fails, it is at risk of aggregation. **V**: amorphous aggregates are the insoluble product of unordered aggregation of misfolded proteins. **VI**: ordered, thermodynamically stable aggregation mediated by β-sheet interactions can lead to amyloid species of lower order (oligomers). **VII**: lower order amyloids can form large, insoluble amyloid fibrils. Misfolded and aggregated protein species (red) are often proteotoxic and deleterious, but can be disaggregated and recovered by the molecular chaperones (blue). **VIII**: off-pathway proteins can also be degraded by proteasomes or autophagy (purple) and this process is also promoted by molecular chaperones. The graphic is not to scale and represents events in a purely qualitative manner.

3.2. Small heat shock proteins

Within the PN, small heat shock proteins (sHsps) are typically described as “first line defenders”, chaperones that buffer unfolded protein substrates against aggregation in an ATP-independent fashion (11), leading to their description as “holdases” (62). The sHsps are evolutionarily old and conserved, ubiquitous molecular chaperones present in all domains of life with implications in neurodegenerative disease, healthy aging, stress resistance, cancer (63) and longevity (64). The genomes of prokaryotes or single-cellular eukaryotes (e.g. yeast) often encode one or two sHsp genes, whereas higher eukaryotes can express a large number of sHsps (65). Plant sHsps are particularly variable (e.g. 23 different sHsps in *O. sativa*), expressed constitutively, developmentally or in response to specific stressors, to different organelles, form a number of sub-families (66) and can be divided into two large classes (67). In metazoans, sHsps are not divided into sub-families, but the 10 human sHsps (also labeled HSPB1-10) still localize to different tissues and are either stress-induced or constitutively expressed. Consequently, human sHsps and their mutations are also implied in motor and neuronal diseases (68).

3.2.1. The structure and activity of small heat shock proteins

Small heat shock proteins range in size from 12 (69) to 43 kDa (12) but their critical feature is the oligomerization into quarternary assemblies of larger size (70). Heterooligomerization of different sHsps is possible (62) and conversely, a small

number of sHsps do not form oligomers (71,72). The structure of sHsps is divided into a disordered, highly variable N-terminal domain (NTD), a central, conserved α-crystallin domain (ACD) and a shorter C-terminal domain (CTD) (73). Due to their flexible nature, only a few sHsp structures have been analyzed: among others, *S. pombe* Hsp16 (74), *M. jannaschii* Hsp16.5 (75,76), *T. aestivum* Hsp16.9 (77) and αB-crystallin (the basis for the name "α-crystallin domain") or HSPB5 (78,79). The ACD consists of a β-sandwich fold and the interaction of two ACDs is the basis of sHsp dimerization, whereas the NTD and the CTDs IXI-motif mediate the assembly of dimers into higher oligomers (73). The assembly of sHsps into oligomers is highly dynamic and a single sHsp may occupy a number of oligomerization states. This plasticity is integral to sHsp function and a shift in oligomer size can lead to activation (80), as can be induced by factors such as heat (81) or reduced pH (82). Heterooligomerization enables additional stabilization and regulation: the insolubility of HSPB5 mutants could be rescued by heterooligomerization with other, native sHsps (83). In turn, excessive phase separation by the nuclear HSPB2 is regulated by HSPB3 (84). Finally, heterooligomers of HSPB5 and HSPB1 (other name: Hsp27) combine the improved thermostability of HSPB1 oligomers with the better chaperone activity of HSPB5 (85).

Larger oligomers of sHsps appear to be spherical and hollow, although this does not define their activity (73): sHsps bind unfolded protein substrates, prevent their aggregation and keep them in a folding-competent state (86). Substrate-sHsp interaction is based on exposed hydrophobic stretches and sHsps can facilitate substrate refolding by ATP-dependent molecular chaperones after forming complexes of variable stoichiometry (87-89). While the dynamic subunit exchange of sHsp oligomers is required for activity, the sHsp-substrate interaction is not dynamic and sHsps do not spontaneously release their substrate (90). Part of the sHsps are promiscuous chaperones while others are more substrate-selective, but all sHsps are sensitive to the surrounding conditions and prevent aggregation of different substrates with varying efficiency (91). Recent studies hinted that the substrate binding of sHsps is based on their domain structure and flexibility: amorphous aggregates are bound by the intrinsically disordered NTD of HSBP5, whereas the fibril forming $A\beta_{1\text{-}40}$ was recognized by the β-sandwich of the ACD (92). Besides data that a heterologous sHsp can alleviate the proteotoxicity of Aβ (93) and that HSPB5

inhibits Aβ fibril elongation (94), other amyloids implied in neurodegeneration are also sHsp substrates: HSPB5 and HSPB1 can inhibit aggregation, elongation and cytotoxicity of α-synuclein fibrils *in vitro* and *in vivo* (95,96). HSPB1 also recognizes tau protein via the ACD (97) and HSPB5 inhibits aggregation and cytotoxicity of Huntingtin (98). Upon co-aggregating with protein substrates, sHsps can still cooperate with ATP-dependent chaperones. Both in prokaryotes and eukaryotes, sHsp-substrate aggregates have an altered shape and are more accessible to disaggregation by Hsp100 members in combination with Hsp70 members (99,100) and in metazoans, by Hsp70 members in cooperation with Hsp110 members (24,25).

3.2.2. SHsps impact protein aggregation beyond being “holdases”

The consideration that sHsps generally perform a singular inhibition of aggregation or “holdase” function is contrasted by the fact that often a multitude of sHsps are expressed in parallel in the same tissue with specific interactions (91,101,102). One factor to integrate the activity of sHsps with the Hsp70 chaperones is the NEF BAG3 (103). Following this, the specific interaction of HSPB8 with BAG3 is required for the aggresome-deposition of ubiquitinated substrates and subsequent recruitment of the autophagy marker p62 (104), tying sHsp activity to the Hsp70-BAG3 autophagy induction (31). More recently, even a direct involvement with p62 and the formation of autophagosomes has been demonstrated (105), implying that HSPB1 or HSPB8 could promote autophagy rather than holding substrates for refolding. Other than autophagy, pro- and eukaryotic sHsps were found to act as “sortases” or “sequestrases” and direct the deposition of aggregated proteins to specific locations (106-108). Furthermore, bacterial YocM or yeast Hsp42 promote cytoprotective aggregation of their substrates as “aggregases” (109,110). Distinct sHsps may then stabilize these aggregates or prime them for disaggregation (111), so they become available in the presence of sufficient Hsp70 chaperones (112) or their specific cochaperones (113).

Indeed, data from *C. elegans* indicate that progressive protein aggregation is a general property of aging (114) coupled to a physiological, age dependent change in PN activity (115). In yeast, this aggregation was shown to be selective, that is, potentially proteotoxic species can be sequestered in this manner to protect the cell (116) and salvageable proteins can be saved for later recovery (117). This

aggregation may be native-like and is directly required for continued viability after stress situations (118,119). For *C. elegans* it was demonstrated that the sHsps (HSP-16.48, SIP-1 / HSP-20A, HSP-17, HSP-21 / Y55F3BR.6, HSP-43) are enriched in such aggregates, more so in the long-lived *daf-2* mutants, and that their depletion could impede this pro-longevity aggregation (120). Promoting aggregation, even into amyloid fibrils, was also shown to be a defensive strategy against amyloidogenic peptides such as *RNQ* (121) or Huntingtin (122). Here as well, sHsps were shown to aid the assembly of cytotoxic amyloid oligomers into larger, insoluble species (123-125). The combination of these recent data indicate that beyond the canonical "holdase function", sHsps may work as "aggregation managers" directing the fate of aggregating proteins as "sequestrases", "sortases" and "aggregases".

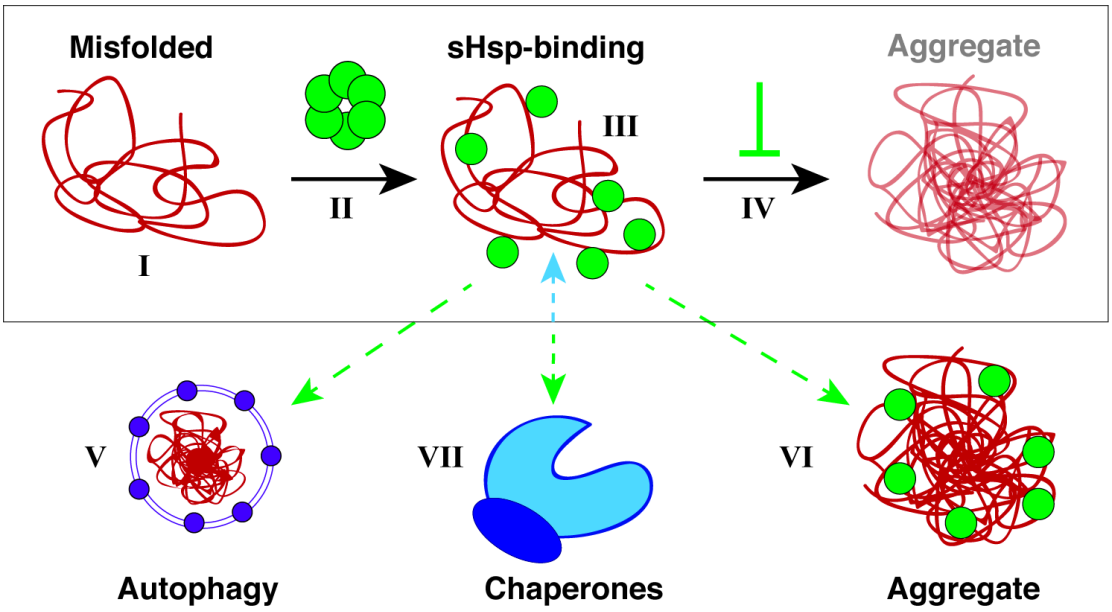

Figure 2: Overview of sHsp activity

The rectangle marks the canonical activity of sHsps. If a protein is misfolded (**I**), it can be recognized by a pool of sHsps in the cell (**II**, depicted as an oligomer). Binding of sHsps results in sHsp-bound species of misfolded proteins (**III**). The multiple mechanisms of sHsps activation or the mode of sHsp-substrate interaction are not depicted here. The formation of insoluble aggregates is inhibited by the sHsps (**IV**). Dashed arrows represent more recent insights into sHsp activity: sHsps may promote degradation (**V**) or selective, site specific aggregate formation (**VI**). Substrate-sHsp binding may also alter how chaperones interact with protein substrates (**VII**).

3.3. The model organism *C. elegans*

The nematode *C. elegans* was first acknowledged in 1974 by S. Brenner as a model organism for biology accessible to genetic studies and with metazoan features such as distinct tissues, e.g. neurons or muscles. *C. elegans* grow into adults of about 1 mm length within 4 days and exist as hermaphrodites with 6 chromosomes or less common males with 5 chromosomes, lacking the gonosome (126). *C. elegans* feeds on bacteria, including *E. coli* in laboratory conditions, and each hermaphrodite lays around 300 eggs during its average lifespan of 2-3 weeks (127). Whole genome sequencing revealed more than 19 000 different genes and a high degree of conservation to the human genome (128), with at least 80 % of genes conserved between both (129). The nematodes are most viable at ambient temperature (around 20 °C), develop from eggs (embryos) to egg-laying adults passing 4 larval stages (L1-L4) and can be kept on agar media (130). Notably, *C. elegans* development is invariant, meaning that starting with the embryo, fixed cell lineages develop, forming adults following a deterministic program where individual cells remain traceable (131). The simple organism has an alimentary system: the muscular pharynx pumping food into the intestine ending in an anus. Additionally, the nematodes have a hypodermis, body wall muscle, an excretory tract, gonads and neurons, resulting in precisely 959 cells (“eutely”) in hermaphrodites and 1031 cells in males (132). The high level of conservation, genetic accessibility and simple structure lead to *C. elegans* being recognized as a model organism with relevance to human physiology and disease (133).

3.3.1. *C. elegans* as a model in aging, proteostasis and neurodegeneration

The percentage of people in the world who are “old” – aged over 60 or over 80 years, is projected to continuously increase over the coming decades (134) and aging correlates with declining proteostasis (135). Consequently, aging is a risk factor for disease, including neurodegeneration. Key findings regarding mechanisms of longevity and health and disease in aging have been made in *C. elegans*, a valuable model organism in this field (136). As a poignant example, mutations in the *C. elegans* genes *age-1* or *daf-2* were demonstrated to drastically extend organismal lifespan at the cost of fertility (137,138). Both share a common pathway dependent

on the downstream factor *daf-16* (139), a fork head transcription factor linking this longevity pathway to insulin-like signaling (ILS) (140). Most importantly, this pathway is conserved in humans (141) and thereby *C. elegans* research unveiled hormonal and nutrient signaling as a pillar in organismal aging (142). A possible pivot of this pathway was identified in stress resistance: long lived *C. elegans* mutants have increased thermotolerance (143). ILS as a factor of longevity was indeed shown to depend on *hsf-1*, a general heat stress regulator inducing the expression of molecular chaperones (among others), thus revealing the PN as an agent of longevity (144). Like aging, stress response is cell non-autonomous (145) and its eventual decline impairs chaperone activity and enables protein aggregation as key factors of aging (114,115). The highly heat-inducible *hsp-16* family is one arm of the ILS / *hsf-1* controlled chaperones which mediate longevity (146) and belong to the 16 different sHsps encoded in the *C. elegans* genome (147). The discoveries regarding the conserved connection between aging, stress and proteostasis have positioned *C. elegans* as a platform for modeling neurodegenerative disease: amyloidosis caused by MAPT (148), α-synuclein (149) or polyQ peptides (150) has been introduced into the *C. elegans* system. Moreover, a number of AD models expressing Aβ have been realized in *C. elegans*. The first model of muscular Aβ revealed the formation of amyloid fibrils *in vivo* (151) and intracellularly (152). While the model expressed $A\beta_{3\text{-}42}$ instead of the intended species $A\beta_{1\text{-}42}$ (153), this could be remedied in a subsequent model (154). The addition of a neuronal model completed an initial set of AD phenotypes in *C. elegans*: muscular expression leads to progressive paralysis and neuronal expression causes defects in chemotaxis and learning (155). The models lacked fluorescent labeling and visualization of Aβ was dependent on extrinsic dyes (152), whereas recent attempts at GFP-labeling revealed non-physiological aggregation behavior in tagged Aβ species (156). Utilizing the fixed cell lines of *C. elegans*, modeling was furthered by expressing Aβ in specific subsets of neurons (157-159). More importantly, the sHsp HSP-16 was shown to interact with heterologous Aβ (160) and overexpression could reduce proteotoxicity of Aβ (161). In summary, *C. elegans* is a powerful system to model amyloidosis *in vivo* and cell-specifically, correlating AD pathology with aging and a complex PN that is amenable to genetic and pharmacologic modulation.

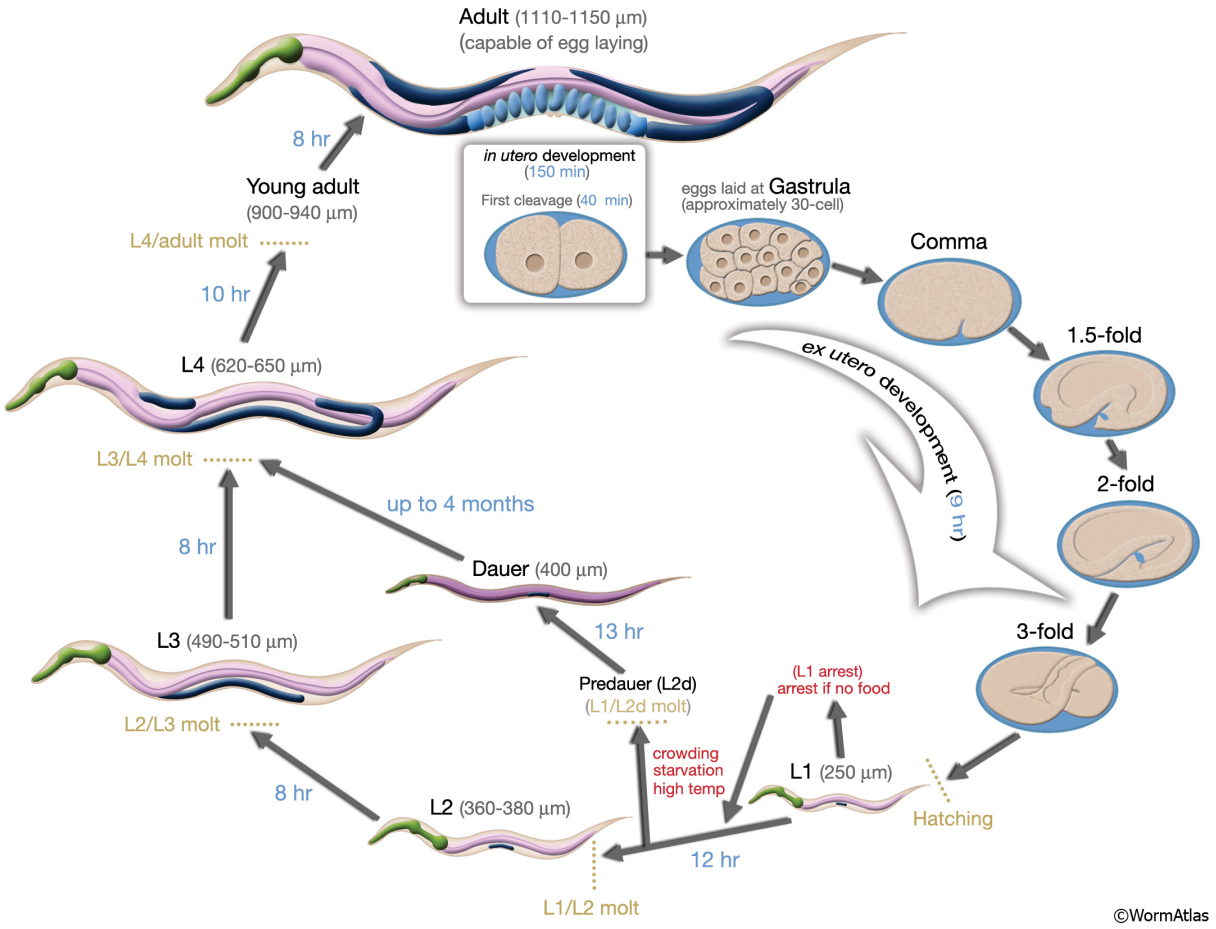

Figure 3: Overview of *C. elegans* life cycle and shape

A depiction of *C. elegans* development, starting with an egg, laid by an adult hermaphrodite, at the center top. Continuing clockwise: stages of development *in ovo* & *ex utero* (eggs not to scale) culminating in hatching. The four larval stages L1-L4 are depicted, underlining their increase in size. Each stage transition requires molting. The possibility of larvae entering a stagnant “Dauer” stage under unfavorable conditions is indicated. Blue letters indicate the relative time spent in each stage. Center top: reproductive adult hermaphrodite with depictions of the pharynx (green), intestine (mauve), gonads (dark blue) and eggs *in utero* (light blue), the most prominent structures. This graphic was taken from *WormAtlas* (162) and is based on work by Byerly *et al.* (130).

3.4. Aims of this study

The role of small heat shock proteins in the proteostasis network has been extensively described over the last three decades, but many knowledge gaps remain in their understanding. Based on previous advances in researching the versatility of sHsps and their unexpected roles in protein aggregation, I aimed to analyze as of yet non-canonical activities of sHsps in the background of *C. elegans* as a metazoan

model organism. Amyloid pathologies such as AD are protein aggregation diseases and therefore inextricably linked to molecular chaperones, including the sHsps. Yet, a consistent model of labeled Aβ pathology in *C. elegans* did not exist. Consequently, I set out to work on the development of an improved model of amyloidosis in *C. elegans* to establish a platform for analyzing the role of molecular chaperones in metazoans *in vivo*. The questions addressed were as follows:

3.4.1. Novel activities of metazoan sHsps

1. Among the numerous sHsps of *C. elegans*, do some have non-canonical chaperone activity?

2. What effect does their chaperone activity have *in vitro* and does it include metazoan pro-aggregation activity?

3. Can the non-canonical activity of *C. elegans* sHsps be verified *in vivo* and which physiological impact does it have?

3.4.2. Improved models of protein folding disease in *C. elegans*

1. Can sub-stoichiometric labeling of Aβ expressed in *C. elegans* provide “native-like” fibril formation?

2. Does this model reiterate established phenotypes of Aβ pathology?

3. Can the novel model reveal new corridors for understanding amyloid pathogenesis and its treatment?

4. Results

4.1. Small heat shock proteins

Small heat shock proteins (sHsps) have been long known to act as first-line defenders and buffers against protein aggregation (11). However, the high number of sHsps in metazoan genomes (10 in humans, 16 in *C. elegans*) hints at diversified modes of action and recent research has brought to light a more complex field of sHsp activities. Notably, this includes facilitated aggregation and deposition in cellular loci of aggregation (163).

4.1.1. Molecular cloning and recombinant expression of sHsps

I set out to elucidate such new modes of sHsp activity by utilizing the availability of *C. elegans* for *in* and *ex vivo* analysis, combined with *in vitro* analysis of sHsp activity, including sHsps which had been analyzed before. The CDS of six sHsps were cloned for His-SUMO-tagged overexpression and subsequent protein purification, with a focus on sHsps that were not extensively analyzed before. In particular, I included *hsp-17*, which was recently analyzed in a recombinant context in *E. coli* (164) and had not been considered in previous studies (165). The construct for *hsp-12.6* was available in Kirstein Laboratory (cloned by Ellen Malovrh). All sHsp CDS were cloned into pSumo to allow for tagged overexpression, purification and subsequently, seamless removal of the His-SUMO-tag by SUMO protease. Table 1 below contains a list of sHsp CDS which were cloned in this study for SUMO-tagged overexpression, including attempts at purification:

Table 1 sHsp CDS available for SUMO-tagged overexpression

sHsp	**Results of purification**
hsp-12.6	Soluble
hsp-17 (Isoform B)	Soluble
hsp-20B / ZK1128.7	Insoluble
hsp-21 / Y55F3BR.6	Insoluble
hsp-25 (Isoform A & B)	A insoluble, B soluble
hsp-43 (Isoform	Insoluble

Names of proteins are given as published, particularly under (147).

HSP-17 was previously excluded from thorough analysis of *C. elegans* sHsps (165) and recent analysis, in a non-physiological context, indicated that it does not exhibit typical sHsp activity (166). HSP-17 was reported to colocalize with age dependent aggregates (120) and preliminary analysis revealed that soluble expression was possible. In the light of data indicating that HSP-17 did not have the classic “holdase” activity, I therefore hypothesized that HSP-17 could play a non-canonical role in protein aggregation and chose it for thorough investigation. HSP-12.6 was included in the study because it was previously analyzed and found to exhibit only little molecular chaperone activity (71), making it an apt control for *in vitro* studies of sHsp activity. Conversely, I did not pursue investigation of other sHsps that were previously described: SIP-1 (82) and HSP-25 (Isoform B; A was insoluble as reported) (167). ZK1128.7 and HSP-43 were insoluble in my hands as reported previously (12,168), which was also true for the completely unresearched Y55F3BR.6 (HSP-21).
After overexpression of recombinant proteins, purification of HSP-17 and HSP-12.6 was carried out by IMAC, followed by anion exchange chromatography. HSP-17 could be isolated as a pure peak from AEC:

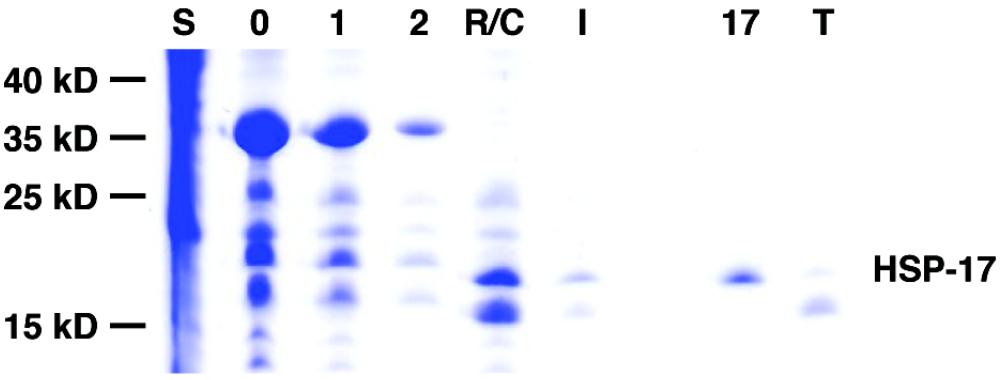

Figure 4: Purification of recombinant HSP-17

SDS-PAGE of samples taken during an exemplary purification of HSP-17. S is the total, unpurified, soluble bacterial lysate; 0-2 are fractions eluted from IMAC; R/C is the rebuffered, pooled sample after removal of SUMO-tag; I is the diluted input for AEC; 17 is the peak containing HSP-17 received from AEC; T is the peak containing SUMO-tag that eluted shortly after. The peak “17” or comparable peaks from other purifications were used for further *in vitro* analysis.

The purified sample of HSP-17 shows a low concentration (approximately 0,3 mg / ml or 20 µM) and was concentrated for *in vitro* analysis by pooling samples in centrifugal filter units with a low MWCO, as necessary.
HSP-12.6 was purified analogously. Notably, the yields of purification were higher than the binding capacity of the anion exchange column used, leading to the purest fraction being washed out prior to elution:

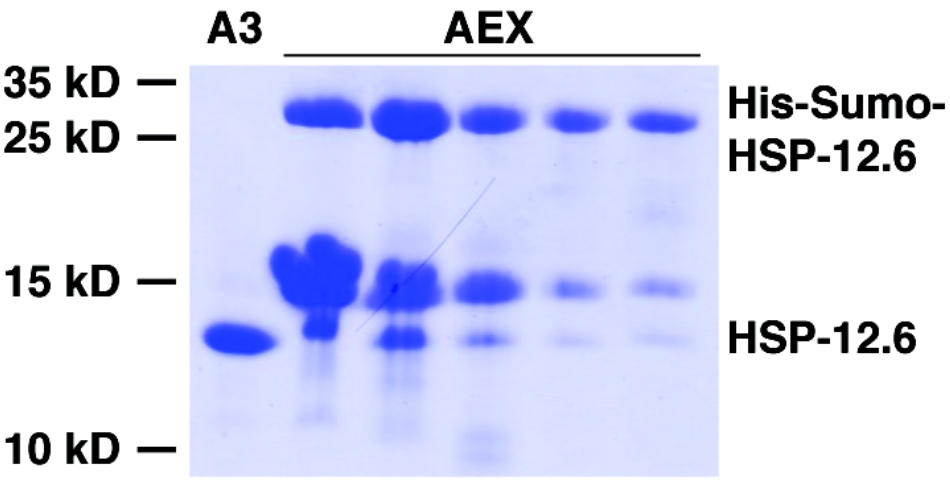

Figure 5: Purification of recombinant HSP-12.6

SDS-PAGE of samples taken during purification of HSP-12.6. AEX marks five peaks eluted from the anion exchange column containing, HSP-12.6, SUMO-tag and SUMO-tagged HSP-12.6; A3 is the fraction that was collected before gradient elution and contains pure HSP-12.6. “A3” was used for further *in vitro* analysis

I noticed that the purification of HSP-17 yielded low amounts of pure protein and wanted to ensure that the sample is indeed intact HSP-17. Intact protein QToF-MS analysis was used to determine the total mass and purity of my protein sample. The experiment yielded one peak containing protein, which was deconvoluted to a major peak of 17417,5 Da (theoretical mass of HSP-17, isoform B: 17417,52 Da) and an unidentified minor peak of 17433,5 Da:

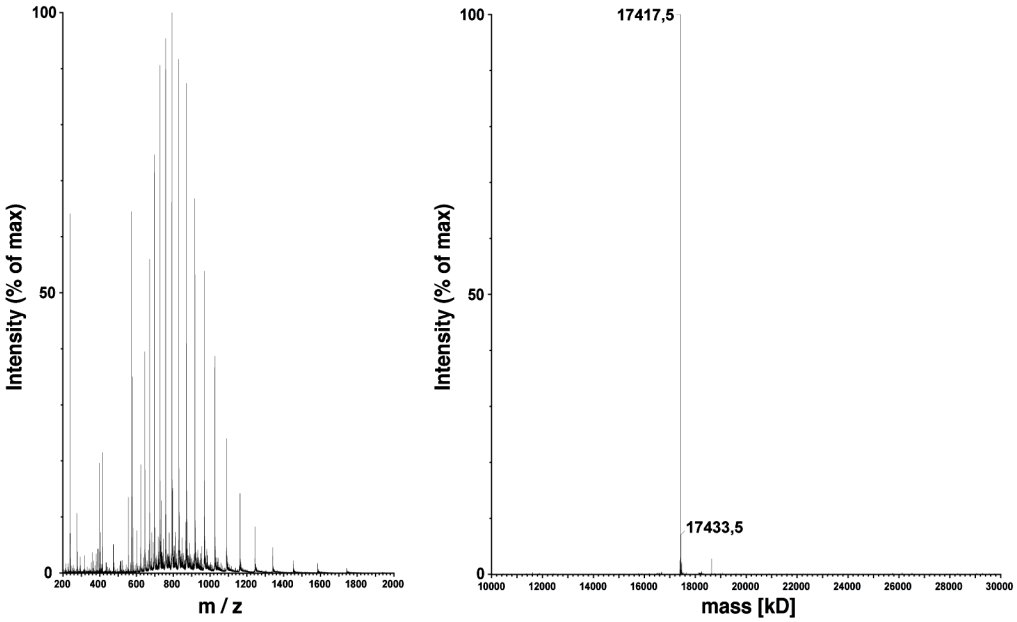

Figure 6: QTof-MS analysis of purified HSP-17

QToF-MS analysis of purified HSP-17. The left side shows the m/z spectrogram of the single protein peak identified (peaks are normalized to the highest peak, values are given in arbitrary units). For the right side, peaks ranging from an absolute m/z ratio between 600 and 1700 were deconvoluted and the x-axis shows the absolute peptide mass. The sample was applied as received from purification and operation of the device was carried out by A. Baumann.

As sHsps have an intrinsic propensity to form higher-order oligomers (62), I also set out to confirm the formation of oligomers by HSP-17 in a native context. To this end I employed SEC to calibrate the elution volume of my sample against proteins of known mass:

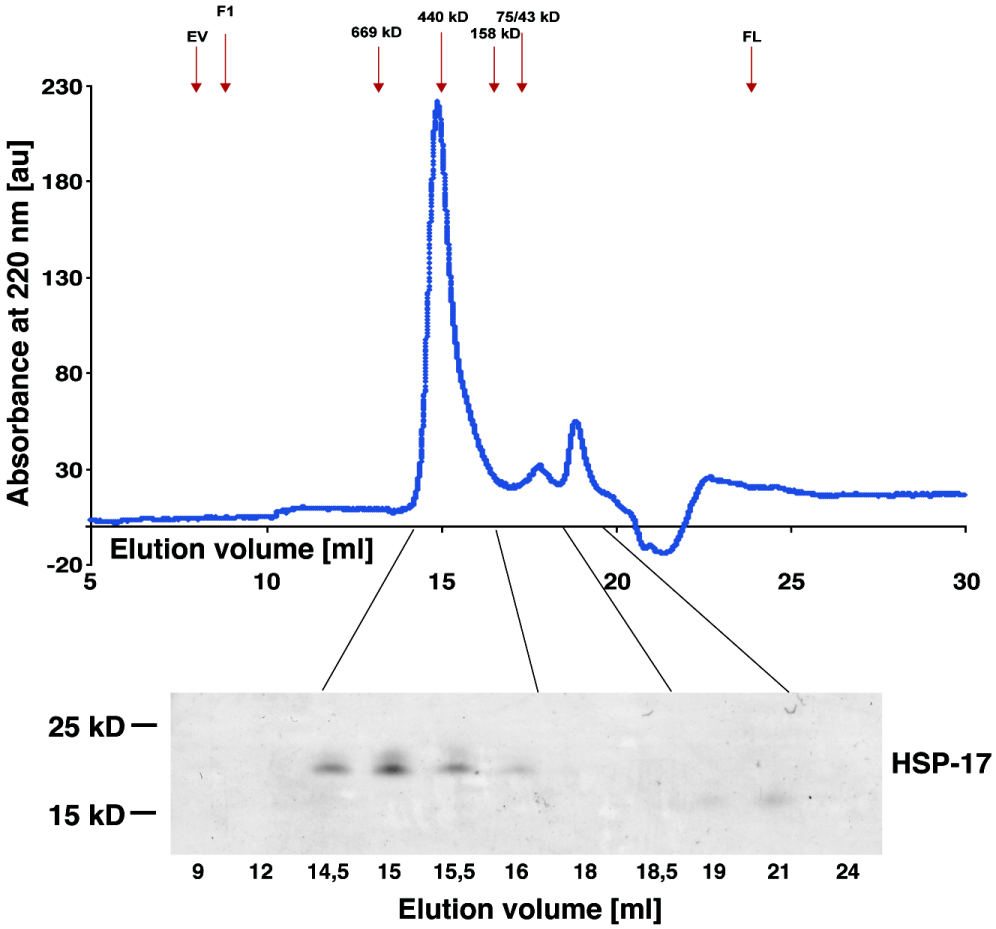

Figure 7: Analytical SEC of purified HSP-17

SEC analysis of purified HSP-17. 100 µl of HSP-17 at a concentration of 1,5 mg / ml were loaded onto an analytical column, which had been calibrated with a high molecular weight calibration kit (indicated by red arrows). Absorbance was measured at 220 nm and is shown in arbitrary units on the y-axis, with the x-axis showing total elution volume. Arrow EV marks the exclusion volume (approximately 8 ml), F1 marks the start of sample fractionation and FL marks the end of sample fractionation. A selection of elution fractions was analyzed by SDS-PAGE, as shown on the bottom.

The peak observed at an elution volume of around 15 ml (> 440 kDa) corresponds to HSP-17, as shown by SDS-PAGE, and indicates formation of an oligomer of around 460 kDa, corresponding to a 26-mer. A similar result was published previously in a study where HSP-17 was purified from insoluble material (166) and I interpret this as confirmation of my sample as intact HSP-17. A second peak, eluting around 19 ml, is likely a trace of SUMO-tag remaining from purification (compare Figure 4). Analogously, I used SEC to assess the native state of HSP-12.6:

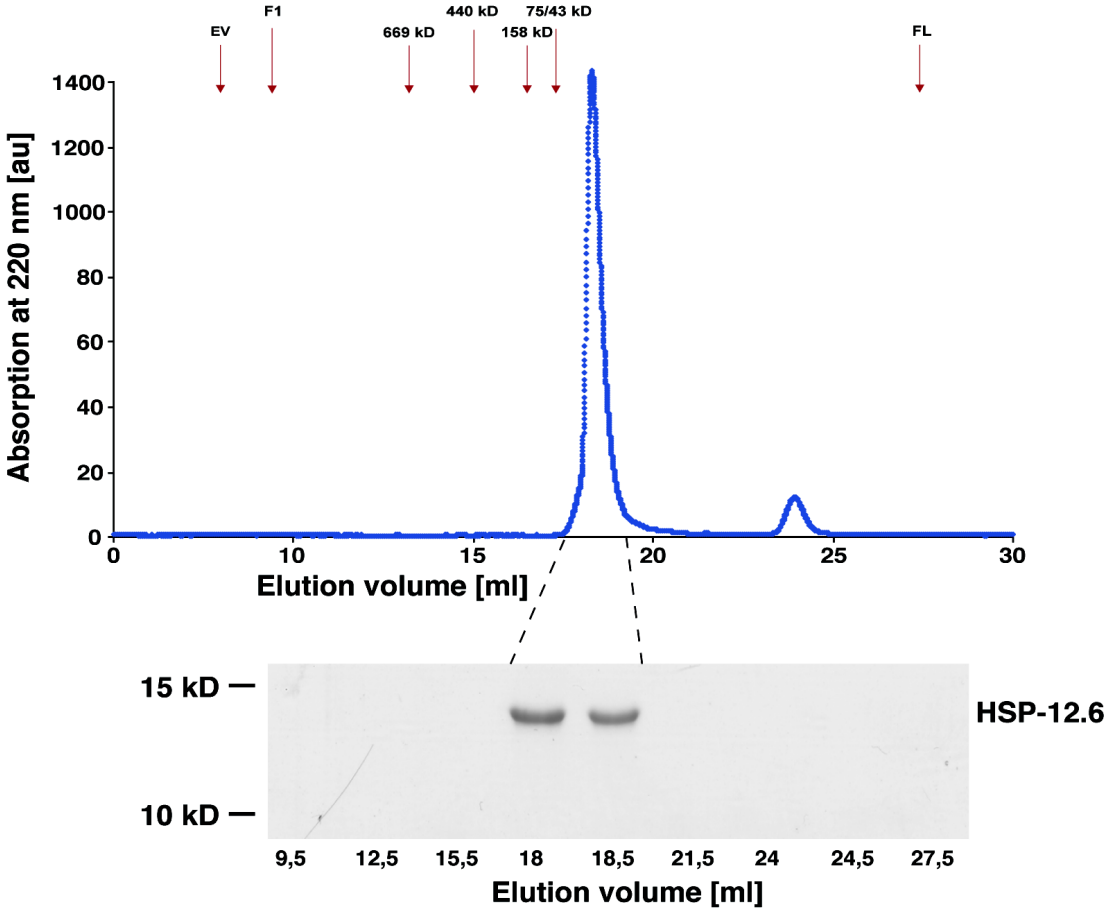

Figure 8 Analytical SEC of purified HSP-12.6

SEC analysis of purified HSP-12.6. 100 µl of HSP-12.6 at a concentration of 5 mg / ml were subjected to an analytical column, which had been calibrated with a high molecular weight calibration kit (indicated by red arrows). Absorbance was measured at 220 nm and is shown in arbitrary units on the y-axis, with the x-axis showing total elution volume. Arrow EV marks the exclusion volume (at approximately 8 ml), F1 marks the start of sample fractionation and FL marks the end of sample fractionation. A selection of elution fractions was analyzed by SDS-PAGE, as shown on the bottom.

The peak at an elution volume of 18 ml corresponds to HSP-12.6, which was confirmed by SDS-PAGE, and I interpret the peak around 24 ml as non-protein material. The elution volume of HSP-12.6 indicates an oligomer size of around 25 kDa (corresponding to a dimer), as described previously (71), confirming my HSP-12.6 samples to be intact and pure.

4.1.2. *In vitro* analysis of HSP-17 activity

It has been long known that sHsps can bind unfolded protein substrates, delay or prevent their aggregation, and keep them in a refolding-competent state (86,169). To assay the molecular chaperone activity of the purified HSP-17, I performed static light scattering assays. This method has been used frequently to demonstrate that sHsps can prevent or delay the aggregation of model substrates such as citrate synthase (CS), malic dehydrogenase (MDH) or glyceraldehyde 3-phosphate dehydrogenase (GAPDH) (91).

When performing analysis of static light scattering on CS, I found that even a high excess of HSP-17 is not sufficient to completely prevent aggregation of CS, however, there is a concentration dependent delay of aggregation by adding HSP-17:

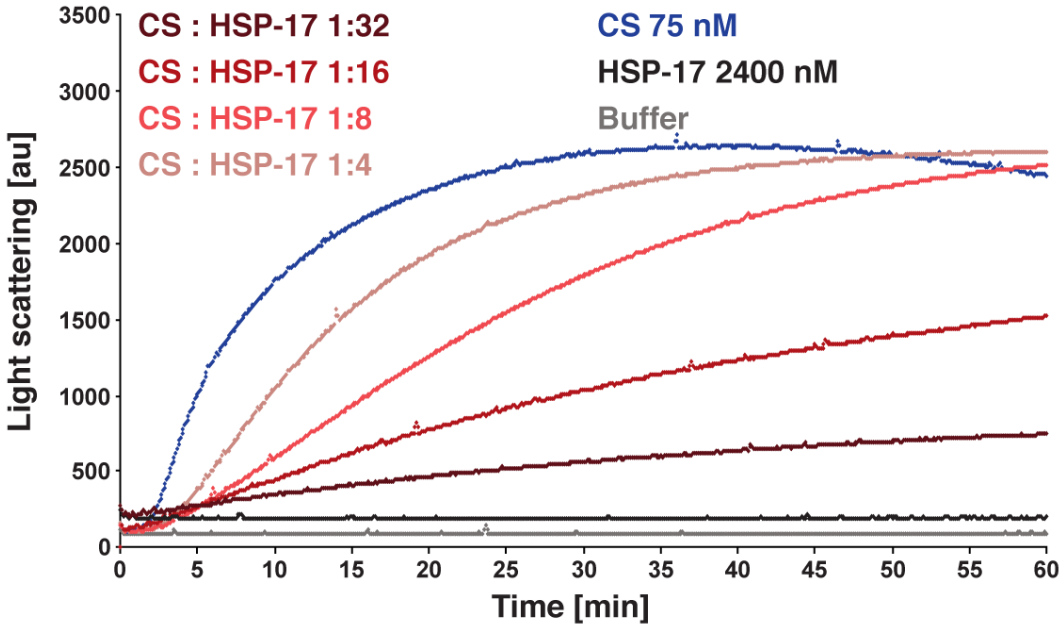

Figure 9: HSP-17 can delay the aggregation of CS

Static light scattering analysis of 75 nM CS, alone (blue curve), or in the presence of increasing concentrations of HSP-17 (red curves, darker shades of red indicate higher concentrations, as visible in the legend). All curves are averages of triplicate measurements. The highest concentration of HSP-17 used, 32-fold / 2400 nM, was analyzed by itself under the same conditions (black curve). The buffer used was also analyzed (grey curve). Light scattering intensity is given in arbitrary units (au).

When performing analogous experiments with GAPDH, the observed inhibition-of-aggregation activity was comparable and only higher concentrations of HSP-17 could delay, but not prevent aggregation of the model substrate:

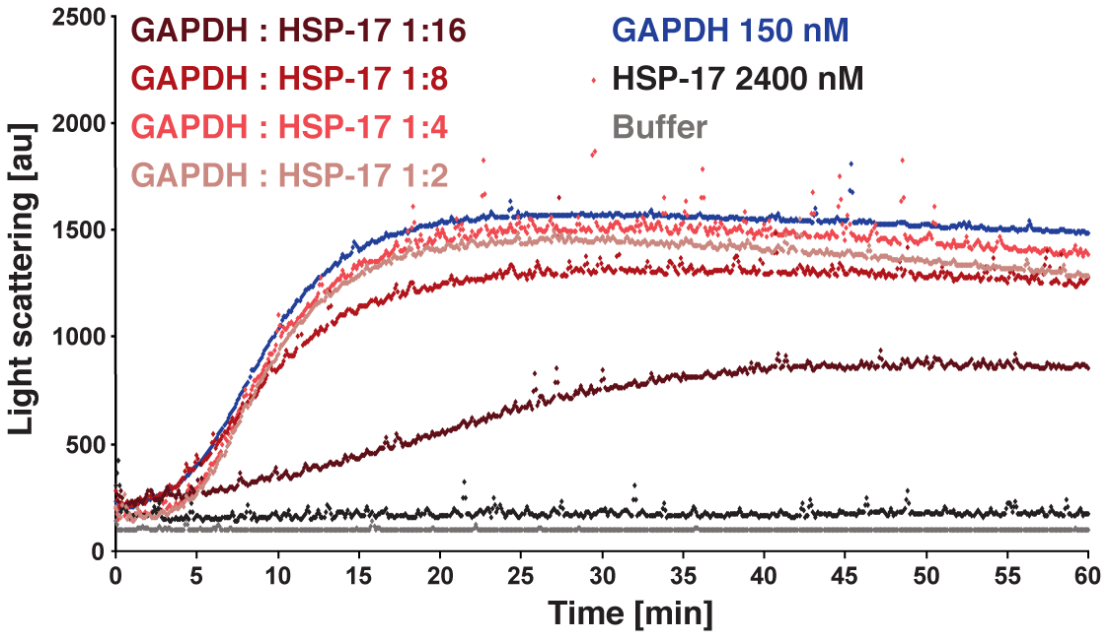

Figure 10: HSP-17 can delay the aggregation of GAPDH

Static light scattering analysis of 150 nM GAPDH, alone (blue curve), or in the presence of increasing concentrations of HSP-17 (red curves, darker shades of red indicate higher concentrations, as visible in the legend). All curves are averages of triplicate measurements. The highest concentration of HSP-17 used, 16-fold / 2400 nM, was analyzed by itself under the same conditions (black curve). The buffer used was also analyzed (grey curve). Light scattering intensity is given in arbitrary units (au).

Based on this observation I concluded that HSP-17 can perform the classical “holdase” activity of sHsps, but only in a limited manner.

Asking whether this is a general activity of HSP-17, I continued by analyzing the activity of HSP-17 on MDH in the same format. Notably, I was unable to observe inhibition of aggregation by HSP-17 as instead, the aggregation of MDH commenced sooner and lead to higher total signal intensities in the presence of HSP-17, even at sub-stoichiometric ratios:

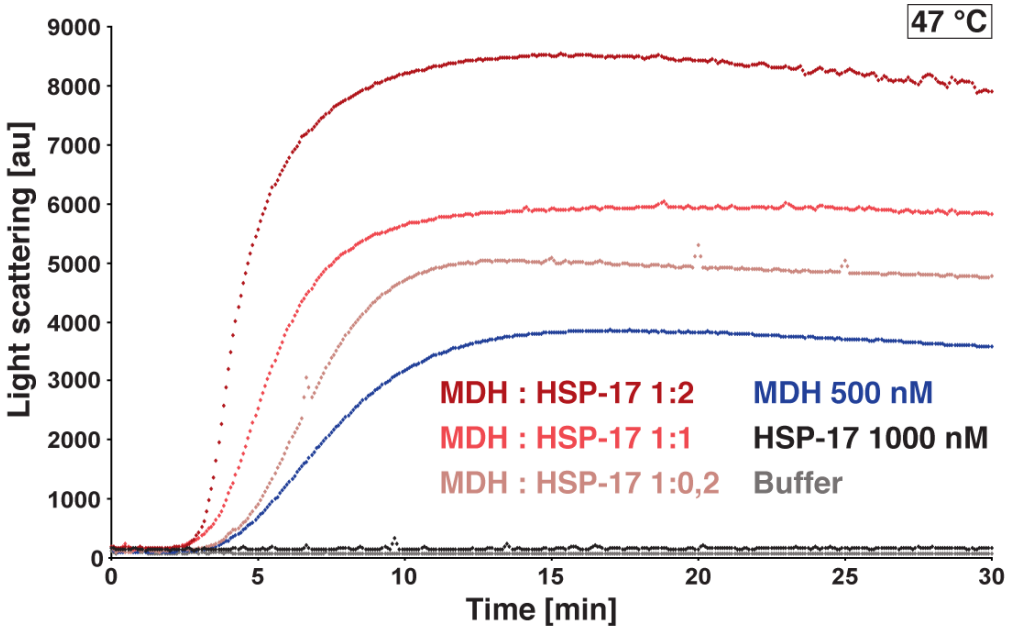

Figure 11: HSP-17 enhances the aggregation of MDH at 47 °C

Static light scattering analysis of 500 nM MDH, alone (blue curve), or in the presence of increasing concentrations of HSP-17 (red curves, darker shades of red indicate higher concentrations, as visible in the legend). All curves are averages of triplicate measurements. The highest concentration of HSP-17 used, 2-fold / 1000 nM, was analyzed by itself under the same conditions (black curve). The buffer used was also analyzed (grey curve). Light scattering intensity is given in arbitrary units (au).

This observation is unusual as it suggests that HSP-17 speeds up the formation of MDH aggregates, which does not match described sHsp activity. I took note of recent observations that yeast Hsp42, one of the two sHsps in yeast, was shown to enable aggregation of MDH at otherwise non-aggregating conditions, which was dubbed “aggregase” activity (110). In the assay described, MDH was subjected to 41 °C, which only allows for slow and incomplete aggregation. Addition of Hsp42 lead to faster aggregation kinetics and a plateau of signal.

I reconstituted this experimental setup with *C. elegans* HSP-17 to investigate if HSP-17 could promote aggregation of MDH at 41 °C. I found that at stoichiometric ratios, HSP-17 could enable the formation of MDH aggregates, as shown by signal plateaus within 60 minutes of measurement:

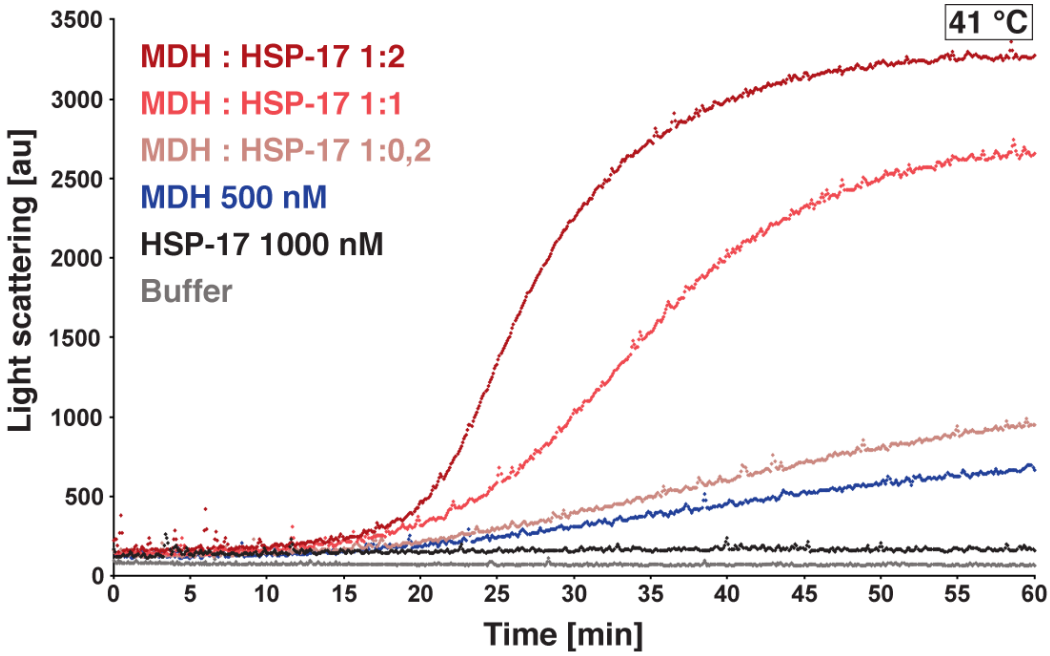

Figure 12: HSP-17 enables the aggregation of MDH at 41 °C

Static light scattering analysis of 500 nM MDH, alone (blue curve), or in the presence of increasing concentrations of HSP-17 (red curves, darker shades of red indicate higher concentrations, as visible in the legend). All curves are averages of triplicate measurements. The highest concentration of HSP-17 used, 2-fold / 1000 nM, was analyzed by itself under the same conditions (black curve). The buffer used was also analyzed (grey curve). Light scattering intensity is given in arbitrary units (au).

I considered the possibility that these observations stem from buffer effects or simple molecular crowding and that any protein added to the aggregation analysis of MDH at 41 °C or 47 °C may produce similar signals in static light scattering. As a first control, I repeated the same experiments with HSP-12.6. HSP-12.6 was reported to not have the classic molecular chaperone activity of sHsps. In comparable assays, HSP-12.6 was titrated to up to 225-fold excess over its substrate with little impact on aggregation (71). I observed at both 41 °C and 47 °C that HSP-12.6 did not affect the aggregation of MDH if added at the same concentration as HSP-17 (see supplementary Figure 1). I conclude that addition of HSP-17, but not *any* sHsp can promote the aggregation of MDH under the given conditions.

It is also conceivable that HSP-17 could delay the aggregation of MDH, as shown for CS and GAPDH in Figures 9 & 10, but the assay conditions chosen for MDH prohibit the inhibition of aggregation *in general*. I therefore utilized HSPB5, also known as αB-crystallin, a viable molecular chaperone (169). HSPB5 should also be able to

inhibit the aggregation of MDH (91) and I applied it under the same assay conditions as before:

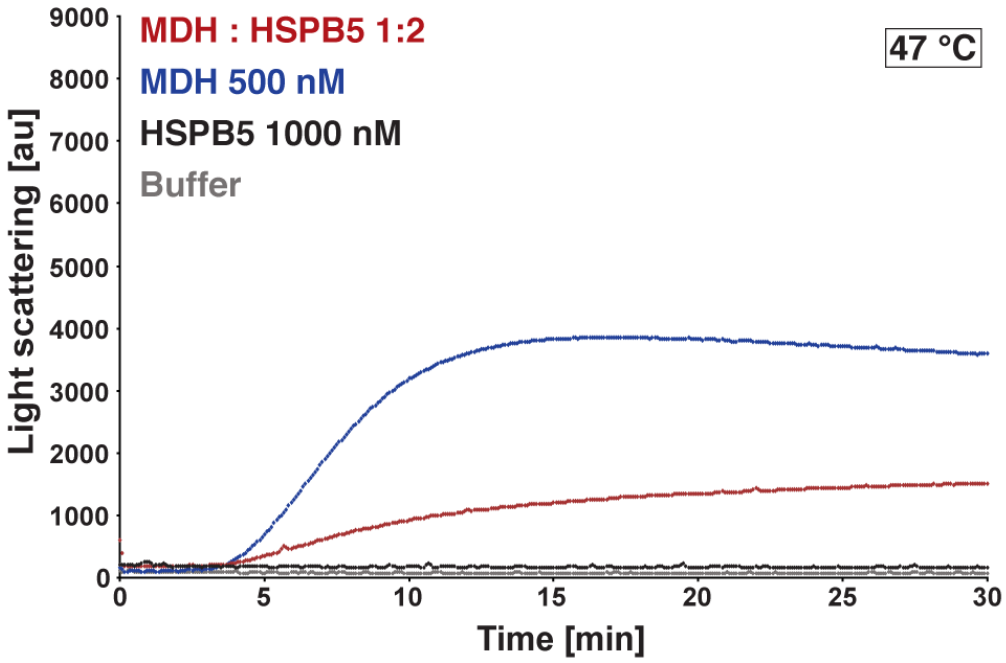

Figure 13: HSPB5 delays aggregation of MDH at 47 °C

Static light scattering analysis of 500 nM MDH, alone (blue curve), or in the presence of increasing concentrations of HSPB5 (red curve). All curves are averages of triplicate measurements. The highest concentration of HSPB5 used, 2-fold / 1000 nM, was analyzed by itself under the same conditions (black curve). The buffer used was also analyzed (grey curve). Light scattering intensity is given in arbitrary units (au).

At 47 °C, as little as two-fold excess of HSPB5 is sufficient to delay the aggregation of MDH. I conclude that it is possible to observe molecular chaperone activity under my assay conditions and – combined with the observation that HSPB5 does not affect aggregation of MDH at 41 °C (see supplementary Figure 2) and the findings for HSP-12.6 – that the pro-aggregation activity is a specific feature of HSP-17.

The obtained data indicate that HSP-17 can act as a molecular “aggregase”. For yeast Hsp42, this activity was linked to an N-terminal “prion-like” domain which was reported to be integral for promoting aggregation (170) (see supplementary Figure 3). Thus, the HSP-17 protein sequence was analyzed with the online tool *PLAAC* to test for prion-like features:

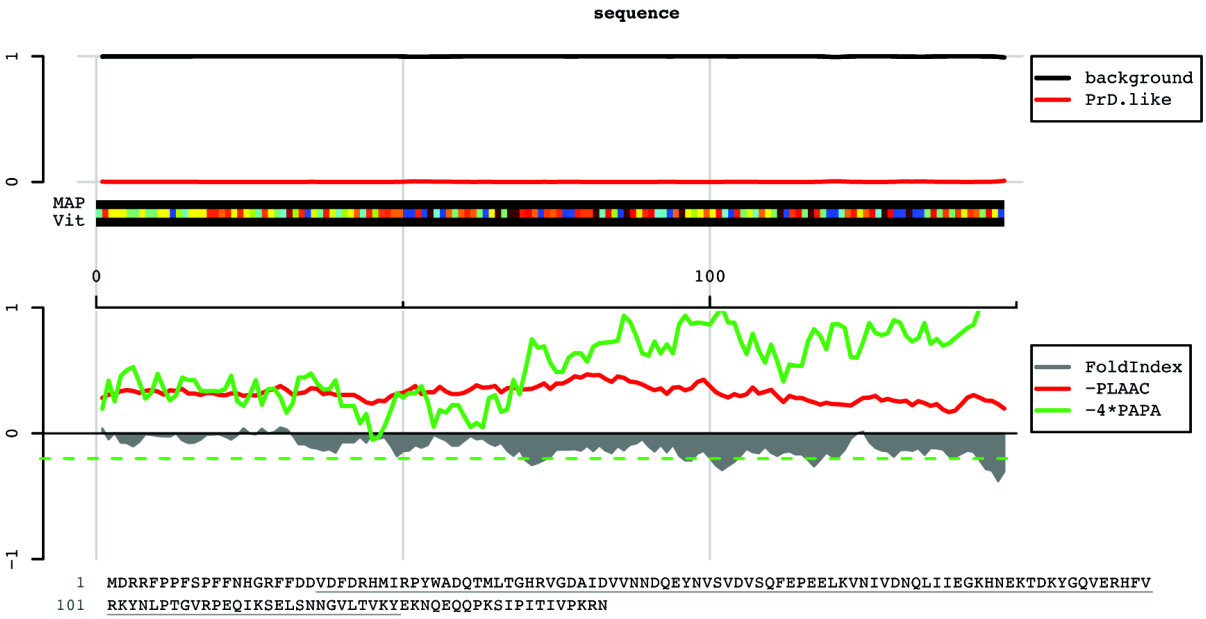

Figure 14: HSP-17 does not have a prion-like domain

Output of a *PLAAC* analysis of the primary sequence of HSP-17 (isoform B), assuming a *C. elegans* background and using a frame of 30 amino acids. On the top, the likelihood of the input sequence (with the x-axis ranging from N- to C-terminus) being like the species background (here: *C. elegans*, black) or prion-domain like (red) is indicated. In the segment below, each colored bar indicates one amino acid, with blue-green colors indicating a higher prion-likelihood and orange-red indicating a lower likelihood. The bars above and below indicate the prion-domain likeness by map algorithm (MAP) or Viterbi algorithm (VIT) (in red or black). The tool integrates other scoring methods to increase its accuracy, as shown below: the measure of intrinsic disorder, potentially coinciding with prion-likeness, is given (*FoldIndex*, grey). *PAPA* (green) indicates a related, non-redundant algorithm to identify prion-like domains (lower values indicate prion-like domains). The dashed green line indicates a threshold for prion-likeness in *PAPA*. Both parameters are provided to supplement *PLAAC* (red). Mathematical transformation (*PLAAC* multiplied by -1, *PAPA* multiplied by -4) are used to visualize all graphs in a similar frame. *PLAAC* could not determine a *COREscore* and the LLR (log-likelihood ratio) is -7,176 (171).

As HSP-17 did not seem to have any prion-like properties, I concluded that the exact interaction site required to enhance the aggregation of model substrates differs between the two proteins. I also took note that Hsp42 can inhibit the aggregation of MDH under the right conditions (170). Since Hsp42 is significantly larger (42,8 kD) than HSP-17 (17,4 kD), I surmise that Hsp42 might exhibit additional features, whereas HSP-17 may be more specialized.

Since HSP-17 interacts with the model substrate MDH and causes aggregation, I considered whether HSP-17 itself would be part of the aggregates formed by its

substrates. To elucidate this, I replicated the conditions depicted in Figures 11 & 12. 500 nM MDH was co-incubated with two-fold excess of HSP-17 at 41 °C or 47 °C, for 30 min (47 °C) or for 60 min (41 °C). The soluble and insoluble fraction were then separated by centrifugation and subjected to SDS-PAGE:

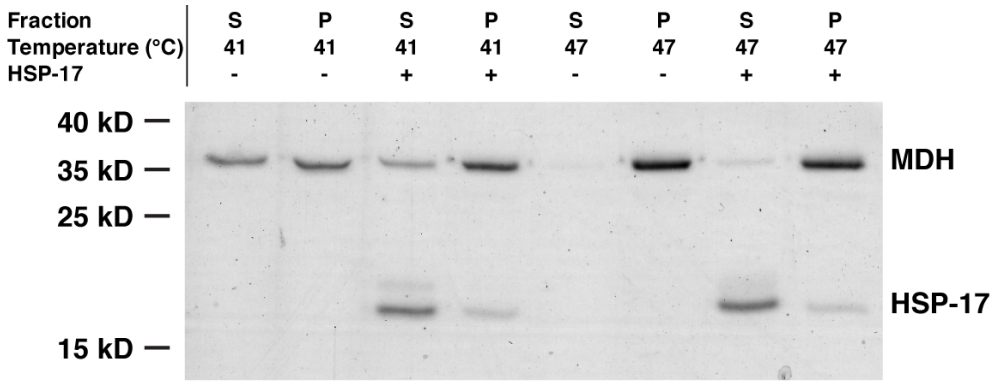

% total MDH	56	44	35	65	1	99	3	97
STDEV (%)	6		4		2		3	
% total HSP-17	-	-	76	24	-	-	78	22
STDEV (%)	-		1		-		3	

Figure 15: HSP-17 co-aggregates with MDH at 41 °C and 47 °C

Sedimentation analysis of MDH after heat treatment, in presence or absence of two-fold excess of HSP-17. The soluble fraction (S) and the insoluble fraction (P) are shown side by side. The protein bands corresponding to MDH (around 36 kDa) or HSP-17 (around 17 kDa) are indicated. The relative intensity of the bands, quantified by Fiji and normalized to 100%, is tabulated below the gel. The numbers represent averages of 3 repeats of the same analysis and the depicted gel is a representative example. The standard deviation is provided for each average band quantification.

My analysis indicates that MDH can be sedimented even in the absence of HSP-17, after heat treatment at 41 °C (less than 50%). The addition of HSP-17 enables two thirds of MDH to be sedimented. At 47 °C, both in the presence or absence of HSP-17, the bulk of MDH became insoluble. This reinforces the observations shown in Figures 11 & 12.

Interestingly, at both temperatures analyzed, 20-25% of total HSP-17 co-sediment with MDH. This is in contrast to the observations from Figures 11 & 12, where HSP-17 (black curves) does not exhibit light scattering when analyzed alone. By this, the sedimentation assay reveals that at least a fraction of HSP-17 will co-sediment with its substrate. I have repeated the same analysis without MDH, by simply analyzing

HSP-17 upon heat treatment. At both 41 °C and 47 °C, HSP-17 remains almost completely soluble (see supplementary Figure 4), as shown in Figures 11 & 12.

So far, I could demonstrate that HSP-17 can facilitate the aggregation of specific substrates such as MDH and a fraction of HSP-17 also becomes a part of these aggregates. What could be the consequence of this co-aggregation in the downstream processes? To tackle this question, I switched to a different model protein substrate, firefly luciferase. Firefly luciferase can be denatured and then used in assays of protein disaggregation and subsequent refolding, where the protein's light-emitting activity is used to quantify recovery from aggregates over time. In metazoans like *C. elegans*, this can be achieved by a combination of HSP-1, HSP-110 (both from the Hsp70 chaperone family) (24) and a mixture of type A and B J-proteins for high disaggregation efficiency (25). Previous studies have shown that co-aggregation of sHsps with their substrates can enhance disaggregation and refolding by molecular chaperones, in bacteria (99) and even in the *C. elegans* system employed here (25) (utilizing the yeast sHsp Hsp26). To asses if HSP-17 affects downstream chaperone processes, I utilized HSP-1, HSP-110, DNJ-12 and DNJ-13 to disaggregate and refold luciferase from aggregates, while quantifying light emission. HSP-17 was added to luciferase before heat denaturation, as illustrated in this experimental schematic:

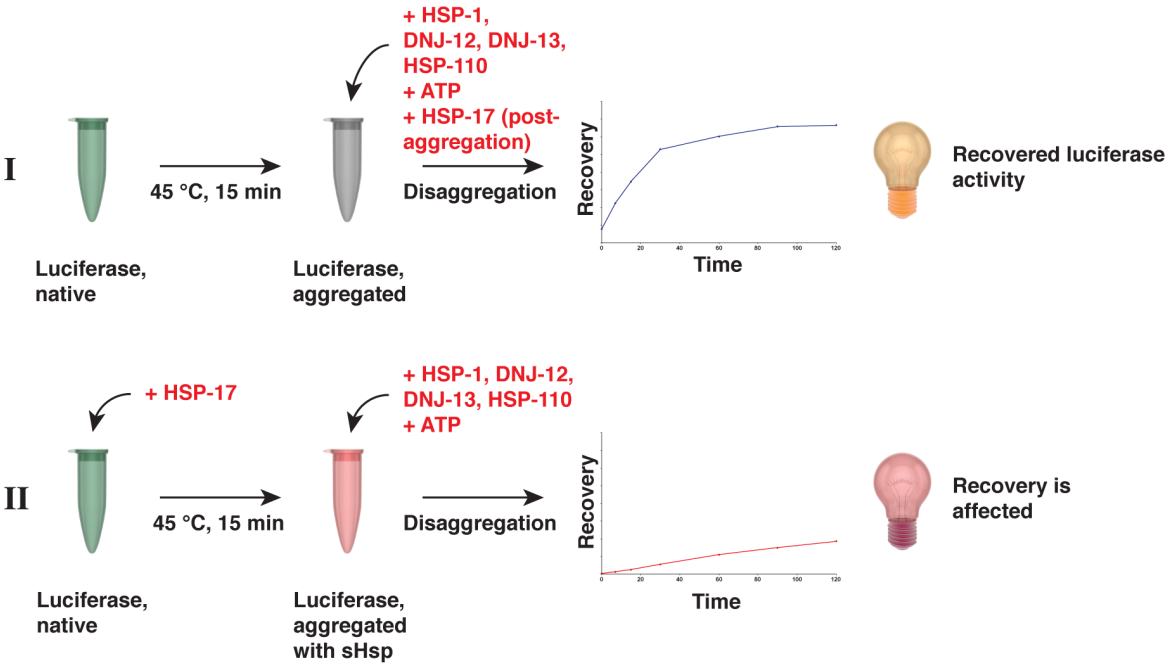

Figure 16: Experimental setup of luciferase assay with HSP-17 co-aggregation

Luciferase is aggregated by heat treatment in absence (I) or presence (II) of HSP-17. Following this, molecular chaperones are added as indicated. If HSP-17 was not added for aggregation, it is heat treated by itself and added with the chaperones (I). Disaggregation is then measured by quantifying light-emitting activity of luciferase over 120 min. For normalization, native luciferase is measured in parallel and assumed to represent 100% signal.

The signal resulting from disaggregation of luciferase by itself or co-aggregated with various concentrations of HSP-17 was then compared:

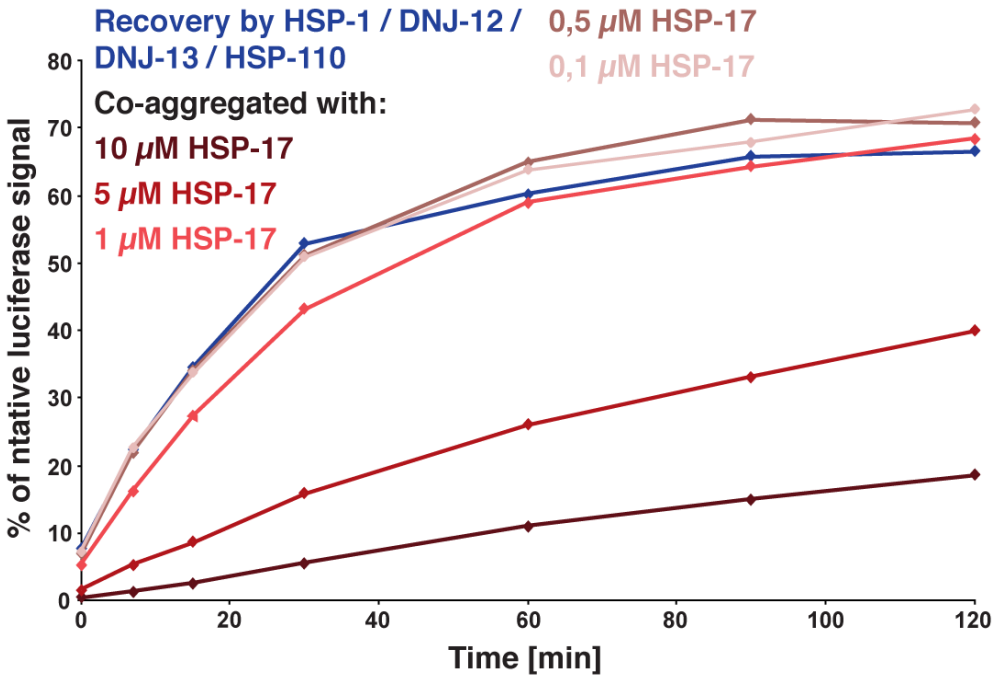

Figure 17: Reactivation of luciferase is inhibited by co-aggregation of HSP-17

Luciferase was aggregated by heat treatment. The disaggregation was carried out by the indicated molecular chaperones and measured by quantifying emitted light, normalized to native luciferase (blue curve). The same measurement was carried out after luciferase was aggregated in the presence of increasing concentrations of HSP-17 (red curves, darker shades of red indicate higher concentrations of HSP-17 as indicated in the legend). All data points are averages of triplicate measurements.

Firstly, these data indicate that the co-aggregation of HSP-17 with luciferase aggregates can inhibit subsequent disaggregation and refolding by the established disaggregation machinery of *C. elegans*. This is reminiscent of observations made for the *E. coli* sHsp IbpA (111). Furthermore, the concentrations of HSP-17 that yield a significant effect are high – close to the concentration of HSP-1 used (4 µM). This may indicate that a competition with molecular chaperones plays a role, likewise reported for bacterial sHsps (112).

Does this mean that co-aggregation of HSP-17 with luciferase is irrelevant and the inhibited disaggregation results from a direct interaction with HSP-70? To elucidate this, I performed the same assay, but heat treated HSP-17 separately and added it to the luciferase afterwards, together with the remaining molecular chaperones (refer to Figure 16):

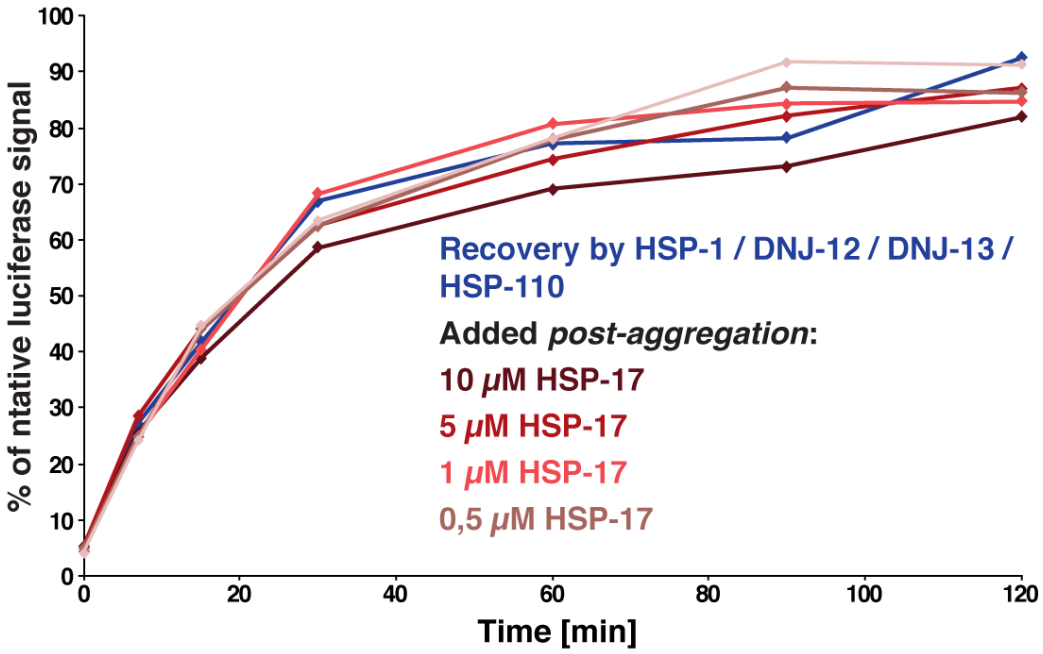

Figure 18: Reactivation of luciferase is unaffected by addition of HSP-17 post-aggregation

Luciferase was aggregated by heat treatment. The disaggregation was carried out by the indicated molecular chaperones and measured by quantifying emitted light, normalized to native luciferase (blue curve). The same measurement was carried out with increasing concentrations of HSP-17 being added for the disaggregation step (red curves, darker shades of red indicate higher concentrations of HSP-17 as indicated in the legend). All data points are averages of triplicate measurements.

In brief, the addition of HSP-17 to luciferase post-aggregation has little to no effect on the efficiency of disaggregation. I conclude from this that HSP-17 has to interact with luciferase during aggregation and co-aggregate to inhibit subsequent disaggregation. To exclude that the observed inhibition of disaggregation is merely a consequence of molecular crowding or unproductive interaction between excess HSP-17 and HSP-1, I performed the same experiments with HSP-12.6 instead of HSP-17. In these experiments, HSP-12.6 could not affect disaggregation of luciferase in any concentration, regardless if added before or after aggregation of luciferase (supplementary Figure 5). Notably, the highest concentration of HSP-12.6 used

(10 µM) could reproducibly facilitate disaggregation of luciferase by the ATP-dependent chaperones if added post-aggregation (this observation, while interesting, will not be discussed further in this work).

The yeast molecular aggregase Hsp42, together with the sHsp-like Btn2, provide cellular sequestrase activity in yeast and are sufficient for the formation of intracellular foci (*INQ* and *CytoQ*) (106). For Btn2, it has been shown that a yeast J-protein, Sis1, is able to alleviate the aggregation of Btn2 dependent foci and allow for disaggregation by molecular chaperones (113). Hence, it is possible that a yet unknown interaction partner is missing in the *in vitro* system that is required to process HSP-17-bound aggregates. This leads me to speculate that members of the 32 J-proteins in *C. elegans*, which form a complex network themselves (19), can alleviate inhibition of disaggregation in a fashion similar to Sis1.

Therefore, analysis of HSP-17 *in vivo* was necessary to fortify my observations *in vitro* with physiological data. Does HSP-17 hetero-oligomerize with other sHsps, bind other molecular chaperones or have preferred substrates? To illuminate this issue, I planned immunoprecipitation experiments of HSP-17 from *C. elegans* lysates. As a first step, polyclonal antibodies for HSP-17 were obtained. Purified HSP-17 was used to immunize rabbits (performed by Pineda Antikörper Service, Berlin, Germany).

Co-IP of HSP-17 was performed followed by MS/MS analysis to identify proteins that are enriched in binding to HSP-17 over a control (where immunoprecipitation was carried out with an anti-GFP antibody). Among the proteins identified were the sHsps Y55F3BR.6 (HSP-21), SIP-1, HSP-16.1 and HSP-12.2 as well as nematode homologs of the model protein GAPDH (GPD-1 & GPD-4). I hypothesize that other sHsps are likely hits in this experiment due to their propensity to interact among each other (62) and that GPD proteins are substrates as shown *in vitro* (see Figure 10).

Subsequently, the 200 most enriched proteins were subjected to a gene ontology (GO) analysis with the *DAVID* online tool, to generate a set of functional annotation data for HSP-17. Below, I provide a curated list of GO-terms identified in this analysis[1]:

1 A dataset containing raw MS/MS-data, the search results derived from my raw data, as well as a list of individual proteins identified has been uploaded to the PRIDE repository. A supplementary table with additional information is also provided (see Data availability, **10.2)**.

Table 2: List of notable GO-terms identified in IP-MS/MS analysis of HSP-17

Nr.	GO-term	Number of proteins matching term	P-value (*DAVID*)
1	Embryo development ending in birth or egg hatching	111	2,04E-25
2	Nematode larval development	88	2,05E-24
3	Reproduction	92	4,75E-24
4	Hermaphrodite genitalia development	25	1,99E-04
5	Receptor-mediated endocytosis	30	8,89E-07
6	Intracellular protein transport	7	2,20E-03
7	Determination of adult lifespan	33	1,25E-05
8	Apoptotic process	20	7,89E-05
9	Oxidation-reduction process	19	6,70E-04

The analysis of GO-terms enriched in MS/MS analysis pointed to at least three physiological functions for HSP-17: the generation of offspring (1 – 4), protein transport and vesicular trafficking (5 & 6) and proteostasis (7 – 9) as shown in table 2. In combination with the individual protein hits mentioned above, I surmise that these findings match with the role described for molecular chaperones and sHsps in particular. Nonetheless, I planned to confirm my findings with a physiological analysis (a list of individual proteins identified as enriched and all derived GO-terms can be found in supplementary table 1, see Data availability, **10.2**). In addition to understanding physiological interaction partners of HSP-17, I asked how abundant HSP-17 is in *C. elegans*. Utilizing the HSP-17 antibodies, I performed *ex vivo* quantification of total HSP-17 from nematode lysates. I obtained an estimate of HSP-17 mass per total mass of protein in cleared lysates (concentrations of other chaperones have been determined previously (27) and are provided for comparison):

Table 3: Absolute quantification of HSP-17 levels in *C. elegans*

Protein	**nMol / total g protein in lysate**
HSP-17	477 ± 154
HSP-1	525 ± 136
HSP-110	566 ± 72
DNJ-12	45 ± 13
DNJ-13	64 ± 7

Standard error of means is indicated for quantification.

The determined concentration levels of HSP-17 in *C. elegans* are high and comparable to HSP-1, which matches my observations from Figures 9-12, where HSP-17 activity is only observed when HSP-17 is present in excess. More importantly, HSP-17 being on a similar level of concentration to HSP-1 supports the findings displayed in Figure 17, where inhibition of disaggregation is observed when HSP-17 was titrated to concentrations close to the level of HSP-1. It is also important to note that I could only analyze whole nematode lysates and the concentrations of the analyzed chaperones may be higher locally, in specific tissues, cells or subcellularly (e.g. in aggregation foci).

4.1.3. *In vivo* analysis of *hsp-17* and its physiological activity

Analysis of the *in vivo* localization of HSP-17, what relevance the protein has in a native context, which proteins might be physiological interaction partners and if HSP-17 can perform an unusual chaperone function in living *C. elegans* necessitated the generation of suitable *in vivo* reporters. I created three transgenic reporter strains of *hsp-17* in *C. elegans*, *phsp-17::GFP* (strain p17G, a transcriptional reporter), *phsp-17::hsp-17::GFP* (strain p17tG, a translational reporter overexpressing HSP-17 with a C-terminal GFP-tag) and *phsp-17::hsp-17::wrmScarlet* (strain p17tR, a translational reporter overexpressing HSP-17 with a C-terminal wrmScarlet-tag). For initial analysis, I performed confocal laser scanning microscopy to visualize the distribution of fluorescent protein in these models[1]:

1 Z-stacks, further elucidating the distribution of HSP-17 within *C. elegans*, are available on the platform Zenodo (see Data availability, **10.1**).

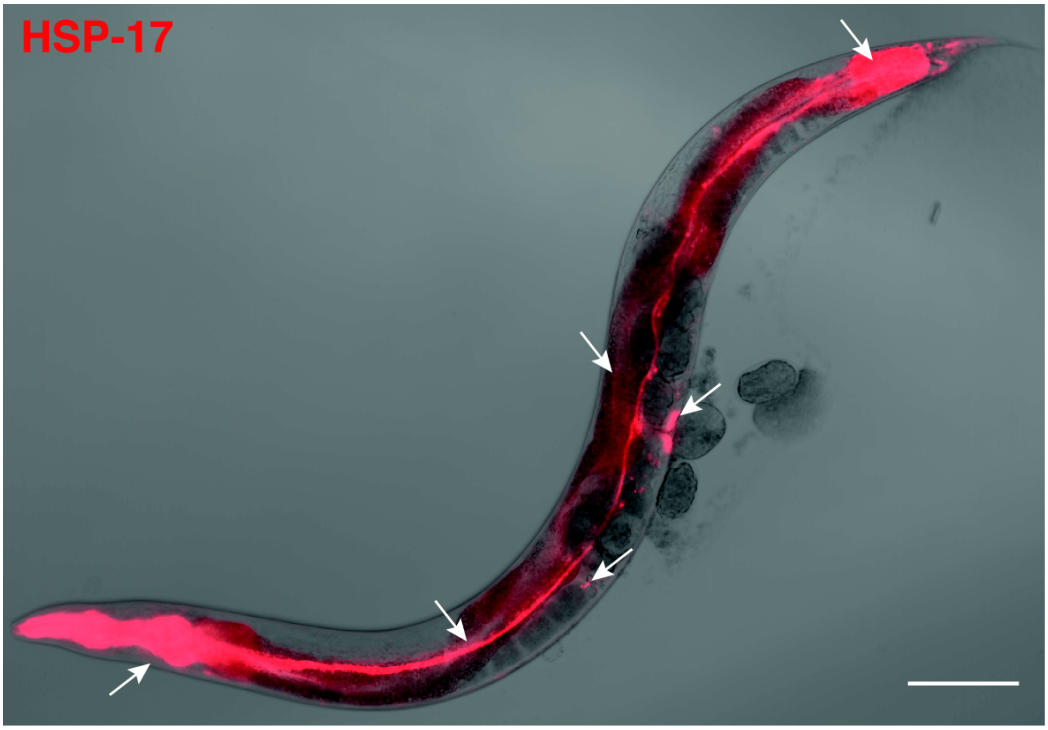

Figure 19: Confocal LSM imaging of translational *hsp-17* reporter strain

LSM of *phsp-17::hsp-17::wrmScarlet*. Whole nematode is visible, including eggs *in utero* & *ex utero*. Image shows an overlay of dissecting microscopy and RFP channel. Scale bar is 100 µm. White arrows mark, from top to bottom: anus / lower end of intestine; diffuse fluorescence in intestine; vulva; pseudocoelomic material; excretory channel; pharynx.

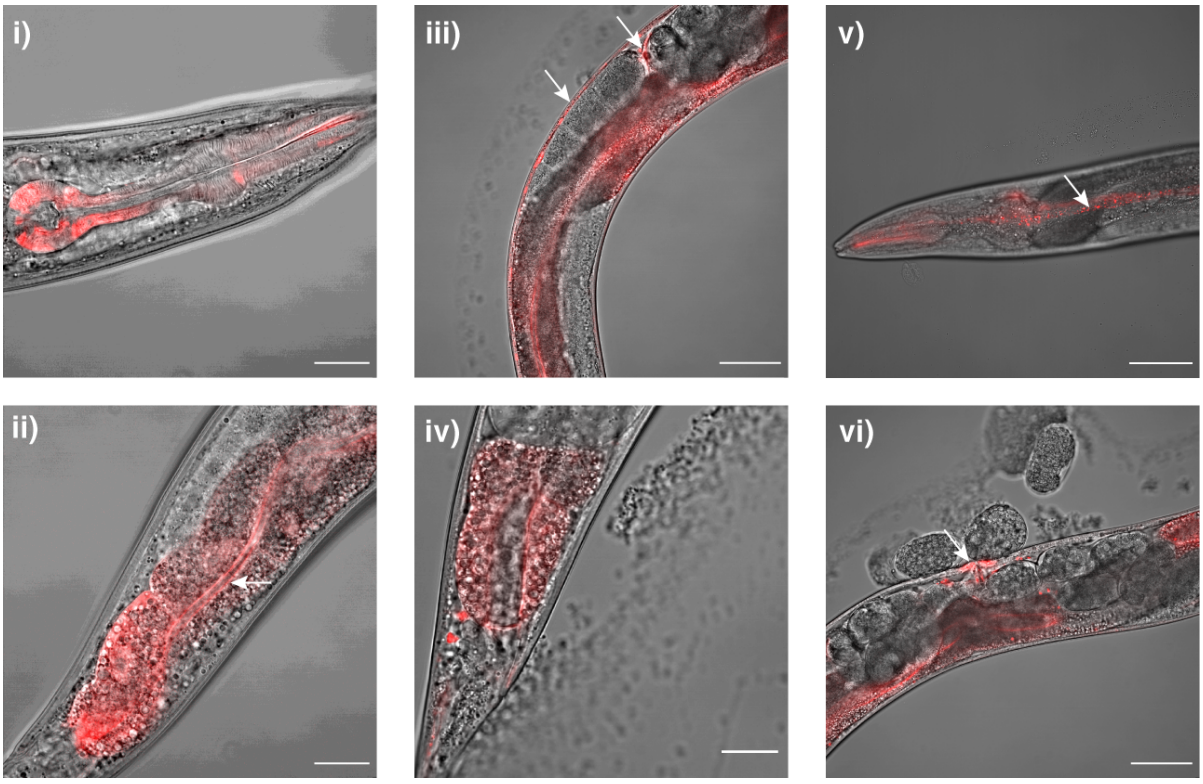

Figure 20: Confocal LSM imaging of translational *hsp-17* reporter strain (detail)

LSM of *phsp-17::hsp-17::wrmScarlet*. Close up images of the above (images show different individuals). Images show an overlay of dissecting microscopy and RFP channel. Scale bars are 20 µm. Images depict: i) HSP-17 localizes to the pharynx. ii) HSP-17 localizes around the endotube, within the intestine. iii) HSP-17 localizes to structures in the pseudocoelom and close to the body wall. iv) In the lower intestine, HSP-17 localizes around the anus. v) HSP-17 localizes to the excretory canal cell, including a line of smaller foci. vi) HSP-17 localizes to the vulva.

HSP-17 is most visibly expressed in the alimentary system (consisting of the pharynx, the intestine and the anus), the excretory canal and also found dispersed to smaller structures in the nematode. This data also matches to a previous automated approach, in which promoter regions where cloned based on computerized predictions. Transcriptional GFP-reporters of many *C. elegans* proteins were generated and analyzed, including HSP-17 (172). Next, I wanted to ascertain that my models express the HSP-17-fluorophore fusion protein as intended and approximate the level of overexpression of the fusion protein. To this end, I performed western blot analysis of lysates of the strains N2, p17tG and p17tR.

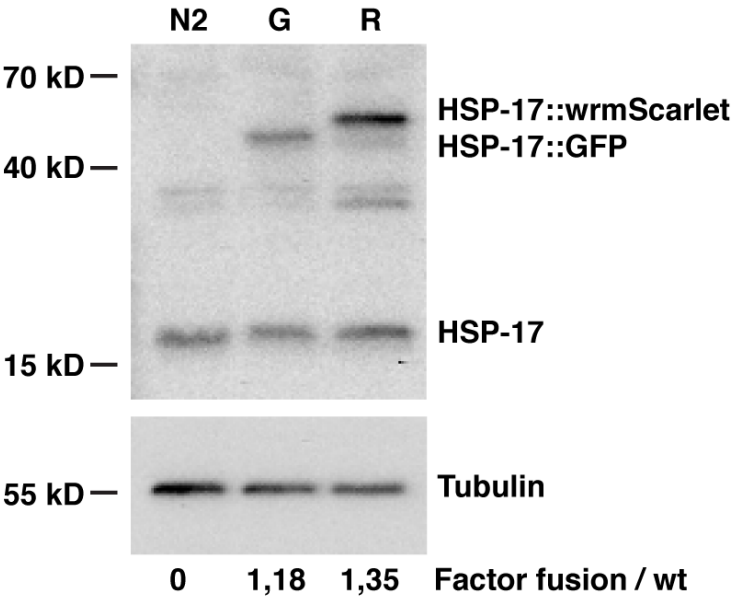

Figure 21: Levels of HSP-17 overexpression in transgenic reporter strains

Lysates of *C. elegans* strains N2 (wild type), p17tG (G) and p17tR (R) were adjusted to the same protein level and western blotted. Detection by antibodies against HSP-17 and Tubulin was performed. Endogenous HSP-17, Tubulin and the fusion proteins were marked. Relative band intensities were quantified by Fiji and normalized to Tubulin. Below the blot, the level of the fusion protein relative to endogenous HSP-17 is provided. The depicted image is representative and the experiment was carried out in three independent repeats, the relative band intensities are given as averages.

The western blot reveals that both the HSP-17-GFP as well as the HSP-17-wrmScarlet fusion can be detected in lysates of the transgenic reporters, but not wild type nematodes. Furthermore, quantification of the bands suggests that the level of the fusion protein is similar to the wild type protein, amounting to a two-fold overexpression of HSP-17 in the translational reporter strains. This also implies that the level of fusion protein approximates the physiological concentration of HSP-17. All lysates analyzed show additional bands at a size slightly smaller than 40 kDa. These bands are either the result of SDS-resistant HSP-17 dimers or due to unspecific binding of the antibody.

The confocal microscopy analyses revealed two structures, the excretory canal (prominently seen in Figure 19) and the endotube (compare Figure 20, ii) which both span the length of the entire nematode. To validate these specific localizations, genetic crosses of p17tR with additional reporter strains were performed. As reporters, the *C. elegans* strain BJ49, expressing IFB-2-CFP in the intestine (intermediary filament-B2 localizes around the endotube (173)), and BK36, expressing GFP to the excretory canal cell were used.

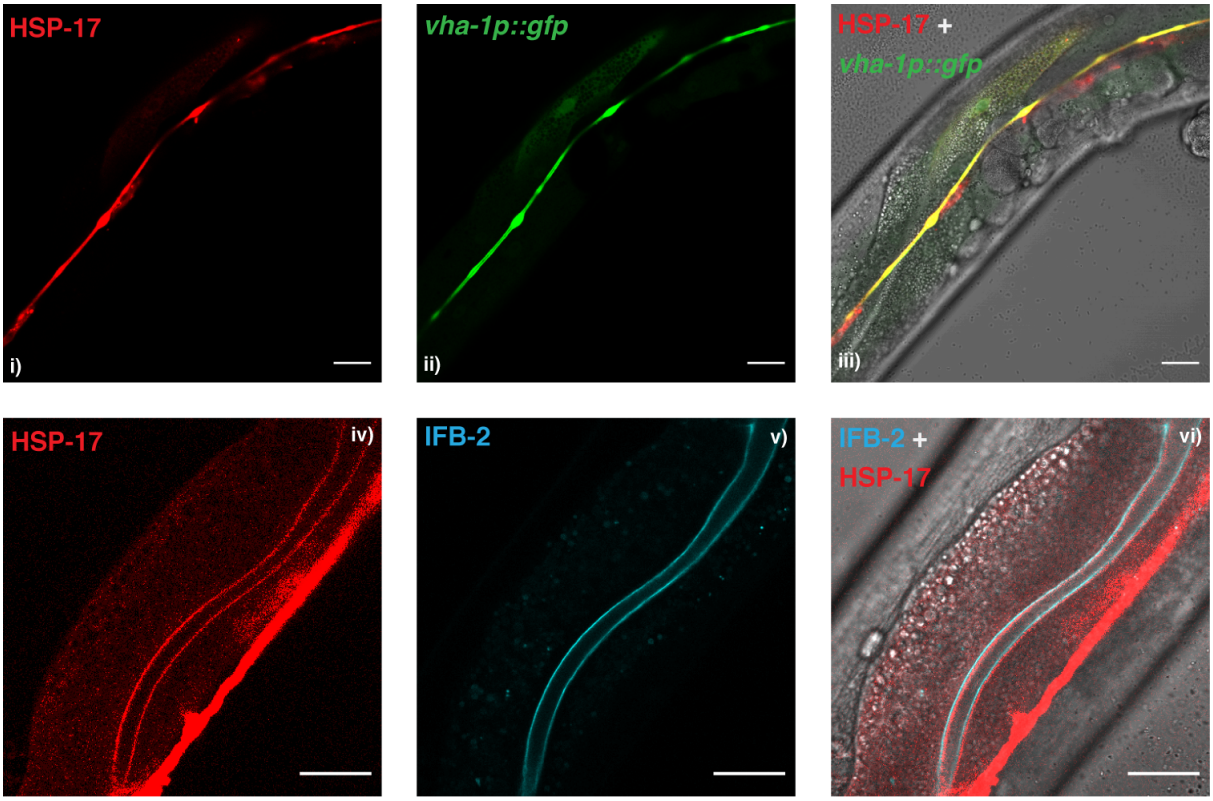

Figure 22: Colocalization of HSP-17 with markers for the excretory canal cell and the intestinal endotube

Representative confocal LSM of *C. elegans* p17tR crossed with strains BK36 (expression of GFP in the excretory canal cell, i-iii) and BJ49 (expression of IFB-2-CFP in the intestine, iv-vi). Separate channels and combined channel are provided, as noted on the images. Scale bars are 20 µm.

The co-expression of fluorophore-tagged reporters confirms that HSP-17 clearly localizes to the excretory canal cell (but does not perfectly overlap with the GFP-reporter) and also localizes to the intestine, particularly to the endotube, where it colocalizes with IFB-2. In an attempt to further observe the subcellular localization of HSP-17 in the intestine, correlative light electron microscopy (CLEM) was employed to generate ultrastructure images of HSP-17 localization within *C. elegans*.

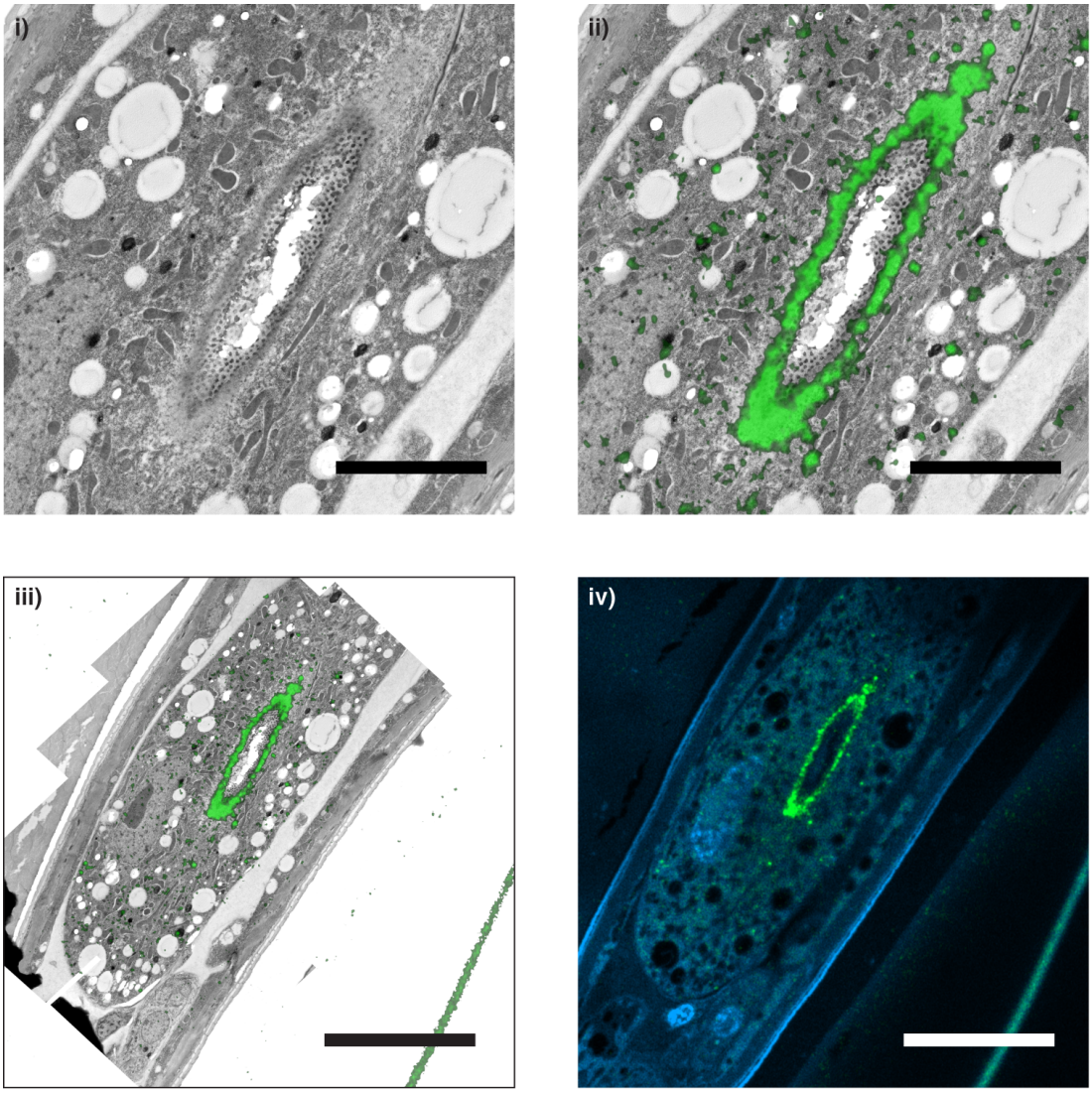

Figure 23: HSP-17 localizes around the apical membrane of the intestinal endotube

CLEM of a *C. elegans* p17tG specimen. A section of an intestinal cell is shown. Image i shows the ultrastructure, including the lumen (in the middle, surrounded by cilia), and lipid droplets (white spheroids). Image ii shows an overlay of HSP-17-GFP fluorescence, notably localizing to the membrane covering the lumen (and some spots outside thereof), but not overlapping with the cilia. Image iii shows the total perspective of the EM-grid including HSP-17-GFP overlay and image iv shows a DAPI-staining of the sample, including HSP-17-GFP overlay. Scale bars are 4 µm (i, ii) or 10 µm (iii, iv). CLEM experiments were performed by D. Puchkov.

The specific enrichment of HSP-17 around the endotube raises the question if HSP-17 in general has a specific subcellular localization, in the intestine and other tissues. I set out to elucidate this by first performing fixation of p17tR nematodes and then conducting a DAPI staining to visualize cellular nuclei in the nematode sample. I then analyzed the samples by LSM:

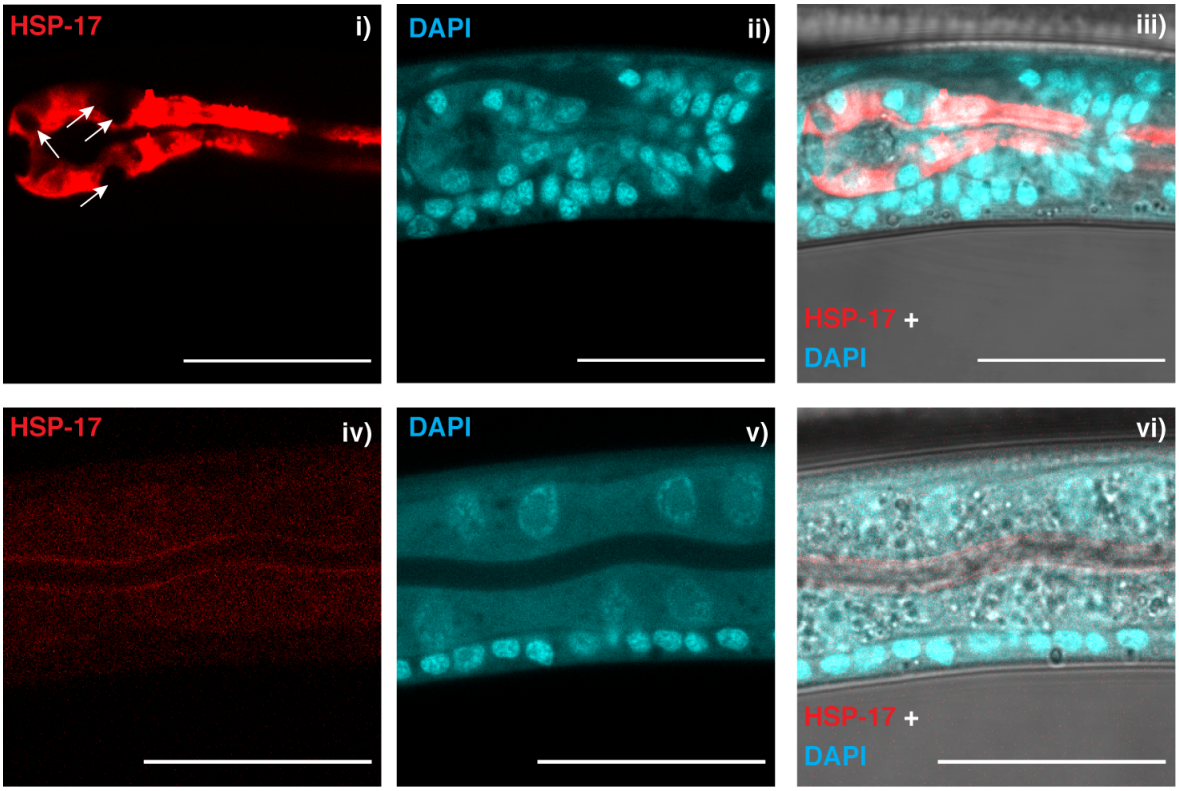

Figure 24: HSP-17 is excluded from cellular nuclei in *C. elegans*

Representative confocal LSM of *C. elegans* p17tR after fixation and DAPI staining. DAPI is visualized by fluorescence (teal). Images i-iii show the pharynx of a young (< 4 days) animal. In image i, representative spots were HSP-17 is excluded are marked by white arrows. Separate channels and combined channel are provided, as noted on the images. Scale bars are 20 µm.

My microscopy analysis suggested that HSP-17-wrmScarlet is excluded from the nucleus. To reinforce these findings, I also conducted an *in silico* analysis of the HSP-17 primary structure, using the integrated online tool *BUSCA* to analyze markers of subcellular localization. Analysis predicted the most likely localization of HSP-17 to be the cytosol (70%), or alternatively the nucleus (30%). As my DAPI staining revealed no nuclear localization of HSP-17, I concluded that HSP-17 is most likely a cytosolic protein.

To complement my two-fold overexpression model of HSP-17 I also generated an RNAi construct to perform a knockdown of *hsp-17*, which was previously unavailable from the Ahringer Library (174). This construct has been utilized in a recent publication of AG Kirstein to successfully deplete HSP-17 by roughly 50 % (175).

With the overexpression lines and the RNAi construct a toolset was available to access physiological roles of HSP-17 in living *C. elegans*. As HSP-17 is a molecular chaperone of high abundance (Table 3), a modulation of HSP-17 protein levels either

by overexpression or RNAi-mediated depletion might affect physiological fitness and stress resistance. For the related *C. elegans* sHsp SIP-1, reduced lifespan and heat survival upon deletion have been reported (82). Here, I set out to asses viability *of C. elegans* upon RNAi-mediated knockdown of *hsp-17*.

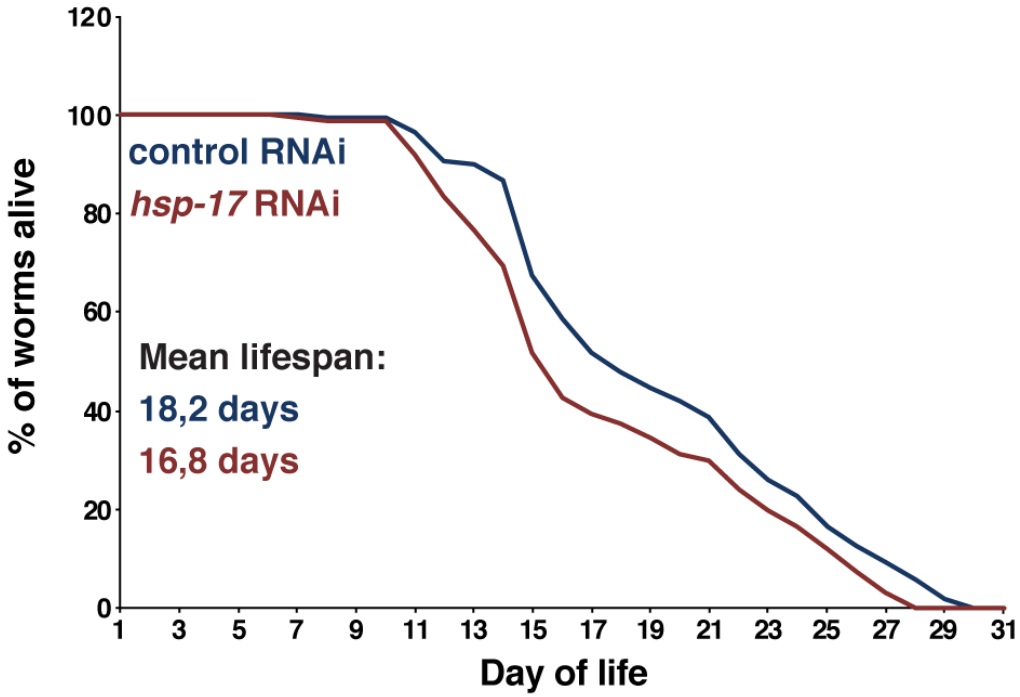

Figure 25: Lifespan of *C. elegans* is decreased upon knockdown of *hsp-17*

N2 nematodes were subjected to control RNAi (blue) or *hsp-17* RNAi (red). The number of living nematodes is given as percentage of total specimen used in the assay. Mean lifespans as determined by the *OASIS* online tool are also provided.

Indeed, knockdown of *hsp-17* has a small, but significant effect on *C. elegans* lifespan, reducing it by about 1,5 days even in the absence of external stressors. This also corroborates the finding that HSP-17 is involved in the adult lifespan from my GO-analysis (Table 2). As an additional readout of fitness, I assayed the fecundity of N2 nematodes subjected to control RNAi or knockdown of *hsp-17*. This dataset was supplemented by analysis of N2 nematodes and the strains p17tG or p17tR in the absence of any RNAi:

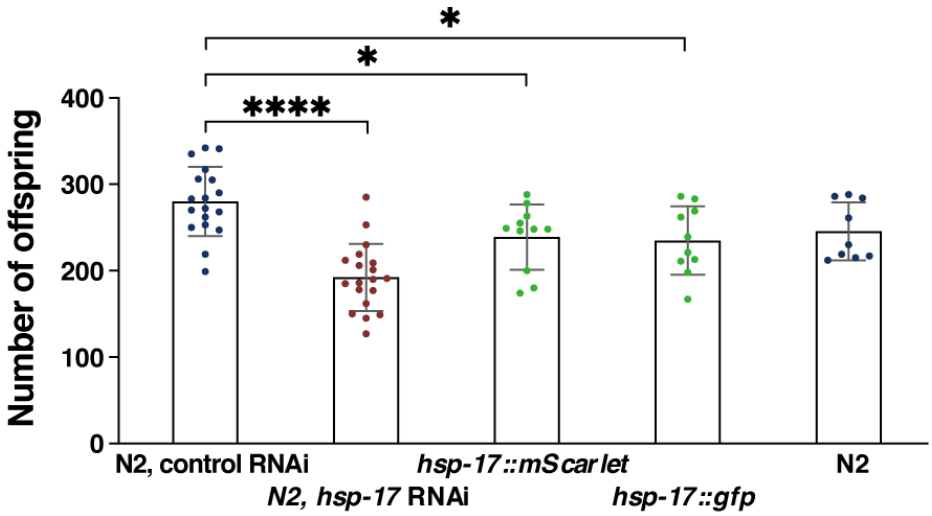

Figure 26: Fecundity of *C. elegans* is decreased upon knockdown of *hsp-17*

For N2 nematodes subjected to control RNAi (blue) or *hsp-17* RNAi (red), the total number of progeny produced was counted. Data is also given for HSP-17 overexpressing nematodes (green) and finally, for N2 animals in the absence of RNAi (blue). Each spot on the graphs marks an individual. One-way ANOVA testing (followed by Bonferroni's multiple comparisons test) was performed. The standard deviation for each column is indicated and significant results are marked by stars (N2 control vs. N2, *hsp-17* RNAi: $p < 0{,}0001$; N2 control RNAi vs. *hsp-17::mScarlet*: $p = 0{,}027$; N2 control RNAi vs. *hsp-17::gfp*: $p = 0{,}016$).

Knockdown of *hsp-17* severely reduces fecundity indicating either a general loss of physiological fitness or a specific defect in the gestation of progeny caused by the reduction of HSP-17. As before, this finding matches the GO-analysis, where HSP-17 was associated with the generation of offspring (Table 2). Notably, overexpression of HSP-17 does not alter fecundity of wild type animals, but both wild type and overexpression nematodes lay a reduced amount of eggs compared to the RNAi control – this may indicate that the bacterial RNAi-feeding strain *E. coli* HT115 itself has a slight effect on egg laying or fecundity.

HSP-17 appeared to be constitutively expressed in my reporter strains and I did not observe induction upon heat stress *in vivo* (although previous *ex vivo* analysis indicated heat stress induction (176)). As is the case for SIP-1, I assumed that HSP-17 expression is not dependent on heat stress, yet the protein may still exert a cytoprotective role during heat stress. Hence, a thermotolerance assay was performed to measure recovery and survival of nematodes subjected to heat stress upon modulation of HSP-17 levels. To this end, nematodes were subjected to heat

stress of 35 °C for 6 h before being allowed to recover at 20 °C for 24 h and surviving animals were counted.

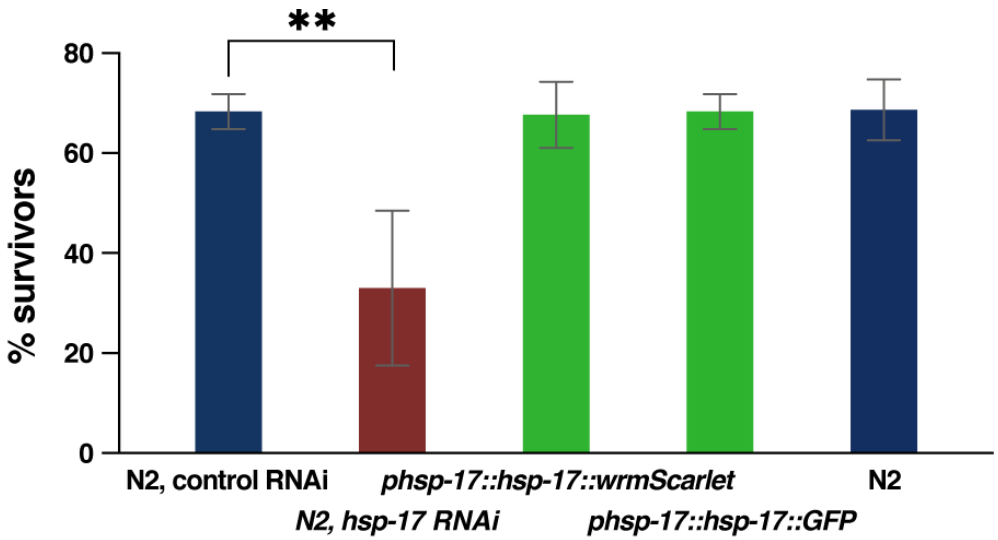

Figure 27: Thermotolerance of *C. elegans* is decreased upon knockdown of *hsp-17*

For N2 nematodes subjected to control RNAi (blue) or *hsp-17* RNAi (red), the percentage of survivors 24 h after heat stress was plotted. Data is also given for HSP-17 overexpressing nematodes (green) and finally, for N2 animals in the absence of RNAi (blue). Experiments were carried out in three independent repeats. One-way ANOVA testing (followed by Dunnett's multiple comparisons test) was performed. The standard deviation for each column is indicated and significant results are marked by stars (N2 control vs. N2, *hsp-17* RNAi: $p < 0{,}0014$).

The experiment revealed a strong defect in heat stress survival for *hsp-17* depleted nematodes. In contrast, overexpression of HSP-17 did not alter survival compared to wild type nematodes or animals subjected to RNAi control conditions. It follows that HSP-17 can confer resistance to heat stress, possibly due to its ability to prevent aggregation of selected substrates, or perhaps by facilitating the aggregation of others.

The specific localization of HSP-17 in the alimentary system of *C. elegans* suggested an involvement of HSP-17 in distinct physiological processes. As shown in Figure 22, HSP-17 localizes to the excretory cell which is implied in water balance and osmoregulation (177) posing the question whether HSP-17 is cytoprotective in osmotic stress. To elucidate this question, I transferred nematodes, on day 4 of life, to NGM-agar plates with 250 mM NaCl (regular: 50 mM) to cause osmotic stress:

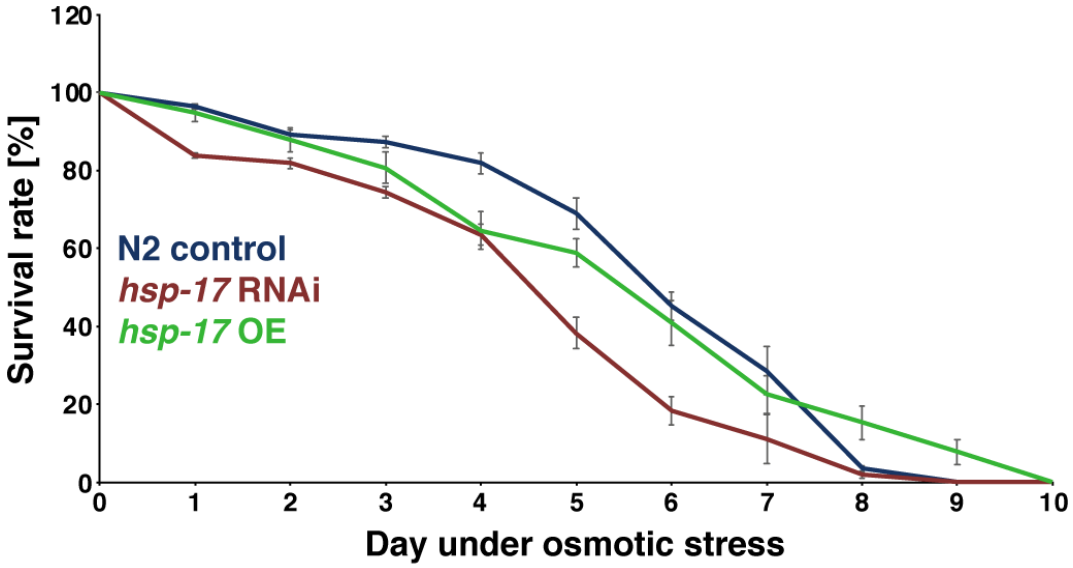

Figure 28: Osmotolerance of *C. elegans* is decreased upon knockdown of *hsp-17*

For N2 nematodes subjected to control RNAi (blue) or *hsp-17* RNAi (red) and for the strain p17tR overexpressing HSP-17 (green), survival under osmotic stress was plotted. Survival is indicated as the percentage of *C. elegans* alive compared to the initial population. Experiments were carried out in three independent repeats. Standard deviation is indicated.

Again, the data indicates that depletion of *hsp-17* slightly diminishes resistance of *C. elegans* to osmotic stress. Conversely, overexpression of HSP-17 does not seem to be beneficial or deleterious. I conclude that HSP-17 plays a role in excretory channel function.

Figures 22 and 23 also show a distinct localization of HSP-17 to the endotube, around the apical membrane of the intestinal lumen. The intestine surrounding the lumen is an interface with nutrients or toxins the nematode comes into contact with and reports that HSP-17 is induced upon heavy metal stress (cadmium), support my observation (176). As C*. elegans* subsists on bacterial cells, the intestinal lumen may furthermore be a site challenged by biotic stressors. Aiming to understand if HSP-17 is relevant in biotic stress defense, I transferred adult nematodes to NGM-agar harboring the pathogenic bacterial strain *Serratia marcescens* DB11.

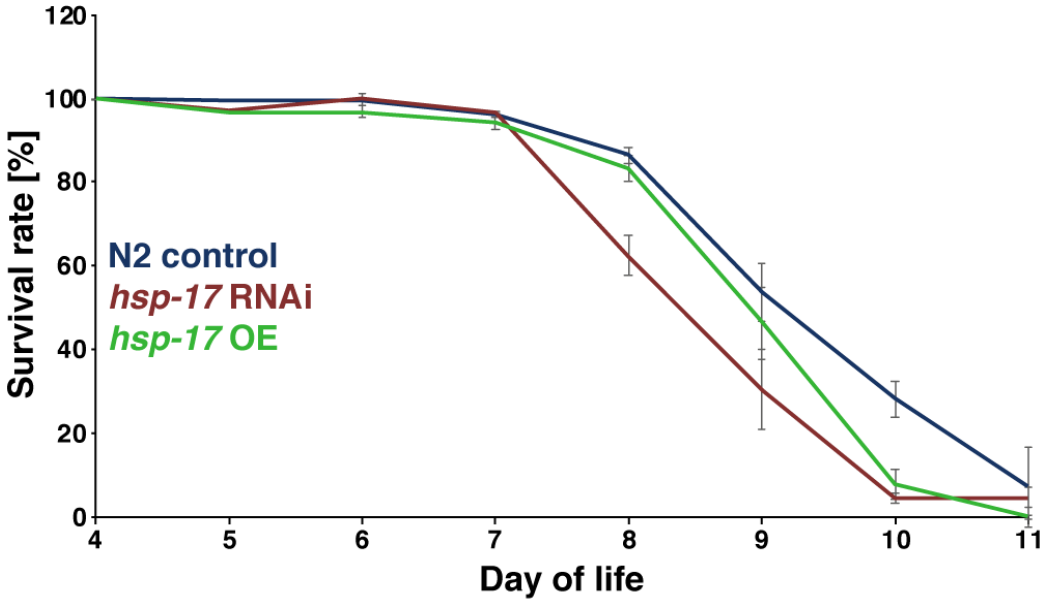

Figure 29: Biotic stress resistance of *C. elegans* is decreased upon knockdown of *hsp-17*

For N2 nematodes subjected to control RNAi (blue) or *hsp-17* RNAi (red) and for the strain p17tR overexpressing HSP-17 (green), survival under biotic stress was plotted. Survival is indicated as the percentage of *C. elegans* alive compared to the initial population. Experiments were carried out in two independent repeats. Standard deviation is indicated.

As with the osmotic stress, I observed a slight defect in *C. elegans* resistance to biotic stress upon depletion of *hsp-17*, leading me to assume that HSP-17 confers resistance to external stressors. It is of note that overexpression of HSP-17 cannot produce a significant change in any of the biomarkers I have explored so far, implying that HSP-17 cytoprotective activity hinges on the interaction of HSP-17 with a limiting substrate or that overexpression of the chaperone causes protein homeostatic imbalance as much as its depletion. I had so far analyzed the distribution of HSP-17 inside *C. elegans* paired with its physiological relevance and the ability to confer resistance to specific stressors. This leaves unanswered, however, which specific substrates HSP-17 might bind and exhibit its chaperone activity on and what the nature of this chaperone activity is. Can HSP-17 enact the molecular aggregase activity described in **3.1.2** *in vivo* and is this part of its cytoprotective function?

4.1.4. HSP-17 acts as a molecular aggregase *in vivo*

The data depicted in Figures 12, 15 and 17 show that *in vitro*, HSP-17 can facilitate the aggregation of a model substrate and become part of the aggregate itself, stabilizing the insoluble species against subsequent disaggregation. To test these observations in a physiological context, I aimed to analyze if HSP-17 localizes to aggregates in living *C. elegans*. The microscopic images depicted in Figures 19 & 20 show the general localization of HSP-17. Although the animals presented there are young, some foci in the intestine can be observed (Figure 19 and Figure 20, vi). However, aggregation is typically related to stress or aging and many *C. elegans* proteins tend to become insoluble upon aging (114). An analysis of old nematodes (14 days) confirms an age-dependent aggregation of HSP-17:

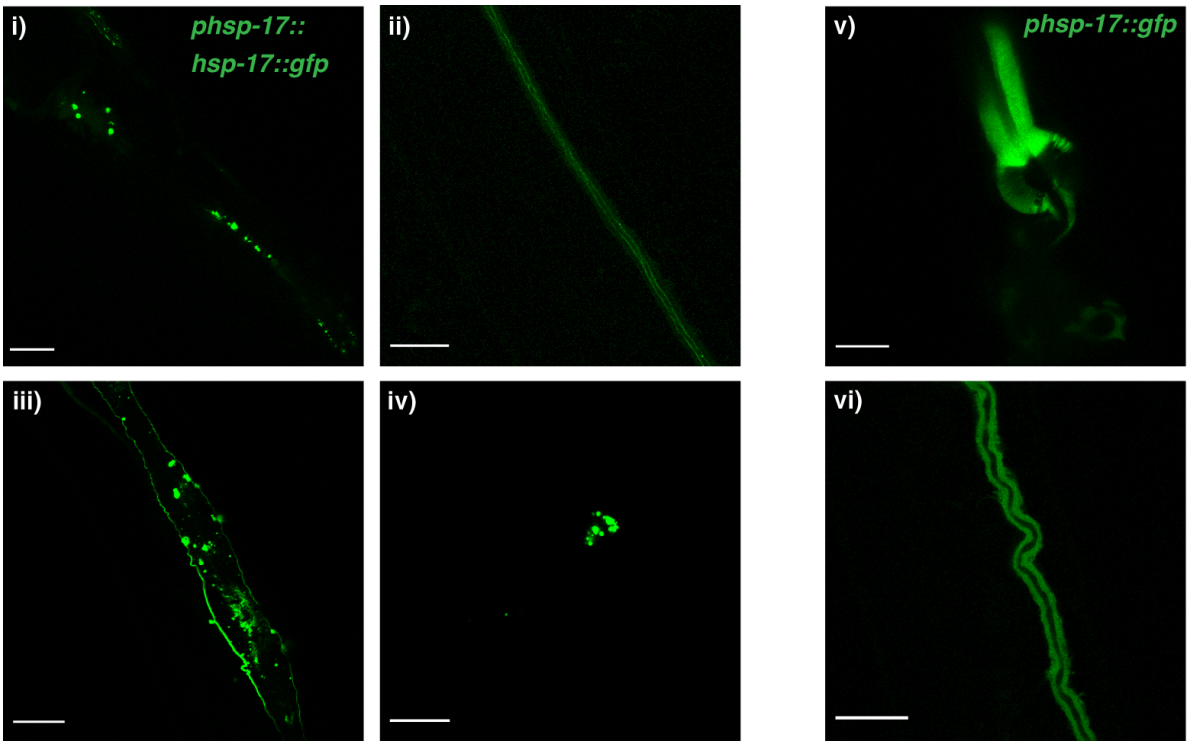

Figure 30: HSP-17-GFP, but not GFP alone, forms foci upon aging in *C. elegans*

Nematodes of the strain p17tG were analyzed at day 14 of life. Images show the head including the pharynx (i), the excretory tract (ii), the intestine and the excretory tract (iii) and the tail (iv). The strain p17G, expressing GFP under *hsp-17* promoter control, was also imaged: (v) shows the pharynx and (vi) shows the excretory tract. Images are representative. Scale bars are 20 µm.

A widespread formation of foci could be observed for HSP-17-GFP with little diffusive material remaining, spanning the head, intestine and tail of *C. elegans*. Notably, a

distinct localization inside the excretory tract remains visible. Conversely, GFP alone under the same promoter shows diffusive behavior even at day 14 of age in the pharynx. While both HSP-17-GFP or GFP alone do not seem to aggregate in the excretory tract, GFP alone is distributed diffusely throughout the entire cell while HSP-17-GFP maintains an inhomogeneous distribution. I conclude from this that HSP-17 has a specific propensity to form foci in *C. elegans* which is independent of the GFP-fusion.

Visualization of foci of HSP-17-GFP as seen in Figure 30 at an ultra-resolved level by CLEM was attempted, to assess whether they have a specific subcellular localization or association. Imaging of the pharyngeal bulb of an adult animal revealed a cellular structure that could be correlated with HSP-17-GFP fluorescence:

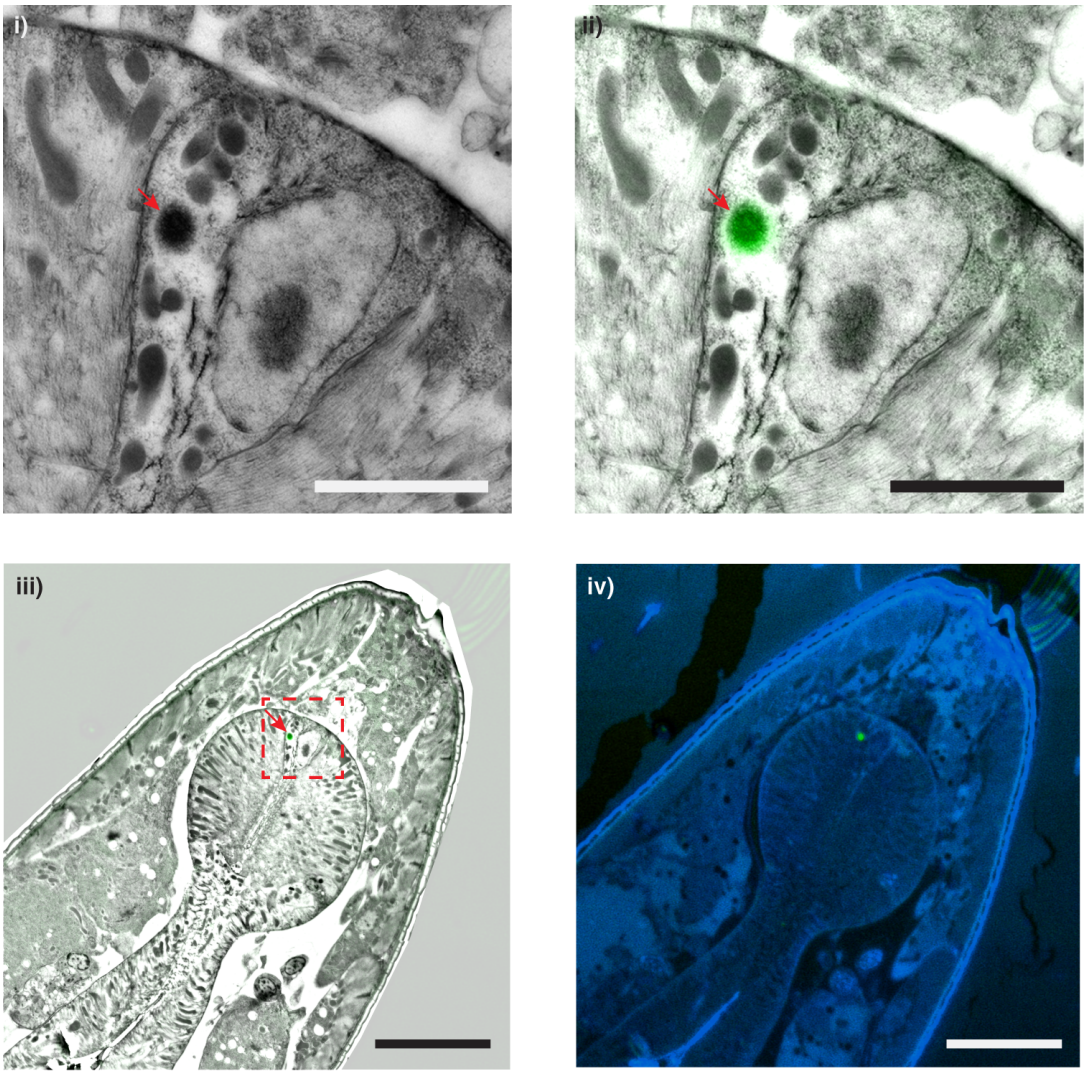

Figure 31: HSP-17 localizes to cellular, electron-dense foci in the pharynx

CLEM of a *C. elegans* p17tG specimen. A section of the pharyngeal bulb and surrounding tissue is shown. Image i shows the ultrastructure of a part of the pharyngeal bulb. Red arrow indicates an electron dense, membrane-less structure. Image ii shows an overlay of HSP-17-GFP fluorescence, colocalizing with the indicated structure. Image iii shows a total perspective of the surrounding EM-grid, including an overlay of the GFP-channel (the structure is indicated by a red arrow and the field of view in i & ii is marked. Image iv shows a DAPI-staining of the sample, including HSP-17-GFP overlay. Scale bars are 2 µm (i, ii) or 10 µm (iii, iv). CLEM experiments were performed by D. Puchkov.

While I was unable to clearly designate any spheroid structure observed by CLEM to be a cellular aggregate, I note that the structure contains HSP-17, is electron dense and adjacent to the nucleus. The structure has uneven edges distinct from nearby spheroids (possibly with membranes). I deduce that this is either a different type of structure to which HSP-17 specifically localizes, or that all spheroids are the same (i. e. aggregates), but HSP-17 does not colocalize with every cellular aggregate.

To biochemically validate this formation of aggregates and quantify it as systemic behavior, I undertook analysis of *C. elegans* proteins *ex vivo*. Revisiting my approach depicted in Figure 15, I first generated lysates of N2 nematodes aged 2, 4, 6 and 8 days respectively. After all lysates were adjusted to the same protein concentration, soluble and insoluble material was separated by centrifugation and analyzed by western blot using HSP-17 polyclonal antibodies.

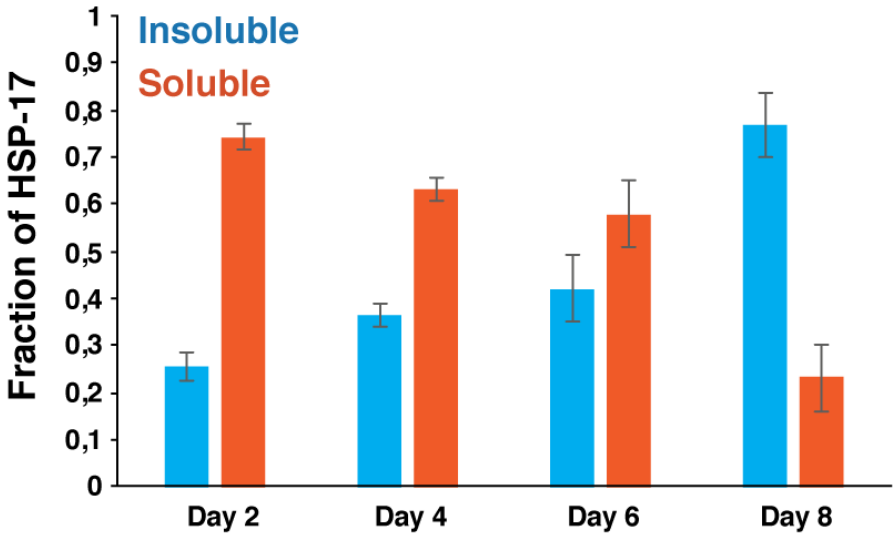

Figure 32: HSP-17 transitions to the insoluble state with age in *C. elegans*

Lysates of N2 nematodes of the indicated age were fractionated into soluble and insoluble fractions and HSP-17 was quantified in each fraction by western-blot immunodetection. The experiment was performed in triplicates and error bars are indicating SEM.

Nematodes were analyzed throughout their reproductive phase (day 4 – day 8), which also marks the onset of aging, proteostatic decline and systemic protein aggregation (115). Indeed, HSP-17 insolubility coincides with this window and by the end of the reproductive phase, the majority of HSP-17 is found in cellular aggregates. This indicates that either HSP-17 itself becomes insoluble upon stress and aging or else that it actively co-aggregates with its protein substrates. I decided to investigate this question by observing if HSP-17 binds to an aggregation-prone protein substrate *in vivo* and the effect it has on the aggregation propensity. As a model, nematodes expressing iQ_{44}-YFP in the intestine were utilized. This polyglutamine protein generates distinct and scorable foci of protein aggregation in an age-dependent manner (178) and presents an opportunity for robust quantification of pro-aggregation activity. It has been demonstrated that intestinal iQ_{44}-YFP is prone to aggregate under osmotic stress, meaning it is vulnerable to at least one stressor that HSP-17 is physiologically implied in (179). I observed nematodes from day 4 to day 8 of life that were either depleted for *hsp-17*, applying a knockdown of *hsp-17,* or overexpressed HSP-17:

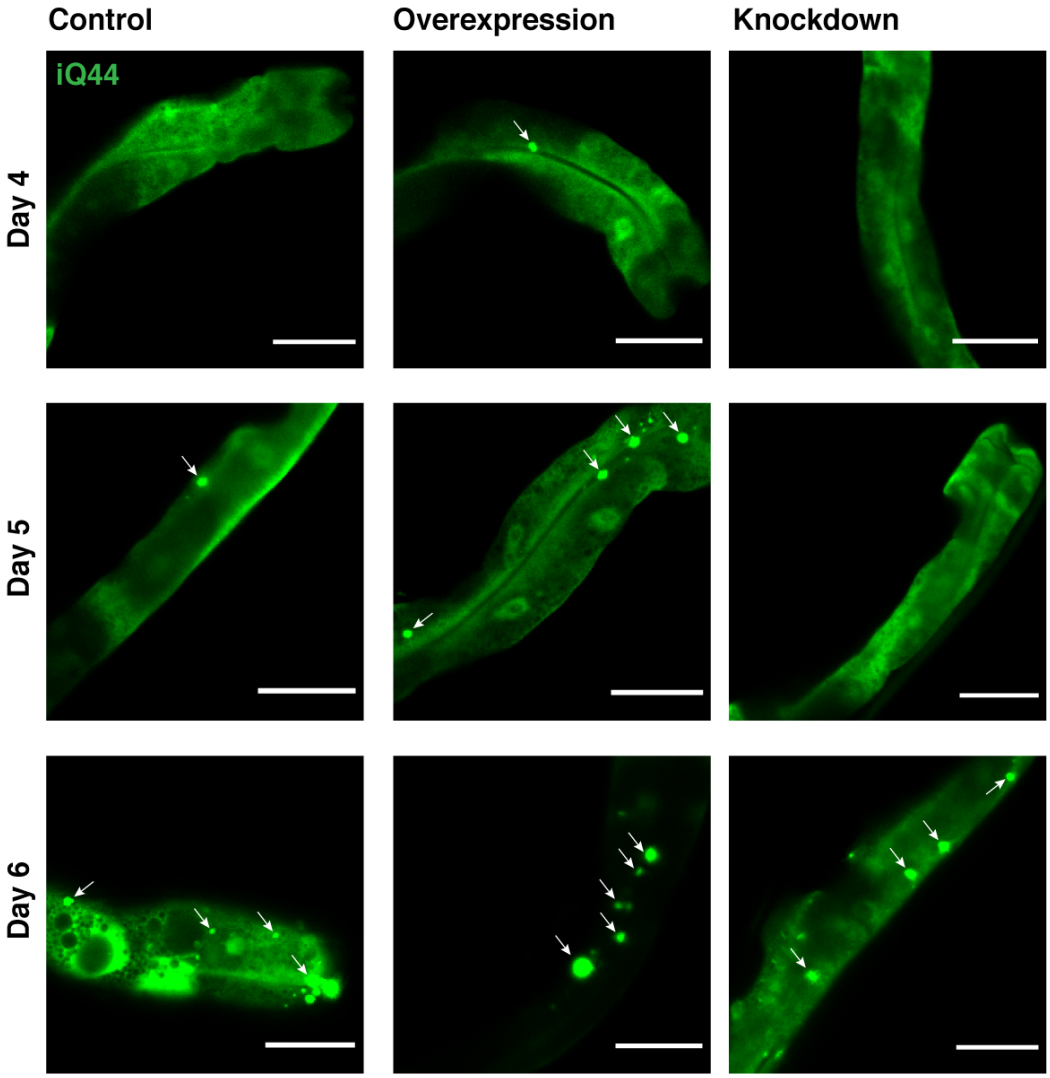

Figure 33: HSP-17 enhances formation of iQ*44*-foci *in vivo*

Confocal laser scanning microscopy of nematodes expressing Q_{44}-YFP to the intestine. Left: control RNAi condition; middle: iQ44-YFP + HSP-17-wrmScarlet overexpression; right: iQ44-YFP + *hsp-17* RNAi. Images show the intestine for day 4, 5 and day 6 (top to bottom) and white arrows indicate cellular foci of aggregation. Images are representative. Scale bars are 20 µm.

I observed that foci in nematodes overexpressing HSP-17 appeared more frequently and earlier compared to the control condition, whereas *hsp-17* RNAi slightly delayed the formation of iQ_{44}-YFP foci. To quantify this effect, the occurrence of foci for each nematode and day of life was counted and grouped into those that exhibited more than zero foci or multiple (> 3) foci:

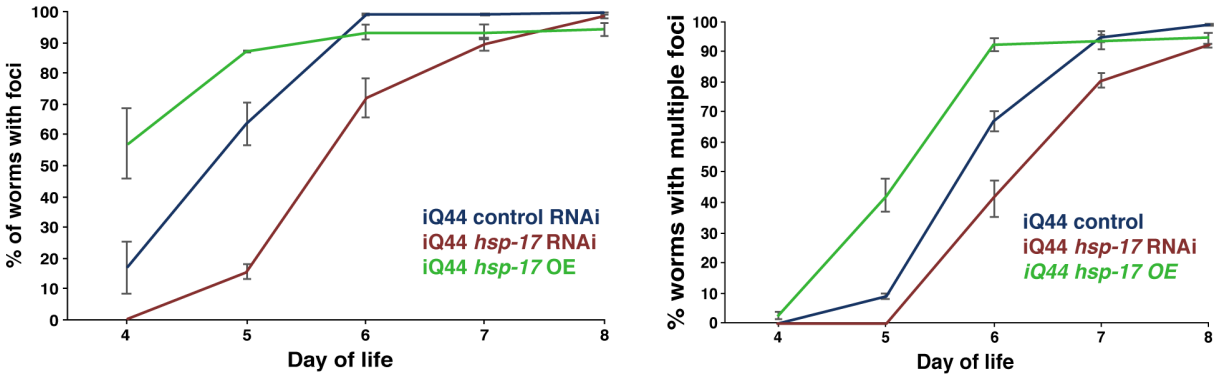

Figure 34: HSP-17 enhances formation of iQ_{44} foci *in vivo* (quantification)

Quantification of foci observed in *C. elegans* as presented in Figure 33. Animals with more than 0 foci (left) or more than 3 foci (right) were counted. Intestinal Q_{44} nematodes subjected to control RNAi (blue) or *hsp-17* RNAi (red) were scored alongside the crossing between iQ44 and p17tR (green). The number of nematodes scored in either group is given as percentage of total animals analyzed. The data resulted from two independent repeats and standard deviation is indicated.

With these data I could demonstrate for the first time that HSP-17 affects the aggregation of a model substrate *in vivo*. Depletion of *hsp-17* can reduce the speed and severity of iQ_{44}-YFP aggregation, while the HSP-17 overexpression enhances it. Is this the consequence of direct binding between HSP-17 and iQ_{44}-YFP, or do I observe increased aggregation of iQ_{44}-YFP because HSP-17 alters cellular proteostasis by binding a different, independent substrate? To address this question, I analyzed whether HSP-17 is colocalizing with iQ_{44}-YFP foci *in vivo* by crossing the strain p17tR with the polyQ-model strain, iQ_{85}-YFP. This strain expresses a highly elongated polyQ-peptide stretch and shows notable foci-formation even in young animals:

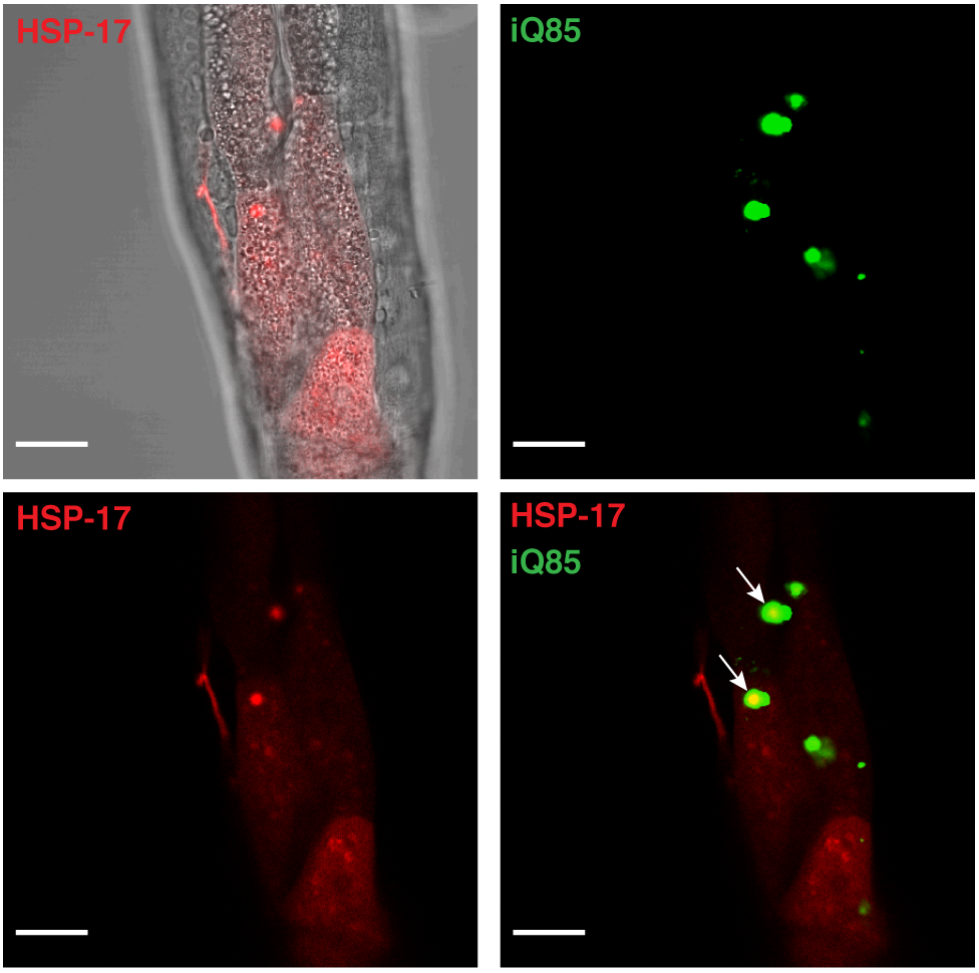

Figure 35: HSP-17 colocalizes with some iQ_{85}-YFP-foci *in vivo*

Microscopies of a crossing between the *hsp-17* translational reporter and an iQ_{85}-YFP polyQ reporter strain. Individual channels for HSP-17-wrmScarlet and iQ_{85}-YFP are provided alongside an overlay. White arrows mark instances of HSP-17-foci colocalizing with iQ_{85}-foci. The image is representative and scale bars are 20 µm.

Not all iQ_{85}-YFP foci colocalize with HSP17-foci and both fusion proteins can form cellular aggregates independently of each other. Nonetheless, the images show that foci of iQ_{85}-YFP can incorporate HSP-17, demonstrating that both proteins interact *in vivo*. This result still leaves the possibility that the interaction between HSP-17 and the polyQ-construct is mediated by or depending on a further, unknown factor. Hence, I decided to assay the interaction of both partners *in vitro*. Purified $HttEx1Q_{48}$ was aggregated in the presence of HSP-17 and the association of HSP-17 to the generated $HttEx1Q_{48}$ fibrils was analyzed by immunogold-labeling using the HSP-17 antibodies. This method has previously been used to visualize the interaction of molecular chaperones with $HttEx1Q_{48}$ fibrils *in vitro* (27).

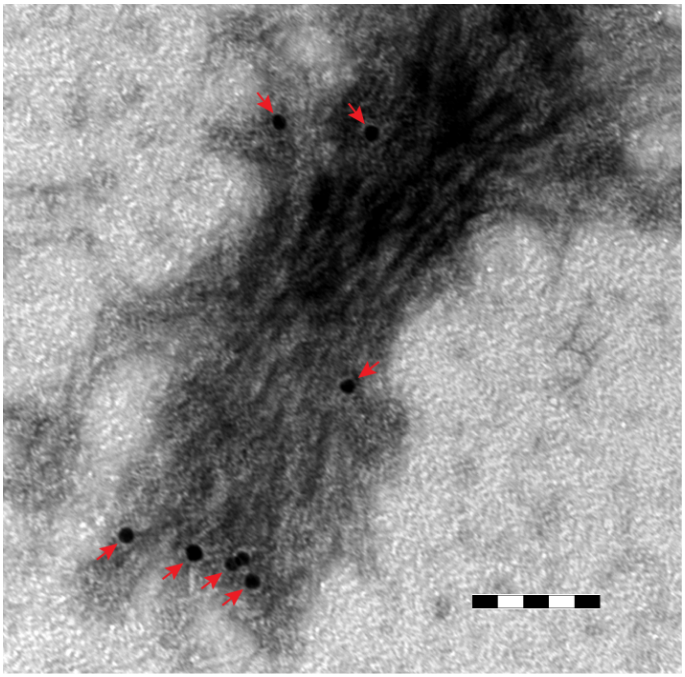

Figure 36: HSP-17 colocalizes with HttEx1Q48 fibrils *in vitro*

HttEx1Q_{48} was aggregated in the presence of 5-fold excess of HSP-17. Fibrillary material was located on the EM-grid for imaging and red arrows indicate immunogold-beads colocalizing with fibrils. Scale bar is 100 nm.

As can be seen in Figure 36, HSP-17 can interact with HttEx1Q_{48} fibrils in the absence of any additional factors. In summary, the intestinal Q_{44}-YFP construct was used to demonstrate molecular aggregase activity of HSP-17 *in vivo*. However, Q_{44}-YFP is an artificial substrate and I thus wanted to analyze endogenous proteins and potential substrates. I set out to identify *in vivo* substrates of HSP-17 for further analysis. First, I crossed the *phsp-17::hsp-17::GFP* translational reporter strain with a reporter strain of a known *C. elegans* stress granule reporter (strain DCD214), *pab-1*, which shares pharyngeal localization (180). Yet, the microscopy images of the crossed strain indicate that HSP-17-GFP and tagRFP-PAB-1 do not colocalize but rather occupy distinct foci within the pharynx (supplementary Figure 6). Notably, the localization of proteins such as PAB-1 to stress granules is associated with prion-like domains, which are absent in HSP-17 (see Figure 14). Thus, I focused on a different protein, KIN-19, which is likewise reported to become insoluble upon organismal aging and to be excluded from stress granules (114,180). I generated a genetic cross of the translational HSP-17-GFP reporter with a reporter expressing KIN-19-tagRFP controlled by the native promoter:

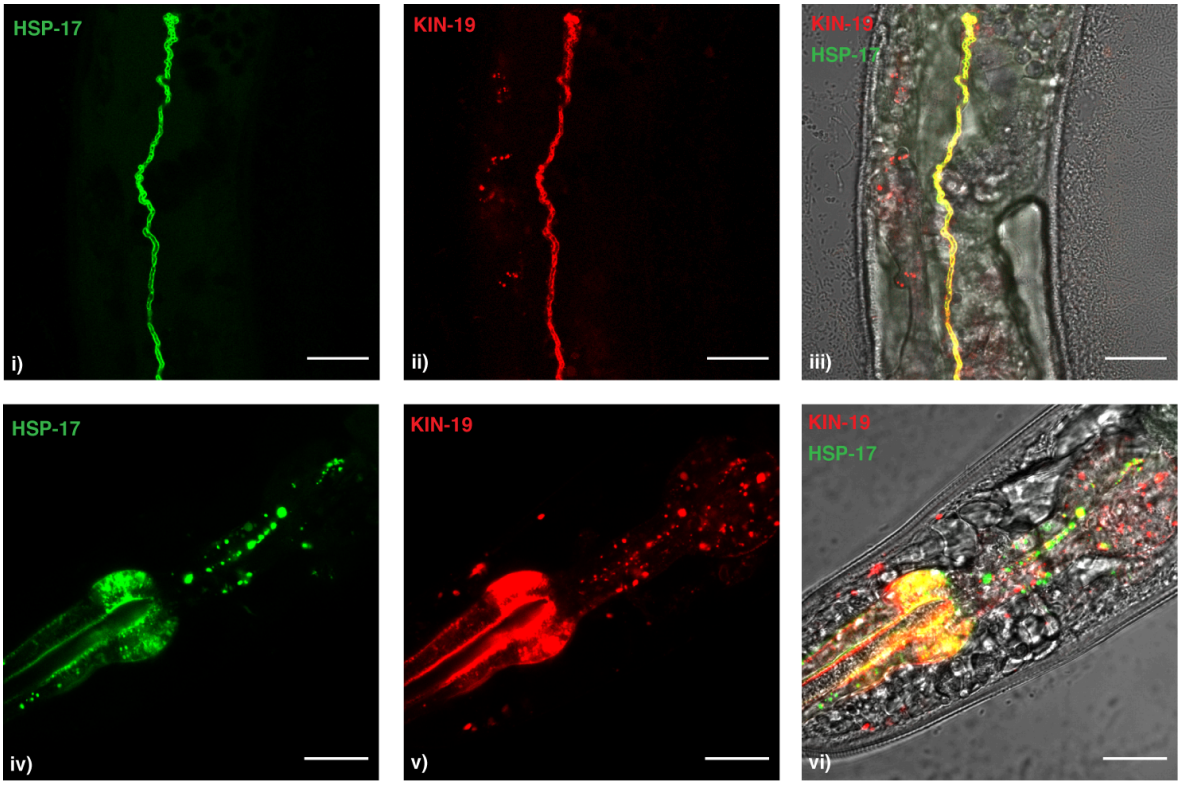

Figure 37: HSP-17 and KIN-19 colocalize in the pharynx and excretory tract

Representative confocal LSM of *C. elegans* p17tG crossed with the strain CF3166 (expression of KIN-19-tagRFP controlled by the native promoter). Separate channels and combined channel are provided, as noted on the images. The excretory tract (i-iii) and the pharynx (iv-vi) have been monitored. Scale bars are 20 µm.

My observation points to a colocalization between KIN-19 and HSP-17, including in foci. This indicates that HSP-17 and KIN-19 co-aggregate, however, I also observed HSP-17 and KIN-19 moieties that did not colocalize.

To quantify colocalization, I analyzed multiple microscopies by the *Fiji* plugin *EzColocalization*. I focused on the pharynx, as this was an area of the nematode marked by a high number of foci for both, KIN-19 and HSP-17. Colocalization analysis between HSP-17-GFP and KIN-19-tagRFP yielded a Pearson's correlation coefficient of 0,58 and a Spearman's rank correlation coefficient of 0,63 (representative images used for the analysis are found in supplementary Figure 7). Assuming values of -1 for the PCC or SRCC to indicate total exclusion, 0 to indicate no correlation and 1 to indicate complete colocalization, I interpret these values as a significant, but not complete colocalization between both proteins.

Consequently, I asked if KIN-19 aggregation is affected by HSP-17. For that, I analyzed groups of nematodes overexpressing KIN-19-tagRFP alone or in

conjunction with HSP-17-GFP overexpression. Furthermore, I subjected KIN-19-tagRFP nematodes to *hsp-17* knockdown by RNAi. The number of KIN-19-tagRFP foci were analyzed in the head region of each nematode and the total number of KIN-19-tagRFP foci for each group of nematodes was quantified:

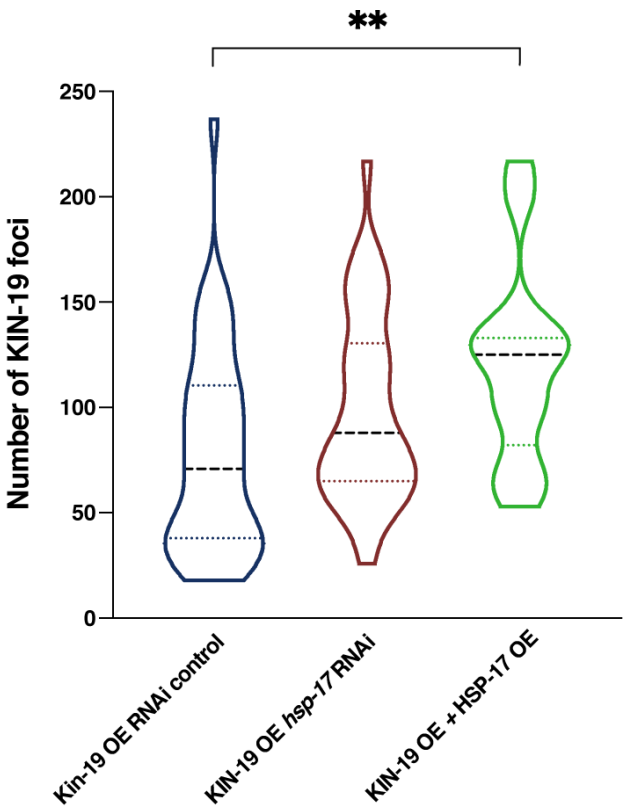

Figure 38: HSP-17 overexpression increases the formation of pharyngeal KIN-19 foci

For nematodes overexpressing KIN-19-tagRFP, the number of fluorescent foci in the head was quantified (blue) and visualized as a violin-plot. Quantification was also carried out for the same strain subjected to *hsp-17* RNAi (red) and for this strain, crossed with a translational reporter overexpressing HSP-17-GFP (green). The experiment was carried out in three independent repeats and one-way ANOVA testing (followed by Bonferroni's multiple comparisons test) was performed. Significant results were indicated by stars (Kin-19 OE control RNAi vs. KIN-19 OE *hsp-17* RNAi: p = 0,0031).

I took these data as confirmation that HSP-17 overexpression can indeed enhance the formation of KIN-19 foci *in vivo*, recapitulating the molecular aggregase activity observed in Figures 11 & 12. Depletion of *hsp-17* did not appear to diminish foci formation of KIN-19. This might be due to the fact that the KIN-19 reporter strain itself constitutes an overexpression condition, and the sensitivity of KIN-19 aggregation depends on a specific ratio to HSP-17. Indeed, maintenance of the KIN-19 overexpressing strain CF3166 revealed severe physiological defects. To correlate an

increase of aggregation of KIN-19 with organismal defects and toxicity, I monitored the development of the same *C. elegans* strains from L1 larval stage to adulthood.

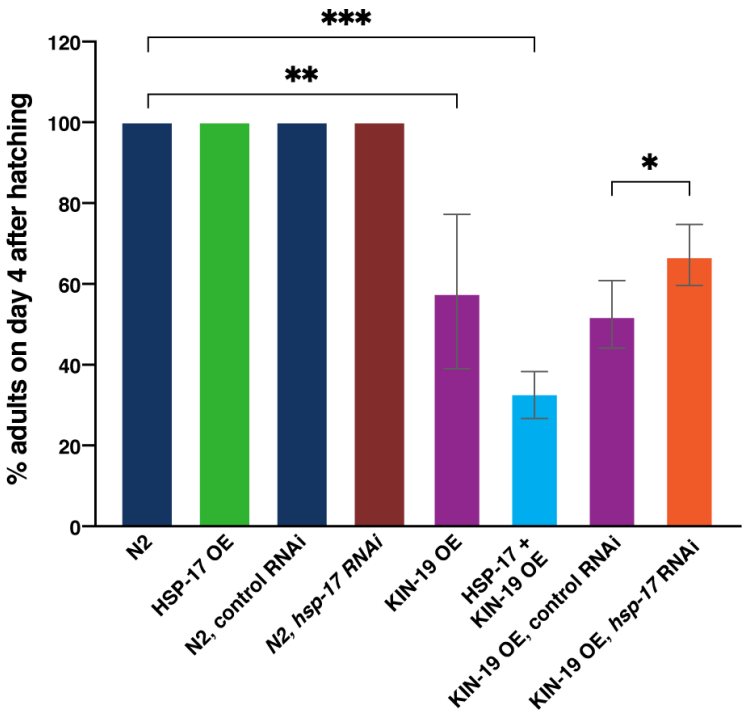

Figure 39: HSP-17 mediates deleterious effects of KIN-19 overexpression

Development was monitored for nematodes starting with L1 larvae and the number of nematodes reaching adulthood by day 4 of life was plotted. N2 nematodes and N2 nematodes subjected to control RNAi (blue) or *hsp-17* RNAi (red), as well as the strain p17tG (green) were used as control. The KIN-19 overexpressing strain CF3166 was subjected to no RNAi or control RNAi (purple) and *hsp-17* RNAi (orange). The crossing of p17tG and CF3166 is depicted in light blue. The experiment was carried out in three independent repeats and one-way ANOVA testing (followed by Sidak's multiple comparisons test) was performed. Significant results were indicated by stars (N2 vs. KIN-19 OE: $p < 0{,}0001$; N2 vs. KIN-19 OE / HSP-17 OE: $p < 0{,}0001$; Kin-19 OE control RNAi vs. KIN-19 OE *hsp-17* RNAi: $p = 0{,}0393$).

I conclude from this experiment that overexpression of KIN-19 has a deleterious effect on *C. elegans* development which is exacerbated by concurrent overexpression of HSP-17. Conversely, knockdown of *hsp-17* in the KIN-19 overexpressing nematode slightly, but significantly, rescues development. In conjunction with the observations from Figures 37 & 38, I interpret these results as confirmation that KIN-19 is an *in vivo* interaction partner of HSP-17, that aggregation of KIN-19 can be enhanced by HSP-17 and that modulation of KIN-19 by HSP-17 is relevant for physiological fitness.

On a final note, HSP-17 was found in my IP-MS/MS approach to be involved in the gestation of offspring and membrane transport (Table 2). Based on my data that HSP-17 localizes to some intestinal membranes (Figures 20, 22 & 23) and is relevant for fecundity in *C. elegans* (Figure 26), I generated a genetic cross between the strain p17tR and the VIT-2-GFP translational reporter strain DH1033 (vitellogenin-2 is an egg yolk protein, synthesized in the intestine and translocated to eggs (181), also found to interact with SIP-1 (82)). While I did not observe major colocalization between the two fluorophores, the crossed nematodes exhibited a dumpy phenotype, as shown in supplementary Figure 8. Furthermore, HSP-17 does seem to colocalize with vesicular structures (compare the "dotted" line around the excretory tract in Figure 20 v, Figure 23 and also refer to Table 2). Hypothesizing that HSP-17 is involved in membrane transport or endo- and exocytosis, I crossed the HSP-17 translational reporter with additional reporter strains[1]. Initial screenings revealed infrequent colocalization between HSP-17 and markers of vesicular traffic (supplementary Figures 9 & 10). In summary, these analyses suggest that HSP-17 plays an undiscovered role in *C. elegans* vesicular traffic, membrane transport and fat metabolism.

4.2. A new model of Aβ toxicity in *C. elegans*

My work on HSP-17, which exhibits a non-canonical chaperone activity, has demonstrated that molecular chaperone activity is strongly dependent on specific protein substrates *in vitro*. Adding to this *in vivo*, many physiological effects can spring from this activity and chaperoning is possible even for non-physiological amyloids like polyQ-peptides. This underlines the need to develop new *in vivo* models to expand the substrate repertoire that can be assayed.

Neurodegenerative disease is often preceded by a collapse of the proteostatic network, a process in which amyloidogenic proteins such as Aβ are either key substrates or agents (10,36). While the membrane protein APP has a homolog in *C. elegans* (the essential APL-1), the Aβ peptide is not encoded and likely vertebrate-specific (182). This has incited the generation of humanized *C. elegans* models of Aβ

1 The list of strains in the materials section shows an oversight of available strains crossed with my HSP-17 reporter, including reporters of endo- and exocytosis (*rab* genes, clathrin).

pathology, expressing the peptide cellularly (151), which have been subsequently improved (154). These models recapitulate the formation of amyloids leading to physiological defects (155) and also reveal action of molecular chaperones such as Hsc70 or sHsps on Aβ (160,161). Nonetheless, existing models forwent labeling of the peptide, mandating visualization of amyloids by staining (151,152) or labeled every moiety of Aβ, preventing “native” amyloid formation (156). A new model with powerful and versatile labeling could enhance the analysis of the chaperone network and sHsps in the context of amyloid pathogeny.

4.2.1. Generation of a new *C. elegans* Aβ model strain

Together with Christian Gallrein (CG), I set out to generate a new model of Aβ pathology in *C. elegans*, combining facile *in vivo* visualization with “native”-like fibrilization properties. To this end, untagged $A\beta_{1-42}$ was expressed in combination with a sub-stoichiometric moiety of labeled $A\beta_{1-42}$. As a label, the high quantum yield, monomeric red-spectrum fluorophore mScarlet (183) was used, in a version optimized for expression in *C. elegans* (wrmScarlet, (184)). To achieve pan-neuronal expression, the promoter region of *rgef-1* was chosen. Because the Aβ peptide lacks an N-terminal methionine, it was headed by a signal peptide for ER-import. This signal peptide is cleaved to yield full-length $A\beta_{1-42}$, which is reportedly retrotranslocated to the cytosol (152,154). Finally, to achieve sub-stoichiometric labeling, the unlabeled Aβ peptide is followed by the IRES-element of *C. elegans hsp-3*, followed by wrmScarlet-$A\beta_{1-42}$. IRES-dependent initiation of translation is less efficient than cap-dependent initiation of translation, leading to a reduced expression of N-terminally tagged $A\beta_{1-42}$ (185,186).

To achieve the desired construct, I performed molecular cloning to replace the CDS of GFP in the vector pPD95.77 with $A\beta_{1-42}$, before adding wrmScarlet to the N-terminus and then cloning the promoter of *rgef-1* into the vector. In parallel, a construct consisting of signal-peptide::$A\beta_{1-42}$::IRES was generated (CG). The latter was then cloned into the first to achieve the depicted construct. Additionally, for expression to the body wall muscle, the promoter of *myo-3* was cloned to replace the promoter of *rgef-1* (CG).

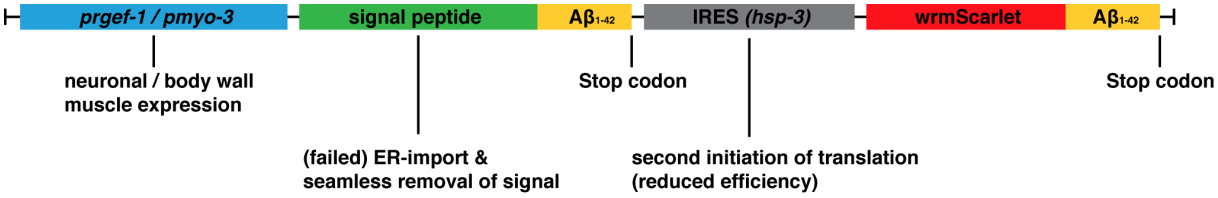

Figure 40: Genetic construct for expression of $A\beta_{1-42}$ in *C. elegans*

The construct cloned for expression of $A\beta_{1-42}$ with sub-stoichiometric expression of wrmScarlet $A\beta_{1-42}$. From 5' to 3': promoter regions of *rgef-1* (pan-neuronal) or *myo-3* (body wall muscle), 5'-methionine-signal peptide (cleaved upon failed ER-entry), full-length $A\beta_{1-42}$, IRES of *hsp-3* for attenuated initiation of translation, wrmScarlet-$A\beta_{1-42}$.

Subsequently, microinjection was performed to generate the neuronal Aβ strain (JKM2 / nAβ). The muscular Aβ strain (JKM7 / mAβ), as well as control strains expressing only wrmScarlet controlled by the promoters of *rgef-1* (JKM3 / nScarlet) or *myo-3* (JKM8 / mScarlet), were generated by microparticle bombardment. All strains except JKM8 were chromosomally integrated (CG).

To confirm successful generation of the planned transgenic strain I performed blotting of lysates of the strains nAβ and mAβ. In parallel, I visualized the generated strains by laser scanning microscopy:

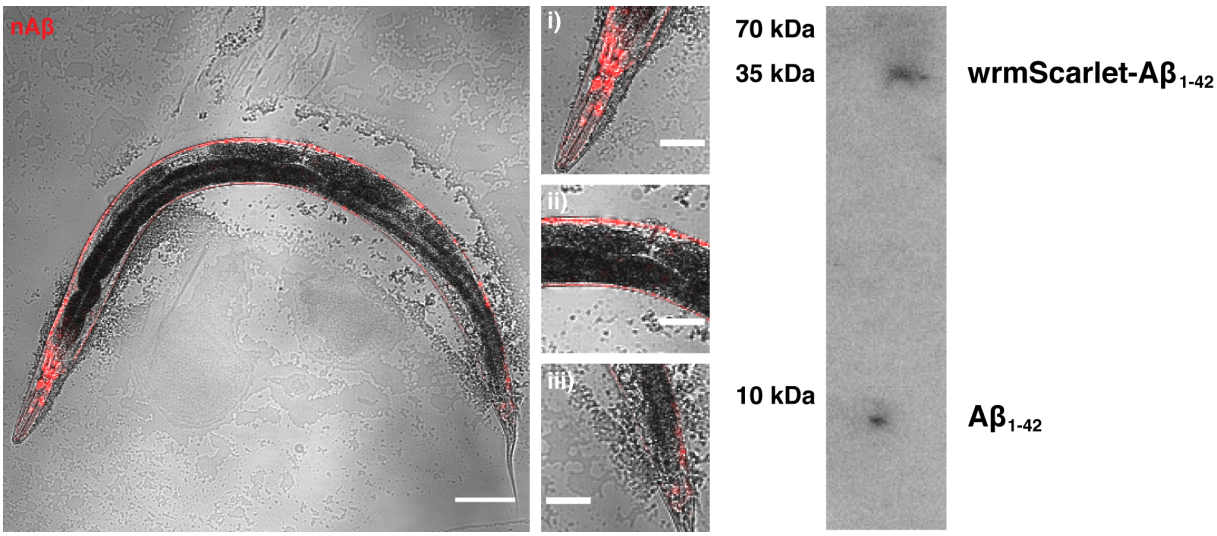

Figure 41: Visualization and biochemical analysis of *C. elegans* strain nAβ

Left side: expression of wrmScarlet-$A\beta_{1-42}$ in neurons of *C. elegans*, with details of head (i), body (ii) and tail (iii). Scale bar is 100 µm for whole animal and 50 µm for detail. Right side: Western blotting of JKM2 lysates with 6E10 antibodies to detect wrmScarlet-$A\beta_{1-42}$ (around 35 kDa) and $A\beta_{1-42}$ (below 10 kDa).

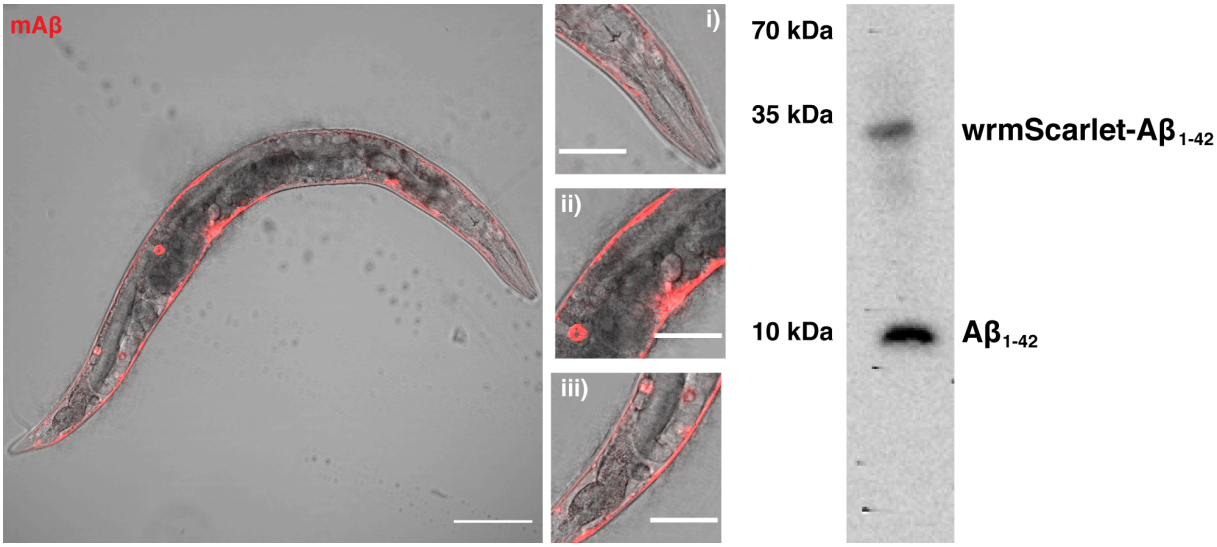

Figure 42: Visualization and biochemical analysis of *C. elegans* strain mAβ

Left side: expression of wrmScarlet-Aβ_{1-42} in body wall muscle of *C. elegans*, with details of head (i), lower body (ii) and tail (iii). Scale bar is 100 µm for whole animal and 50 µm for detail. Right side: Western blotting of JKM7 lysates with 6E10 antibodies to detect wrmScarlet-Aβ_{1-42} (around 35 kDa) and Aβ_{1-42} (around 10 kDa).

By western blotting I could demonstrate that co-expression of the tagged and untagged Aβ moiety was achieved as planned. In addition, microscopy demonstrated that wrmScarlet-Aβ_{1-42} is present in *C. elegans* neurons or body wall muscle, respectively. The signal acquired from blotting JKM2 lysates is very faint (Figure 41), implying that the total mass of the peptide expressed to the neurons is a relatively small fraction of total protein mass per nematode. By comparison, detection of Aβ in JKM7 lysates leads to a stronger signal (Figure 42). I surmise that the total mass of Aβ peptide expressed to body wall muscles per nematode is higher and therefore more suitable for biochemical analysis. To estimate the relative levels of labeled and unlabeled Aβ in the model, I performed additional western blot experiments with the muscular strain to perform quantification by band intensity. I observed a high variance in the relative levels of labeled to unlabeled Aβ, implying uneven blotting or detection efficiency for Aβ (Supplementary Figure 11).

A key feature of the new AD model is that a large moiety of unlabeled Aβ peptide is to interact with a smaller fraction of labeled peptide, to combine easy visualization with unhindered formation of fibrils. To demonstrate that both moieties interact, I prepared lysates of mAβ nematodes and used them for an immunoprecipitation

experiment (with anti-GFP antibodies, binding wrmScarlet) followed by western blotting. If both moieties of Aβ interact *in vivo*, pulldown of wrmScarlet-Aβ should be sufficient to enrich unlabeled Aβ:

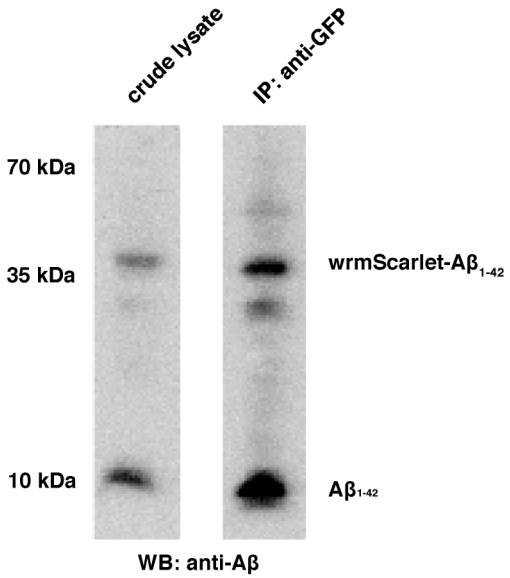

Figure 43: Immunoprecipitation of Aβ peptide in *C. elegans* strain mAβ

Lysates of mAβ were used to perform IP of wrmScarlet-$A\beta_{1-42}$ by anti-GFP antibodies, followed by western blotting with anti-Aβ-antibodies. On the left side, whole lysate was blotted. On the right side, the IP-sample was blotted. In both lanes, labeled and unlabeled peptide were detected as indicated. Detection was carried out with 6E10 antibodies.

Notably, IP of wrmScarlet-$A\beta_{1-42}$ was sufficient to enrich the sample for unlabeled $A\beta_{1-42}$, implying that both peptides interact *in vivo*, as intended in the experimental design. Following the establishment of the new model strains, I then set out to analyze the impact of $A\beta_{1-42}$ overexpression on the *C. elegans* organism *in* and *ex vivo*. To validate the use of the model it had to be demonstrated that $A\beta_{1-42}$ overexpression has deleterious effects *in vivo*, including defects that were previously observed. Moreover, the fluorescently labeled wrm-Scarlet-$A\beta_{1-42}$ would need to provide information on localization and aggregation of Aβ in living *C. elegans*.

4.2.2. Biochemical analysis of *C. elegans* $A\beta_{1-42}$ model strains

I first set out to characterize the *in vivo* interactome of $A\beta_{1-42}$ overexpressed in *C. elegans* through IP-MS/MS experiments. Two main questions can be addressed in

this fashion: does the *C. elegans* proteostasis network exert molecular chaperone activity in this humanized model of Aβ pathology and does the peptide have deleterious effects on specific cellular mechanisms? I performed immunoprecipitation with 6E10 anti-Aβ-antibodies on lysates of mAβ and nAβ. As controls for background and antibody specificity, the strains expressing muscular or neuronal wrmScarlet, but not Aβ, were used. Analysis of the samples by MS/MS was performed and proteins that were either significantly detected exclusively in the mAβ and nAβ fractions, or significantly increased in those fractions compared to the controls, were considered to be enriched and thus part of the Aβ interactome[1].

For mAβ, a large set of proteins was identified as significantly enriched, including the Hsc70-family chaperone HSP-1 and the sHsp HSP-16.41. Both were reported to be interacting with Aβ previously in the muscular mAβ model CL2006 (160). Moreover, I identified the Hsp90 homolog DAF-21 and the ER-chaperone CNX-1 (calnexin). Other chaperones were identified that had not previously been reported to interact with Aβ *in vivo*: the J-proteins DNJ-2, DNJ-13, DNJ-19 and DNJ-29. The identification of numerous molecular chaperones as Aβ interaction partners indicates that the peptide is recognized as misfolded or proteotoxic. To visualize the enrichment of proteins detected by IP-MS/MS, I generated a volcano plot:

1 Raw data for the IP-MS/MS experiments and resulting search files, as well as experimental parameters, have been uploaded to the PRIDE repository. A supplementary table with additional information is also provided (see data availability, **10.3**).

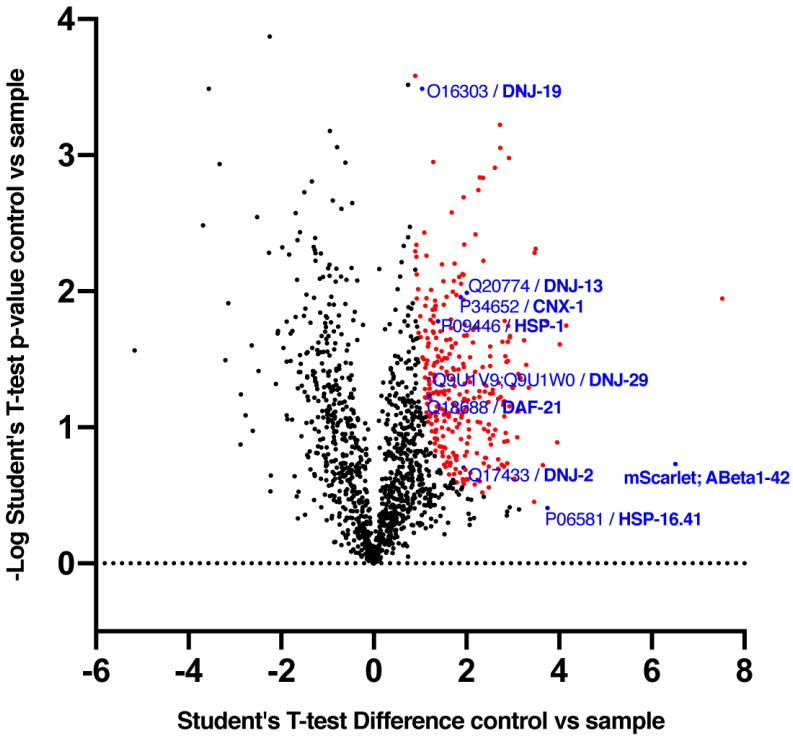

Figure 44: Volcano plot of IP-MS/MS results (mAβ)

Each dot represents a protein identified by IP-MS/MS and red dots are proteins significantly enriched. Proteins of particular interest have been labeled in blue, including the target of IP, wrmScarlet-Aβ. The x-axis can be considered a measure of enrichment in the sample and the y-axis a measure of significance ($-\log_2$). IP-MS/MS analysis was performed in triplicates. One set of sample and control was similar to each other and censored from the final result.

IP-MS/MS analysis of nAβ yielded only a small number of significantly enriched proteins. Comparing the western blots in Figures 41 & 42 already demonstrated that the total fraction of Aβ peptide upon neuronal overexpression is very low and difficult to detect biochemically. Hence, I also cannot exclude false-positive protein hits. Unsurprisingly, previous proteomic analyses of Aβ overexpression in *C. elegans* have also focused on muscular models (160,187). Nonetheless the chaperone protein F44E5.4 (HSP-70) was identified in the neuronal model strain, as previously reported (187), hinting that molecular chaperones are involved in remodeling Aβ in the neurons as in the muscles. To exemplify the resulting data, I prepared another volcano plot:

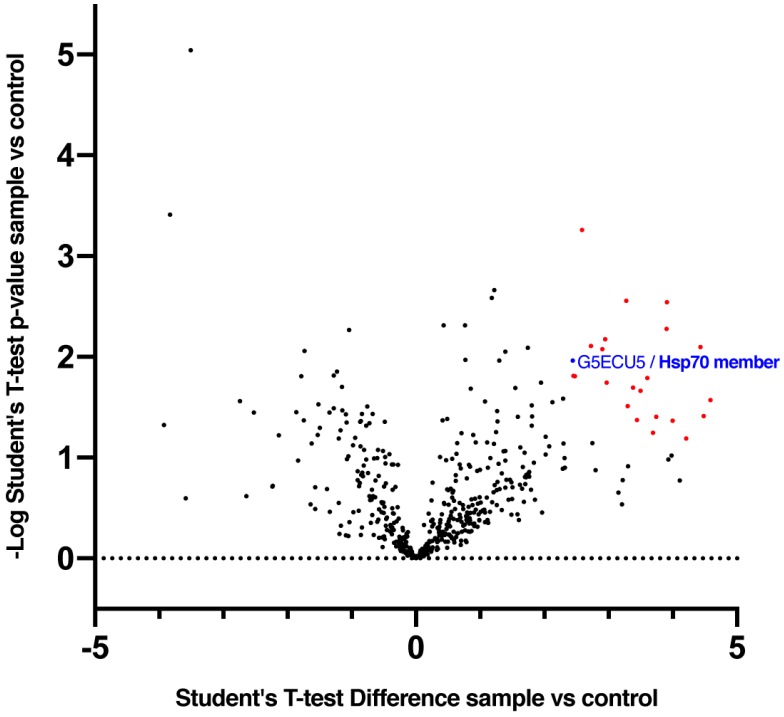

Figure 45: Volcano plot of IP-MS/MS results (nAβ)

Each dot represents a protein identified by IP-MS/MS and red dots are proteins significantly enriched. Proteins of particular interest have been labeled in blue. The x-axis can be considered a measure of enrichment in the sample and the y-axis a measure of significance ($-\log_2$). IP-MS/MS was performed as a triplicate experiment.

The small dataset generated from the neuronal strain was insufficient for systemic analysis. However, close to 300 proteins were identified (Figure 44, colored dots) in the muscular strain. Based on the assumption that many cellular features such as membranes, protein transport and protein folding or degradation are conserved in all cells, I decided to analyze the muscular model as a proxy for organismal effects of Aβ. To systemically analyze the large set of enriched proteins identified from mAβ, I performed functional annotation analysis using the online tool *DAVID* to generate GO-terms for the mAβ strain:

Table 4: List of notable GO-terms identified in IP-MS/MS analysis of mAβ

Nr.	GO-term	Number of proteins matching term	P-value (*DAVID*)
1	Receptor-mediated endocytosis	54	1,05E-13
2	Cullin deneddylation	5	4,30E-6
3	Endoplasmatic reticulum UPR	9	2,99E-4
4	Protein transport	11	1,70E-3
5	Secretion by cell	8	2,16E-3
6	Apoptotic process	35	7,38E-9
7	Determination of adult lifespan	42	1,77E-4
8	Protein folding	10	2,34E-4
9	Response to starvation	5	8,78E-3
10	Response to heat	7	9,35E-3
11	Locomotion	64	2,15E-7
12	Body morphogenesis	29	6,11E-4
13	Oxidation-reduction process	24	2,80E-3

In the selection of GO-terms I present, a number of terms relate to protein homeostasis (6-10). Indeed, stress response upon Aβ overexpression in body wall muscle was reported ((188), by induction of *hsp-16* promoter) and these terms mirror the selection of individual chaperones presented above. I surmise that the model undergoes proteotoxic stress as intended. Motility (11-12) is also implied in the dataset and it has been shown that muscular Aβ expression in *C. elegans* can lead to progressive paralysis (151,189). Moreover, redox-process (13) is among my hits, matching previous reports that Aβ overexpression can lead to an impairment of redox-homeostasis (190), as does proteotoxic stress in general (191). Finally, GO-terms related to protein trafficking, membrane- and vesicular transport as well as secretion (1-5) are significant among my identified proteins. This may be due to the peptide being targeted to the ER, or a more general membrane-damaging effect of Aβ, which has recently been described in *C. elegans* (56). This observation may point to intercellular spreading of Aβ occurring in the new model, which is a hallmark of amyloid pathology (58).

To reinforce these proteomic observations, subsequent experiments had to be carried out. First, TEM analysis of the strains mAβ and nAβ was performed. For both strains, adult nematodes on day 10 of life were analyzed:

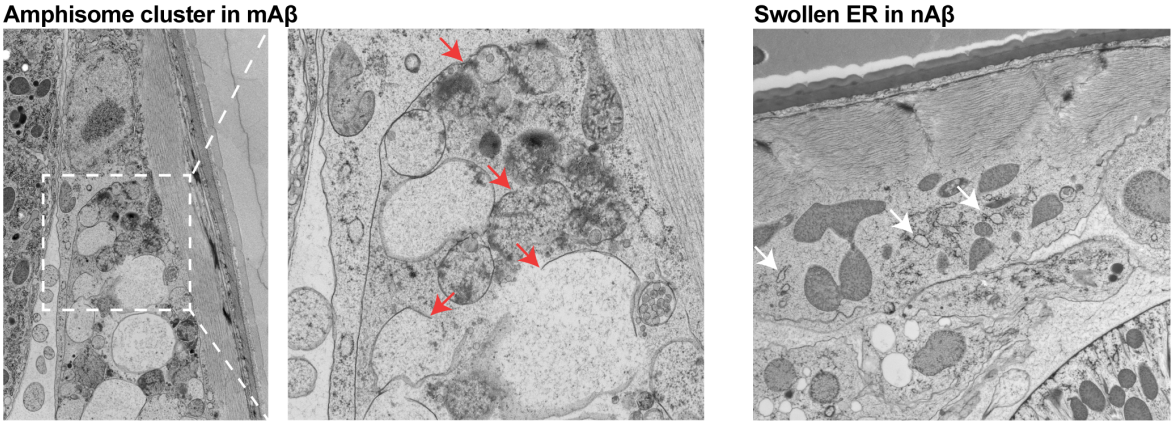

Figure 46: TEM of amphisomes and swollen ER in mAβ and nAβ

TEM was performed on mAβ and nAβ nematodes and representative images are presented. On the left side, muscular tissue of mAβ is shown and in the middle, a zoom as indicated by the dashed white lines in the left image. The red arrows indicate instances of incomplete or aberrant membrane structures. On the right side, an image of nAβ is presented and the white arrows indicate instances of swollen ER. TEM experiments were performed by Dmytro Puchkov.

For the muscular strain, striking clusters of incomplete membrane structures, of either endo-/exosomal, lysosomal or autophagosomal nature (hence referred to as “amphisomes”) were frequently detected (Figure 46 left side and zoom). These structures could be interpreted as loci of failed autophagy, which is commonly reported in AD pathology (192). Furthermore, in the context of Aβ spreading, these structures could represent aberrant multivesicular bodies resulting from Aβ trafficking (193). In the neuronal model, amphisome formation was less pronounced, but bloated ER-structures were frequently observed. While the ultrastructural analysis of mAβ and nAβ did not yield identical findings, it can be concluded that both models show aberrant autophagy or impairments in the endo-membrane system and that the neuronal model has defects in the ER.

I attempted to corroborate these findings with further biochemical analyses. First, I crossed the strains JKM2, 3, 7 and 8 with a strain bearing a YFP-reporter controlled by the *hsp-3* promoter region. As HSP-3 (BiP-homolog) is an ER-chaperone, it is induced upon ER-stress and both the GO-terms in table 4 as well as the TEM

analysis indicate that this should occur. I quantified the induction of YFP in nematodes on day 7 of life for each crossed strain compared to the respective control strains:

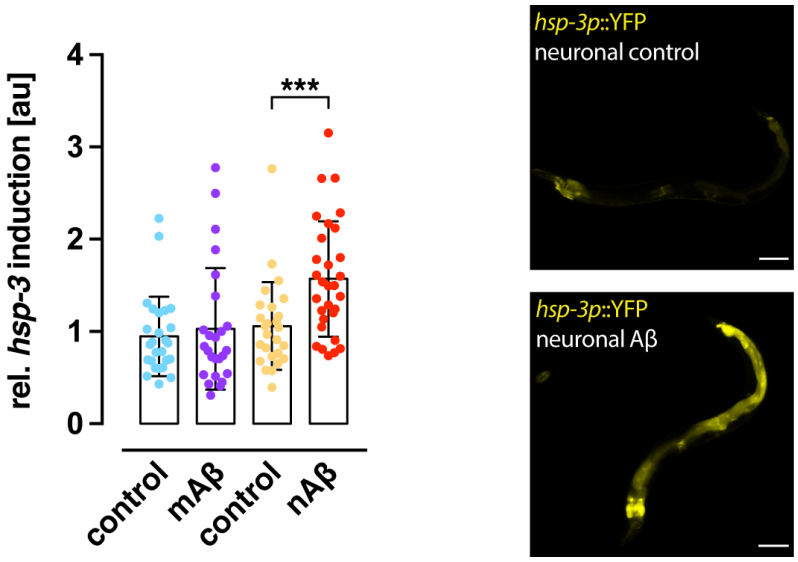

Figure 47: Quantification of *phsp-3* induction by overexpression of Aβ

Left side: YFP-fluorescence in nematode intestines was quantified for 10-20 nematodes in three independent experiments. The y-axis indicates the fold-induction normalized to the controls (set as 1). One-way ANOVA testing was performed. The muscular control (cyan) was compared to mAβ (purple) and the neuronal control was compared to nAβ (red) by Bonferroni's multiple comparisons test and significant results were indicated by stars (neuronal control vs. nAβ: p = 0,0003). Right side: microscopies exemplifying the induction of YFP in the neuronal control (top) or nAβ (bottom). Scale bars are 50 µm.

My analysis revealed that, in line with the observations from TEM, the ER stress response is induced in the nAβ background. This is also in line with my observations from the IP-MS/MS experiment on mAβ (Table 4, 1-6), although YFP-induction in the muscular strain was not significant. Indeed, mAβ did not show the swollen ER phenotype in TEM experiments (Figure 46, right side). I conclude that while there might be an involvement of ER stress in mAβ, this effect is too subtle to be detected by methods other than MS/MS.

TEM experiments also pointed to defects in autophagy upon Aβ overexpression (Figure 46, left side). Since the observed amphisomes can be interpreted as remainders of failed initiation of autophagy, I set out to biochemically analyze expression levels of autophagy markers in the Aβ background. Using *C. elegans*

lysates of young adult animals, I performed western blotting with subsequent detection utilizing anti-SQST-1 antibodies or anti-LGG-1 antibodies. SQST-1 is a homolog of human p62 (an adaptor and substrate of autophagy) and LGG-1 is a homolog of human LC3 (an initiator of phagophore formation). Detection was carried out as described previously (175):

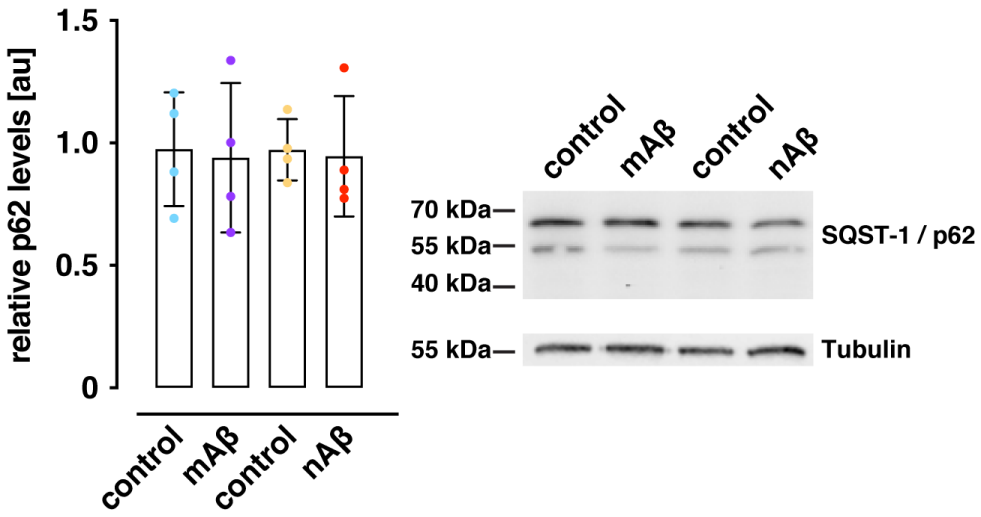

Figure 48: Quantification of SQST-1 in $A\beta_{1-42}$ expressing nematodes

Left side: SQST-1 expression levels were quantified in three independent experiments. The y-axis indicates the fold-induction normalized to the controls (set as 1). One-way ANOVA testing was performed. The muscular control (cyan) was compared to mAβ (purple) and the neuronal control was compared to nAβ (red) by Sidak's multiple comparisons test (no significant differences). Right side: an exemplary western blot showing bands for SQST-1 in samples and controls (both bands correspond to SQST-1 (175). In the same experiment, tubulin was detected as a loading control (lower part).

For SQST-1, no change in cellular levels was detected in the Aβ background. This can indicate that expression or turnover of SQST-1, a substrate of autophagy, remains unaltered. To complement this analysis, LGG-1 needed to be quantified analogously:

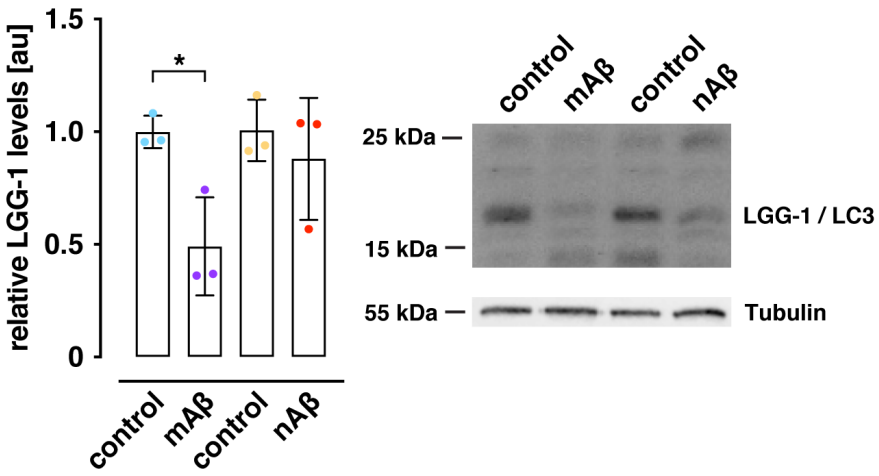

Figure 49: Quantification of LGG-1 in Aβ background

Left side: LGG-1 expression levels were quantified in three independent experiments. The y-axis indicates the fold-induction normalized to the controls (set as 1). One-way ANOVA testing was performed. The muscular control (cyan) was compared to mAβ (purple) and the neuronal control was compared to nAβ (red) by Sidak's multiple comparisons test and significant results were indicated by stars (muscular control vs. m Aβ: p = 0,0112). Right side: an exemplary western blot showing bands for LGG-1 in samples and controls. In the same experiment, tubulin was detected as a loading control (lower part).

In this experiment, LGG-1 levels in mAβ were significantly reduced but did not differ significantly in the neuronal model. Reduction of LGG-1 paired with constant levels of SQST-1 implies defects in initiation of autophagy (175) and this matches the previous observation of aberrant membrane clusters or amphisomes (Figure 46, left side).
To summarize, by IP-MS/MS analysis I could demonstrate an induction of proteotoxic stress, the involvement of molecular chaperones and other organismal defects, all of which are in agreement with described models of Aβ pathology. Furthermore, defects in autophagy (in the muscular model) and a deleterious effect on the ER (in the neuronal model) could be confirmed on the ultrastructural and biochemical level.

4.2.3. Primary vulnerable neurons

The principal utility of labeling Aβ in this approach is tracking the distribution and aggregation state of wrmScarlet-Aβ in *C. elegans in vivo*. Due to the interaction with labeled Aβ (see Figure 43), the distribution of unlabeled Aβ could be inferred. Fluorescence lifetime imaging microscopy (FLIM) was employed to quantify the

progression of Aβ aggregation over age. In brief, observing the fluorescence lifetime of wrmScarlet can be used to monitor and quantify the aggregation and formation of amyloid fibrils by Aβ, more so than simple distribution of the fluorophore (i. e. into cellular foci). A reduction of the fluorescence lifetime τ, compared to the control, implies that the fluorophore is located in a microenvironment adjacent to aggregated or fibrillar material (194). Nematodes on days 3, 4, 7 or 10 of life were analyzed to quantify the aggregation state of Aβ (FLIM experiments by CG).

The generated FLIM data indicated an age-dependent decline of fluorescence lifetime of wrmScarlet in those strains overexpressing Aβ. By contrast, the decline of fluorescence lifetime was mild for the control strains where Aβ is absent. From this, it could be concluded that aggregation of Aβ occurs and is directly affecting the microenvironment of wrmScarlet. The difference between control and Aβ strains emerged on day 4 of life, coinciding with the onset of proteostatic decline (115) and became more pronounced at later stages of life.

Most importantly, FLIM-analysis of nAβ revealed that starting on day 3 of life, in a small fraction of neurons, aggregation of Aβ as measured by fluorescence lifetime is more pronounced than in other neurons. This group of six neurons located in the anterior ganglion displayed early aggregates, hinting that they are particularly vulnerable to Aβ overexpression.

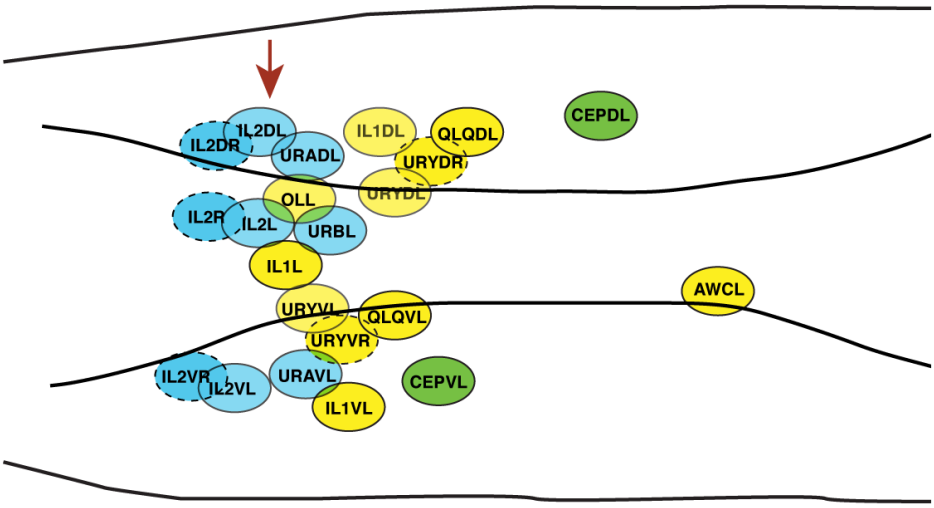

Figure 50: Detection of neurons in nAβ vulnerable to aggregation

A visualization depicting select neurons located in the anterior ganglion of *C. elegans*. Cholinergic neurons are marked blue, dopaminergic neurons are marked green, glutamatergic neurons are marked yellow. Black lines roughly indicate the shape of the nematodes skin and the pharynx. Dashed outlines indicate neurons that are on the opposite site of their respective counterpart. The red arrow roughly indicates the expected position of the vulnerable neurons. This graphic was adapted from published literature (195,196).

The intriguing observation that a specific subset of neurons stands at the beginning of Aβ aggregation and possibly proteostatic collapse necessitated further investigation. Recent research has revealed that initial populations of aggregated, proteotoxic Aβ can spread inside an organism and promote pathology in adjacent cells, or systemically (57,58,197), fortifying the hypothesis that Aβ pathogeny progresses in a cascade-like manner. Additionally, proteomic (Table 4, 1-5) and biochemical (Figures 47 - 49) findings underline the involvement of protein transport and membrane stress in the Aβ model. Following the hypothesis that the observed vulnerable neurons are key in promoting organismal pathology, it was mandatory to elucidate their identity. Based on their specific location, previous knowledge about the (deterministic) development of *C. elegans* neurons (Figure 50) and reports that cholinergic neurons are characteristically vulnerable to Aβ pathology (198,199), the six IL2 neurons were predicted as likely candidates. To confirm this, I cloned the promoter of *klp-6*, which is expressed in the IL2 neurons (200), to generate a transcriptional reporter ([*pklp6::GFP*]). A transgenic *C. elegans* strain was generated by microinjection (CG), and I performed crossing with the strain nAβ. By microscopy, I could confirm that the vulnerable neurons overlapped with the GFP-reporter:

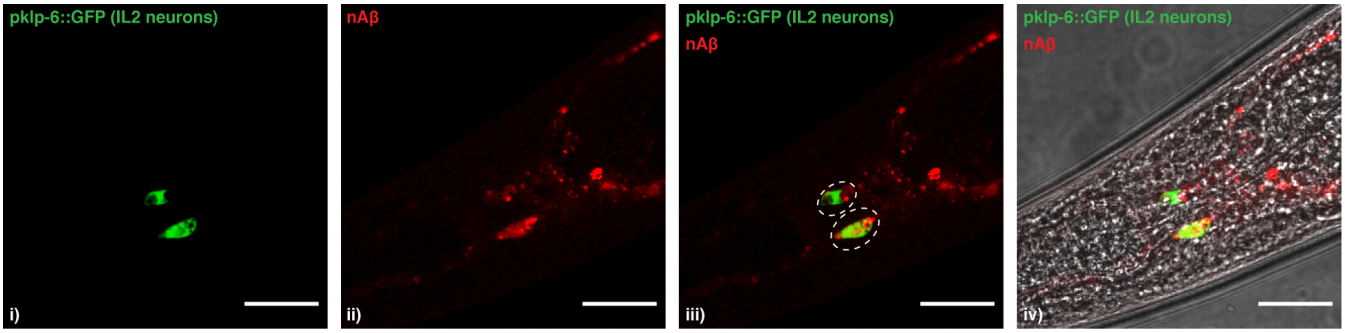

Figure 51: Colocalization between IL2 transcriptional reporter and nAβ

Laser scanning microscopy showing GFP expressed to the IL2 neurons (i), neuronal wrm-Scarlet Aβ, (ii), the overlay of both channels (iii) and an image including both channels and dissection microscopy (iv). The white dashed spheroids indicate the location of the IL2 neurons and the overlap between the GFP marker and Aβ. The scale bar is 20 µm.

If the identified set of six IL2 neurons is an early hot spot of Aβ aggregation and moreover, key in spreading organismal pathology, modulation of Aβ in these neurons should have a systemic effect. A short hairpin (shAβ) construct of the configuration *Aβ$_{1-42}$ forward/reverse::sl2* was generated (CG), which could be used to achieve cell-specific knockdown of Aβ$_{1-42}$ paired with the appropriate promoter (201,202). I cloned the construct into the vector pPD95.77 + *pklp-6*, partially removing GFP, to achieve IL2-specific knockdown of Aβ. In parallel, the promoter of *tol-1* was used in the same fashion to achieve knockdown in URY neurons, which are physically close to IL2 neurons (Figure 50), as a control for cell-specificity, and both constructs were used to generate transgenic strains by microinjection (CG). Crossing was performed to generate the strains nAβxshAβ(IL2) and nAβxshAβ(URY) which should result in attenuated expression of Aβ in the respective neurons. Then, FLIM analysis was performed on nematodes on day 4 of life to validate the effect of the cell-specific knockdown (CG).

The data obtained by CG indicated that cell-specific knockdown of Aβ in IL2 neurons could reduce the relative abundance of Aβ aggregates in head neurons, coupled to longer fluorescence lifetimes. This can be taken as evidence that cell-specific treatment reduces the burden of Aβ proteotoxicity beyond the targeted cells. To assess if there was an amelioration of systemic pathology, additional physiological experiments were performed: the lifespan of nematodes treated with cell-specific RNAi of Aβ was assayed in combination with a swim-exhaustion assay.

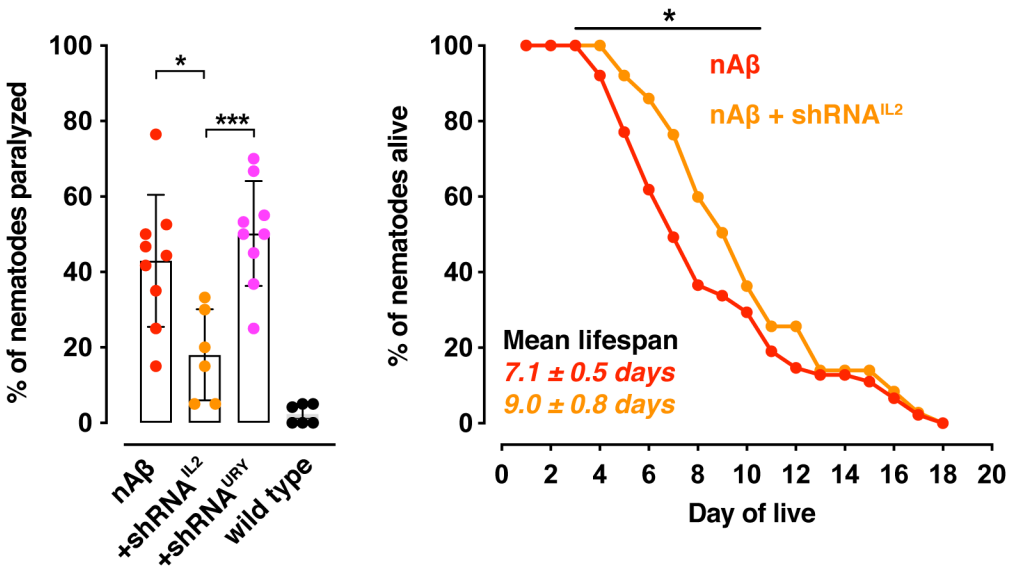

Figure 52: Cell-specific knockdown of Aβ in IL2 neurons ameliorates proteotoxicity

Left side: A scatter dot-plot of the fraction of nematodes that were paralyzed after 30 min in a swim-exhaustion assay. The strain nAβ (red), nAβ subjected to cell-specific Aβ knockdown in IL2 neurons (yellow) and the same, but targeted to URY neurons (magenta) are presented. Wild type N2 nematodes (black) are also shown for comparison. One-way ANOVA testing was performed, followed by Bonferroni's multiple comparisons test. Significant results are indicated by stars. Swim-exhaustion assay data was prepared together with CG. Right side: Lifespan assay of nAβ (red) and nAβ treated with cell-specific knockdown of Aβ in IL2 neurons. The fraction of surviving nematodes per day of live is presented, as well as the mean lifespan for each strain. The black line indicates the timespan for which a log-rank test was performed and the significance is indicated by a star ($p < 0{,}01$). The experiment was performed together with Sara Ayala Mariscal and results are presented for a total of 100-150 assayed nematodes. Log-rank testing was performed by CG.

The additional assays demonstrated that cell-specific depletion of Aβ in Il2 neurons can systemically improve fitness in response to exhaustion and slightly ameliorates the significantly reduced lifespan of nAβ during the reproductive phase (also compare Figure 25 for wild-type lifespans).

In conclusion, cell-specific knockdown in the identified IL2 neurons, but not the adjacent URY neurons, ameliorates the impact of neuronal Aβ overexpression in the newly generated AD model. Both nAβ and nAβxsh(URY) demonstrated a similar ratio of neurons with aggregated material on day 4 of live. Likewise, attenuation of Aβ overexpression in URY neurons does not rescue the decline in fluorescence lifetime observed. More importantly, depleting Aβ only in these IL2 neurons improves

organismal fitness of the assayed nematodes. This supports the hypothesis that IL2 neurons are specifically vulnerable to Aβ proteotoxicity and present a starting point for spreading of pathology to other cells.

5. Discussion

5.1. The non-canonical *C. elegans* sHsp HSP-17

The proteostasis network (PN) aids in protein folding, defends the proteome against stressors that would lead to protein misfolding and aggregation and, if this fails, protects the cell against deleterious effects of aberrant proteins. Molecular chaperones are the main agents of the PN, aiding other proteins in reaching and maintaining their correct fold and re-achieving it upon misfolding or otherwise promoting their degradation. Failure of this process can be caused by aging, mutation or external insults and is equally causative of aging and neurodegenerative disease (10,32). As part of the chaperone network, small heat shock proteins are ATP-independent, ubiquitous, highly expressed and bind unfolded protein substrates, buffering them against aggregation. The sHsp substrate is thereby made available for ATP-dependent molecular chaperones, to perform disaggregation and refolding (11,62).

In the work presented here, I have analyzed the non-canonical small heat shock protein HSP-17 from *C. elegans*. HSP-17 was shown to exhibit limited conventional molecular chaperone capacity (e.g. suppression of aggregation) and instead, acted as a „molecular aggregase“. This term was coined previously for yeast Hsp42, which can act in a cytoprotective manner by promoting aggregation (110). Here, I have demonstrated for HSP-17 as the first metazoan protein to promote the aggregation of the model substrate MDH *in vitro* and both artificial Q_{40}-YFP as well as endogenous KIN-19 substrates *in vivo*. The physiological significance of HSP-17 was elucidated, showing that it is cytoprotective under basal and stressed conditions, relevant for reproduction and development and most present in the alimentary system.

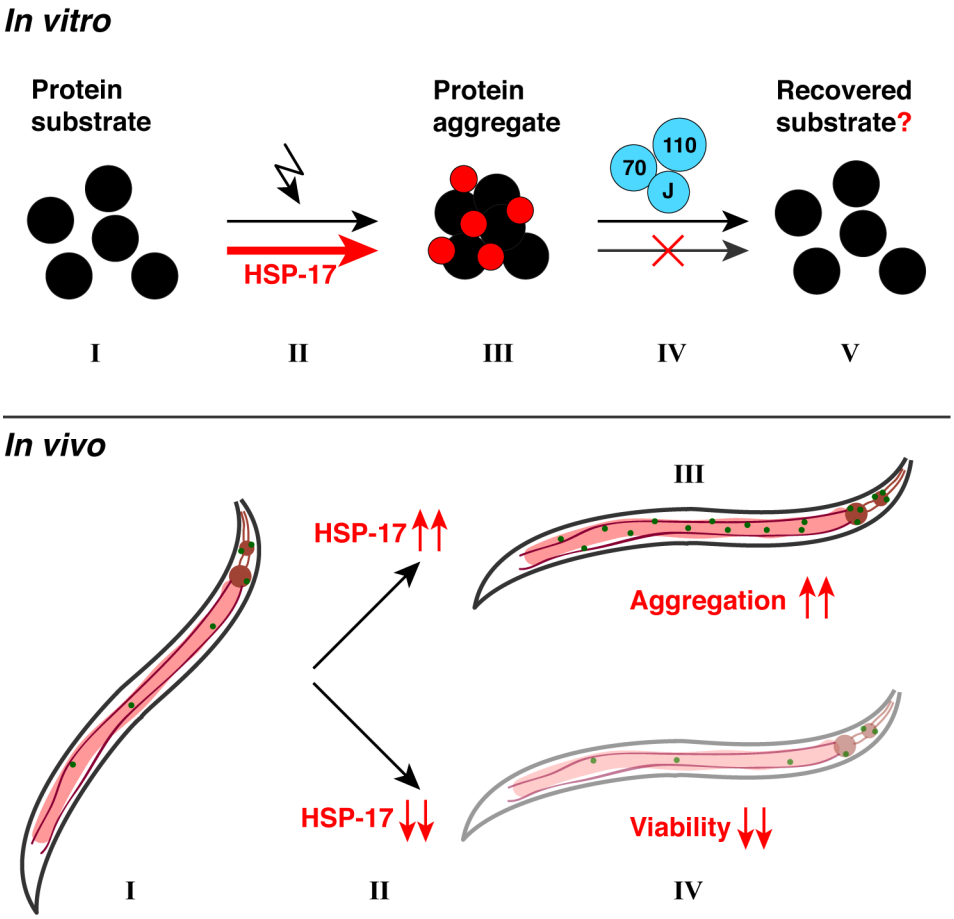

Figure 53: Overview of HSP-17 activity

In vitro: Native protein substrates such as MDH or Luciferase were utilized (I). The substrates aggregate due to proteotoxic challenges such as external stressors or aging. Red: HSP-17 can enhance aggregation for the selected substrates (II). Red: HSP-17 can become insoluble alongside the substrate, potentially altering the resulting aggregate (III). Protein aggregates can be recovered by ATP-dependent molecular chaperones (such as the triad of HSP-1, HSP-110 and J-Proteins in *C. elegans*). Red: HSP-17 partially inhibits this recovery (IV). After disaggregation and refolding by chaperones, native proteins are recovered. Red: it remains to be uncovered if HSP-17 activity will result in recovery or if HSP-17 can alter the fate of aggregated protein substrates, i. e. to be segregated (V). *In vivo*: HSP-17 is most notably expressed to the pharynx, the intestine and the excretory canal cell as indicated by red hues in the schematic depiction of *C. elegans*. Green dots represent aggregated protein (I). HSP-17 was overexpressed in a transgenic model strain or depleted by RNAi (II). The aggregation of the selected protein substrates (KIN-19, polyQ peptides) is enhanced upon HSP-17 overexpression (III). The viability of *C. elegans* (i. e. fecundity or resistance against select stressors) is reduced upon depletion of HSP-17 (IV).

5.1.1. HSP-17 promotes aggregation, but is an inefficient molecular chaperone

It has been understood for a long time that small heat shock proteins are part of the cellular chaperones and maintain the solubility of their protein substrates in various tissues (86,169). Higher organisms like humans express a large number of different sHsps and the efficiency of this process varies greatly for each sHsp, the specific substrate and the surrounding medium (91). Similarly, *C. elegans* expresses multiple sHsps (147), which inhibit the aggregation of model substrates even at 4-fold molecular excess (82,203) while others do not act as chaperones even at 200-fold excess (71).

Here, I undertook analysis of HSP-17 chaperone activity. I first found that HSP-17 can prevent the aggregation of select model substrates only partially and at high molecular excess compared to other *C. elegans* sHsps. This has been reported for additional *C. elegans* or mammalian sHsps (69,72) and raised the possibility that HSP-17 fulfills an additional activity besides acting as a molecular chaperone. Indeed, *in vitro* chaperone activity assays with MDH as a substrate revealed that HSP-17 can promote the aggregation of this substrate. This partially mirrors the activity of yeast Hsp42, one of two yeast sHsps, which can both promote or inhibit aggregation of MDH under specific conditions (110) and is the first instance of this activity reported in a metazoan. HSP-17 is smaller than Hsp42, which provides a possible explanation why it does not exhibit both activities equally. Furthermore, aggregase activity of Hsp42 was attributed to a prion-like domain (170), which is absent in HSP-17. From this I conclude that HSP-17 promotes aggregation by a different mechanism that remains to be discovered.

The observation that a chaperone family member would promote aggregation poses the question what selection benefit enhanced protein aggregation has. In yeast, Hsp42 was shown to be relevant for viability under recurring heat stress (110) and required for the aggregation of substrates at specific intracellular sites (106,108). Molecular aggregase activity has also been reported for *B. subtilis* YocM, a protein relevant under osmotic stress conditions (109) and likewise, HSP-17 has been shown to be protective in *C. elegans in vivo* under both of these stresses. Furthermore, HSP-17 colocalized with aggregates *in vivo*, but not those of the aggregation-prone, stress-granule associated PAB-1 (180). CLEM data of HSP-17-

GFP in the pharynx further corroborates this, demonstrating that HSP-17 colocalizes with distinct, but not all, electron-dense objects in the pharynx. This implies that like Hsp42, HSP-17 is not involved *in all*, but specific cellular aggregation events and it appears that promotion of aggregation activity is beneficial at least under certain stress conditions. Additionally, the human sHsp HSPB8 was reported to cooperate with BAG-3 in site-specific aggregate deposition (104) and in combination with the findings from yeast, *B. subtilis* or *C. elegans*, it appears that selective protein aggregation is conserved. In the case of Hsp42 dependent aggregate formation, it was shown that aggregate formation is not synonymous with failure of proteostasis (204). Research also demonstrated that the aggregation of aberrant proteins can be cytoprotective (116) and that selective protein insolubility may indeed be a function of the PN, segregating proteotoxic species or preserving valuable proteins for resolubilization (118). This remains true for *C. elegans*, where protein-specific aggregation is a common process in aging (114). Here as well, selective formation of protein aggregates is required for viability under stress conditions, and sHsps, notably including HSP-17, are enriched in these aggregates (120). I surmise that HSP-17 could be a part of these cytoprotective aggregation processes by directing, timing and promoting the aggregation of specific substrates.

5.1.2. HSP-17 co-aggregates with substrates and affects aggregate processing

When small heat shock proteins bind unfolded protein substrates, they typically maintain them in a soluble or reversibly aggregated state without further processing. This provides a reservoir of salvageable proteins to be refolded by Hsp70 family members in conjunction with J-proteins, which is a conserved process from bacteria and yeast to mammals and plants (13,87-89). In monocellular organisms, co-aggregation of sHsps enhances the recovery of substrates by the Hsp70 or Hsp100 machinery (100), even when using heterologous sHsps (99), but substrates are not released from sHsps in the absence of additional chaperones (205,206). More recently, the Hsp70 and J-protein based disaggregation of aggregated proteins has been demonstrated for humans and *C. elegans* and likewise, co-aggregation of the heterologous yeast Hsp26 enhances recovery in these systems (24,25).

My experiments have shown that HSP-17 does partially co-aggregate with MDH while enhancing its aggregation, whereas HSP-17 alone does not seem to readily separate to the insoluble fraction *in vitro*. Furthermore, it was observed *in vivo* that the fraction of insoluble HSP-17 increases with age in *C. elegans* and that HSP-17-GFP localizes to cellular foci in aged nematodes. Yet, when HSP-17 co-aggregates with luciferase as a substrate, unlike with yeast Hsp26, subsequent recovery is not enhanced and instead, increasing concentrations of HSP-17 inhibited the recovery of luciferase. The concentration at which this occurs (> 1 µM HSP-17) is not stoichiometric to luciferase (15 nM) but to the chaperones used (HSP-1: 4 µM). Similar effects had been described for *E. coli*, where the sHsp IbpB is required for enhanced disaggregation, while IpbA alone inhibits it (111). In this case, the inhibition of recovery can be alleviated by a Hsp70 member leading to the hypothesis that recovery of such aggregates is controlled by the abundance of free Hsp70 (112). Comparable results are available for the yeast sequestrase Btn2, functionally related to Hsp42, which also enables localized aggregation of protein substrates. Subsequent recovery is enhanced, but only in the presence of J-protein Sis1 (113). In the human system, BAG-3 was shown to integrate the activity of sHsps with the Hsp70-machinery to achieve improved protein refolding (103). In this light it is possible that HSP-17 co-aggregation creates aggregates that can be recovered in presence of either an excess of Hsp70 members or possibly a co-chaperone such as a J-protein or a BAG-protein. The aggregation of proteins and subsequent recovery are beneficial to stress survival and aging (119,120) and therefore, controlling aggregation and disaggregation of proteins could confer selective advantages. Small heat shock proteins like HSP-17 would play a role in these processes keeping protein aggregates inert during unfavorable conditions, reducing the folding burden on the chaperone machinery and allow for recovery once chaperone capacity is available.

Conversely, maintaining the solubility of protein substrates may not be a physiologically beneficial outcome in all cases. The co-incubation of human HSPB5 with $A\beta_{1-40}$ *in vitro* is sufficient to prevent the formation of amyloid-fibrils. Yet, this can increase proteotoxicity in subsequent cell culture assays, indicating that the chaperoned, non-fibrillar Aβ species are more deleterious (207). On the other hand, mouse HSPB1 induces the assembly of smaller Aβ oligomers into larger assemblies, reducing cytotoxicity (124). The trend of insoluble amyloids being less deleterious

has been shown for polyQ peptides as well, as cell survival was demonstrated to be dependent on inclusion body formation in a HttEx1Q_{47}-GFP model (122) and involvement of chaperones in this inclusion body formation has been confirmed more recently (208). I could demonstrate that HSP-17 not only colocalizes with heterologously expressed polyQ fibrils *in vivo* and *in vitro*, but also that the formation of Q_{44}-YFP foci in the *C. elegans* intestine correlates with overexpression or depletion of HSP-17. HSP-17 might thus belong to a branch of the PN that protects cells by segregating proteotoxic species without maintaining solubility.

5.1.3. HSP-17 is relevant for viability and KIN-19 is its substrate *in vivo*

Small heat shock proteins are ubiquitous parts of the PN and often upregulated upon heat stress (163), although organisms maintain stress-inducible and constitutive sHsps in parallel. For example, yeast Hsp26 is heat induced and heat activated (209), whereas yeast Hsp42 is constitutively expressed and active under non heat stress conditions (210), but still relevant for survival under heat stress (110). In *C. elegans*, the sHsps HSP-25 or HSP-43 are constitutively expressed in body wall muscle, cell junctions or the reproductive system (165), while others like SEC-1 / SIP-1 are developmentally regulated and localized to eggs and the uterus (211). The ubiquitous HSP-16.2 is notably induced by and protective during heat stress (203) and has also been shown to be induced by proteotoxic stress following heterologous Aβ overexpression, being protective under this condition (161).

Here, I have demonstrated that *C. elegans* HSP-17 is constitutively expressed and most present in the alimentary system (consisting of the pharynx, the intestine and the anus) as well as the excretory canal cell, a localization it only shares with the HSP-16 members (under stressed conditions). Like Hsp42**,** the constitutive HSP-17 was shown to be protective under thermal stress and previous studies indicated that HSP-17 can additionally be upregulated by heat stress (176). The prominent localization of HSP-17 to the excretory canal cell, implied in osmoregulation (177), aligns with my observation that HSP-17 is protective under osmotic stress. It is interesting that one of the few other known molecular aggregases**,** *B. subtilis* YocM**,** is also protective under osmotic stress (109). Osmotic stress affects protein homeostasis in the intestine and can induce the aggregation of Q_{44}-YFP (179), which I also showed to be modulated by HSP-17. The localization of HSP-17 to the

alimentary system, and particularly around the intestinal endotube, also supports my finding that HSP-17 is relevant during biotic stress and previous reports that HSP-17 is induced by heavy metal stress (176). I found that HSP-17 is relevant for fecundity and the development of offspring, although unlike SIP-1 (82), HSP-17 does not interact with VIT-2. Nonetheless, it is possibly involved in the transport of nutrients to eggs, which depends on vitellogenins synthesized in the intestine (181). In combination, the localization of HSP-17 to the intestine, membranes, and the involvement of HSP-17 in reproduction and various stress conditions indicate a role in maintaining intestinal homeostasis with an impact on fecundity. HSP-17 was relevant for lifespan *in vivo* and combined with my *in vitro* findings, these data point to HSP-17 being a part of the PN that constitutively performs a non-canonical chaperone activity in the cytosol of the alimentary system and the excretory tract.

Finally, I could show HSP-17 to colocalize with KIN-19, a casein kinase homolog, *in vivo*. KIN-19 was previously reported to be a protein with high propensity to become insoluble in age (114). Additionally, HSP-17 overexpression lead to an increase in KIN-19 foci in the pharynx, indicating that KIN-19 is a physiological substrate of molecular aggregase activity. I have shown for HSP-17 to not colocalize with PAB-1 or nuclei, matching the reported aggregation pattern of KIN-19 (114,180). Observations that KIN-19 overexpression leads to defect in *C. elegans* larval development are supported by findings that KIN-19 is involved in the formation of the embryo (212), the regulation of cell division during development (213) and cell fate determination (214). In this context, comparison to the mycobacterial sHsp HspX is interesting. HspX was shown to enhance the aggregation of select substrates and promote their polar localization, and was labeled a “pro-aggregase” and “polar sortase” (107). By analogy, the link between HSP-17, KIN-19, cell division and development may be based on protein aggregate formation and sorting in conjunction with cell division events.

Intriguingly, concurrent overexpression of HSP-17 exacerbated this effect, whereas depletion of HSP-17 slightly ameliorated the developmental defects. In studies analyzing the effect of osmotic stress on protein aggregation in *C. elegans*, KIN-19 was also reported to be aggregation-prone under this stress condition alongside polyQ peptides (8). This provides another link to the involvement of HSP-17 with osmotic stress and the excretory canal cell. Taken together, these findings indicate

that deleterious KIN-19 dysregulation is moderated by HSP-17, possibly by affecting its aggregation during development, stress and aging. By this mechanism, HSP-17 might pose an example of physiologically controlled, specific protein aggregation.

5.2. A new model of Aβ pathology in *C. elegans*

In neurodegenerative diseases such as Alzheimer's disease, a pivotal factor is the aggregation of the APP cleavage product amyloid-β_{1-42} and subsequent – hypothetical – prion-like spreading of its aggregates within the organism (36). However, clinical attempts targeting this peptide have remained fruitless and the exact involvement of amyloids like Aβ or MAPT is subject to discussion (51). Therefore, models are still needed to explore the basis of Aβ aggregation and the trajectory it has within living organisms. Previous endeavors created muscular (151) or neuronal (155) models of Aβ toxicity in *C. elegans*, but forwent labeling. Furthermore, Aβ proteotoxicity was also analyzed in the context of select neurons: glutamatergic neurons (159), ASE neurons (157) or BAG neurons (158). In all of these studies, unlabeled Aβ was used. Attempts at generating a model of GFP-labeled Aβ expression in *C. elegans* neurons revealed that consistent labeling of Aβ lead to formation of Aβ oligomers, but not amyloid fibrils (156).

Here, in a project carried out together with Christian Gallrein, a new model of Aβ proteotoxicity in *C. elegans* was generated, which expressed unlabeled Aβ alongside a smaller moiety of labeled Aβ. Following successful generation of transgenic strains expressing Aβ in neurons or body wall muscle of *C. elegans*, I could demonstrate that both labeled and unlabeled peptide are present in the transgenic model and that both moieties of Aβ interact. Proteomic and biochemical analysis revealed that the newly generated models were under proteotoxic stress and exhibited dysfunctions in the endo-membrane system, autophagy and protein sorting, mirroring previous observations on *C. elegans* models of Aβ toxicity. Notably, the IL2 neurons of *C. elegans* specifically proved more vulnerable to Aβ proteotoxicity than other neurons and mark the beginning of systemic Aβ pathology. Targeted depletion of Aβ in these neurons provided systemic amelioration of Aβ proteotoxicity, providing an important perspective on the amyloid-cascade hypothesis and possible treatments.

This type of model might then serve as a bridge for PN activity and aid in transferring findings for *C. elegans* chaperones, including sHsps, to the human system.

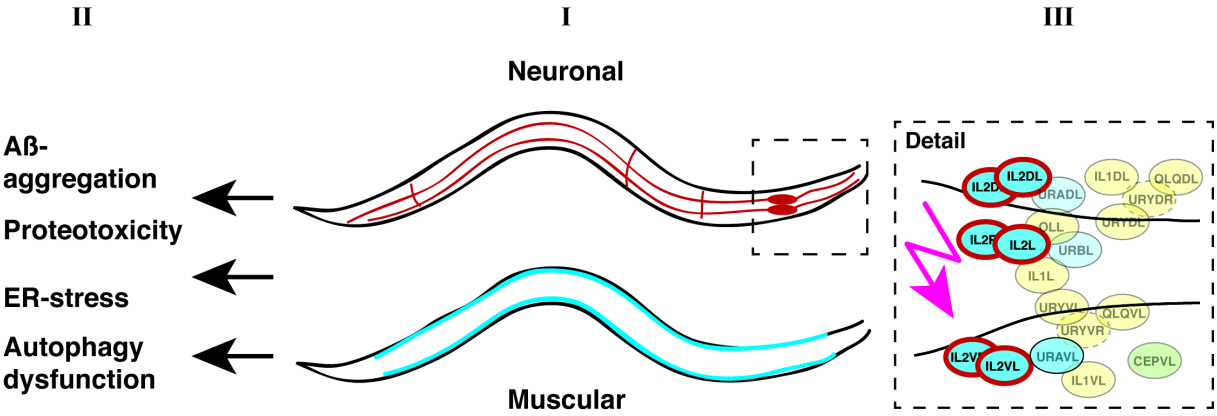

Figure 54: A new model of Aβ pathology in *C. elegans*

Overview of crucial observations in the generated model (sketch). A model of Aβ pathology with sub-stoichiometric labeling was generated for neurons (red) and body wall muscle (blue). The fluorophore used is wrmScarlet in both cases (I). The models reprised hallmark features of Aβ proteotoxicity (II). *In vivo* microscopy revealed that a subset of head neurons was more vulnerable to Aβ aggregation than other neurons. The eutelic nature of *C. elegans* allowed to identify these as the IL2 neurons and they appear to be pivotal in systemic Aβ pathology. Nematode anatomy was adapted from *WormAtlas* (215). Head neuron organization was adapted from published literature (195,196).

5.2.1. Sub-stoichiometric labeling enables a new model of Aβ pathology

A fluorophore-labeled model of Aβ pathology in *C. elegans* was created that allowed for concurrent unhindered aggregation and fibril formation by an unlabeled moiety of Aβ (216,217) and the intended pathology was confirmed for neuronal and body wall muscle expression. In the new model, the Aβ peptide is targeted to the ER and returned to the cytosol after cleavage due to the used signal peptide (152,154), although it is understood that a large portion of Aβ pathology takes place in the extracellular space (218). Nonetheless, intracellular Aβ was demonstrated to play a role in pathology as well (219-221), which allowed me to investigate the impact of Aβ in the cell.

Among the chaperones interacting with mAβ *in vivo* were J-proteins, including the stress inducible members DNJ-13 & DNJ-19, which are expressed in muscular tissue (19) and the calnexin homolog CNX-1, pointing to the involvement of ER-stress in the model. The identified Hsp90 member DAF-21 is also relevant to muscle homeostasis

(222). These chaperones had not been identified as Aβ interactors so far, but confirm proteotoxicity in the muscles and the ER. The HSP-16 family is a group of heat-inducible sHsps (223) which were identified in previous analyses of *C. elegans* mAβ models (160) and reported to be upregulated and cytoprotective in response to Aβ proteotoxicity (161). Together with the constitutive Hsc70 member HSP-1 (224) identified in mAβ, IP-MS/MS from the neuronal model revealed interaction with the Hsc70 member F44E5.4. Interaction with Aβ peptide of these Hsc70 members and HSP-16 members previously identified (160,187) demonstrate reproducibility in *C. elegans* models of Aβ pathology. Furthermore, the identification of a number of PN members points to a general proteotoxic effect of Aβ in the newly generated model and gene ontology analysis by the *DAVID* functional annotation tool corroborated these data.

In particular, the GO term locomotion has been identified and indeed, in muscular Aβ models of *C. elegans*, progressive paralysis has been reported as a symptom (188,189). Likewise, the involvement of redox processes in the new Aβ model supports the understanding that oxidative stress plays a role in Aβ pathology (225) and that redox homeostasis is linked to protein homeostasis (191). Notably, the terms RME and cullin-deneddylation imply an involvement of endocytosis, UPR^{ER} points to ER-stress and the terms secretion by cell and protein transport further corroborate this, hinting at issues in protein trafficking. These findings were confirmed by TEM and *in vivo* analysis. My observations may stem in part from targeting the Aβ peptide to the ER, although it does not remain there. Nonetheless, these data show that Aβ can perturb membrane transport and ER function and, taken together, reinforce the idea of dysfunctional protein sorting and membrane damage as a mechanism in Aβ pathology (56).

For the muscular model mAβ, structures were prominently observed which could be endosomes, exosomes, lysosomes or autophagosomes that failed to form and were labeled as “amphisomes”. This could tie in to findings that Aβ accumulates in multivesicular bodies (in neurons), which provide a site for fibril formation and potential export of Aβ from the cell (193). A connection between the observed amphisomes and the described multivesicular bodies matches my observations in the ER and the endomembrane system and through export of aggregated Aβ, points

to a pathway of Aβ spreading (58). Conversely, defects in autophagy leading to the induction of incomplete autophagosomes have been described in combination with Aβ (192). Autophagic flux is reported to be faulty in Aβ pathology (226) and I have quantified the levels of the p62 homolog SQST-1 and the LC3 homolog LGG-1 to assess this effect, ultimately concluding that cells fail at initiating autophagy and it does not proceed (175). In short, by proteomics and biochemical analysis, I could demonstrate that protein trafficking, the endomembrane system and autophagy are disturbed in the newly generated models, positioning them as a platform to assay known and hypothetical defects in Aβ pathology.

5.2.2. IL2 neurons mark the onset of organismal Aβ aggregation and pathology

In FLIM experiments carried out by Christian Gallrein on the neuronal model nAβ, it became evident that the onset of Aβ aggregation takes place in a specific subset of head neurons. These neurons were then identified as the IL2 neurons. RNAi-mediated knockdown of Aβ exclusively in the IL2 neurons, but not in the adjacent URY neurons, ameliorated the relative amount of aggregates and lead to an increase in fluorescence lifetime and thus reduced aggregation of Aβ in head neurons *overall*. The depletion of Aβ specifically in IL2 neurons also improved paralysis symptoms, compared to the nAβ control and caused a slight, yet significant, improvement in the median lifespan. These data imply that on one hand, there is a mechanism that renders IL2 neurons more susceptible to Aβ proteotoxicity and on the other, that failure of proteostasis in these neurons allows for systemic pathology – or treatment.
IL2 neurons were demonstrated to be necessary in dauer larvae of *C. elegans* to induce nictation behavior, a dispersal strategy with putative benefits under stressed conditions (227). In adult, non-dauer nematodes, no specific function was reported for IL2 neurons (200), however they were identified as part of the neurons expressing the neuropeptide Y-receptor like NPR-1 (228). IL2 neurons are cholinergic, motor neuron-like, activated by acetylcholine (229) and belong to the neurons specifically expressing the nicotinic acetylcholine receptor subunits DEG-3 and DES-2, which have been associated with vulnerability to neurodegeneration (230). The data available makes it difficult to link the vulnerability of IL2 neurons to a specific function

or position within the *C. elegans* organism, but based on the described properties I speculate that specific receptors may play a role.

Crucially, in the human system a vulnerability of cholinergic neurons to Aβ pathology was also reported (198,199), specifically in the nucleus basalis (231), which has opened up possibilities of pharmaceutical palliative treatment in AD (232). There is evidence that this cell-type specific vulnerability is a common feature of amyloidosis – α-synuclein, a pivotal amyloid in PD, was shown in *C. elegans* to have more severe effects on dopaminergic neurons (149) and proteotoxic polyQ-peptides were shown to most severely affect motor neurons (150). I thereby conclude that the cholinergic IL2 neurons are specifically affected by Aβ due to their characteristic configuration and this mirrors the vulnerability of other neuron types to the respective amyloids. Importantly, modelling this effect in *C. elegans* allowed for the first time to pinpoint this to a specific type of neurons rather than a general group of neurons or a brain region, due to the compact and eutelic nature of *C. elegans*. *In vivo* labeling and monitoring of this process provided an age-resolved dataset of this crucial vulnerability that cannot be achieved in cell culture or *post mortem* brain biopsies.

5.3. Outlook

5.3.1. HSP-17 and facilitated aggregation

In this work I have presented *C. elegans* HSP-17 as the first metazoan sHsp to promote substrate aggregation *in vitro* and *in vivo*, a mechanism distinct from the well described activity of sHsps to prevent aggregation of substrates. This effect was physiologically relevant and targeted to select substrates, native and non-native. Following this line, it will be interesting to identify additional sHsps exhibiting molecular aggregase activity, particularly in the human system. Previous research strongly focused on chaperones inhibiting or reverting substrate aggregation and research on chaperones facilitating and directing aggregation will provide new perspectives on the PN and neurodegenerative disease. For HSP-17, it will be helpful to elucidate what identifies substrates for molecular aggregase activity, in what manner HSP-17 confers insolubility to them and how the resulting protein aggregates are changed. These findings could shed new light on general mechanisms to identify aggregase substrates, understand the properties of protein

aggregates and their management in relation to organismal health. In the context of *C. elegans* physiology, HSP-17 seems to be the first sHsp predominantly active in the intestine and its involvement in membrane transport or the generation of offspring remains to be elucidated.

5.3.2. A new model to visualize the progression of Aβ pathology

The data I present cover a new model of Aβ in *C. elegans* which combines the benefits of fluorescent labeling and native-like expression. The utility of the model could be confirmed as it fulfills the expected constitution and reiterates established and putative hallmarks of Aβ pathology. The differentiated nature of *C. elegans* allowed for the precise identification of IL2 neurons as hotspots of proteotoxicity. Thus, the new model could be beneficial for the identification of such cell-type specific vulnerabilities in mice or humans to facilitate the development of therapy. Importantly, the mechanisms by which IL2 neurons are vulnerable to amyloid pathology need to be elucidated, followed by transferring these findings to higher eukaryotes. In parallel, it will be interesting to assay the modulation of Aβ proteotoxicity in *C. elegans* in a cell-specific manner, including by small molecules or the activity of molecular chaperones such as the sHsps. Thus, the model presented here could serve as an initial platform for precise analysis and amelioration of Aβ aggregation in neurons.

6. Material and methods

6.1. Chemicals & solutions

Standard chemicals for laboratory use were obtained from Sigma Aldrich (St. Louis, USA), Carl Roth (Karlsruhe, Germany) and Merck (Darmstadt, Germany). Chemicals used in particular were:

Table 5: List of chemicals and solutions used in this work

Product	Company
Acetone	Sigma Aldrich
Acetonitrile	Carl Roth
Acetic acid	VWR, Radnor, USA
Agar-Agar Kobe 1	Carl Roth
Agarose	Bio+Sell, Nürnberg, Germany
Ambion™ TRIzol™ reagent	Thermo Fisher Scientific, Waltham, USA
Ampicillin	Carl Roth
Ammonium persulfate	Carl Roth
L-Arginine	Carl Roth
Adenosine triphosphate	Carl Roth
β-mercaptoethanol	Carl Roth
Bacto™ Peptone	BD Biosciences, New Jersey, USA
Bromophenol blue	Carl Roth
Bovine serum albumin	Carl Roth
Calcium chloride	Carl Roth
Chloramphenicol	Carl Roth
2-Chloroacetamide	Sigma Aldrich
Chloroform	Fisher Scientific, Schwerte, Germany
Cholesterol	Sigma Aldrich
cOmplete™ protease inhibitor cocktail	Roche Diagnostics, Mannheim, Germany
Coomassie Brilliant Blue R-250	Carl Roth
L-Cysteine	Carl Roth
Cy5-*N*-Hydroxysuccinimide	GE Healthcare, Buckinghamshire, UK
4´,6-diamidino-2-phenylindole	Carl Roth
Dimethyl sulfoxide	Carl Roth
Deoxynucleotidetriphosphates	Thermo Fisher Scientific, Waltham, USA
Dithiothreitol	Carl Roth
Ethylenediaminetetraacetic acid	Carl Roth
Ethanol	VWR, Radnor, USA
Epoxy	Sigma Aldrich

Formaldehyde (37 %)	Carl Roth
L-Glutamic acid	Sigma Aldrich
L-Glutathione, reduced	AppliChem GmbH, Darmstadt, Germany
D-Luciferin	Sigma Aldrich
Glycerol	Carl Roth
Glycin	Carl Roth
Glycylglycine	AppliChem GmbH, Darmstadt, Germany
Gold powder, 0,33 micron / 99,9 %	Chempur, Karlsruhe, Germany
Halocarbon Oil 700	Sigma Aldrich
HEPES (4-(2-hydroxyethyl)-1-piperazineethanesulfonic acid)	Carl Roth
HM20 resin	Polysciences, Eppelheim, Germany
Hydrochloric acid (32 %)	Carl Roth
Imidazole	Carl Roth
Isopropyl-β-D-1-thiogalactopyranosid	Thermo Fisher Scientific, Waltham, USA
Isopropyl alcohol	VWR, Radnor, USA
LB agar	Serva, Heidelberg, Germany
LB media	Carl Roth
Levamisole	AppliChem GmbH, Darmstadt, Germany
Magnesium acetate	Carl Roth
Magnesium chloride	Carl Roth
Magnesium Sulfate	Carl Roth
Manganese(II) chloride	AppliChem GmbH, Darmstadt, Germany
Methanol	Carl Roth
Milk powder	Carl Roth
Mono- & dipotassium phosphate	Carl Roth
Monosodium citrate	Carl Roth
Mono- & disodium phosphate	Carl Roth
MOPS (3-(*N*-morpholino)propanesulfonic acid)	AppliChem GmbH, Darmstadt, Germany
NP-40 Surfactant Amps®	Thermo Fisher Scientific, Waltham, USA
Nuclease free water	Carl Roth
Phosphoenolpyruvic acid	AppliChem GmbH, Darmstadt, Germany

Pierce® BCA Reagents A & B	Thermo Fisher Scientific, Waltham, USA
Phenylmethylsulfonyl fluoride	Sigma Aldrich
Polyvinylpyrrolidone	Sigma Aldrich
RedSafe™ Nucleic acid staining solution	Fisher Scientific, Schwerte, Germany
RIPA lysis buffer, 10x	Merck Millipore, Burlington, USA
Rotiphorese® Gel 30 (37.5:1) Acrylamide : Bisacrylamide solution	Carl Roth
Roti®-Quant (for Bradford assay)	Carl Roth
Roti®-Block, 10x	Carl Roth
Rubidium chloride	AppliChem GmbH, Darmstadt, Germany
Sodium dodecyl sulfate	Carl Roth
SOC-media	New England Biolabs, Ipswich, USA
Sodium azide	Carl Roth
Sodium chloride	Carl Roth
Sodium hydroxide	Carl Roth
Spermidine	Sigma Aldrich
Potassium acetate	Carl Roth
Potassium chloride	Carl Roth
Potassium hydroxide	Carl Roth
Sodium hypochlorite solution	Fisher Scientific, Schwerte, Germany
Streptomycin (Gibco)	Thermo Fisher Scientific, Waltham, USA
Tannic acid	Sigma Aldrich
Tris(2-carboxyethyl)phosphine	Sigma Aldrich
Tetramethylethylenediamine	Carl Roth
Tetracycline	Carl Roth
Tricin	AppliChem GmbH, Darmstadt, Germany
Tris(hydroxymethyl)aminomethane	Carl Roth
Triton X-100	Carl Roth
Tween 20	Carl Roth
Uranyl acetate	Sigma Aldrich

6.2. Gel markers and loading dyes

Table 6: List of gel markers and loading dyes used in this work

Product	Company
DNA loading dye (6x)	Thermo Fisher Scientific, Waltham, USA
GeneRuler™ (1kb & 50 bp)	Thermo Fisher Scientific, Waltham, USA
PageRuler™ Prestained Protein Ladder	Thermo Fisher Scientific, Waltham, USA

6.3. Enzymes

6.3.1. Enzymes (general)

Table 7: List of restriction enzymes used in this work

Product	Company
Citrate synthase	Sigma Aldrich
DNAse I	AppliChem GmbH, Darmstadt, Germany
FastAP Alkaline Phosphatase (1U / µl)	Thermo Fisher Scientific, Waltham, USA
Glyceraldehyde 3-phosphate dehydrogenase	Sigma Aldrich
Herculase II Fusion DNA Polymerase	Agilent, Santa Clara, USA
Luciferase	Sigma Aldrich
Lysozyme	Carl Roth
Malate dehydrogenase	Sigma Aldrich
Phusion® High-Fidelity DNA Polymerase	Kirstein Lab
PreScission™ Protease	GE Healthcare, Buckinghamshire, UK
Proteinase K	Thermo Fisher Scientific, Waltham, USA
Pyruvate kinase	Sigma Aldrich
SUMO protease (Ulp1 fragment)	Kirstein Lab
T4 DNA Ligase (1U / µl) incl. buffer	Thermo Fisher Scientific, Waltham, USA
Trypsin	Carl Roth

6.3.2. Restriction Enzymes

All restriction enzymes used and CutSmart® Buffer have been bought from New England Biolabs, Ipswich, USA.

6.4. Antibodies

Table 8: List of antibodies used in this work

Antibody	Dilution used in Western blot	Company
Anti-amyloid-β-peptide, mouse (4G8 & 6E10)	1 : 1000	BioLegend, San Diego, USA
Anti-GFP, rabbit	-	Enzo Life Sciences, Farmingdale, USA
Anti-HSP-17, rabbit	1 : 2500 / 1 : 4000	Kirstein lab / Pineda Antikörper Service, Berlin, Germany
Anti-LGG-1, rabbit	1 : 1000	Kirstein lab / Pineda Antikörper Service, Berlin, Germany
Anti-SQST-1/p62, rabbit	1 : 1000	Kirstein lab / Pineda Antikörper Service, Berlin, Germany
Anti-α-tubulin, mouse	1 : 2500	Sigma Aldrich
Cy3-anti-rabbit, goat	1 : 10000	Thermo Fisher Scientific, Waltham, USA
Anti-mouse IR 800, goat	1 : 10000	LI-COR, Lincoln, USA
Goat-anti-rabbit IgG (H+L) ML, conjugated with 12 nm colloidal gold	-	Jackson Laboratories, Bar Harbor, USA
Pierce® goat-anti-mouse IgG + IgM (H+L), peroxidase conjugated	1 : 10000 / 1 : 15000	Thermo Fisher Scientific, Waltham, USA
Pierce® goat-anti-rabbit IgG (H+L), peroxidase conjugated	1 : 10000 / 1 : 15000	Thermo Fisher Scientific, Waltham, USA

6.5. Buffers and media

All buffers and media used, excluding buffers provided by commercial sources (i. e. buffers for commercial enzymes).

6.5.1. General use

Table 9: List of buffers used in this work

Solution	Preparation
Antibody buffer A (AbA)	1x PBS; 1% BSA; 0,5% Triton-X-100
Assay buffer (luciferase assay)	25 mM Glycylglycin; 100 mM KCl; 15 mM $MgCl_2$; 5 mM ATP
C. elegans lysis buffer	20 mM HEPES-KOH; 110 mM KAc; 2 mM $MgAc_2$; pH 7,4
Coomassie staining solution	40% Methanol (v/v); 10% Acetic acid (v/v); 50% H_2O (v/v); 0,5% Coomassie brilliant blue (w/v)
Coomassie destaining / fixing solution	40% Methanol (v/v); 10% Acetic acid (v/v); 50% H_2O (v/v)
Formaldehyde solution	4% Formaldehyde in 100 mM K_2HPO_4; pH 7,2
HMK (luciferase assay)	50 mM HEPES-KOH; 100 mM KCl; 5 mM $MgCl_2$; 1 mM DTT; 10 µM BSA; pH 7,4
HMK (general use)	30 mM HEPES-KOH; 140 mM KCl; 5 mM $MgCl_2$; pH 7,4
Light scattering buffer (CS)	40 mM HEPES-KOH; pH 7,4 Buffer is filtered and degassed.
Light scattering buffer (GAPDH)	1x PBS; pH 7,4 Buffer is filtered and degassed. For dialysis and storage of aliquots, 1 mM DTT and 5% (v/v) glycerol are added.
Light scattering buffer (MDH)	30 mM HEPES-KOH; 5 mM $MgCl_2$; 50 mM KCl; pH 7,4

	Buffer is filtered and degassed.
M9	58 g Na_2HPO_4; 30 g KH_2PO_4; 5 g NaCl; 10 g NH_4Cl_2 in one liter of H_2O. Solution is sterilized by autoclaving.
NGM agar	3 g NaCl; 2,5 g Bacto Peptone; 17 g Agar Agar Kobe 1; 5 mg cholesterol; 1 mM $CaCl_2$; 1 mM $MgSO_4$; 25 mM KH_2PO_4; pH 6 in one liter of H_2O.
NGM agar, RNAi	As NGM agar, supplemented with 1 mM Ampicillin and 1 mM IPTG.
PBS (10x)	1,37 M NaCl; 27 mM KCl; 100 mM Na_2HPO_4; 18 mM KH_2PO_4 Sterilized by autoclaving.
PBST (1x)	1x PBS supplemented with 0,05% (v/v) Tween 20.
PCR buffer 0 (10x)	100 mM Tris; 500 mM KCl; 1% Triton X-100 (v/v); pH 8,8
PCR buffer I (10x)	100 mM Tris; 500 mM KCl; 20 mM $MgCl_2$; 1% Triton X-100 (v/v); pH 8,8
PCR buffer II (10x)	100 mM Tris; 500 mM KCl; 20 mM $MgSO_4$; 1% Triton X-100 (v/v); pH 8,8
PVP solution	10 mg PVP in 500 µl H_2O; 99,5 ml Ethanol.
Pyruvate kinase solution (luciferase assay)	20 µl of pyruvate kinase stock in 75 µl of HMK (for luciferase assay, approximately 20 u of Pyruvate kinase). 5 µl of 200 mM ATP are added directly before used.
Sample loading buffer (SDS-PAGE, 2x)	50% (v/v) 4x sample loading buffer; 50% H_2O; 100 mM DTT
Sample loading buffer (SDS-PAGE, 4x)	100 mM Tris-HCl; 4%SDS (w/v); 30% glycerol (v/v); 0,02% (w/v) bromophenol-blue
SEC running buffer	30 mM HEPES-KOH; 140 mM KCl; 5 mM

	$MgCl_2$; pH 7,4 Buffer is filtered and degassed.
SDS-PAGE running buffer (10x)	250 mM Tris; 1,92 M Glycin; 1% (w/v) SDS
Separating gel buffer (SDS-PAGE)	1,5 M Tris-HCl; 0,4% SDS (w/v); pH 8,8
Stacking gel buffer (SDS-PAGE)	0,5 M Tris-HCl; 0,4% SDS (w/v); pH 6,8
TAE (50x)	242 g Tris; 5,71% acetic acid; 50 mM EDTA (pH 8) in one liter of H_2O.
TBS (10x)	200 mM Tris; 1,5 M NaCl Solution is filtered by autoclaving.
TBST (10x)	200 mM Tris; 1,5 M NaCl; 1% Tween 20 (v/v) Solution is filtered by autoclaving.
TFB1	100 mM RbCl; 80 mM MnCl; 10 mM $CaCl_2$; 30 mM KAc; 15% glycerol (v/v) Adjusted to pH 5,3 with acetic acid; sterilized by filtration
TFB2	67 mM RbCl; 75 mM $CaCl_2$; 10 mM MOPS; 15% glycerol (v/v); pH 7,5 Sterilized by filtration
Transfer buffer (Western blot)	192 mM glycine; 25 mM Tris; 20% methanol
Tricine SDS-PAGE anode buffer	2 M Tris-HCl; pH 8,9
Tricine SDS-PAGE cathode buffer	100 mM Tris-HCl, 100 mM Tricine; 0,5% SDS (w/v)
Tricine SDS-PAGE gel buffer	5 M Tris-HCl; 0,5% SDS (w/v); pH 8,45

6.5.2. Recombinant protein purification

Solution	**Preparation**
Lysis / Wash buffer (HttEx1 constructs) **LWB**	50 mM NaH_2PO_4; 5 mM Tris; 150 mM NaCl; 5 mM $MgCl_2$; pH 8 A pinch of DNAseI is added shortly before use for lysis. 0,1% (v/v) Trition X-100 is added shortly before use for washing.
Dialysis buffer (HttEx1 constructs) **DB**	50 mM Tris; 150 mM NaCl; 1 mM EDTA; 5% (v/v) glycerol; pH 7,4
Elution buffer **EB**	30 mM HEPES-KOH; 50 mM KCl; 5 mM $MgCl_2$; 10% glycerol (v/v); pH 7,4
Elution buffer **EB2** (HttEx1 constructs)	50 mM NaH_2PO_4; 5 mM Tris; 150 mM NaCl; 5 mM $MgCl_2$; pH 8 20 mM reduced glutathione are added shortly before use and the pH is adjusted to 8,6.
High salt buffer **HSB**	30 mM HEPES-KOH; 1M KCl; 0,05% Tween 20; pH 7,4 20 mM imidazole and 1 mM TCEP are added shortly before use.
High salt buffer 2 **HSB2**	30 mM HEPES-KOH; 1M KCl; 5 mM $MgCl_2$; pH 7,4 Buffer is filtered and degassed.
Low salt buffer **LSB**	30 mM HEPES-KOH; 50 mM KCl; pH 7,4 20 mM imidazole and 1 mM TCEP are added shortly before use. For dialysis, no imidazole is added and 1 mM TCEP is replaced by 1 mM β-Mercaptoethanol.
Low salt buffer 2 **LSB2**	30 mM HEPES-KOH; 25 mM KCl; 5 mM $MgCl_2$; pH 7,4 Buffer is filtered and degassed.
Lysis buffer **LB**	30 mM HEPES-KOH; 500 mM KCl; 5 mM $MgCl_2$; 10% glycerol (v/v); pH 7,4

20 mM imidazole; 1 mM PMSF; a pinch of DNAseI and cOmplete protease inhibitor are added shortly before use.

6.6. Kits

Table 10: List of laboratory kits used in this work

Product	Company
Maxima First Strand cDNA Synthesis Kit	Thermo Fisher Scientific, Waltham, USA
Pierce® ECL Western Blot Substrate	Thermo Fisher Scientific, Waltham, USA
QIAquick gel extraction kit	Qiagen, Hilden, Germany
NucleoSpin® Plasmid Isolation Kit	Macherey-Nagel, Düren, Germany
NucleoSpin® RNA Isolation Kit	Macherey-Nagel, Düren, Germany
ZR Plasmid Miniprep Classic	Zymo Research, Irvine, USA
Gel filtration high molecular weight calibration kit	GE Healthcare, Chalfont St. Giles, UK

6.7. Primers

Primers were purchased from BioTeZ, Berlin, Germany.

Table 11: List of primers used in this work

Primer	Sequence
hsp-17f	ccagtgggtctcaggtggtATGGATCGTCGTTTTCCACC
hsp-17r	ataagaatgcggccgcTCAGTTTCTCTTTGGCACAATTGTG
hsp-20Af	ccagtgggtctcaggtggtATGTCTTCTCTCTGCCCATACACTGG
hsp-20Ar	ataagaatgcggccgcTTAGTGCTTTCCGGTGGTGGTGG
hsp-20Bf	ccagtgcgtctcaggtggtATGCATCATGTTGATTTTGATGATG
hsp-20Br	ataagaatgcggccgcTTAAACAATTGATGTCACACTTC
hsp-21f	ccagtgggtctcaggtggtATGGCTACGTTCAACACTACAAGC
hsp-21r	ataagaatgcggccgcTTATTGCTTCTGTTGCTCGG
hsp-25af	ccagtgggtctcaggtggtATGCCCACGTACACTCGAAC

hsp-25bf	ccagtgggtctcaggtggtATGCCCACGTACACTCGAAC
hsp-25r	ataagaatgcggccgcTCATTGCTGGATTGCCAATTG
hsp-43f	ccagtgggtctcaggtggtATGACTCTTGCAACCCGTCATGC
hsp-43r	ataagaatgcggccgcTTAATATGTCTTGCGGAGAATTTG
phsp-12.6f	cagtcagcatgcCATGTCACAATGTTGTTTCC
phsp-12.6r	cagtcagtcgacCTTGGCAAAAGTTTTTGG
phsp-17f	cagtcagcatgcAACTGGTTTTTAAAGATTGG
phsp-17r	ataagaatgtcgacTTTATAATAGTTTCTGAAAATC
p17+17f	cagtcacccgggATGGATCGTCGTTTTCCACC
p17+17r	ataagaataccggtatGTTTCTCTTTGGCACAATTGTG
p17+17+Scaf	ataagaataccggtGGTCAGCAAGGGAGAGGCAG
p17+17+Scar	gatcgcgatgcagcaccagttaaagtctaCTTGTAGAGCTCGTCCATTCC
rSeq	CCAGTGAAAAGTTCTTCTCC
Integration	GGAACCGCTTCCAACCGTGTGAGATGTCAACAATATGGAGGA TATGGAGC
hsp-17 RNAif	ataagaatggtaccatGGACACCGAGTAGGAGATGC
hsp-17 RNAir	cagtcaaagcttTCAGTCTTCTCGTTATGCTTTCC
Abetaf	ccagtgggtctcaggtggtGATGCAGAATTCCGACATGAC
Abetar	ataagaatgcggccgcTTACGCTATGACAACACCGC
AbetaBf	cagtcaaacggtcagtcagctagcGATGCAGAATTCCGACATGAC
AbetaBr	ataagaatctcgagctaCGCTATGACAACACCGCCCACC
wrmScaf	cagtcaaccggtcagtcatctagaATGGTCAGCAAGGGAGAGGC
wrmScar	ataagaatgctagcCTTGTAGAGCTCGTCCATTCC
rgeff	cagtcagcatgcCAAGACTAATTTTCGATTAACC
rgefr	ataagaatatcgatataagaataccggtCGTCGTCGTCGTCGATGCCGTC
AbetaSL2f	ataagaataccggtGATGCAGAATTCCGACATGAC
AbetaSL2r	ataagaatctcgagGATGCGTTGAAGCAGTTTCC
pklp-6f	cagtcagcatgcGTTGGAAAGTTTGGTAAGTTGC
pklp-6r	ataagaatggtaccatGGTATTCTGAAAAGTTCAAC
revSeqSL	TTAAACTTACTCCCATGACGC

6.8. Plasmids

Table 12: List of plasmids used in this work

Plasmid	Source
pPD95.77 (GFP) [1]	Kirstein Lab
(expression of transgenes in *C. elegans*; includes GFP)	
pSumo [1]	Kirstein Lab
(recombinant expression of His-SUMO tagged proteins in *E. coli*)	
pSumo + HSP-1	Kirstein Lab
pSumo + HSP-110	Kirstein Lab
pSumo + DNJ-12	Kirstein Lab
pSumo + DNJ-13	Kirstein Lab
pSumo + HSP-12.6	Kirstein Lab
pL4440 (RNAi-feeding vector for *C. elegans)* [1]	Kirstein Lab
pDONR221 + $A\beta_{1-42}$	Wanker Lab
pGEX-6P-1 + GST-HttEx1Q48	Wanker Lab
pGEX-6P-1 + GST-HttEx1Q48Stop1c	Kirstein Lab
pPD95.77 + [*prgef-1::GFP*]	Kirstein Lab
pEY54 + [*pklp-6::mNeptune2.5*]	Hobert Lab
pSEM87 + [*wrmScarlet-twk-18*]	Boulin Lab

6.9. Laboratory equipment and devices

Table 13: List of devices used in this work

Product	Company
Agarose gel electrophoresis systems	Carl Roth, Sigma Aldrich
Anion exchange chromatography column – Resource™ Q	GE Healthcare, Chalfont St. Giles, UK
Centrifuge – Heraeus Fresco 17	Thermo Fisher Scientific, Waltham, USA
Centrifuge – 3K12	SIGMA, Osterode am Harz, Germany
Centrifuge – Ministar	VWR, Radnor, USA

1 Vector maps are shown in supplementary materials 12-14.

Centrifuge – Sorvall LYNX 6000 incl. Rotor F9-6x1000 LEX	Thermo Fisher Scientific, Waltham, USA
Electron Microscope – Zeiss 900	Zeiss, Oberkochen, Germany
Laboratory scales 440-49N & PCB	Kern, Balingen, Germany
Centrifuge – 5417C incl. rotor F45-30-11	Eppendorf, Hamburg, Germany
Flaming/Brown micropipette puller – P97	Sutter Instrument, Novato, USA
Fluorescence microscope M165FC	Leica, Wetzlar, Germany
Fluorescence spectrometer Jasco FP8300	Jasco, Pfungstadt, Germany
Freezer KM-DU73Y1E	Panasonic, Kadoma, Japan
Freeze substitution processor - AFS	Leica, Wetzlar, Germany
FPLC system – ÄKTA Explorer	GE Healthcare, Chalfont St. Giles, UK
Heating block incubator – HLC	Ditabis, Pforzheim, Germany
High pressure freezer HPM100	Leica, Wetzlar, Germany
Homogenizer – Precellys® 24	Bertin Technologies, Montigny-le-Bretonneux, France
Ice maker – Scotsman AF80	Wolf Laboratories, York, UK
Imaging system – Lumi-Imager F1TM	Boehringer, Mannheim, Germany
Imaging system – Odyssey® Image System FC	LI-COR, Lincoln, USA
Incubator – Heraeus Kelvitron	Thermo Fisher Scientific, Waltham, USA
Incubator – HerA Therm	Thermo Fisher Scientific, Waltham, USA
Incubator – TC255	Lovibond, Amesbury, UK
Inverted phase contrast microscope – DMI 3000B	Leica, Wetzlar, Germany
Laser scanning microscopes LSM780 & LSM510	Zeiss, Oberkochen, Germany
Magnetic reaction vessel rack – MagRack™ 6	GE Healthcare, Chalfont St. Giles, UK
Microfluidizer – LM10	Microfluidics, Westwood, USA
Microinjection pump – FemtoJet®	Eppendorf, Hamburg, Germany
Microinjection needle holder –	Eppendorf, Hamburg, Germany

InjectMan® 4	
Microwave – HMT75M451	Robert Bosch GmbH, Stuttgart, Germany
Magnetic stirrer – RET basic	IKA, Staufen, Germany
Mass spectrometer – UltiMate 3000 RSLC nano LC system coupled to Orbitrap Elite	Thermo Fisher Scientific, Waltham, USA
“Nanodrop” Spectrophotometer – NanoVue Plus	GE Healthcare, Chalfont St. Giles, UK
Micropipettes	Brand, Wertheim, Germany
PCR cycler – Mastercycler Gradient	Eppendorf, Hamburg, Germany
pH meter	Mettler Toledo, Ohio, USA
Pipettor – Pipetboy	Integra Bioscience, Integra, Germany
Plate reader – F200 Pro	Tecan, Männedorf, Germany
Power supply – PowerPac HC / Basic	Bio-Rad, Hercules, USA
QTof-MS system	Waters Corporation, Milford, USA
Quartz glass cuvettes – QS; including Hellmanex™ III cleaning solution	Hellma Analytics, Müllheim, Germany
SDS-PAGE system – Mini PROTEAN cell chambers	Bio-Rad, Hercules, USA
“Semi dry” blotting system – Turbo™ Transfer System	Bio-Rad, Hercules, USA
Size exclusion chromatography column – HiLoad® Superdex 75 16/600	GE Healthcare, Chalfont St. Giles, UK
Spectrophotometer – V-1200	VWR, Radnor, USA
Size exclusion chromatography column – Superose® 6 10/300 GL	GE Healthcare, Chalfont St. Giles, UK
Shaking incubator – Innova 4230	New Brunswick Scientific, Edison, USA
Shaking incubator – Multitron Pro	Infors HT, Bottmingen, Switzerland
Shaking incubator – SM-30 control	Edmund Bühler GmbH, Hechingen, Germany
Stereomicroscope – SMZ 745	Nikon, Tokio, Japan
FPLC injection loop –	GE Healthcare, Chalfont St. Giles, UK

0,5 ml / 5 ml / 50 ml (*Superloop*)	
Microtome	Leica, Wetzlar, Germany
Ultracentrifuge – OPTIMA	Beckman Coulter, Brea, USA
UPLC system – Acquity H-Class Plus incl. XEVOG2-XS QTof analyzer	Waters Corporation, Milford, USA
UPLC protein BEH column - Acquity	Waters Corporation, Milford, USA
Rolling incubator – RS-TR-5	Phoenix Instruments, Garbsen, Germany
Vacuum pump	KNF Lab, New Jersey, USA
Vortex mixer – Vortex-Genie® 2	Scientific Industries, Bohemia, USA
“Wet” western blotting system – Mini Trans-Blot® Cell	Bio-Rad, Hercules, USA

6.10. Consumables

Table 14: List of consumables used in this work

Product	**Company**
Blotting paper sheets	Sartorius, Göttingen, Germany
Centrifugal filter units – Amicon, 10 kDa MWCO; 0,5 ml	Merck Millipore, Burlington, USA
Centrifugal filter units – Spin-X UF, 10 kDa MWCO; 5 ml	Corning Life Sciences, Corning, USA
Culture plates (single)	Sarstedt, Nümbrecht, Germany
Dialysis membrane – Spectra/Por® molecular membrane tubing (6-8 kDa)	Spectrum Chemical Manufacturing Corporation, New Brunswick, USA
EM Grids	Sigma Aldrich
Glass cover slips	Carl Roth
Glass slides	Carl Roth
Gloves, latex	neoLab, Heidelberg, Germany
Gloves, nitril – Kimtech Sterling®	Kimberly-Clark, Dallas, USA
Glutathione Sepharose 4B GST-tagged protein purification resin	GE Healthcare, Chalfont St. Giles, UK
Gravity flow columns	Bio-Rad, Hercules, USA

Kwik-Fil™ borosilicate glass capillaries 1B100F-4	World Precision Instruments, Sarasota, USA
Membrane filter (round), 0,2 µM cut-off – OE66	GE Healthcare, Chalfont St. Giles, UK
Membrane filter (syringe mounted), 0,2 µM cut-off - FiltroPur	Sarstedt, Nümbrecht, Germany
Microdialysis devices – Xpress Dialyzer	Scienova, Jena, Germany
Nickel NTA agarose resin	Abbott Laboratories, North Chicago, USA
Optical adhesive film for well-plates	Carl Roth
Parafilm	Bemis, Neenah, USA
Pasteur pipettes	Carl Roth
PCR tubes (single)	Sarstedt, Nümbrecht, Germany
PCR tubes (stripes)	Kisker Biotech, Steinfurt, Germany
Pierce™ Protein A/G magnetic beads	Thermo Fisher Scientific, Waltham, USA
Pipette tips	Sarstedt, Nümbrecht, Germany
Platinum wire	Carl Roth
Polystyrene cuvettes, disposable - Rotilabo®	Carl Roth
Precellys® lysing kits (0,5 ml & 2 ml)	Bertin Technologies, Montigny-le-Bretonneux, France
PVDF-membrane; 0,2 µM – Roti®-Fluoro	Carl Roth
Reversed-phase chromatography matrix – Poroshell 120 EC-C18, 2,7 µm	Agilent Technologies, Santa Clara, USA
Reaction Tubes, low binding reaction tubes (1,5 ml; 2 ml; 15 ml, 50 ml)	Sarstedt, Nümbrecht, Germany
Serological pipettes	Sarstedt, Nümbrecht, Germany
Ultracentrifuge reaction tubes (1,5 ml)	Beckman Coulter, Brea, USA
96-well plates, clear	Techno Plastic Products, Trasadingen, Switzerland
96-well plates, white	Corning Life Sciences, Corning, USA
384-well plates, black	Corning Life Sciences, Corning, USA

6.11. *C. elegans* strains

6.11.1. Strains generated for or used in this work

Table 15: List of C. elegans strains generated for or used in this work

Designation	Description	Source
p12.6	[*phsp-12.6::gfp*]	This project
p12.6tG	[*phsp-12.6::hsp-12.6::gfp*]	This project
p17G	[*phsp-17::gfp*]	This project
p17tG	[*phsp-17::hsp-17:gfp*]	This project
p17tR	[*phsp-17::hsp-17::wrmScarlet*]	This project
BJ49	kcIs6 [*ifb-2p::ifb-2::CFP*]	Leube Lab
BK36	qpIs11 [*vha-1p::GFP + unc-119(+)]* I	CGC
CF3166	muEx473 [*kin-19p::kin-19::tagRFP + tph-1p::GFP*]	CGC
DCD214	uqIs24 [*myo-2p::tagRFP::pab-1*]	David Lab
DH1033	bIs1 [*vit-2::GFP + rol-6(su1006)]*	CGC
JKM2 (nAβ)	[*rgef-1p::Signalpeptide-Abeta(1-42)::hsp-3(IRES)::wrmScarlet-Abeta(1-42)::unc-54(3'UTR) + rps-0p::HygroR*]	Kirstein Lab
JKM3	[*rgef-1p::wrmScarlet::unc-54(3'UTR) + rps-0p::HygroR*]	Kirstein Lab
JKM7 (mAβ)	[*myo-3p::Signalpeptide-Abeta(1-42)::hsp-3(IRES)::wrmScarlet-Abeta(1-42)::unc-54(3'UTR) + rps-0p::HygroR*]	Kirstein Lab
JKM8	Ex [*myo-3p::wrmScarlet-Abeta::unc-54(3'UTR) + rps-0p::HygroR*]	Kirstein Lab
N2	“Wild type”	CGC
OG412	drIs20 [*vha-6p::Q_{44}::YFP + rol-6(su1006) + pBluescript II*]	CGC
mQ_0	*[unc-54p::YFP]*	Morimoto Lab
iQ_{85}	[*vha-6p::Q_{85}::YFP*]	Morimoto Lab
RT2676	pwIs974 [*pcc1::tagRFP::chc-1*]Cbunc-119	Grant Lab

RT2676 + p17tG	The construct for p17tG was injected into RT2676 to generate an extrachromosomal array.	This study
RT311	pwIs69 [*vha6p::GFP::rab-11+Cbr-unc-119(+)]*	CGC
RT327	pwIs170 [*vha6p::GFP::rab-5+Cbr-unc-119(+)]*	CGC
RT476	wIs170 [*vha6p::GFP::rab-7 + Cbr-unc-119(+)]*	CGC
RT525	pwIs206 [*vha6p::GFP::rab-10+Cbr-unc-119(+)]*	CGC
SJ4143	zcIs17 [*ges-1::GFP(mit)*]	CGC
shAbeta (IL2)	[*pklp-6::shAbeta::SL“::Scramble+myo-2p::GFP*]	This study
shAbeta (URY)	[*ptol-1::shAbeta::SL2::GFP*]	Kirstein Lab
WH346	ojIs34 [*GFP::car-1 + unc-119(+)]*	CGC

6.11.2. Crossed strains generated for this work

Table 16: List of C. elegans strains crossed for this work

Strain A	**Strain B**
p17tG	DCD214
p17tG	JKM3
p17tR	RT311
p17tR	RT327
p17tR	RT476
p17tR	RT525
p17tR	BK36
p17tR	BJ49
p17tR	SJ4143
p17tR	DH1033
p17tR	OG412
p17tR	iQ_{85}
BIJ34	JKM3
BIJ34	JKM8
mQ_0	JKM3

mQ_0	JKM8

In each row, crossing between strain *A* and *B* (AxB) is indicated.

6.12. Bacterial strains

Table 17: List of bacterial strains used in this work

Strain	**Genotype**
BL21 (DE3) pRare	*E. coli* [*fhuA2 [lon] ompT gal (λ DE3) [dcm] ΔhsdS* pRARE (Cam^R) *λ DE3 = λ sBamHIo ΔEcoRI-B int:: (lacI::PlacUV5::T7 gene1) i21 Δnin5*]
C3040 NEB® stable competent	*E. coli* [F' *proA+B+ lacI^q Δ(lacZ)M15 zzf::Tn10* (Tet^R) *Δ(ara-leu) 7697 araD139 fhuA ΔlacX74 galK16 galE15 e14- Φ80dlacZΔM15 recA1 relA1 endA1 nupG rpsL* (Str^R) *rph spoT1 Δ(mrr-hsdRMS-mcrBC)*]
DB11	*Serratia marcescens* (insect pathogenic Gram-negative bacterium) [*Kan^R, Tet^R, Strep^R*]
DH5α	*E. coli* [*dlacZ Delta M15 Delta(lacZYA-argF) U169 recA1 endA1 hsdR17(rK-mK+) supE44 thi-1 gyrA96 relA1*]
HT115 (DE3)	*E. coli* [*F-, mcrA, mcrB, IN(rrnD-rrnE)1, rnc14::Tn10(DE3 lysogen: lacUV5 promoter -T7 polymerase*] (*C. elegans* RNAi strain)
OP50	*E. coli* (*C. elegans* food source), Uracil auxotroph

6.13. Software and online tools

Table 18: List of software and online tools used in this work

Software	**Creator / Company**
Amplify4	Bill Engels (University of Wisconsin)
BLAST	NCBI, Bethesda, USA
BUSCA	Savojardo *et al.*, University of Bologna,

	Italy (233)
DAVID functional annotation tool	Laboratory of Human Retrovirology and Immunoinformatics, Frederick, USA (234,235)
EzColocalization	Stauffer *et al.* (236)
Fiji	Various (237,238)
E-RNAi	Horn & Boutros, DKFZ Heidelberg, Germany (239)
EndNote X9	Clarivate Analytics, Philadelphia, USA
Excel	Microsoft Corporation, Redmond, USA
Illustrator	Adobe Inc., San José, USA
OASIS – online application for survival analysis	Yang *et al.* (240)
Perseus	Max Planck Institute of Biochemistry (241)
Photoshop	Adobe Inc., San José, USA
PLAAC	Lancaster *et al.* (171)
Prism 8	GraphPad Software, San Diego, USA
PRIDE – proteomics identifications database	EMBL-EBI, Cambridge, UK (242)
Serial Cloner 2.6.1	Franck Perez (Serial Basics)
Word	Microsoft Corporation, Redmond, USA

6.14. *In vitro* methods

6.14.1. Plasmid DNA preparation

For preparation of plasmid DNA, *E. coli* cells (commonly DH5α) were grown overnight in LB-media, supplemented with 100 µg / ml Ampicillin, until stationary, at 37 °C. Plasmids containing polyQ constructs were instead grown in *E. coli* C3040 cells. Cells were harvested by centrifugation (20000 x g, 1 min) and the supernatant was discarded. The step was repeated until the desired volume of cells had been collected. The isolation of plasmids was carried out with the *NucleoSpin Plasmid Isolation Kit*, following the manufacturer's instructions. The DNA was collected in a

1,5 ml reaction vessel and concentrations determined with a *Nanodrop* Spectrophotometer, by measuring absorption at 320, 260 & 280 nm (243). Plasmids were stored at -20 °C.

6.14.2. *C. elegans* RNA preparation

For preparation of *C. elegans* RNA, nematodes were harvested by washing them off NGM-agar plates with M9 media followed by centrifugation. After removal of the supernatant, per plate, 250 µl of *Trizol* reagent were added to the pellet. The mixture was agitated on a vortex mixer for 1 min at RT followed by 20 min at 4 °C. The mixture was then incubated resting on ice for 12 min. 50 µl of chloroform were added before agitating the pellet manually. The mixture was let to rest for 3 min at RT before centrifugation at 15300 x g, at 4 °C. The supernatant was then processed with the *NucleoSpin RNA Isolation Kit*, according to the manufacturer's instructions. The concentration of RNA was determined as above, before storage at -80 °C.

6.14.3. cDNA preparation

cDNA was prepared from *C. elegans* RNA preparations with the *Maxima First Strand cDNA Synthesis Kit*, according to the manufacturer's instructions, using 500 ng of RNA for each run. cDNA was used immediately or stored at -20 °C.

6.14.4. PCR methods

PCR was performed in a *Mastercycler Gradient* PCR thermocycler. In general, PCR was carried out in 50 or 20 µl volumes of water supplemented with 10x PCR buffer I; 0,4 mM nucleotide mix (0,1 mM of each nucleoside triphosphate); 1 µl of template (i. e. plasmid carrying the gene of interest or cDNA); 0,3 µM of each primer and 1 µl of Phusion DNA Polymerase.

To perform PCR directly from *C. elegans*, a solution of 1 mg / ml Proteinase K in PCR buffer I was prepared. Roughly 10 animals were transferred into 10 µl of the mixture and heated to 65 °C for at least 90 min before inactivation at 95 °C for at least 30 min. The resulting 10 µl were used as the template for PCR (based on a method developed by Ian Chin-Sang, Queens University, Canada and (244)).

A standard PCR program was used for every experiment (i.e. initial melting at 98 °C for 1 min, followed by at least 34 cycles of melting, annealing and elongation at 72 °C for 40 sec and one final step of elongation for 10 minutes. As a standard annealing temperature, 55 °C was used. Alternatively, *Amplify4* was used to calculate annealing temperatures of primers *in silico*.

If PCR experiments did not succeed, up to 8% of DMSO were added to the reaction mix, annealing temperatures were reduced or optimized by gradient PCR; PCR buffer I was exchanged to PCR buffer II or 0 (allowing to manually adjust Mg^{2+} concentrations) or the initial melting step was increased to 5 min, *ad libitum*, in no particular order. To amplify long target DNA strands, elongation times were increased to 2 / 20 min.

6.14.5. Cloning methods

For His-SUMO-tagged recombinant expression of proteins in *E. coli*, the CDS of the respective protein was amplified by PCR using the indicated primers and template. The amplified construct was isolated by agarose gel electrophoresis followed by isolation using the *QIAquick* gel extraction kit. Agarose gel electrophoresis was performed in 1x TAE buffer using *RedSafe* for nucleotide staining, following the manufacturer's instructions, adjusting agarose concentrations *ad libitum* (between 1 and 2 % w/v). The purified DNA and the vector pSUMO were digested using the indicated restriction enzymes. After dephosphorylation by Alkaline Phosphatase, the prepared insert and vector were ligated by T4 DNA ligase, using a ratio of vector : insert of 1:1; 1:3 and 1:5. Ligation was carried out overnight, at 15 °C, before transformation into *E. coli* DH5α.

Unless specified otherwise, enzymes and kits were used following the manufacturer's instructions. *Serial Cloner* was used to establish cloning strategies and generate the resulting constructs *in silico*. The generated plasmids were confirmed by commercial DNA sequencing services, using a primer recognizing the T7 promotor provided by the company (LGC Genomics, Berlin, Germany and SourceBioscience, Nottingham, UK).

Table 19: List of primer pairs used for cloning into pSumo

Target CDS	Primers used	Restriction enzymes used
hsp-17	hsp-17 f & r	*BsaI* & *NotI*
hsp-17+Cystein	hsp-17 f & hsp-17r+C	*BsaI* & *NotI*
hsp-20B	hsp-20B f & r	*BsmBI* & *NotI*
hsp-21	hsp-21 f & r	*BsaI* & *NotI*
hsp-25a	hsp-25 f & r	*BsaI* & *NotI*
hsp-25b	hsp-25b f & hsp-25r	*BsaI* & *NotI*
hsp-43	hsp-43 f&r	*BsaI* & *NotI*
A$\beta_{1\text{-}42}$	Abeta f & r	*BsaI* & *NotI*

For the generation of constructs for *C. elegans* transformation, the vector pPD95.77 was used. Promotor sequences were amplified from purified genomic DNA (Kirstein Lab), plasmid DNA (see list of plasmids) or directly from *C. elegans* (transcriptional reporters). CDS were amplified from pSumo or plasmid DNA and cloned into the promoter constructs (translational reporters). Constructs generated follow the pattern [*promoter::gfp* or [*promotor::cds::gfp*]. The construct [*phsp-17::hsp-17::gfp*] was used to generate [*phsp-17::hsp-17::wrmScarlet*]. The construct for the JKM-strains is described in the results section. The primers M13 reverse (provided by sequencing service, binds 5' of the construct) and rSeq (binds GFP / wrmScarlet) were used for sequencing. The primer revSeqSL was used to sequence the A$\beta_{1\text{-}42}$ stem-loop construct.

Table 20: List of primer pairs used for cloning into pPD95.77

Target Sequence	Primers used	Restriction enzymes used
wrmScarlet, for hsp-17	p17+ 17 + Sca f & r	*AgeI* & *BtgZI*
phsp-17	p17 f & r	*SphI* & *SalI*
hsp-17	p17+ 17 f & r	*XmaI* & *AgeI*
hsp-12.6	p12.6 + 12.6 f & r	*XmaI* & *KpnI*
A$\beta_{1\text{-}42}$ *(replacing GFP)*	AbetaB f & r	*NheI* & *XhoI*
Aβ*Sl2 (replacing GFP)*	AbetaSL2 f & r	*AgeI* & *XhoI*
wrmScarlet, for A$\beta_{1\text{-}42}$	wrmSca f & r	*XbaI* & *NheI*
prgef-1	rgef f & r	*SphI* & *KpnI*

pklp-6	pklp-6 f & r	*SphI* & *KpnI*

For the generation of new RNAi constructs, partial sequences of the protein of interest CDS have been sub-cloned into the *C. elegans* RNAi-feeding vector pL4440 (245). The exact target and the primer sequences have been determined with the web-tool E-RNAi (239). Sequencing was performed to confirm the constructs using primers binding the T7-promoter.

Table 21: List of primer pairs used for cloning into pL4440

Target CDS	**Primers used**	**Restriction enzymes used**
hsp-17	hsp-17 RNAi f & r	*KpnI* & *HindIII*

6.14.6. Generation of competent *E. coli* cells

To generate competent *E. coli* DH5α, 1 L of LB-media supplemented with 20 mM $MgSO_4$ and 10 mM KCl were induced with 10 ml of a stationary culture of *E. coli* DH5α and grown to an OD_{600} between 0,6 and 0,8. Cells were then incubated on ice for 10 min before centrifugation at 14000 x g and 4 °C. The pellet was resuspended in 300 ml of TFB1 and incubated for 20 min on ice. Cells were centrifuged for 5 min at 1500 x g and 4 °C. The resulting pellet was resuspended in 20 ml of cold TFB2; the cells were then flash frozen in liquid nitrogen and stored at -80 °C.

6.14.7. Bacterial transformation

To transform competent *E. coli*, 100 µl of cells were thawed on ice and mixed with ligation mixtures (from molecular cloning) or plasmids of interest. The mixture was incubated on ice for at least 20 min before heat shock at 42 °C for 1 min. The cells were returned to ice for 5 min and then mixed with 1 ml of LB-media for incubation at 37 °C for at least 60 min. Cells were then plated on LB-agar supplied with ampicillin or used to induce liquid precultures.

6.14.8. Expression of recombinant proteins

The recombinant overexpression of proteins for *in vitro* assays was carried out in *E. coli* BL21 (DE3) pRare. Competent BL21 cells were mixed with a vector carrying the CDS of the POI in an expression cassette (i. e. pSumo or pGex) and transformed as described. After transformation, cells were grown to stationary phase overnight in presence of 100 µg / ml Ampicillin and 25 µg / ml Chloramphenicol. On the next day, the preculture was used to induce the required volume of main culture (between 1 and 4 l) in a ratio of 1 : 100, using the same antibiotics. The main culture was grown at 37 °C to an OD_{600} between 0,5 and 0,8 before induction with IPTG. After a set time, cells were harvested by centrifugation at 8000 x g (first run) and 30000 x g (second run). Pellets were flash frozen in liquid nitrogen and stored at -20 °C. Conditions of induction and expression are indicated in the table.

Table 22: List of expression conditions for recombinant proteins

Recombinant protein	**Concentration of IPTG for induction**	**Temperature of overexpression**	**Time of overexpression**
$A\beta_{1-42}$	0,5 mM	37 °C	4 h
HSP-12.6	1 mM	30 °C	16 h
HSP-17	0,5 mM	30 °C	4 h
other sHsps	0,5 mM	20 °C	16 h
HSP-1, HSP-110, DNJ-12, DNJ-13	1 mM	20 °C	16 h
$HttEx1Q_{48}$	1 mM	18 °C	16 h

6.14.9. Generation of polyclonal antibodies

Polyclonal anti-HSP-17 antibodies were generated by immunizing rabbits with purified HSP-17 (Pineda, Germany). The immunized sera were tested against purified HSP-17 and against wild type *C. elegans* lysates.

6.14.10. Nickel-affinity chromatography.

For immobilized-metal affinity chromatography (IMAC), bacterial pellets from recombinant overexpression were resuspended in approximately 10 times their volume of (LB) by agitation with a glass stick and on a magnetic stirrer. The bacteria were then lysed using an LM10 microfluidizer in three cycles at 18000 psi. The lysates were centrifuged at 30000 x g for 20 minutes and the cleared lysate was mixed with approximately 1 ml of Ni-NTA per liter of main culture (for all sHsps except HSP-12.6, 0,25 ml of beads were used per liter of main culture). After incubating the beads for 90 min on a rolling mixer, they were passed through a plastic gravity flow column to attain an even bedding of beads. The beads were washed with 25 ml of HSB followed by 25 ml of LSB, before addition of 3 ml EB. The beads were agitated for 30 min before the first elution fraction was collected. An additional 7 ml of EB were added and collected by gravity flow in fractions. The fractions were tested for protein by mixing small drops with Bradford solution; fractions containing protein were then pooled. For 1 mg of total protein, 4 µg of SUMO-protease were added to remove the tag over 2 hours. If a further chromatography step was planned (i. e. anion exchange), the protein was concentrated to around 5 ml by centrifugal filter devices. Following removal of tag, reverse nickel-affinity chromatography was performed: the protein mixture was incubated with 1 ml of nickel beads, equilibrated in LSB, for 10 min, before flow-through was collected by gravity flow. All steps were performed on ice and samples were taken for analysis by SDS-PAGE.

6.14.11. GST-tagged protein purification

For GST-sepharose chromatography (of $HttEx1Q_{48}Stop1c$[1]), bacterial pellets from recombinant overexpression were resuspended in approximately 10 times their volume of LWB (including DNaseI) by agitation with a glass stick and on a magnetic stirrer. The bacteria were then lysed using an LM10 microfluidizer in three cycles at 18000 psi. The lysates were centrifuged at 30000 x g for 40 minutes and the cleared lysate was mixed with approximately 1 ml of GST-sepharose beads per liter of main culture. After incubating the beads for 60 min on a rolling mixer, they were passed

1 For the “Stop1c” construct, the C-terminal stop codon was slightly altered to ensure full-length expression of the construct.

through a plastic gravity flow column to attain an even bedding of beads. The beads were washed with 25 ml of LWB (including Triton X-100) followed by 25 ml of LWB (no Triton X-100), before addition of 3 ml EB. The beads were agitated for 30 min before the elution fraction was collected by gravity flow and readied for dialysis.

6.14.12. Dialysis

For proteins purified by IMAC without need for further chromatography, removal of tag was performed during dialysis of the pooled, eluted protein fractions overnight. The protein solution was mixed with the SUMO-protease and filled into dialysis tubing before being placed in at least 2 L of LSB, at 4 °C, under gentle agitation by a magnetic stir bar. HttEx1Q_{48} constructs were dialyzed against DB. After dialysis, protein was collected and purification was continued with reverse nickel-affinity chromatography as described above. The solution was then aliquoted and flash-frozen in liquid nitrogen before storage at -80 °C.

6.14.13. Anion exchange chromatography (AEC)

Following nickel-affinity chromatography, the flow-through of reverse nickel-affinity chromatography was diluted to 50 ml in LSB2 and cleared by syringe-filter. The protein solution was loaded into a 50 ml *Superloop* and injected onto a ResourceQ anion-exchange chromatography column equilibrated in LSB2. The column was washed with 5 CV of LSB2 before elution of protein by a gradient of LSB2 to HSB2 over 25 CV. Fractions containing the POI were determined (in the first run) by SDS-PAGE. The fractions containing the protein of interest were pooled, aliquoted and flash-frozen in liquid nitrogen before storage at -80 °C. Chromatography was carried out using an FPLC (ÄKTA Explorer) at 4 °C, following the manufacturer's instructions.

6.14.14. Size exclusion chromatography (SEC)

For preparative SEC, protein samples (from nickel-affinity or anion-exchange chromatography) were concentrated to 5 ml using centrifugal filter devices and cleared by syringe filtration. Samples were then loaded onto a *HiLoad Superdex 75*

16/600 column, equilibrated in SEC running buffer, utilizing a 5 ml injection loop. The run was performed in the same buffer, following the manufacturer's instructions, at 4 °C, at a flow rate of 1 ml / min. Fractions containing protein were collected and analyzed before pooling fractions containing the POI and aliquotizing them. Proteins were flash frozen in liquid nitrogen and stored at -80 °C.

For analytical SEC, purified and aliquoted protein samples were concentrated to 500 µl using centrifugal filter devices and cleared by centrifugation. Samples were loaded onto a *Superose 6 10/300 GL* column, equilibrated in SEC running buffer, from a 500 µl injection loop. The run was performed in the same buffer, following the manufacturer's instructions, at 20 °C, at a flow rate of 0,4 ml / min. Samples of fractions were collected for further analysis by SDS-PAGE.

6.14.15. SDS-PAGE

SDS-Polyacrylamide gels for protein analysis were prepared in a commercial system (*Bio-Rad*). In brief, the separation gel was loaded into the assembly and covered with isopropanol which was removed after the gel had solidified. The gel was then covered with the stacking gel, into which the respective gel comb for 10 or 15 pockets was inserted. For gradient gels, two separation gels were prepared, taken up in equal volume into a serological pipette, pre-mixed by taking in air and then cast (based on a method by Tal Lorberbaum, Columbia University). The composition of the gels was as follows (amounts given for two 0,75 mm gels or 1 1,5 mm gel):

Table 23: Recipes used for SDS-Gels

Tris-Glycine gel components (10% / 12,5% / 15%)	**Separation gel**	**Stacking gel**
Acrylamide / Bisacrylamide mixture (30%)	2,67 ml / 3,33 ml / 4 ml	1,5 ml
Separation gel buffer	2 ml	-
Stacking gel buffer	-	2,5 ml
H_2O	3,33 ml / 2,67 ml / 2 ml	6 ml
APS	80 µl	100 µl
TEMED	8 µl	10 µl

Tris-Tricine gel components (4% / 14% / 20%)		
Acrylamide / Bisacrylamide mixture (30%)	1,33 ml / 4,72 ml / 6,66 ml	0,97 ml
Tris-Tricine gel buffer	3,33 ml	2,5 ml
50 % glycerol stock	0 ml / 2 ml / 0 ml	
H_2O	-	6,55 ml
APS	33 µl	50 µl
TEMED	10 µl	30 µl

Samples for the gel were mixed in a 1:1 ratio with 2x SDS-PAGE sample loading buffer and denatured at 98 °C for at least 10 min. Prestained protein ladder was added as provided. After loading, Tris-Glycine gels were run at constant current (25 mA per gel). Tris-Tricine gels were run at constant voltage (70 V for stacking gel, 150 V for separation gel). Migration of proteins was stopped *ad libitum*. 14% Tris-Tricine gels were used for HSP-17. For HSP-12.6, 15% Tris-Glycine gels were used. Aβ was analyzed with 10-20% Tris-Tricine gels. SQST-1 and LGG-1 were analyzed with 12,5% Tris-Glycine gels on the *TransBlot Turbo* system.

6.14.16. Protein gel staining methods

Protein gels were transferred to Coomassie staining solution for staining and fixation for at least 15 min. After staining, the mixture was washed off at least twice with H_2O, followed by incubation in destaining / fixing solution for 1 h. Gels were then transferred to fresh destaining solution and further destained as desired.

6.14.17. Protein quantification

Quantification of proteins by Bradford assay was carried out in clear 96-well plates. Bradford reagent was prepared according to the manufacturer's instructions and placed into the required wells, in 200 µl volumes, excluding border wells. For each Sample, 1 µl was pipetted into the reagent, in triplicates. A row of 10 wells of reagent without sample was prepared as a background sample. A calibration curve was

prepared from BSA, ranging from 1 to 10 mg / ml (1 mg increments) BSA for *C. elegans* lysates or 0-5 – 7 mg / ml (0,5, 1, 1,5, 2, 3, 4, 5, 6, 7) BSA for purified protein samples. After mixing the samples and incubating for 5 min at most, the absorption of each sample at 595 nm was determined in a plate reader. Protein concentrations were determined using the calibration curve. A fresh calibration was prepared for every experiment.

6.14.18. Immunoprecipitation

Independent populations of young *C. elegans* adults (N2 for HSP-17 or JKM2/7 for Aβ) were lysed in triplicates and centrifuged for 5 min at 8000 x g to remove insoluble material before being adjusted to the same total protein concentration. After adding 10 µl of antibody binding the POI (anti-HSP-17 polyclonal antibody or anti-Aβ 6E10), the mixture was incubated for 16 h. As control, the same procedure was carried out in triplicates using anti-GFP antibodies (for HSP-17) or the worm strains JKM3/8 (for Aβ). 25 µl magnetic beads loaded with Protein A/G were washed three times with TBST, one time with HMK and added to the mixture. After incubation for 90 min, the beads were washed with TBST three times and samples eluted by boiling in 2x SDS sample buffer. Following this, samples were further incubated at 55 °C for 30 minutes before alkylation with 15 mM chloroacetamide in the dark, for 30 min.

For immunoprecipitation followed by Western blotting (for Aβ), lysis was carried out in RIPA lysis buffer and anti-GFP antibody was used. Separation of magnetic beads from liquid phase was carried out using a magnetic reaction vessel rack.

6.14.19. Proteomic analysis of immunoprecipitation samples

Prior to MS/MS analysis, samples were separated by SDS-PAGE until they had migrated into the separation gel for approximately 2 cm. The individual lanes were excised (excluding the stacking gel and the loading-dye front). Subsequent steps were performed by Heike Stephanowitz (FMP): protein digestion from gel bands was carried out using trypsin at an enzyme-to-protein ration of 1:20 (w/w) at 37 °C overnight as described previously (246).

LC/MS analysis was performed using an UltiMate 3000 RSLC nano LC system coupled on-line to an Orbitrap Elite mass spectrometer (Thermo Fisher Scientifc).

Reversed-phase separation was performed using a 50 cm analytical column (in-house packed with Poroshell 120 EC-C18, 2.7µm, Agilent Technologies) with a 120 min gradient. MS1 scans were performed in the orbitrap using 60,000 resolution; MS2 scans were acquired in the ion trap with an AGC target of 5E3 and maximum injection time of 50 ms.

Label free quantification was performed as previously published (247). Proteins enriched in the sample condition over the control condition, or proteins that were identified in the sample, but not in the control condition, were considered to be enriched.

Data analysis including label free quantification was performed using MaxQuant (version 1.6.1.0) using the following parameters: MS ion mass tolerance: 4.5 ppm; MS2 ion mass tolerance: 0.5 Da; variable modification: Cys carbamidomethyl, Met oxidation, Propionamide; allowed number of mis-cleavage: 2, database: SwissProt database of *C. elegans* whole proteome (10/2016 27944 sequences and 12832868 residues searched); label free quantification and match between runs were enabled. Results were reported at 1% FDR at the protein level.

6.14.20. Intact protein QTof-MS

Intact proteins were analyzed using a *Waters* H-class instrument equipped with a quaternary solvent manager, a *Waters* sample manager-FTN, a *Waters* PDA detector and a *Waters* column manager with an Acquity UPLC protein BEH C4 column (300 Å, 1.7 µm, 2.1 mm x 50 mm). Proteins were eluted at a column temperature of 80 °C with a flow rate of 0.3 ml/min. The following gradient was used: A = H_2O + 0.01% formic acid, B = acetonitrile + 0.01% formic acid. 5-95% B 0-6 min at 40 °C. Mass analysis was conducted with a *Waters* XEVO G2-XS QTof analyzer. Proteins were ionized in positive ion mode applying a cone voltage of 40 kV. Raw data was deconvoluted with MaxEnt 1. Operation of the device was carried out by A. Baumann (FMP).

6.14.21. Light scattering

For light scattering, the POI was thawed and centrifuged for 1 min at 14000 x g before concentrations were determined by Bradford assay. MDH as a substrate was

pelleted (from ammonium-sulfate suspension) by centrifugation for 1 min at 14000 x g. Then, the supernatant was discarded and replaced with the light scattering buffer. GAPDH and CS were dialyzed against their respective light scattering buffers before being used as substrates for light scattering or aliquoted and flash frozen in liquid nitrogen before storage at -20 °C and treated like the POI for further experiments (248).

Before each experiment, the cuvettes and stir bars were rinsed with H_2O, ethanol, H_2O and the respective light scattering buffer. Between samples, the rinse was repeated with H_2O and buffer. For measurements, the required volume of buffer (total volume in cuvette: 1 ml) was inserted into the cuvette and measured under the indicated conditions. The measurement was stopped when the baseline stabilized and the buffer had reached the intended temperature. The POI was then added and measured until a stable baseline was reached. Subsequently, the substrate of aggregation was added and the measurement started (the mixture was supplemented with 2 mM DTT for MDH). After measurements, the cuvette and stir bar were returned to Hellmanex cleaning solution (3% in H_2O, at 30 °C). The buffers used for each substrate are indicated in the materials section.

Table 24: Fluorimeter settings used for static light scattering

Fluorimeter setting	**Value**
Slit width	2,5 nm each
Sensitivity	medium
Interval	5 s
Wavelength	360 nm and 550 nm (for 47 °C) or 360 nm and 600 nm (for 41 °C)
Cuvette holder temperature	47,2 °C or 41,2 °C (MDH); 43,2 °C (CS); 45,2 °C (GAPDH)
Remaining settings	Set to default

6.14.22. Sedimentation of MDH aggregates

Aggregation experiments with MDH were carried out under the same conditions as static light scattering experiments, but in 50 µl of total volume. The indicated concentration of MDH was incubated at 47 °C for 30 min or at 41 °C for 60 min in MDH light scattering buffer. HSP-17 was added to experiments as indicated in the results section. For separation of soluble and insoluble material, the mixture was centrifuged at 20000 x g for 30 min before supernatant was removed and mixed with 2x SDS sample buffer. The pellet was resolubilised in 50 µl of the same buffer before addition of 2x SDS sample buffer.

6.14.23. Luciferase disaggregation and refolding assay

For luciferase assay, all POI indicated were thawed and concentrations determined by Bradford assay. A Luciferase mixture was prepared as follows: Luciferase was diluted from stock to 15 nM (in HMK) and kept as native or heat treated for 15 min at 45 °C. For heat treatment, sHsps were included in the mixture as described in the results section. For addition of sHsps after luciferase heat treatment, sHsps in the respective amount were heat treated separately.
The final assay mixture was prepared to a volume of 125 µl as indicated:

Table 25: Reaction mixture for luciferase assay

Component	**Amount added**
Pyruvate kinase solution	9,25 µl
Phosphoenolpyruvate	3,6 mM
HSP-1	4 µM
DNJ-12	1 µM
DNJ-13	1 µM
HSP-110	2 µM
sHsp	as indicated in results section
Luciferase mixture	42 µl (added directly before measurement)
HMK	as needed for 125 µl final volume

Samples were measured in triplicates. For each sample, 100 µl of assay buffer were prepared in a white flat bottom 96-well plate. For measurement, 5 µl of the reaction mixture were transferred to the assay buffer, followed by 100 µl of 1 µM luciferin solution. Luminescence was then detected in a plate reader, after 5 s of orbital shaking. Measurements were carried out at t_0 (when the luciferase mixture is added into the reaction mixture) and after 7; 15; 30; 60; 90 and 120 minutes.

6.14.24. Transmission electron microscopy

For TEM analysis, 3 µM $HttEx1Q_{48}$ were incubated in HMK after addition of 1,4 µl Prescission protease per 100 µl of sample (t_0). Samples were flash frozen in liquid nitrogen at t_0 and after 18 h. Small heat shock proteins were added to the mixture as indicated in the results section. Further preparation and mounting of samples for TEM analysis, including immunogold-labeling, were carried out by D. Puchkov (FMP), as described previously (27).

6.14.25. Western blotting

Western blotting was carried out after SDS-PAGE in a wet chamber (*Bio-Rad*). In brief, PVDF membrane was wetted in methanol for 1 min before 5 min equilibration in transfer buffer. The SDS-PAGE gel was also transferred to transfer buffer before assembling the blot as per the manufacturer's instructions. Western blots were performed at constant voltage of 100 V for 90 min. Samples containing $A\beta_{1-42}$ were blotted for no longer than 60 min. After blotting, membranes were blocked for 1 h in 5% (w/v) milk powder. For $A\beta_{1-42}$, 4% BSA (w/v) was used instead. Primary antibody incubation was carried out overnight at 4 °C in 1x Roti Block. Incubation with anti-Huntingtin antibodies was carried out in 3% milk powder instead. Secondary antibodies were incubated for 60 to 90 min in 1x Roti Block. Detection of peroxidase-conjugated antibodies was carried out using ECL-reagent, following the manufacturer's instructions, utilizing the *Lumi-Imager*. Fluorophore-conjugated antibodies were detected using the *Odyssey* system.

Semi-dry blotting was carried out analogously, using the buffer provided by the manufacturer and following the pre-set programs of the *Turbo Transfer System* (*Bio-Rad*).

6.14.26. Absolute protein quantification *ex vivo*

To quantify absolute levels of HSP-17 in *C. elegans*, lysates were generated from nematode populations of the same age in triplicates and centrifuged for 5 min at 8000 x g to remove insoluble material. Lysates were then analyzed by Bradford assay and adjusted to the same protein level before labeling with 0,625 pmol / µl Cy5-NHS for 15 minutes in the dark. The samples were then blotted (using 1 µg to 17,5 µg of lysate protein) in parallel to calibration samples of purified HSP-17 of a known concentration. HSP-17 was detected by anti-HSP-17 antibody (primary) and anti-rabbit-peroxidase conjugated antibody (secondary) on the *Lumi-Imager* system. HSP-17 concentration in the samples was then calculated based on the calibration; Cy5 fluorescence at 700 nm was detected by *Odyssey* system and used for normalization.

6.15. *C. elegans* methods

6.15.1. Maintenance of *C. elegans*

C. elegans was kept on NGM-agar plates seeded with *E. coli* OP50 as food source at 20 °C for experimentation and growth or at 15 °C for maintenance, adhering to standard protocols (249). To avoid starvation, worms were transferred to new media at least once a week by a platinum wire pick using a dissecting or fluorescence microscope. To generate lysates of *C. elegans*, worms were collected using M9 buffer and transferred to *Precellys* lysing kits in *C. elegans* lysis buffer. Lysis was performed for all experiments in 3 steps of shaking for 10 seconds at 6000 rpm.

6.15.2. Crossing of *C. elegans*

To cross *C. elegans* strains, 7 young adult males of one strain were placed on a NGM-agar plate with one young adult hermaphrodite of the second strain. To

generate males of a strain of interest, N2 males were crossed with that strain (N2 males were maintained by crossing them with N2 hermaphrodites). To generate an initial population of N2 males, youg adult N2 hermaphrodites were exposed to heat shock (30 °C, 6h) and their offspring was screened for males. Successfully nematodes were identified by microscopy and isolated until homozygous offspring were identified.

6.15.3. Synchronization of *C. elegans*

To synchronize *C. elegans* populations, NGM-agar plates containing eggs were washed with M9 buffer to remove hatched animals. The eggs were subsequently transferred to a new plate and left to hatch.
Alternatively, bleaching was carried out. From a plate containing gravid hermaphrodites, nematodes were washed off using M9 buffer and transferred to a 15 ml reaction vessel. To a volume of 7,5 ml of M9 buffer, 0,5 ml of 10 M NaOH and 2 ml of sodium hypochlorite solution were added. The worms were agitated by vortex mixer for approximately 4 minutes, before being sedimented by centrifugation at 500 x g for 1 min, removal of the bleaching solution and washing with H_2O. The wash was repeated two times with M9 buffer. After centrifugation at 500 x g for 1 min, liquid was removed, retaining a volume of around 500 µl. The mixture was transferred to NGM-agar plates and eggs were left to hatch overnight.

6.15.4. RNAi experiments with *C. elegans*

For RNAi-mediated knockdown of genes of interest in *C. elegans*, NGM-agar plates (RNAi) were seeded with *E. coli* HT115 instead of *E. coli* OP50. The bacteria carried the plasmid p4440L containing the RNAi-construct for the respective gene, or an empty vector for control. Bacteria were grown in LB-media supplemented with 10 µg / ml Tetracycline and 100 µg / ml Ampicillin. Two hours before seeding, bacteria were induced with 1 mM IPTG. Nematodes were kept on the plates from hatching, as described above. Bacteria carrying RNAi-constructs not generated for this work were taken from the Ahringer Library (250).

6.15.5. Transformation of *C. elegans* by microinjection

Transgenic strains of *C. elegans* were generated by microinjection, following established methods (251). Needles for microinjection were pulled from glass capillaries using a horizontal micropipette puller. Injection mixes contained the vector pPD95.77, including the gene of interest, purified by Zymo Kit and eluted in nuclease free water. Concentrations of the vector were adjusted for each gene (typically less than 10 ng / µl). To provide background DNA, GeneRuler DNA-ladder was added (to a concentration of 150 ng / µl). Alternatively, co-injection of 1 µg / µl of oligonucleotides (the primer “Integration”) has been utilized to generate chromosomally integrated translational reporters as described previously (for the strains p17tG & p17tR) (252). After transformation, injected worms were isolated and their offspring screened for transgenic (fluorescent) animals.

6.15.6. Transformation of *C. elegans* by gene bombardment

For transformation of *C. elegans* by gene gun, established protocols were utilized (253,254). In brief, a large population of young adult hermaphrodite nematodes was prepared (around 10 NGM-agar plates per construct to be bombarded). For each construct, 1 mg of gold particles were mixed with 100 µl spermidine solution and sonicated. After 10 min of incubation at RT, 10 µg of the DNA to be used (i. e. the vector pPD95.77) were mixed with 100 µl of the gold solution and incubated for 10 min at RT. This was repeated after adding 360 µl H_2O. 100 µl 1M $CaCl_2$ were added before vortex mixing the solution for 10 s. The mixture was then incubated for 10 min at RT before centrifugation at 17000 x g for 30 s. The gold particles were washed 3 times with 500 µl of ethanol, dried, and resuspended in PVP solution.
In parallel, the nematodes for transformation were collected in M9 buffer and left to settle on ice. Empty NGM-agar plates were seeded with 12 µl of OP50 before cooling down on ice. The nematodes were transferred to the dried OP50 spots to achieve a dense distribution of animals before shooting them with the gold particles. The bombardment was carried out using a custom-made gene gun. After bombardment, worms were transferred to new NGM-agar plates and screened for transgenic (fluorescent) progeny on the following days. Transgenic nematodes were isolated and kept in culture.

6.15.7. Fixation and DAPI staining of *C. elegans*

For nuclear staining of *C. elegans* nematodes were harvested and washed three times with M9 media. After incubation on ice for 5 min, the nematodes were mixed with 500 µl of formaldehyde solution for 30 min. Nematodes were then washed three times with PBST before being transferred to a 500 µg / ml solution of DAPI in AbA. The specimens were incubated for 2 h in the dark, on a rolling mixer. They were then washed two times with AbA for 30 min before a final wash in AbA overnight. Subsequently, the nematodes were imaged by LSM as described below.

6.15.8. Confocal laser scanning microscopy

Imaging of *C. elegans* was carried out on a confocal laser scanning microscope (LSM780). Nematodes chosen for imaging were mounted on pads of 2% agarose in H_2O, on glass slides. The worms were placed inside a drop of 2 mM levamisole to anesthetize them. Parameters of imaging, such as aperture, laser intensity or filter sets were chosen to provide adequate imaging and kept constant for each experiment. Image material generated was displayed, analyzed and prepared for Figures with *Fiji*.

6.15.9. Developmental assay

For developmental assay, 10 L1 nematodes for each condition analyzed were placed on NGM-agar plates, in three independent replicates. For each day, worms were scored for their developmental stage (L1, L2-L3, L4, adult, lost). Worms that were not found or died were censored and not considered for analysis.

6.15.10. Life span assay

To analyze life span of *C. elegans* strains, the indicated number of hermaphrodite nematodes was transferred to fresh NGM-agar plates as L1 larvae. RNAi conditions and strains were used as reported in the results section. Experiments were carried out in triplicates with approximately 100 – 150 animals per condition. For each day, all observed nematodes were scored as alive, dead (worms not moving upon physical stimulation) or missing (missing worms were censored and excluded from analysis). Worms were transferred to new NGM-agar plates to provide food and

separate them from their progeny as required. The Oasis online tool was used to analyze the resulting data (240), displaying median lifespan and the percentage fraction of alive worms.

6.15.11. Fecundity assay

For fecundity assays, the indicated number of L4 nematodes were isolated on NGM-agar plates and the number of eggs laid was counted for each specimen on each day. Nematodes were passaged to new plates to separate them from their progeny. Each experiment was performed in three independent replicates for each condition analyzed.

6.15.12. Thermotolerance assay

To assay thermotolerance, young adult (day 4 old) hermaphrodites were placed on NGM-agar plates and exposed to heat shock at 35°C for 6 hours and then transferred to 20 °C for 24 hours before survivors were counted. Three independent repeats were performed with 25 nematodes for each condition. The percentages of the surviving nematodes were analyzed.

6.15.13. Osmotic stress assay

To assay osmotic stress in *C. elegans*, young adult hermaphrodites were transferred to NGM-agar plates that had been prepared with 250 mM NaCl (five-fold the normal concentration). For each condition, 20 worms were assayed in three independent replicates. Survival of the worms was observed for each day and they were transferred to new plates to separate them from their progeny. For RNAi conditions, nematodes were kept on RNAi-plates from hatching onwards before they were transferred to the osmotic stress plates.

6.15.14. Biotic stress assay

To assay stress by pathogenic bacteria in *C. elegans*, young adult hermaphrodites were transferred to NGM-agar plates that had been seeded with *Serratia marcescens* DB11 instead of *E. coli* OP50. Survival of the nematodes was observed for each day, for 20 nematodes in three independent replicates. The experiment was carried out in

parallel with OP50, to normalize the expected survival for each condition. *S. marcescens* DB11 was grown at 25 °C, in presence of 10 µg / ml Tetracycline, 50 µg / ml Streptomycin and 35 µg / ml Kanamycin.

6.15.15. Quantification of KIN-19 foci

To quantify pharyngeal KIN-19 foci in *C. elegans*, LSM images of the pharynx were taken for each nematode. For each specimen analyzed, bright-field microscopy was used to identify a comparable z-layer before an image was taken including tagRFP fluorescence. The images generated were analyzed by *Fiji*. To quantify individual foci, the head or intestine of the worm was defined as a region of interest to be analyzed by the “Find Maxima” feature, using default settings.

6.15.16. Fractionation of insoluble material from *C. elegans*

To fractionate soluble and insoluble proteins from *C. elegans*, populations of the indicated age were collected and lysed. Centrifugation was carried out at 500 x g for 3 min to pellet cell debris and nematode cuticula before supernatant of all conditions was quantified by Bradford assay and normalized. For each condition, 50 µl of normalized lysates were centrifuged at 20000 x g for 30 min at 4 °C. Supernatant was mixed with 2x SDS-loading buffer; the pellet was resolubilized in 50 µl lysis buffer before mixing with 2x SDS-loading buffer. Analysis of the fractions was carried out by SDS-PAGE and Western blotting.

6.15.17. Analysis of iQ-foci by counting

To quantify formation of intestinal polyQ-foci in *C. elegans*, 20 nematodes for each condition were analyzed by fluorescence microscopy in two independent repeats. Starting on day 4 of life, for each worm and day, polyQ-foci were counted (by YFP-fluorescence). Nematodes were scored and clustered to display either no foci, one or more foci, 3 or more foci and finally 10 or more foci.

6.15.18. Analysis of relative fluorescence intensity

To quantify fluorescence levels in whole nematodes, wide field images were taken by LSM780 for each specimen analyzed, using the respective fluorescence filter (YFP for phsp3::yfp). The z-level was adjusted by bright field to be comparable in each case. Images were analyzed in *Fiji*. Each nematode was defined as a region of interest to measure “Integrated density”, “Area” and “Mean gray value”. Fluorescence levels were considered to be integrated density divided by area; with the mean gray value of a random non-nematode pixels being the background (usually 0).

6.15.19. Swim-exhaustion assay

To assess paralysis of *C. elegans* in response to physical exhaustion, three sets of 20 nematodes per condition, on day 4 of live, were placed into a column of 3-4 mm M9 media and slightly dispersed. After 30 minutes of incubation at rt, the number of nematodes moving was scored and plotted as the fraction of total nematodes used. Experiments were performed in triplicates.

6.16. Statistical analysis and *in silico* analysis

6.16.1. Statistical analysis

Statistical analysis was performed using *Excel* (to determine standard deviations and standard error of means) and *Prism* (for ANOVA testing). By *Prism*, p-values < 0,05 were considered significant: p < 0,05 (*), < 0,01 (**), < 0,001 (***), < 0,0001 (****). Dunnett’s multiple comparisons test (for a fixed control), Bonferroni’s multiple comparisons test (no fixed control) or Sidak’s multiple comparisons test (more powerful than Bonferroni) were applied as suggested by the software. To assess survival distribution, a log-rank test was performed, considering p < 0,01 as (*).

6.16.2. *In silico* analysis of protein sequences

In silico prediction of prion-like amino acid sequences in proteins was carried out by the online tool *PLAAC*, using *C. elegans* background frequencies. Prediction of

protein subcellular localization of proteins by amino acid sequences was carried out by *BUSCA*, using default settings.

6.16.3. Image analysis

Image analysis was carried out using *Adobe Photoshop* (for general presentation of image material) and *Fiji* (for additional preparation of microscopies and image analysis). Quantification from images was carried out from raw data where applicable. The *Fiji* plugin *EzColocalization* was used for *C. elegans* analysis of colocalization between fluorophore tagged proteins, without cell identification, using standard settings.

6.16.4. Gene ontology analysis

Gene ontology analysis was carried out using the functional annotation tool of the *DAVID* online resource. Proteins enriched in IP-MS/MS experiments were entered into the tool to determine gene ontology terms that are significantly enriched in the dataset.

7. References

1. Kim, Y. E., Hipp, M. S., Bracher, A., Hayer-Hartl, M., and Hartl, F. U. (2013) Molecular chaperone functions in protein folding and proteostasis. *Annu Rev Biochem* **82**, 323-355
2. Anfinsen, C. B., Haber, E., Sela, M., and White, F. H., Jr. (1961) The kinetics of formation of native ribonuclease during oxidation of the reduced polypeptide chain. *Proc Natl Acad Sci U S A* **47**, 1309-1314
3. Balchin, D., Hayer-Hartl, M., and Hartl, F. U. (2016) In vivo aspects of protein folding and quality control. *Science* **353**, aac4354
4. Ellis, R. J. (2001) Macromolecular crowding: an important but neglected aspect of the intracellular environment. *Current Opinion in Structural Biology* **11**, 114-119
5. Ellis, R. J., and Minton, A. P. (2006) Protein aggregation in crowded environments. *Biol Chem* **387**, 485-497
6. Lindquist, S. (1986) The heat-shock response. *Annu Rev Biochem* **55**, 1151-1191
7. Morimoto, R. I. (2008) Proteotoxic stress and inducible chaperone networks in neurodegenerative disease and aging. *Genes Dev* **22**, 1427-1438
8. Burkewitz, K., Choe, K., and Strange, K. (2011) Hypertonic stress induces rapid and widespread protein damage in C. elegans. *Am J Physiol Cell Physiol* **301**, C566-576
9. Hartl, F. U., Bracher, A., and Hayer-Hartl, M. (2011) Molecular chaperones in protein folding and proteostasis. *Nature* **475**, 324-332

10. Hipp, M. S., Kasturi, P., and Hartl, F. U. (2019) The proteostasis network and its decline in ageing. *Nat Rev Mol Cell Biol* **20**, 421-435
11. Haslbeck, M., and Vierling, E. (2015) A first line of stress defense: small heat shock proteins and their function in protein homeostasis. *J Mol Biol* **427**, 1537-1548
12. Ding, L., and Candido, E. P. (2000) HSP43, a small heat-shock protein localized to specific cells of the vulva and spermatheca in the nematode Caenorhabditis elegans. *Biochem J* **349**, 409-412
13. Parsell, D. A., Kowal, A. S., Singer, M. A., and Lindquist, S. (1994) Protein disaggregation mediated by heat-shock protein Hsp104. *Nature* **372**, 475-478
14. Mogk, A., Tomoyasu, T., Goloubinoff, P., Rudiger, S., Roder, D., Langen, H., and Bukau, B. (1999) Identification of thermolabile Escherichia coli proteins: prevention and reversion of aggregation by DnaK and ClpB. *EMBO J* **18**, 6934-6949
15. Kirstein, J., Moliere, N., Dougan, D. A., and Turgay, K. (2009) Adapting the machine: adaptor proteins for Hsp100/Clp and AAA+ proteases. *Nat Rev Microbiol* **7**, 589-599
16. Tyedmers, J., Mogk, A., and Bukau, B. (2010) Cellular strategies for controlling protein aggregation. *Nat Rev Mol Cell Biol* **11**, 777-788
17. Mayer, M. P. (2013) Hsp70 chaperone dynamics and molecular mechanism. *Trends Biochem Sci* **38**, 507-514
18. Kampinga, H. H., and Craig, E. A. (2010) The HSP70 chaperone machinery: J proteins as drivers of functional specificity. *Nat Rev Mol Cell Biol* **11**, 579-592
19. Arnsburg, K. (2017) *Characterization of chaperone signatures and neurodegenerative diseases using the*
model organism C. elegans. Dr. rer. nat., Humboldt-University of Berlin
20. Craig, E. A., and Marszalek, J. (2017) How Do J-Proteins Get Hsp70 to Do So Many Different Things? *Trends Biochem Sci* **42**, 355-368
21. Glover, J. R., and Lindquist, S. (1998) Hsp104, Hsp70, and Hsp40: A novel chaperone system that rescues previously aggregated proteins. *Cell* **94**, 73-82
22. Shorter, J. (2011) The mammalian disaggregase machinery: Hsp110 synergizes with Hsp70 and Hsp40 to catalyze protein disaggregation and reactivation in a cell-free system. *PLoS One* **6**, e26319
23. Andreasson, C., Fiaux, J., Rampelt, H., Mayer, M. P., and Bukau, B. (2008) Hsp110 is a nucleotide-activated exchange factor for Hsp70. *J Biol Chem* **283**, 8877-8884
24. Rampelt, H., Kirstein-Miles, J., Nillegoda, N. B., Chi, K., Scholz, S. R., Morimoto, R. I., and Bukau, B. (2012) Metazoan Hsp70 machines use Hsp110 to power protein disaggregation. *EMBO J* **31**, 4221-4235
25. Nillegoda, N. B., Kirstein, J., Szlachcic, A., Berynskyy, M., Stank, A., Stengel, F., Arnsburg, K., Gao, X., Scior, A., Aebersold, R., Guilbride, D. L., Wade, R. C., Morimoto, R. I., Mayer, M. P., and Bukau, B. (2015) Crucial HSP70 co-chaperone complex unlocks metazoan protein disaggregation. *Nature* **524**, 247-251
26. Gao, X., Carroni, M., Nussbaum-Krammer, C., Mogk, A., Nillegoda, N. B., Szlachcic, A., Guilbride, D. L., Saibil, H. R., Mayer, M. P., and Bukau, B. (2015) Human Hsp70 Disaggregase Reverses Parkinson's-Linked alpha-Synuclein Amyloid Fibrils. *Mol Cell* **59**, 781-793
27. Scior, A., Buntru, A., Arnsburg, K., Ast, A., Iburg, M., Juenemann, K., Pigazzini, M. L., Mlody, B., Puchkov, D., Priller, J., Wanker, E. E., Prigione, A., and Kirstein, J. (2018) Complete suppression of Htt fibrilization and disaggregation of Htt fibrils by a trimeric chaperone complex. *EMBO J* **37**, 282-299
28. Lindquist, S., and Kim, G. (1996) Heat-shock protein 104 expression is sufficient for thermotolerance in yeast. *Proceedings of the National Academy of Sciences of the United States of America* **93**, 5301-5306

29. Amm, I., Sommer, T., and Wolf, D. H. (2014) Protein quality control and elimination of protein waste: the role of the ubiquitin-proteasome system. *Biochim Biophys Acta* **1843**, 182-196
30. Yu, L., Chen, Y., and Tooze, S. A. (2018) Autophagy pathway: Cellular and molecular mechanisms. *Autophagy* **14**, 207-215
31. Johansen, T., and Lamark, T. (2011) Selective autophagy mediated by autophagic adapter proteins. *Autophagy* **7**, 279-296
32. Labbadia, J., and Morimoto, R. I. (2015) The biology of proteostasis in aging and disease. *Annu Rev Biochem* **84**, 435-464
33. Soto, C., and Pritzkow, S. (2018) Protein misfolding, aggregation, and conformational strains in neurodegenerative diseases. *Nat Neurosci* **21**, 1332-1340
34. Ciechanover, A., and Kwon, Y. T. (2017) Protein Quality Control by Molecular Chaperones in Neurodegeneration. *Front Neurosci* **11**, 185
35. Gan, L., Cookson, M. R., Petrucelli, L., and La Spada, A. R. (2018) Converging pathways in neurodegeneration, from genetics to mechanisms. *Nat Neurosci* **21**, 1300-1309
36. Chiti, F., and Dobson, C. M. (2017) Protein Misfolding, Amyloid Formation, and Human Disease: A Summary of Progress Over the Last Decade. *Annu Rev Biochem* **86**, 27-68
37. Knowles, T. P., Vendruscolo, M., and Dobson, C. M. (2014) The amyloid state and its association with protein misfolding diseases. *Nat Rev Mol Cell Biol* **15**, 384-396
38. Alzheimer, A. (1907) Über eine eigenartige Erkrankung der Hirnrinde. *Allg Zeitschr f Psychiatr. u Psych-Gerichtl Med* **64**, 146-148
39. Alzheimer, A., Stelzmann, R. A., Schnitzlein, H. N., and Murtagh, F. R. (1995) An English translation of Alzheimer's 1907 paper, "Uber eine eigenartige Erkankung der Hirnrinde". *Clin Anat* **8**, 429-431
40. Mucke, L. (2009) Neuroscience: Alzheimer's disease. *Nature* **461**, 895-897
41. Patterson, C. (2018) WorldAlzheimerReport2018. *Alzheimer's Disease International*
42. Wimo, A., and Prince, M. (2010) WorldAlzheimerReport2010. *Alzheimer's Disease International*
43. Shao, W., Peng, D., and Wang, X. (2017) Genetics of Alzheimer's disease: From pathogenesis to clinical usage. *J Clin Neurosci* **45**, 1-8
44. Ziegler-Graham, K., Brookmeyer, R., Johnson, E., and Arrighi, H. M. (2008) Worldwide variation in the doubling time of Alzheimer's disease incidence rates. *Alzheimers Dement* **4**, 316-323
45. Bertram, L., and Tanzi, R. E. (2012) The genetics of Alzheimer's disease. *Prog Mol Biol Transl Sci* **107**, 79-100
46. De Strooper, B., Saftig, P., Craessaerts, K., Vanderstichele, H., Guhde, G., Annaert, W., Von Figura, K., and Van Leuven, F. (1998) Deficiency of presenilin-1 inhibits the normal cleavage of amyloid precursor protein. *Nature* **391**, 387-390
47. Plant, L. D., Boyle, J. P., Smith, I. F., Peers, C., and Pearson, H. A. (2003) The production of amyloid beta peptide is a critical requirement for the viability of central neurons. *Journal of Neuroscience* **23**, 5531-5535
48. Puzzo, D., Privitera, L., Leznik, E., Fa, M., Staniszewski, A., Palmeri, A., and Arancio, O. (2008) Picomolar amyloid-beta positively modulates synaptic plasticity and memory in hippocampus. *J Neurosci* **28**, 14537-14545
49. Beyreuther, K., Bush, A. I., Dyrks, T., Hilbich, C., Konig, G., Monning, U., Multhaup, G., Prior, R., Rumble, B., Schubert, W., Small, D. H., Weidemann, A., and Masters, C. L. (1991) Mechanisms of Amyloid Deposition in Alzheimers-Disease. *Annals of the New York Academy of Sciences* **640**, 129-139

50. Hardy, J. A., and Higgins, G. A. (1992) Alzheimer's disease: the amyloid cascade hypothesis. *Science* **256**, 184-185
51. Gulisano, W., Maugeri, D., Baltrons, M. A., Fa, M., Amato, A., Palmeri, A., D'Adamio, L., Grassi, C., Devanand, D. P., Honig, L. S., Puzzo, D., and Arancio, O. (2018) Role of Amyloid-beta and Tau Proteins in Alzheimer's Disease: Confuting the Amyloid Cascade. *J Alzheimers Dis* **64**, S611-S631
52. Bloom, G. S. (2014) Amyloid-beta and tau: the trigger and bullet in Alzheimer disease pathogenesis. *JAMA Neurol* **71**, 505-508
53. Tomiyama, T., Nagata, T., Shimada, H., Teraoka, R., Fukushima, A., Kanemitsu, H., Takuma, H., Kuwano, R., Imagawa, M., Ataka, S., Wada, Y., Yoshioka, E., Nishizaki, T., Watanabe, Y., and Mori, H. (2008) A new amyloid beta variant favoring oligomerization in Alzheimer's-type dementia. *Ann Neurol* **63**, 377-387
54. Spires-Jones, T. L., and Hyman, B. T. (2014) The intersection of amyloid beta and tau at synapses in Alzheimer's disease. *Neuron* **82**, 756-771
55. De Strooper, B., and Karran, E. (2016) The Cellular Phase of Alzheimer's Disease. *Cell* **164**, 603-615
56. Julien, C., Tomberlin, C., Roberts, C. M., Akram, A., Stein, G. H., Silverman, M. A., and Link, C. D. (2018) In vivo induction of membrane damage by beta-amyloid peptide oligomers. *Acta Neuropathol Commun* **6**, 131
57. Ruiz-Riquelme, A., Lau, H. H. C., Stuart, E., Goczi, A. N., Wang, Z., Schmitt-Ulms, G., and Watts, J. C. (2018) Prion-like propagation of beta-amyloid aggregates in the absence of APP overexpression. *Acta Neuropathol Commun* **6**, 26
58. Jucker, M., and Walker, L. C. (2018) Propagation and spread of pathogenic protein assemblies in neurodegenerative diseases. *Nat Neurosci* **21**, 1341-1349
59. (2020) 2020 Alzheimer's disease facts and figures. *Alzheimers & Dementia*
60. Menzies, F. M., Fleming, A., and Rubinsztein, D. C. (2015) Compromised autophagy and neurodegenerative diseases. *Nat Rev Neurosci* **16**, 345-357
61. Calamini, B., Silva, M. C., Madoux, F., Hutt, D. M., Khanna, S., Chalfant, M. A., Saldanha, S. A., Hodder, P., Tait, B. D., Garza, D., Balch, W. E., and Morimoto, R. I. (2011) Small-molecule proteostasis regulators for protein conformational diseases. *Nat Chem Biol* **8**, 185-196
62. Treweek, T. M., Meehan, S., Ecroyd, H., and Carver, J. A. (2015) Small heat-shock proteins: important players in regulating cellular proteostasis. *Cell Mol Life Sci* **72**, 429-451
63. Carra, S., Alberti, S., Benesch, J. L. P., Boelens, W., Buchner, J., Carver, J. A., Cecconi, C., Ecroyd, H., Gusev, N., Hightower, L. E., Klevit, R. E., Lee, H. O., Liberek, K., Lockwood, B., Poletti, A., Timmerman, V., Toth, M. E., Vierling, E., Wu, T., and Tanguay, R. M. (2019) Small heat shock proteins: multifaceted proteins with important implications for life. *Cell Stress Chaperones* **24**, 295-308
64. Vos, M. J., Carra, S., Kanon, B., Bosveld, F., Klauke, K., Sibon, O. C., and Kampinga, H. H. (2016) Specific protein homeostatic functions of small heat-shock proteins increase lifespan. *Aging Cell* **15**, 217-226
65. Kriehuber, T., Rattei, T., Weinmaier, T., Bepperling, A., Haslbeck, M., and Buchner, J. (2010) Independent evolution of the core domain and its flanking sequences in small heat shock proteins. *FASEB J* **24**, 3633-3642
66. Waters, E. R. (2013) The evolution, function, structure, and expression of the plant sHSPs. *J Exp Bot* **64**, 391-403
67. Hochberg, G. K. A., Shepherd, D. A., Marklund, E. G., Santhanagoplan, I., Degiacomi, M. T., Laganowsky, A., Allison, T. M., Basha, E., Marty, M. T., Galpin, M. R., Struwe, W. B., Baldwin, A. J., Vierling, E., and Benesch, J. L. P. (2018)

Structural principles that enable oligomeric small heat-shock protein paralogs to evolve distinct functions. *Science* **359**, 930-934
68. Mymrikov, E. V., Seit-Nebi, A. S., and Gusev, N. B. (2011) Large potentials of small heat shock proteins. *Physiol Rev* **91**, 1123-1159
69. Kokke, B. P. A., Leroux, M. R., Candido, E. P. M., Boelens, W. C., and de Jong, W. W. (1998) Caenorhabditis elegans small heat-shock proteins Hsp12.2 and Hsp12.3 form tetramers and have no chaperone-like activity. *Febs Letters* **433**, 228-232
70. Fu, X. (2014) Chaperone function and mechanism of small heat-shock proteins. *Acta Biochim Biophys Sin (Shanghai)* **46**, 347-356
71. Leroux, M. R., Ma, B. J., Batelier, G., Melki, R., and Candido, E. P. (1997) Unique structural features of a novel class of small heat shock proteins. *J Biol Chem* **272**, 12847-12853
72. van de Klundert, F. A. J. M., Smulders, R. H. P. H., Gijsen, M. L. J., Lindner, R. A., Jaenicke, R., Carver, J. A., and De Jong, W. W. (1998) The mammalian small heat-shock protein Hsp20 forms dimers and is a poor chaperone. *European Journal of Biochemistry* **258**, 1014-1021
73. Haslbeck, M., Weinkauf, S., and Buchner, J. (2019) Small heat shock proteins: Simplicity meets complexity. *J Biol Chem* **294**, 2121-2132
74. Hanazono, Y., Takeda, K., Oka, T., Abe, T., Tomonari, T., Akiyama, N., Aikawa, Y., Yohda, M., and Miki, K. (2013) Nonequivalence observed for the 16-meric structure of a small heat shock protein, SpHsp16.0, from Schizosaccharomyces pombe. *Structure* **21**, 220-228
75. Shi, J., Koteiche, H. A., McDonald, E. T., Fox, T. L., Stewart, P. L., and McHaourab, H. S. (2013) Cryoelectron microscopy analysis of small heat shock protein 16.5 (Hsp16.5) complexes with T4 lysozyme reveals the structural basis of multimode binding. *J Biol Chem* **288**, 4819-4830
76. Kim, K. K., Kim, R., and Kim, S. H. (1998) Crystal structure of a small heat-shock protein. *Nature* **394**, 595-599
77. van Montfort, R. L., Basha, E., Friedrich, K. L., Slingsby, C., and Vierling, E. (2001) Crystal structure and assembly of a eukaryotic small heat shock protein. *Nat Struct Biol* **8**, 1025-1030
78. Jehle, S., van Rossum, B., Stout, J. R., Noguchi, S. M., Falber, K., Rehbein, K., Oschkinat, H., Klevit, R. E., and Rajagopal, P. (2009) alphaB-crystallin: a hybrid solid-state/solution-state NMR investigation reveals structural aspects of the heterogeneous oligomer. *J Mol Biol* **385**, 1481-1497
79. Bagneris, C., Bateman, O. A., Naylor, C. E., Cronin, N., Boelens, W. C., Keep, N. H., and Slingsby, C. (2009) Crystal structures of alpha-crystallin domain dimers of alphaB-crystallin and Hsp20. *J Mol Biol* **392**, 1242-1252
80. Stengel, F., Baldwin, A. J., Painter, A. J., Jaya, N., Basha, E., Kay, L. E., Vierling, E., Robinson, C. V., and Benesch, J. L. (2010) Quaternary dynamics and plasticity underlie small heat shock protein chaperone function. *Proc Natl Acad Sci U S A* **107**, 2007-2012
81. Stromer, T., Fischer, E., Richter, K., Haslbeck, M., and Buchner, J. (2004) Analysis of the regulation of the molecular chaperone Hsp26 by temperature-induced dissociation: the N-terminal domail is important for oligomer assembly and the binding of unfolding proteins. *J Biol Chem* **279**, 11222-11228
82. Fleckenstein, T., Kastenmuller, A., Stein, M. L., Peters, C., Daake, M., Krause, M., Weinfurtner, D., Haslbeck, M., Weinkauf, S., Groll, M., and Buchner, J. (2015) The Chaperone Activity of the Developmental Small Heat Shock Protein Sip1 Is Regulated by pH-Dependent Conformational Changes. *Mol Cell* **58**, 1067-1078

83. Hussein, R. M., Benjamin, I. J., and Kampinga, H. H. (2015) Rescue of alphaB Crystallin (HSPB5) Mutants Associated Protein Aggregation by Co-Expression of HSPB5 Partners. *PLoS One* **10**, e0126761
84. Morelli, F. F., Verbeek, D. S., Bertacchini, J., Vinet, J., Mediani, L., Marmiroli, S., Cenacchi, G., Nasi, M., De Biasi, S., Brunsting, J. F., Lammerding, J., Pegoraro, E., Angelini, C., Tupler, R., Alberti, S., and Carra, S. (2017) Aberrant Compartment Formation by HSPB2 Mislocalizes Lamin A and Compromises Nuclear Integrity and Function. *Cell Rep* **20**, 2100-2115
85. Aquilina, J. A., Shrestha, S., Morris, A. M., and Ecroyd, H. (2013) Structural and functional aspects of hetero-oligomers formed by the small heat shock proteins alphaB-crystallin and HSP27. *J Biol Chem* **288**, 13602-13609
86. Jakob, U., Gaestel, M., Engel, K., and Buchner, J. (1993) Small heat shock proteins are molecular chaperones. *J Biol Chem* **268**, 1517-1520
87. Lee, G. J., Roseman, A. M., Saibil, H. R., and Vierling, E. (1997) A small heat shock protein stably binds heat-denatured model substrates and can maintain a substrate in a folding-competent state. *Embo Journal* **16**, 659-671
88. Ehrnsperger, M., Graber, S., Gaestel, M., and Buchner, J. (1997) Binding of non-native protein to Hsp25 during heat shock creates a reservoir of folding intermediates for reactivation. *Embo Journal* **16**, 221-229
89. Veinger, L., Diamant, S., Buchner, J., and Goloubinoff, P. (1998) The small heat-shock protein IbpB from Escherichia coli stabilizes stress-denatured proteins for subsequent refolding by a multichaperone network. *J Biol Chem* **273**, 11032-11037
90. Friedrich, K. L., Giese, K. C., Buan, N. R., and Vierling, E. (2004) Interactions between small heat shock protein subunits and substrate in small heat shock protein-substrate complexes. *J Biol Chem* **279**, 1080-1089
91. Mymrikov, E. V., Daake, M., Richter, B., Haslbeck, M., and Buchner, J. (2017) The Chaperone Activity and Substrate Spectrum of Human Small Heat Shock Proteins. *J Biol Chem* **292**, 672-684
92. Mainz, A., Peschek, J., Stavropoulou, M., Back, K. C., Bardiaux, B., Asami, S., Prade, E., Peters, C., Weinkauf, S., Buchner, J., and Reif, B. (2015) The chaperone alphaB-crystallin uses different interfaces to capture an amorphous and an amyloid client. *Nat Struct Mol Biol* **22**, 898-905
93. Sakono, M., Utsumi, A., Zako, T., Abe, T., Yohda, M., and Maeda, M. (2013) Formation of non-toxic Abeta fibrils by small heat shock protein under heat-stress conditions. *Biochem Biophys Res Commun* **430**, 1259-1264
94. Shammas, S. L., Waudby, C. A., Wang, S., Buell, A. K., Knowles, T. P., Ecroyd, H., Welland, M. E., Carver, J. A., Dobson, C. M., and Meehan, S. (2011) Binding of the molecular chaperone alphaB-crystallin to Abeta amyloid fibrils inhibits fibril elongation. *Biophys J* **101**, 1681-1689
95. Cox, D., and Ecroyd, H. (2017) The small heat shock proteins alphaB-crystallin (HSPB5) and Hsp27 (HSPB1) inhibit the intracellular aggregation of alpha-synuclein. *Cell Stress Chaperones* **22**, 589-600
96. Cox, D., Whiten, D. R., Brown, J. W. P., Horrocks, M. H., San Gil, R., Dobson, C. M., Klenerman, D., van Oijen, A. M., and Ecroyd, H. (2018) The small heat shock protein Hsp27 binds alpha-synuclein fibrils, preventing elongation and cytotoxicity. *J Biol Chem* **293**, 4486-4497
97. Freilich, R., Betegon, M., Tse, E., Mok, S. A., Julien, O., Agard, D. A., Southworth, D. R., Takeuchi, K., and Gestwicki, J. E. (2018) Competing protein-protein interactions regulate binding of Hsp27 to its client protein tau. *Nat Commun* **9**, 4563

98. Oliveira, A. O., Osmand, A., Outeiro, T. F., Muchowski, P. J., and Finkbeiner, S. (2016) alphaB-Crystallin overexpression in astrocytes modulates the phenotype of the BACHD mouse model of Huntington's disease. *Hum Mol Genet* **25**, 1677-1689
99. Mogk, A., Schlieker, C., Friedrich, K. L., Schonfeld, H. J., Vierling, E., and Bukau, B. (2003) Refolding of substrates bound to small Hsps relies on a disaggregation reaction mediated most efficiently by ClpB/DnaK. *J Biol Chem* **278**, 31033-31042
100. Cashikar, A. G., Duennwald, M., and Lindquist, S. L. (2005) A chaperone pathway in protein disaggregation. Hsp26 alters the nature of protein aggregates to facilitate reactivation by Hsp104. *J Biol Chem* **280**, 23869-23875
101. Fontaine, J. M., Sun, X., Benndorf, R., and Welsh, M. J. (2005) Interactions of HSP22 (HSPB8) with HSP20, alphaB-crystallin, and HSPB3. *Biochem Biophys Res Commun* **337**, 1006-1011
102. Arrigo, A. P. (2013) Human small heat shock proteins: protein interactomes of homo- and hetero-oligomeric complexes: an update. *FEBS Lett* **587**, 1959-1969
103. Rauch, J. N., Tse, E., Freilich, R., Mok, S. A., Makley, L. N., Southworth, D. R., and Gestwicki, J. E. (2017) BAG3 Is a Modular, Scaffolding Protein that physically Links Heat Shock Protein 70 (Hsp70) to the Small Heat Shock Proteins. *J Mol Biol* **429**, 128-141
104. Guilbert, S. M., Lambert, H., Rodrigue, M. A., Fuchs, M., Landry, J., and Lavoie, J. N. (2018) HSPB8 and BAG3 cooperate to promote spatial sequestration of ubiquitinated proteins and coordinate the cellular adaptive response to proteasome insufficiency. *FASEB J*, fj201700558RR
105. Haidar, M., Asselbergh, B., Adriaenssens, E., De Winter, V., Timmermans, J. P., Auer-Grumbach, M., Juneja, M., and Timmerman, V. (2019) Neuropathy-causing mutations in HSPB1 impair autophagy by disturbing the formation of SQSTM1/p62 bodies. *Autophagy*, 1-18
106. Miller, S. B., Ho, C. T., Winkler, J., Khokhrina, M., Neuner, A., Mohamed, M. Y., Guilbride, D. L., Richter, K., Lisby, M., Schiebel, E., Mogk, A., and Bukau, B. (2015) Compartment-specific aggregases direct distinct nuclear and cytoplasmic aggregate deposition. *EMBO J* **34**, 778-797
107. Zhang, Y. W., Zhu, J. H., Wang, Z. Q., Wu, Y., Meng, X., Zheng, X., and Javid, B. (2019) HspX promotes the polar localization of mycobacterial protein aggregates. *Sci Rep* **9**, 14571
108. Specht, S., Miller, S. B., Mogk, A., and Bukau, B. (2011) Hsp42 is required for sequestration of protein aggregates into deposition sites in Saccharomyces cerevisiae. *J Cell Biol* **195**, 617-629
109. Hantke, I., Schafer, H., Janczikowski, A., and Turgay, K. (2019) YocM a small heat shock protein can protect Bacillus subtilis cells during salt stress. *Mol Microbiol* **111**, 423-440
110. Ungelenk, S., Moayed, F., Ho, C. T., Grousl, T., Scharf, A., Mashaghi, A., Tans, S., Mayer, M. P., Mogk, A., and Bukau, B. (2016) Small heat shock proteins sequester misfolding proteins in near-native conformation for cellular protection and efficient refolding. *Nat Commun* **7**, 13673
111. Ratajczak, E., Zietkiewicz, S., and Liberek, K. (2009) Distinct activities of Escherichia coli small heat shock proteins IbpA and IbpB promote efficient protein disaggregation. *J Mol Biol* **386**, 178-189
112. Zwirowski, S., Klosowska, A., Obuchowski, I., Nillegoda, N. B., Pirog, A., Zietkiewicz, S., Bukau, B., Mogk, A., and Liberek, K. (2017) Hsp70 displaces small heat shock proteins from aggregates to initiate protein refolding. *EMBO J* **36**, 783-796

113. Ho, C. T., Grousl, T., Shatz, O., Jawed, A., Ruger-Herreros, C., Semmelink, M., Zahn, R., Richter, K., Bukau, B., and Mogk, A. (2019) Cellular sequestrases maintain basal Hsp70 capacity ensuring balanced proteostasis. *Nat Commun* **10**, 4851
114. David, D. C., Ollikainen, N., Trinidad, J. C., Cary, M. P., Burlingame, A. L., and Kenyon, C. (2010) Widespread protein aggregation as an inherent part of aging in C. elegans. *PLoS Biol* **8**, e1000450
115. Labbadia, J., and Morimoto, R. I. (2015) Repression of the Heat Shock Response Is a Programmed Event at the Onset of Reproduction. *Mol Cell* **59**, 639-650
116. Escusa-Toret, S., Vonk, W. I., and Frydman, J. (2013) Spatial sequestration of misfolded proteins by a dynamic chaperone pathway enhances cellular fitness during stress. *Nat Cell Biol* **15**, 1231-1243
117. Miller, S. B., Mogk, A., and Bukau, B. (2015) Spatially organized aggregation of misfolded proteins as cellular stress defense strategy. *J Mol Biol* **427**, 1564-1574
118. Wallace, E. W., Kear-Scott, J. L., Pilipenko, E. V., Schwartz, M. H., Laskowski, P. R., Rojek, A. E., Katanski, C. D., Riback, J. A., Dion, M. F., Franks, A. M., Airoldi, E. M., Pan, T., Budnik, B. A., and Drummond, D. A. (2015) Reversible, Specific, Active Aggregates of Endogenous Proteins Assemble upon Heat Stress. *Cell* **162**, 1286-1298
119. Saad, S., Cereghetti, G., Feng, Y., Picotti, P., Peter, M., and Dechant, R. (2017) Reversible protein aggregation is a protective mechanism to ensure cell cycle restart after stress. *Nat Cell Biol* **19**, 1202-1213
120. Walther, D. M., Kasturi, P., Zheng, M., Pinkert, S., Vecchi, G., Ciryam, P., Morimoto, R. I., Dobson, C. M., Vendruscolo, M., Mann, M., and Hartl, F. U. (2015) Widespread Proteome Remodeling and Aggregation in Aging C. elegans. *Cell* **161**, 919-932
121. Douglas, P. M., Treusch, S., Ren, H. Y., Halfmann, R., Duennwald, M. L., Lindquist, S., and Cyr, D. M. (2008) Chaperone-dependent amyloid assembly protects cells from prion toxicity. *Proc Natl Acad Sci U S A* **105**, 7206-7211
122. Arrasate, M., Mitra, S., Schweitzer, E. S., Segal, M. R., and Finkbeiner, S. (2004) Inclusion body formation reduces levels of mutant huntingtin and the risk of neuronal death. *Nature* **431**, 805-810
123. Mannini, B., Cascella, R., Zampagni, M., van Waarde-Verhagen, M., Meehan, S., Roodveldt, C., Campioni, S., Boninsegna, M., Penco, A., Relini, A., Kampinga, H. H., Dobson, C. M., Wilson, M. R., Cecchi, C., and Chiti, F. (2012) Molecular mechanisms used by chaperones to reduce the toxicity of aberrant protein oligomers. *Proc Natl Acad Sci U S A* **109**, 12479-12484
124. Ojha, J., Masilamoni, G., Dunlap, D., Udoff, R. A., and Cashikar, A. G. (2011) Sequestration of toxic oligomers by HspB1 as a cytoprotective mechanism. *Mol Cell Biol* **31**, 3146-3157
125. Binger, K. J., Ecroyd, H., Yang, S., Carver, J. A., Howlett, G. J., and Griffin, M. D. (2013) Avoiding the oligomeric state: alphaB-crystallin inhibits fragmentation and induces dissociation of apolipoprotein C-II amyloid fibrils. *FASEB J* **27**, 1214-1222
126. Brenner, S. (1974) The genetics of Caenorhabditis elegans. *Genetics* **77**, 71-94
127. Markaki, M., and Tavernarakis, N. (2010) Modeling human diseases in Caenorhabditis elegans. *Biotechnol J* **5**, 1261-1276
128. Consortium, C. e. S. (1998) Genome sequence of the nematode C. elegans: a platform for investigating biology. *Science* **282**, 2012-2018
129. Lai, C. H., Chou, C. Y., Ch'ang, L. Y., Liu, C. S., and Lin, W. (2000) Identification of novel human genes evolutionarily conserved in Caenorhabditis elegans by comparative proteomics. *Genome Res* **10**, 703-713
130. Byerly, L., Cassada, R. C., and Russell, R. L. (1976) The life cycle of the nematode Caenorhabditis elegans. *Developmental Biology* **51**, 23-33

131. Sulston, J. E., and Horvitz, H. R. (1977) Post-embryonic cell lineages of the nematode, Caenorhabditis elegans. *Dev Biol* **56**, 110-156
132. Altun, Z. F. H., D. H. (2020) Handbook of C. elegans Anatomy. In WormAtlas.
133. Hariharan, I. K., and Haber, D. A. (2003) Yeast, flies, worms, and fish in the study of human disease. *N Engl J Med* **348**, 2457-2463
134. United Nations Department of Economic and Social Affairs, P. D. (2015) World Population Ageing
2015. United Nations
135. Naidoo, N., Ferber, M., Master, M., Zhu, Y., and Pack, A. I. (2008) Aging impairs the unfolded protein response to sleep deprivation and leads to proapoptotic signaling. *J Neurosci* **28**, 6539-6548
136. Niccoli, T., and Partridge, L. (2012) Ageing as a risk factor for disease. *Curr Biol* **22**, R741-752
137. Friedman, D. B., and Johnson, T. E. (1988) A mutation in the age-1 gene in Caenorhabditis elegans lengthens life and reduces hermaphrodite fertility. *Genetics* **118**, 75-86
138. Kenyon, C., Chang, J., Gensch, E., Rudner, A., and Tabtiang, R. (1993) A C-Elegans Mutant That Lives Twice as Long as Wild-Type. *Nature* **366**, 461-464
139. Dorman, J. B., Albinder, B., Shroyer, T., and Kenyon, C. (1995) The age-1 and daf-2 genes function in a common pathway to control the lifespan of Caenorhabditis elegans. *Genetics* **141**, 1399-1406
140. Ogg, S., Paradis, S., Gottlieb, S., Patterson, G. I., Lee, L., Tissenbaum, H. A., and Ruvkun, G. (1997) The Fork head transcription factor DAF-16 transduces insulin-like metabolic and longevity signals in C. elegans. *Nature* **389**, 994-999
141. Willcox, B. J., Donlon, T. A., He, Q., Chen, R., Grove, J. S., Yano, K., Masaki, K. H., Willcox, D. C., Rodriguez, B., and Curb, J. D. (2008) FOXO3A genotype is strongly associated with human longevity. *Proc Natl Acad Sci U S A* **105**, 13987-13992
142. Greer, E. L., and Brunet, A. (2008) Signaling networks in aging. *J Cell Sci* **121**, 407-412
143. Lithgow, G. J., White, T. M., Melov, S., and Johnson, T. E. (1995) Thermotolerance and extended life-span conferred by single-gene mutations and induced by thermal stress. *Proc Natl Acad Sci U S A* **92**, 7540-7544
144. Morley, J. F., and Morimoto, R. I. (2004) Regulation of longevity in Caenorhabditis elegans by heat shock factor and molecular chaperones. *Mol Biol Cell* **15**, 657-664
145. Prahlad, V., Cornelius, T., and Morimoto, R. I. (2008) Regulation of the cellular heat shock response in Caenorhabditis elegans by thermosensory neurons. *Science* **320**, 811-814
146. Walker, G. A., and Lithgow, G. J. (2003) Lifespan extension in C-elegans by a molecular chaperone dependent upon insulin-like signals. *Aging Cell* **2**, 131-139
147. Aevermann, B. D., and Waters, E. R. (2008) A comparative genomic analysis of the small heat shock proteins in Caenorhabditis elegans and briggsae. *Genetica* **133**, 307-319
148. Kraemer, B. C., Zhang, B., Leverenz, J. B., Thomas, J. H., Trojanowski, J. Q., and Schellenberg, G. D. (2003) Neurodegeneration and defective neurotransmission in a Caenorhabditis elegans model of tauopathy. *Proc Natl Acad Sci U S A* **100**, 9980-9985
149. Lakso, M., Vartiainen, S., Moilanen, A. M., Sirvio, J., Thomas, J. H., Nass, R., Blakely, R. D., and Wong, G. (2003) Dopaminergic neuronal loss and motor deficits in Caenorhabditis elegans overexpressing human alpha-synuclein. *J Neurochem* **86**, 165-172

150. Brignull, H. R., Moore, F. E., Tang, S. J., and Morimoto, R. I. (2006) Polyglutamine proteins at the pathogenic threshold display neuron-specific aggregation in a pan-neuronal Caenorhabditis elegans model. *J Neurosci* **26**, 7597-7606
151. Link, C. D. (1995) Expression of human beta-amyloid peptide in transgenic Caenorhabditis elegans. *Proc Natl Acad Sci U S A* **92**, 9368-9372
152. Link, C. D., Johnson, C. J., Fonte, V., Paupard, M. C., Hall, D. H., Styren, S., Mathis, C. A., and Klunk, W. E. (2001) Visualization of fibrillar amyloid deposits in living, transgenic Caenorhabditis elegans animals using the sensitive amyloid dye, X-34. *Neurobiology of Aging* **22**, 217-226
153. McColl, G., Roberts, B. R., Gunn, A. P., Perez, K. A., Tew, D. J., Masters, C. L., Barnham, K. J., Cherny, R. A., and Bush, A. I. (2009) The Caenorhabditis elegans A beta 1-42 model of Alzheimer disease predominantly expresses A beta 3-42. *J Biol Chem* **284**, 22697-22702
154. McColl, G., Roberts, B. R., Pukala, T. L., Kenche, V. B., Roberts, C. M., Link, C. D., Ryan, T. M., Masters, C. L., Barnham, K. J., Bush, A. I., and Cherny, R. A. (2012) Utility of an improved model of amyloid-beta (Abeta(1)(-)(4)(2)) toxicity in Caenorhabditis elegans for drug screening for Alzheimer's disease. *Mol Neurodegener* **7**, 57
155. Dosanjh, L. E., Brown, M. K., Rao, G., Link, C. D., and Luo, Y. (2010) Behavioral phenotyping of a transgenic Caenorhabditis elegans expressing neuronal amyloid-beta. *J Alzheimers Dis* **19**, 681-690
156. Ochiishi, T., Doi, M., Yamasaki, K., Hirose, K., Kitamura, A., Urabe, T., Hattori, N., Kinjo, M., Ebihara, T., and Shimura, H. (2016) Development of new fusion proteins for visualizing amyloid-beta oligomers in vivo. *Sci Rep* **6**, 22712
157. Cotella, D., Hernandez-Enriquez, B., Wu, X., Li, R., Pan, Z., Leveille, J., Link, C. D., Oddo, S., and Sesti, F. (2012) Toxic role of K+ channel oxidation in mammalian brain. *J Neurosci* **32**, 4133-4144
158. Sinnige, T., Ciryam, P., Casford, S., Dobson, C. M., de Bono, M., and Vendruscolo, M. (2019) Expression of the amyloid-beta peptide in a single pair of C. elegans sensory neurons modulates the associated behavioural response. *PLoS One* **14**, e0217746
159. Treusch, S., Hamamichi, S., Goodman, J. L., Matlack, K. E., Chung, C. Y., Baru, V., Shulman, J. M., Parrado, A., Bevis, B. J., Valastyan, J. S., Han, H., Lindhagen-Persson, M., Reiman, E. M., Evans, D. A., Bennett, D. A., Olofsson, A., DeJager, P. L., Tanzi, R. E., Caldwell, K. A., Caldwell, G. A., and Lindquist, S. (2011) Functional links between Abeta toxicity, endocytic trafficking, and Alzheimer's disease risk factors in yeast. *Science* **334**, 1241-1245
160. Fonte, V., Kapulkin, W. J., Taft, A., Fluet, A., Friedman, D., and Link, C. D. (2002) Interaction of intracellular beta amyloid peptide with chaperone proteins. *Proc Natl Acad Sci U S A* **99**, 9439-9444
161. Fonte, V., Kipp, D. R., Yerg, J., 3rd, Merin, D., Forrestal, M., Wagner, E., Roberts, C. M., and Link, C. D. (2008) Suppression of in vivo beta-amyloid peptide toxicity by overexpression of the HSP-16.2 small chaperone protein. *J Biol Chem* **283**, 784-791
162. Altun, Z. F., Hall, D. H., and Herndon, L. A. (2006) WormAtas Hermaphrodite Handbook - Introduction. *WormAtlas*
163. Mogk, A., Ruger-Herreros, C., and Bukau, B. (2019) Cellular Functions and Mechanisms of Action of Small Heat Shock Proteins. *Annu Rev Microbiol* **73**, 89-110
164. Ezemaduka, A. N., Yu, J., Shi, X., Zhang, K., Yin, C. C., Fu, X., and Chang, Z. (2014) A small heat shock protein enables Escherichia coli to grow at a lethal temperature of

50 degrees C conceivably by maintaining cell envelope integrity. *J Bacteriol* **196**, 2004-2011
165. Candido, E. P. (2002) The small heat shock proteins of the nematode Caenorhabditis elegans: structure, regulation and biology. *Prog Mol Subcell Biol* **28**, 61-78
166. Zhang, K., Ezemaduka, A. N., Wang, Z., Hu, H., Shi, X., Liu, C., Lu, X., Fu, X., Chang, Z., and Yin, C. C. (2015) A novel mechanism for small heat shock proteins to function as molecular chaperones. *Sci Rep* **5**, 8811
167. Ding, L., and Candido, E. P. (2000) HSP25, a small heat shock protein associated with dense bodies and M-lines of body wall muscle in Caenorhabditis elegans. *J Biol Chem* **275**, 9510-9517
168. Krause, M. (2013) *Structural and functional characterization of small heat shock proteins of the nematode Caenorhabditis elegans.* Dr. rer. nat, Technische Universität München
169. Horwitz, J. (1992) Alpha-Crystallin Can Function as a Molecular Chaperone. *Proceedings of the National Academy of Sciences of the United States of America* **89**, 10449-10453
170. Grousl, T., Ungelenk, S., Miller, S., Ho, C. T., Khokhrina, M., Mayer, M. P., Bukau, B., and Mogk, A. (2018) A prion-like domain in Hsp42 drives chaperone-facilitated aggregation of misfolded proteins. *J Cell Biol*
171. Lancaster, A. K., Nutter-Upham, A., Lindquist, S., and King, O. D. (2014) PLAAC: a web and command-line application to identify proteins with prion-like amino acid composition. *Bioinformatics* **30**, 2501-2502
172. Sarov, M., Murray, J. I., Schanze, K., Pozniakovski, A., Niu, W., Angermann, K., Hasse, S., Rupprecht, M., Vinis, E., Tinney, M., Preston, E., Zinke, A., Enst, S., Teichgraber, T., Janette, J., Reis, K., Janosch, S., Schloissnig, S., Ejsmont, R. K., Slightam, C., Xu, X., Kim, S. K., Reinke, V., Stewart, A. F., Snyder, M., Waterston, R. H., and Hyman, A. A. (2012) A genome-scale resource for in vivo tag-based protein function exploration in C. elegans. *Cell* **150**, 855-866
173. Husken, K., Wiesenfahrt, T., Abraham, C., Windoffer, R., Bossinger, O., and Leube, R. E. (2008) Maintenance of the intestinal tube in Caenorhabditis elegans: the role of the intermediate filament protein IFC-2. *Differentiation* **76**, 881-896
174. Kim, W. (2013) Ortholist. Greenwald Laboratory
175. Feleciano, D. R., Juenemann, K., Iburg, M., Bras, I. C., Holmberg, C. I., and Kirstein, J. (2019) Crosstalk Between Chaperone-Mediated Protein Disaggregation and Proteolytic Pathways in Aging and Disease. *Front Aging Neurosci* **11**, 9
176. Ezemaduka, A. N., Wang, Y., and Li, X. (2017) Expression of CeHSP17 Protein in Response to Heat Shock and Heavy Metal Ions. *J Nematol* **49**, 334-340
177. Nelson, F. K., and Riddle, D. L. (1984) Functional-Study of the Caenorhabditis-Elegans Secretory-Excretory System Using Laser Microsurgery. *Journal of Experimental Zoology* **231**, 45-56
178. Mohri-Shiomi, A., and Garsin, D. A. (2008) Insulin signaling and the heat shock response modulate protein homeostasis in the Caenorhabditis elegans intestine during infection. *J Biol Chem* **283**, 194-201
179. Moronetti Mazzeo, L. E., Dersh, D., Boccitto, M., Kalb, R. G., and Lamitina, T. (2012) Stress and aging induce distinct polyQ protein aggregation states. *Proc Natl Acad Sci U S A* **109**, 10587-10592
180. Lechler, M. C., Crawford, E. D., Groh, N., Widmaier, K., Jung, R., Kirstein, J., Trinidad, J. C., Burlingame, A. L., and David, D. C. (2017) Reduced Insulin/IGF-1 Signaling Restores the Dynamic Properties of Key Stress Granule Proteins during Aging. *Cell Rep* **18**, 454-467

181. Grant, B., and Hirsh, D. (1999) Receptor-mediated endocytosis in the Caenorhabditis elegans oocyte. *Molecular Biology of the Cell* **10**, 4311-4326
182. Ewald, C. Y., and Li, C. (2012) Caenorhabditis elegans as a model organism to study APP function. *Exp Brain Res* **217**, 397-411
183. Bindels, D. S., Haarbosch, L., van Weeren, L., Postma, M., Wiese, K. E., Mastop, M., Aumonier, S., Gotthard, G., Royant, A., Hink, M. A., and Gadella, T. W. J. (2016) mScarlet: a bright monomeric red fluorescent protein for cellular imaging. *Nature Methods* **14**, 53-56
184. El Mouridi, S., Lecroisey, C., Tardy, P., Mercier, M., Leclercq-Blondel, A., Zariohi, N., and Boulin, T. (2017) Reliable CRISPR/Cas9 Genome Engineering in Caenorhabditis elegans Using a Single Efficient sgRNA and an Easily Recognizable Phenotype. *G3 (Bethesda)* **7**, 1429-1437
185. Li, D., and Wang, M. (2012) Construction of a bicistronic vector for the co-expression of two genes in Caenorhabditis elegans using a newly identified IRES. *Biotechniques* **52**, 173-176
186. Kaufman, R. J., Murtha, P., and Davies, M. V. (1987) Translational efficiency of polycistronic mRNAs and their utilization to express heterologous genes in mammalian cells. *The EMBO Journal* **6**, 187-193
187. Hassan, W. M., Dostal, V., Huemann, B. N., Yerg, J. E., and Link, C. D. (2015) Identifying Abeta-specific pathogenic mechanisms using a nematode model of Alzheimer's disease. *Neurobiol Aging* **36**, 857-866
188. Link, C. D., Cypser, J. R., Johnson, C. J., and Johnson, T. E. (1999) Direct observation of stress response in Caenorhabditis elegans using a reporter transgene. *Cell Stress & Chaperones* **4**, 235-242
189. Cohen, E., Bieschke, J., Perciavalle, R. M., Kelly, J. W., and Dillin, A. (2006) Opposing activities protect against age-onset proteotoxicity. *Science* **313**, 1604-1610
190. Butterfield, D. A., Castegna, A., Lauderback, C. M., and Drake, J. (2002) Evidence that amyloid beta-peptide-induced lipid peroxidation and its sequelae in Alzheimer's disease brain contribute to neuronal death. *Neurobiology of Aging* **23**, 655-664
191. Kirstein, J., Morito, D., Kakihana, T., Sugihara, M., Minnen, A., Hipp, M. S., Nussbaum-Krammer, C., Kasturi, P., Hartl, F. U., Nagata, K., and Morimoto, R. I. (2015) Proteotoxic stress and ageing triggers the loss of redox homeostasis across cellular compartments. *EMBO J* **34**, 2334-2349
192. Nixon, R. A., Wegiel, J., Kumar, A., Yu, W. H., Peterhoff, C., Cataldo, A., and Cuervo, A. M. (2005) Extensive involvement of autophagy in Alzheimer disease: an immuno-electron microscopy study. *J Neuropathol Exp Neurol* **64**, 113-122
193. Willen, K., Edgar, J. R., Hasegawa, T., Tanaka, N., Futter, C. E., and Gouras, G. K. (2017) Abeta accumulation causes MVB enlargement and is modelled by dominant negative VPS4A. *Mol Neurodegener* **12**, 61
194. Kaminski Schierle, G. S., Bertoncini, C. W., Chan, F. T. S., van der Goot, A. T., Schwedler, S., Skepper, J., Schlachter, S., van Ham, T., Esposito, A., Kumita, J. R., Nollen, E. A. A., Dobson, C. M., and Kaminski, C. F. (2011) A FRET sensor for non-invasive imaging of amyloid formation in vivo. *Chemphyschem* **12**, 673-680
195. White, J. G., Southgate, E., Thomson, J. N., and Brenner, S. (1986) The structure of the nervous system of the nematode Caenorhabditis elegans. *Philos Trans R Soc Lond B Biol Sci* **314**, 1-340
196. Bargmann, C. I., and Avery, L. (1995) Laser killing of cells in Caenorhabditis elegans. *Methods Cell Biol* **48**, 225-250
197. Pedrero-Prieto, C. M., Flores-Cuadrado, A., Saiz-Sanchez, D., Ubeda-Banon, I., Frontinan-Rubio, J., Alcain, F. J., Mateos-Hernandez, L., de la Fuente, J., Duran-

Prado, M., Villar, M., Martinez-Marcos, A., and Peinado, J. R. (2019) Human amyloid-beta enriched extracts: evaluation of in vitro and in vivo internalization and molecular characterization. *Alzheimers Res Ther* **11**, 56
198. Bowen, D. M., Smith, C. B., White, P., and Davison, A. N. (1976) Neurotransmitter-related enzymes and indices of hypoxia in senile dementia and other abiotrophies. *Brain* **99**, 459-496
199. Davies, P., and Maloney, A. J. (1976) Selective loss of central cholinergic neurons in Alzheimer's disease. *Lancet* **2**, 1403
200. Peden, E. M., and Barr, M. M. (2005) The KLP-6 kinesin is required for male mating behaviors and polycystin localization in Caenorhabditis elegans. *Curr Biol* **15**, 394-404
201. Esposito, G., Di Schiavi, E., Bergamasco, C., and Bazzicalupo, P. (2007) Efficient and cell specific knock-down of gene function in targeted C. elegans neurons. *Gene* **395**, 170-176
202. Wei, X., Potter, C. J., Luo, L., and Shen, K. (2012) Controlling gene expression with the Q repressible binary expression system in Caenorhabditis elegans. *Nat Methods* **9**, 391-395
203. Leroux, M. R., Melki, R., Gordon, B., Batelier, G., and Candido, E. P. (1997) Structure-function studies on small heat shock protein oligomeric assembly and interaction with unfolded polypeptides. *J Biol Chem* **272**, 24646-24656
204. Saarikangas, J., and Barral, Y. (2015) Protein aggregates are associated with replicative aging without compromising protein quality control. *Elife* **4**
205. Wang, K., and Spector, A. (2000) alpha-crystallin prevents irreversible protein denaturation and acts cooperatively with other heat-shock proteins to renature the stabilized partially denatured protein in an ATP-dependent manner. *Eur J Biochem* **267**, 4705-4712
206. Haslbeck, M., Miess, A., Stromer, T., Walter, S., and Buchner, J. (2005) Disassembling protein aggregates in the yeast cytosol. The cooperation of Hsp26 with Ssa1 and Hsp104. *J Biol Chem* **280**, 23861-23868
207. Stege, G. J., Renkawek, K., Overkamp, P. S., Verschuure, P., van Rijk, A. F., Reijnen-Aalbers, A., Boelens, W. C., Bosman, G. J., and de Jong, W. W. (1999) The molecular chaperone alphaB-crystallin enhances amyloid beta neurotoxicity. *Biochem Biophys Res Commun* **262**, 152-156
208. Chen, J. Y., Parekh, M., Seliman, H., Bakshinskaya, D., Dai, W., Kwan, K., Chen, K. Y., and Liu, A. Y. C. (2018) Heat shock promotes inclusion body formation of mutant huntingtin (mHtt) and alleviates mHtt-induced transcription factor dysfunction. *J Biol Chem* **293**, 15581-15593
209. Haslbeck, M., Walke, S., Stromer, T., Ehrnsperger, M., White, H. E., Chen, S., Saibil, H. R., and Buchner, J. (1999) Hsp26: a temperature-regulated chaperone. *EMBO J* **18**, 6744-6751
210. Haslbeck, M., Braun, N., Stromer, T., Richter, B., Model, N., Weinkauf, S., and Buchner, J. (2004) Hsp42 is the general small heat shock protein in the cytosol of Saccharomyces cerevisiae. *EMBO J* **23**, 638-649
211. Linder, B., Jin, Z., Freedman, J. H., and Rubin, C. S. (1996) Molecular characterization of a novel, developmentally regulated small embryonic chaperone from Caenorhabditis elegans. *J Biol Chem* **271**, 30158-30166
212. Shirayama, M., Soto, M. C., Ishidate, T., Kim, S., Nakamura, K., Bei, Y., van den Heuvel, S., and Mello, C. C. (2006) The Conserved Kinases CDK-1, GSK-3, KIN-19, and MBK-2 Promote OMA-1 Destruction to Regulate the Oocyte-to-Embryo Transition in C. elegans. *Curr Biol* **16**, 47-55

213. Walston, T., Tuskey, C., Edgar, L., Hawkins, N., Ellis, G., Bowerman, B., Wood, W., and Hardin, J. (2004) Multiple Wnt signaling pathways converge to orient the mitotic spindle in early C. elegans embryos. *Dev Cell* **7**, 831-841
214. Banerjee, D., Chen, X., Lin, S. Y., and Slack, F. J. (2010) kin-19/casein kinase Ialpha has dual functions in regulating asymmetric division and terminal differentiation in C. elegans epidermal stem cells. *Cell Cycle* **9**, 4748-4765
215. Altun, Z. F., Hall, D. H., and Herndon, L. A. (2005) WormAtlas Hermaphrodite Handbook - Nervous System - General Description. *WormAtlas*
216. Pinotsi, D., Michel, C. H., Buell, A. K., Laine, R. F., Mahou, P., Dobson, C. M., Kaminski, C. F., and Kaminski Schierle, G. S. (2016) Nanoscopic insights into seeding mechanisms and toxicity of alpha-synuclein species in neurons. *Proc Natl Acad Sci U S A* **113**, 3815-3819
217. Young, L. J., Kaminski Schierle, G. S., and Kaminski, C. F. (2017) Imaging Abeta(1-42) fibril elongation reveals strongly polarised growth and growth incompetent states. *Phys Chem Chem Phys* **19**, 27987-27996
218. Sepulcre, J., Sabuncu, M. R., Becker, A., Sperling, R., and Johnson, K. A. (2013) In vivo characterization of the early states of the amyloid-beta network. *Brain* **136**, 2239-2252
219. Billings, L. M., Oddo, S., Green, K. N., McGaugh, J. L., and LaFerla, F. M. (2005) Intraneuronal Abeta causes the onset of early Alzheimer's disease-related cognitive deficits in transgenic mice. *Neuron* **45**, 675-688
220. Kobro-Flatmoen, A., Nagelhus, A., and Witter, M. P. (2016) Reelin-immunoreactive neurons in entorhinal cortex layer II selectively express intracellular amyloid in early Alzheimer's disease. *Neurobiol Dis* **93**, 172-183
221. Toh, W. H., Tan, J. Z., Zulkefli, K. L., Houghton, F. J., and Gleeson, P. A. (2017) Amyloid precursor protein traffics from the Golgi directly to early endosomes in an Arl5b- and AP4-dependent pathway. *Traffic* **18**, 159-175
222. Gaiser, A. M., Kaiser, C. J., Haslbeck, V., and Richter, K. (2011) Downregulation of the Hsp90 system causes defects in muscle cells of Caenorhabditis elegans. *PLoS One* **6**, e25485
223. Stringham, E. G., Dixon, D. K., Jones, D., and Candido, E. P. (1992) Temporal and spatial expression patterns of the small heat shock (hsp16) genes in transgenic Caenorhabditis elegans. *Mol Biol Cell* **3**, 221-233
224. Arnsburg, K., and Kirstein-Miles, J. (2014) Interrelation between protein synthesis, proteostasis and lifespan. *Current Genomics* **15**, 66-75
225. Markesbery, W. R. (1997) Oxidative Stress Hypothesis in Alzheimer's Disease. *Free Radical Biology and Medicine* **23**, 134-147
226. Bordi, M., Berg, M. J., Mohan, P. S., Peterhoff, C. M., Alldred, M. J., Che, S., Ginsberg, S. D., and Nixon, R. A. (2016) Autophagy flux in CA1 neurons of Alzheimer hippocampus: Increased induction overburdens failing lysosomes to propel neuritic dystrophy. *Autophagy* **12**, 2467-2483
227. Lee, H., Choi, M. K., Lee, D., Kim, H. S., Hwang, H., Kim, H., Park, S., Paik, Y. K., and Lee, J. (2011) Nictation, a dispersal behavior of the nematode Caenorhabditis elegans, is regulated by IL2 neurons. *Nat Neurosci* **15**, 107-112
228. Coates, J. C., and de Bono, M. (2002) Antagonistic pathways in neurons exposed to body fluid regulate social feeding in Caenorhabditis elegans. *Nature* **419**, 925-929
229. Pereira, L., Kratsios, P., Serrano-Saiz, E., Sheftel, H., Mayo, A. E., Hall, D. H., White, J. G., LeBoeuf, B., Garcia, L. R., Alon, U., and Hobert, O. (2015) A cellular and regulatory map of the cholinergic nervous system of C. elegans. *Elife* **4**

230. Yassin, L., Gillo, B., Kahan, T., Halevi, S., Eshel, M., and Treinin, M. (2001) Characterization of the DEG-3/DES-2 receptor: A nicotinic acetylcholine receptor that mutates to cause neuronal degeneration. *Mol Cell Neurosci* **17**, 589-599
231. Whitehouse, P. J., Price, D. L., Clark, A. W., Coyle, J. T., and DeLong, M. R. (1981) Alzheimer disease: evidence for selective loss of cholinergic neurons in the nucleus basalis. *Ann Neurol* **10**, 122-126
232. Summers, W. K., Majovski, L. V., Marsh, G. M., Tachiki, K., and Kling, A. (1986) Oral tetrahydroaminoacridine in long-term treatment of senile dementia, Alzheimer type. *N Engl J Med* **315**, 1241-1245
233. Savojardo, C., Martelli, P. L., Fariselli, P., Profiti, G., and Casadio, R. (2018) BUSCA: an integrative web server to predict subcellular localization of proteins. *Nucleic Acids Res* **46**, W459-W466
234. Huang da, W., Sherman, B. T., and Lempicki, R. A. (2009) Systematic and integrative analysis of large gene lists using DAVID bioinformatics resources. *Nat Protoc* **4**, 44-57
235. Huang da, W., Sherman, B. T., and Lempicki, R. A. (2009) Bioinformatics enrichment tools: paths toward the comprehensive functional analysis of large gene lists. *Nucleic Acids Res* **37**, 1-13
236. Stauffer, W., Sheng, H., and Lim, H. N. (2018) EzColocalization: An ImageJ plugin for visualizing and measuring colocalization in cells and organisms. *Sci Rep* **8**, 15764
237. Schindelin, J., Arganda-Carreras, I., Frise, E., Kaynig, V., Longair, M., Pietzsch, T., Preibisch, S., Rueden, C., Saalfeld, S., Schmid, B., Tinevez, J. Y., White, D. J., Hartenstein, V., Eliceiri, K., Tomancak, P., and Cardona, A. (2012) Fiji: an open-source platform for biological-image analysis. *Nat Methods* **9**, 676-682
238. Rueden, C. T., Schindelin, J., Hiner, M. C., DeZonia, B. E., Walter, A. E., Arena, E. T., and Eliceiri, K. W. (2017) ImageJ2: ImageJ for the next generation of scientific image data. *BMC Bioinformatics* **18**, 529
239. Horn, T., and Boutros, M. (2010) E-RNAi: a web application for the multi-species design of RNAi reagents--2010 update. *Nucleic Acids Res* **38**, W332-339
240. Yang, J. S., Nam, H. J., Seo, M., Han, S. K., Choi, Y., Nam, H. G., Lee, S. J., and Kim, S. (2011) OASIS: online application for the survival analysis of lifespan assays performed in aging research. *PLoS One* **6**, e23525
241. Tyanova, S., Temu, T., Sinitcyn, P., Carlson, A., Hein, M. Y., Geiger, T., Mann, M., and Cox, J. (2016) The Perseus computational platform for comprehensive analysis of (prote)omics data. *Nat Methods* **13**, 731-740
242. Perez-Riverol, Y., Csordas, A., Bai, J., Bernal-Llinares, M., Hewapathirana, S., Kundu, D. J., Inuganti, A., Griss, J., Mayer, G., Eisenacher, M., Perez, E., Uszkoreit, J., Pfeuffer, J., Sachsenberg, T., Yilmaz, S., Tiwary, S., Cox, J., Audain, E., Walzer, M., Jarnuczak, A. F., Ternent, T., Brazma, A., and Vizcaino, J. A. (2019) The PRIDE database and related tools and resources in 2019: improving support for quantification data. *Nucleic Acids Res* **47**, D442-D450
243. Desjardins, P., and Conklin, D. (2010) NanoDrop microvolume quantitation of nucleic acids. *J Vis Exp*
244. Williams, B. D., Schrank, B., Huynh, C., Shownkeen, R., and Waterston, R. H. (1992) A genetic mapping system in Caenorhabditis elegans based on polymorphic sequence-tagged sites. *Genetics* **131**, 609-624
245. Timmons, L., and Fire, A. (1998) Specific interference by ingested dsRNA. *Nature* **395**, 854
246. Lange, S., Sylvester, M., Schumann, M., Freund, C., and Krause, E. (2010) Identification of Phosphorylation-Dependent Interaction Partners of the Adapter

Protein ADAP using Quantitative Mass Spectrometry: SILAC vs O-18-Labeling. *Journal of Proteome Research* **9**, 4113-4122
247. Cox, J., Hein, M. Y., Luber, C. A., Paron, I., Nagaraj, N., and Mann, M. (2014) Accurate proteome-wide label-free quantification by delayed normalization and maximal peptide ratio extraction, termed MaxLFQ. *Mol Cell Proteomics* **13**, 2513-2526
248. Haslbeck, M., and Buchner, J. (2015) Assays to characterize molecular chaperone function in vitro. *Methods Mol Biol* **1292**, 39-51
249. Stiernagle, T. (2006) Maintenance of C. elegans. (Community, T. C. e. R. ed., WormBook
250. Kamath, R. S., Fraser, A. G., Dong, Y., Poulin, G., Durbin, R., Gotta, M., Kanapin, A., Le Bot, N., Moreno, S., Sohrmann, M., Welchman, D. P., Zipperlen, P., and Ahringer, J. (2003) Systematic functional analysis of the Caenorhabditis elegans genome using RNAi. *Nature* **421**, 231-237
251. Evans, T. C. (2006) Transormation and microinjection. (Community, T. C. e. R. ed., WormBook
252. Mello, C. C., Kramer, J. M., Stinchcomb, D., and Ambros, V. (1991) Efficient gene transfer in C.elegans: extrachromosomal maintenance and integration of transforming sequences. *EMBO J* **10**, 3959-3970
253. Wilm, T., Demel, P., Koop, H. U., Schnabel, H., and Schnabel, R. (1999) Ballistic transformation of Caenorhabditis elegans. *Gene* **229**, 31-35
254. Radman, I., Greiss, S., and Chin, J. W. (2013) Efficient and rapid C. elegans transgenesis by bombardment and hygromycin B selection. *PLoS One* **8**, e76019

8. Supplemental Information

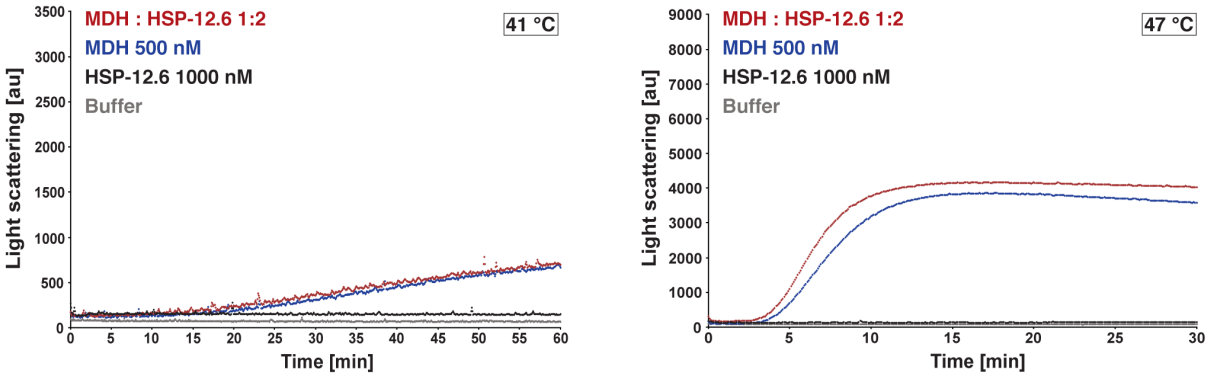

Supplementary Figure 1: HSP-12.6 does not affect aggregation of MDH at 41 °C or 47 °C

Static light scattering analysis of 500 nM MDH, alone (blue curves), or in the presence of 1 µM HSP-12.6 (red curves). All curves are averages of triplicate measurements. The same concentration of HSP-12.6 used, 2-fold / 1000 nM, was analyzed by itself under identical conditions (black curves). The buffer used was also analyzed (grey curves). Light scattering intensity is given in arbitrary units (au). Left side shows analysis at 41 °C, right side shows analysis at 47 °C.

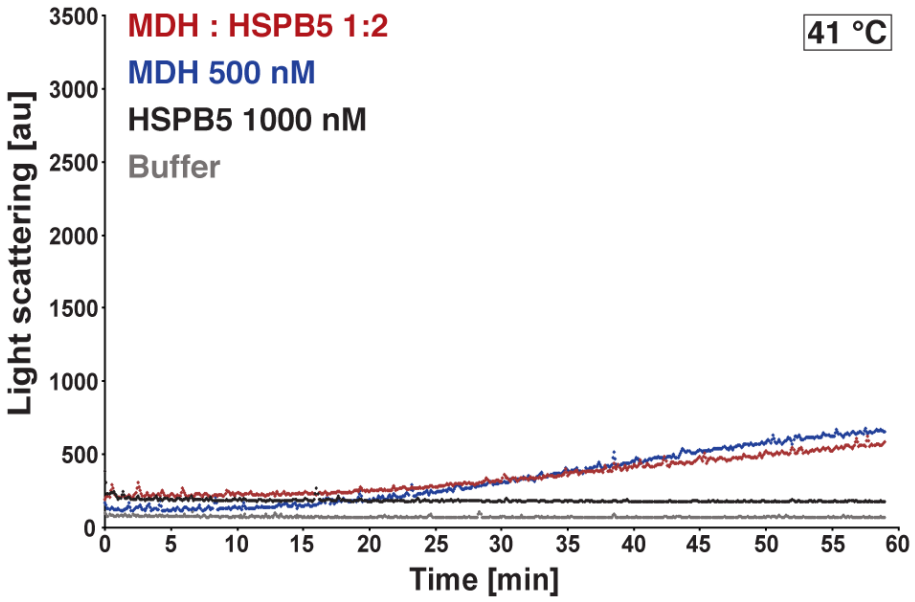

Supplementary Figure 2: HSPB5 does not affect aggregation of MDH at 41 °C

Static light scattering analysis of 500 nM MDH, alone (blue curve), or in the presence of 1 µM HSPB5 (red curve). All curves are averages of triplicate measurements. The same concentration of HSPB5 used, 2-fold / 1000 nM, was analyzed by itself under identical conditions (black curve). The buffer used was also analyzed (grey curve). Light scattering intensity is given in arbitrary units (au).

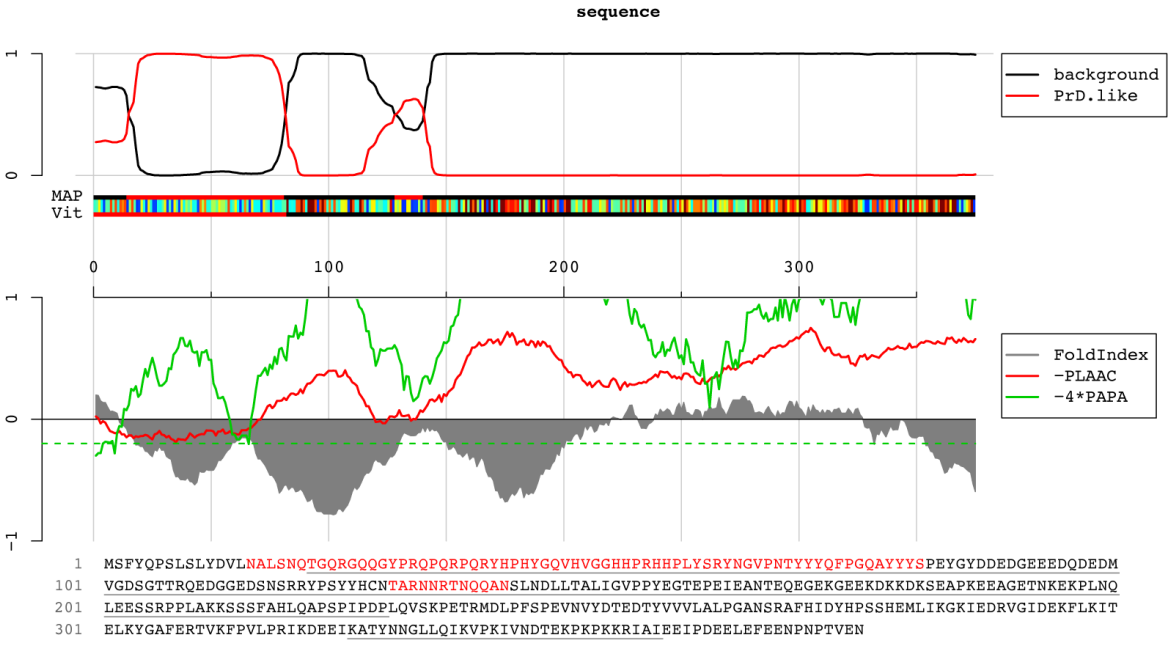

Supplementary Figure 3: Hsp42 contains a prion-like domain

Exemplary analysis of Hsp42 by *PLAAC*, showing that Hsp42 contains a prion-like domain as previously reported (170). See Figure 14 for a comparison of HSP-17. *PLAAC* calculated a *COREscore* and an LLR (log-likelihood ratio) of 11,937.

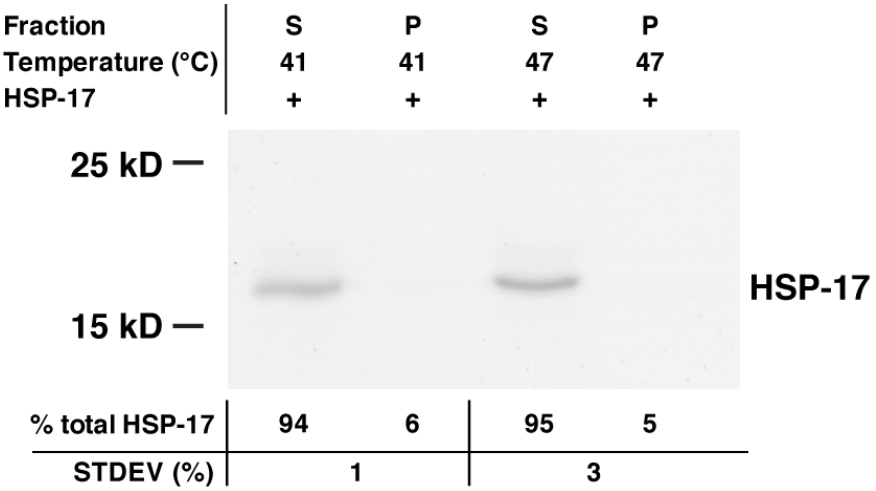

Supplementary Figure 4: HSP-17 cannot be sedimented after heat treatment at 41 °C or 47 °C

Sedimentation analysis of HSP-17 after heat treatment, at 41 °C or 47 °C. The soluble fraction (S) and the insoluble fraction (P) are shown side by side. The bands corresponding to HSP-17 (around 17 kDa) are indicated. The relative intensity of the bands, quantified by Fiji and normalized to 100%, is tabulated below the gel. The numbers given are the result of 3 repeats of the same analysis, the gel shown is representative.

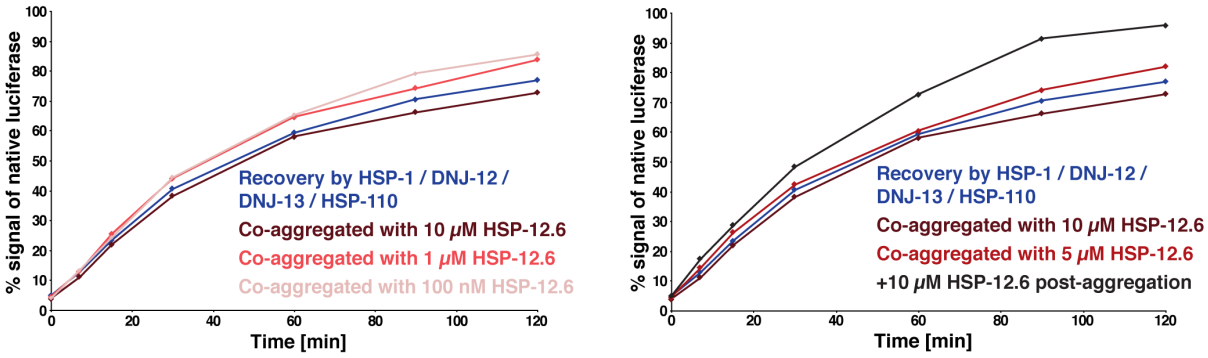

Supplementary Figure 5: Reactivation of luciferase is unaffected by addition of HSP-12.6

Luciferase was aggregated by heat treatment. The disaggregation was carried out by the indicated molecular chaperones and measured by quantifying emitted light, normalized to native luciferase (blue curve). The same measurement was carried out with increasing concentrations of HSP-12.6 being added to luciferase before aggregation (left side), or (right side) for the disaggregation step (red curves, darker shades of red indicate higher concentrations of HSP-12.6 as indicated in the legend). All data points are averages of triplicate measurements.

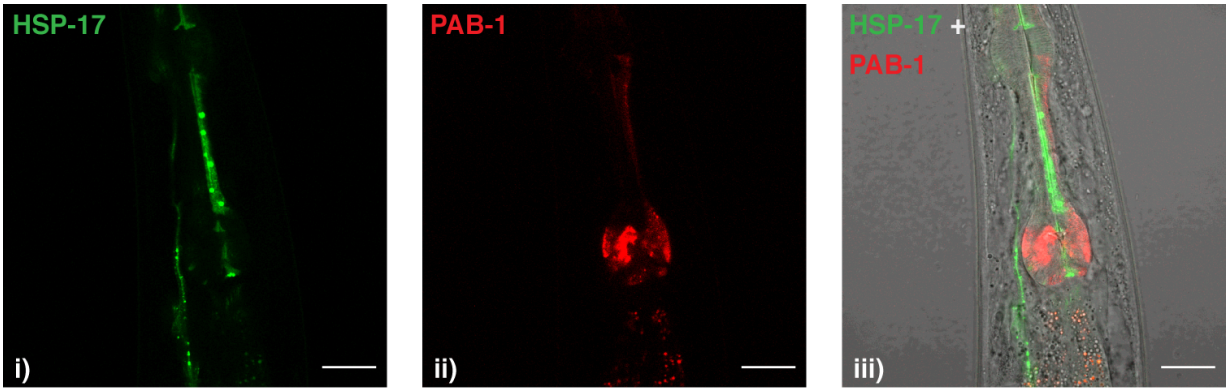

Supplementary Figure 6: HSP-17 and PAB-1 do not colocalize in the pharynx

Representative confocal LSM of *C. elegans* p17tG crossed with the strain DCD214 (expression of tagRFP-PAB-1 to the pharynx). Separate channels and combined channel are provided, as noted on the images. Scale bars are 20 µm.

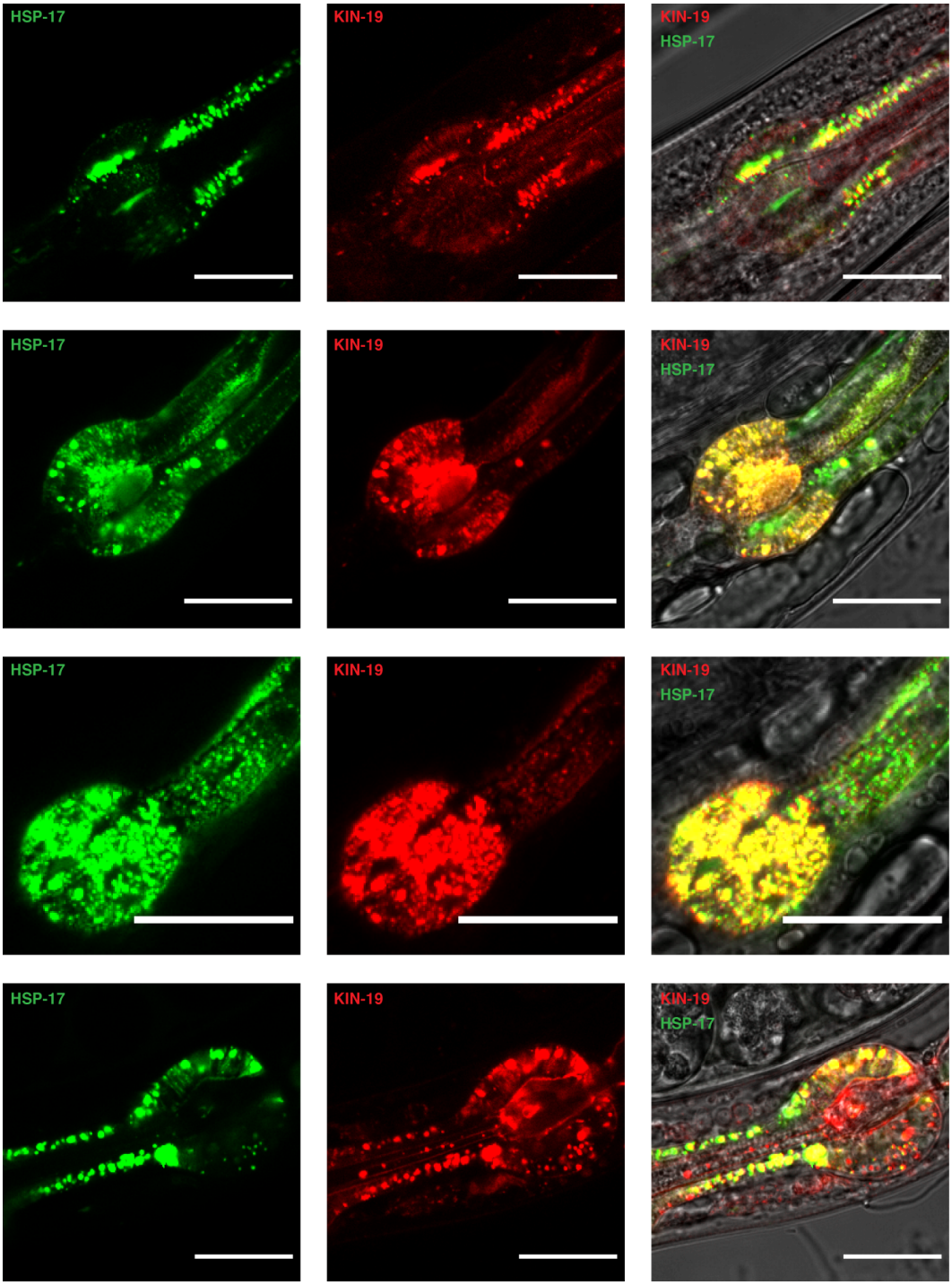

Supplementary Figure 7: HSP-17 and KIN-19 colocalize in the pharynx

Representative confocal LSM of *C. elegans* p17tG crossed with the strain CF3166 (expression of KIN-19-tagRFP controlled by the native promoter). Separate channels and combined channel are provided, as noted on the images. The pharynx of multiple nematodes was analyzed and quantification using the *Fiji* plugin *EzColocalization* yielded a PCC of 0,58 (standard deviation is 0,19) and an SRCC of 0,63 (standard deviation is 0,08). A total of 9 nematodes were analyzed. Scale bars are 20 µm.

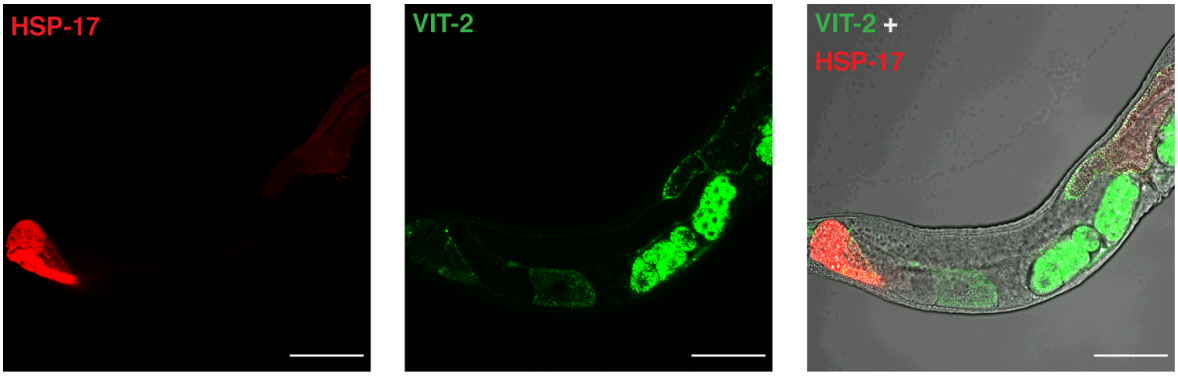

Supplementary Figure 8: HSP-17 does not colocalize with VIT-2 in the intestine

Representative confocal LSM of *C. elegans* p17tR crossed with the strain DH1033 (expression of VIT-2-GFP to the intestine). Separate channels and combined channel are provided, as noted on the images. Scale bars are 50 µm.

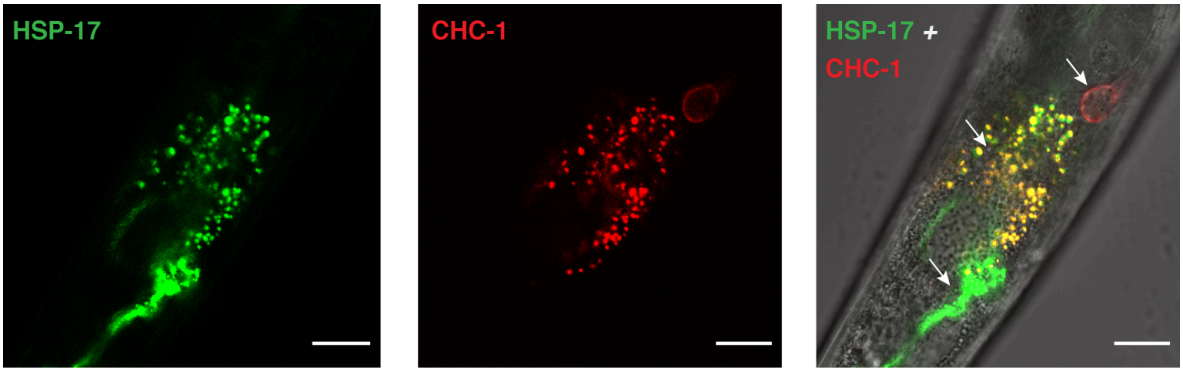

Supplementary Figure 9: HSP-17 shows limited colocalization with CHC-1

Representative confocal LSM of *C. elegans* p17tG microinjected into the strain RT2676 (expression of tagRFP-CHC-1 to the intestine, *chc-1* being a *C. elegans* homolog of clathrin heavy chain). The arrows in the third frame are pointing to foci of unique tagRFP-CHC-1 localization, colocalization between both in the upper intestine, and unique HSP-17-GFP localization. Separate channels and combined channel are provided, as noted on the images. Scale bars are 20 µm.

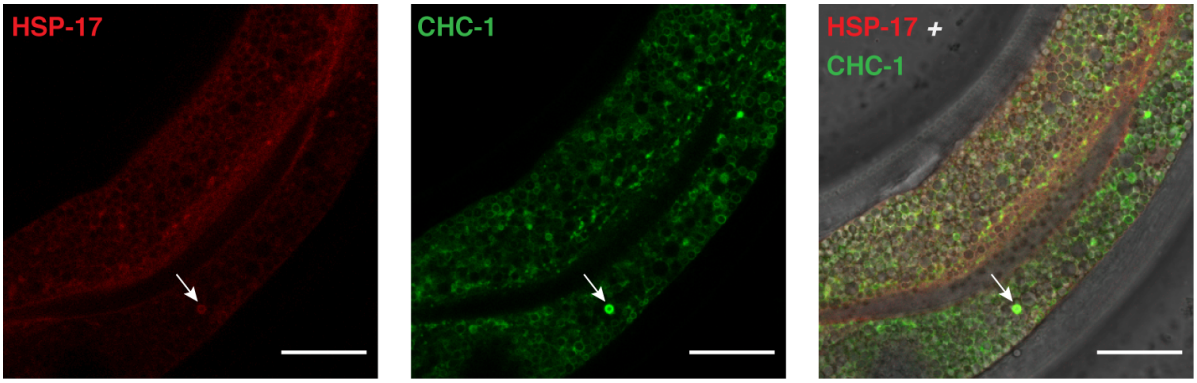

Supplementary Figure 10: HSP-17 shows infrequent colocalization with RAB-7

Representative confocal LSM of *C. elegans* p17tR crossed with the strain RT476 (expression of GFP-RAB-7 to the intestine). The arrows are pointing to a vesicle like structure where HSP-17-wrmScarlet and GFP-RAB-7 colocalize. Separate channels and combined channel are provided, as noted on the images. Scale bars are 20 µm.

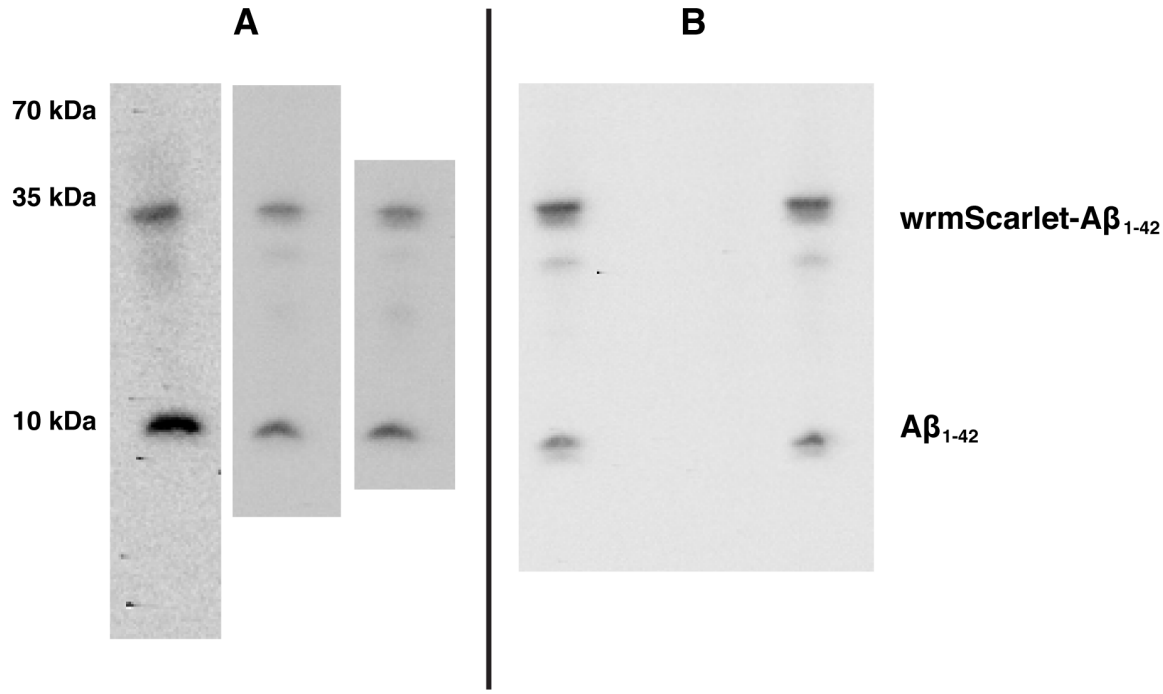

Supplementary Figure 11: Western blotting of *C. elegans* strain mAβ lysates

A: Western blotting of JKM7 lysates with 6E10 antibodies to detect wrmScarlet-Aβ_{1-42} (around 35 kDa) and Aβ_{1-42} (around 10 kDa). Three experiments of independent sample nematodes are provided and the unlabeled Aβ moiety appears to be in abundance (by about 5-fold as quantified by *Fiji*). B: analogous analysis of the same strain with the same method (two independent nematode groups, analyzed in parallel). The labeled Aβ moiety appears to be in excess.

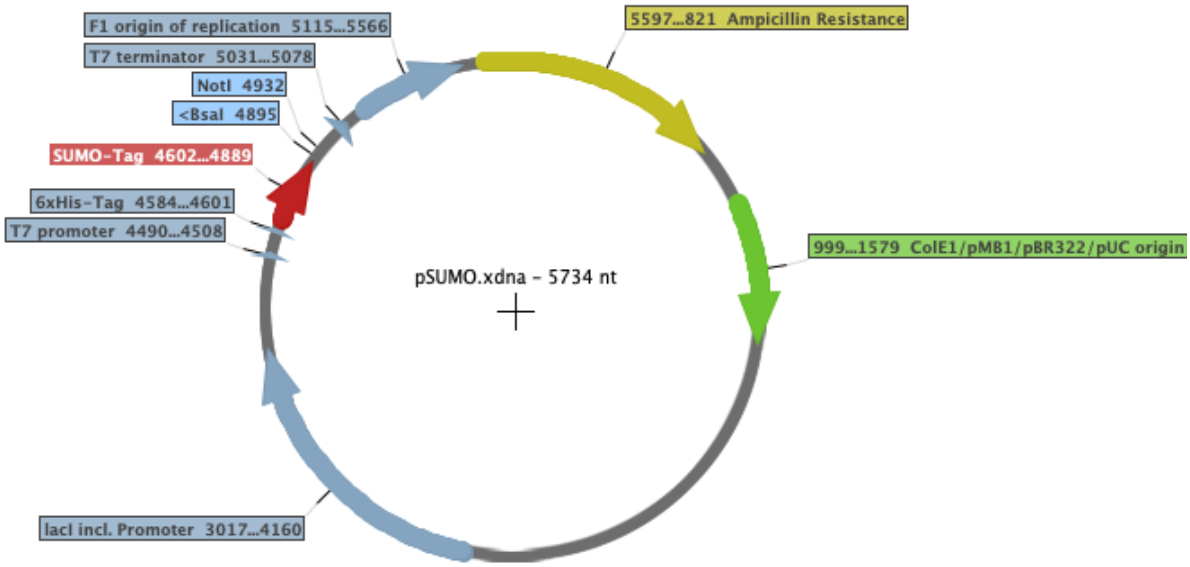

Supplementary Figure 12: Vector map of pSumo

A vector map of pSumo, used for expression of His-SUMO-tagged recombinant proteins. The restriction sites for NotI and BsaI used for molecular cloning are indicated, as are the location of the 6xHis-tag and T7 promoter regions. The vector carries an ampicillin resistance gene.

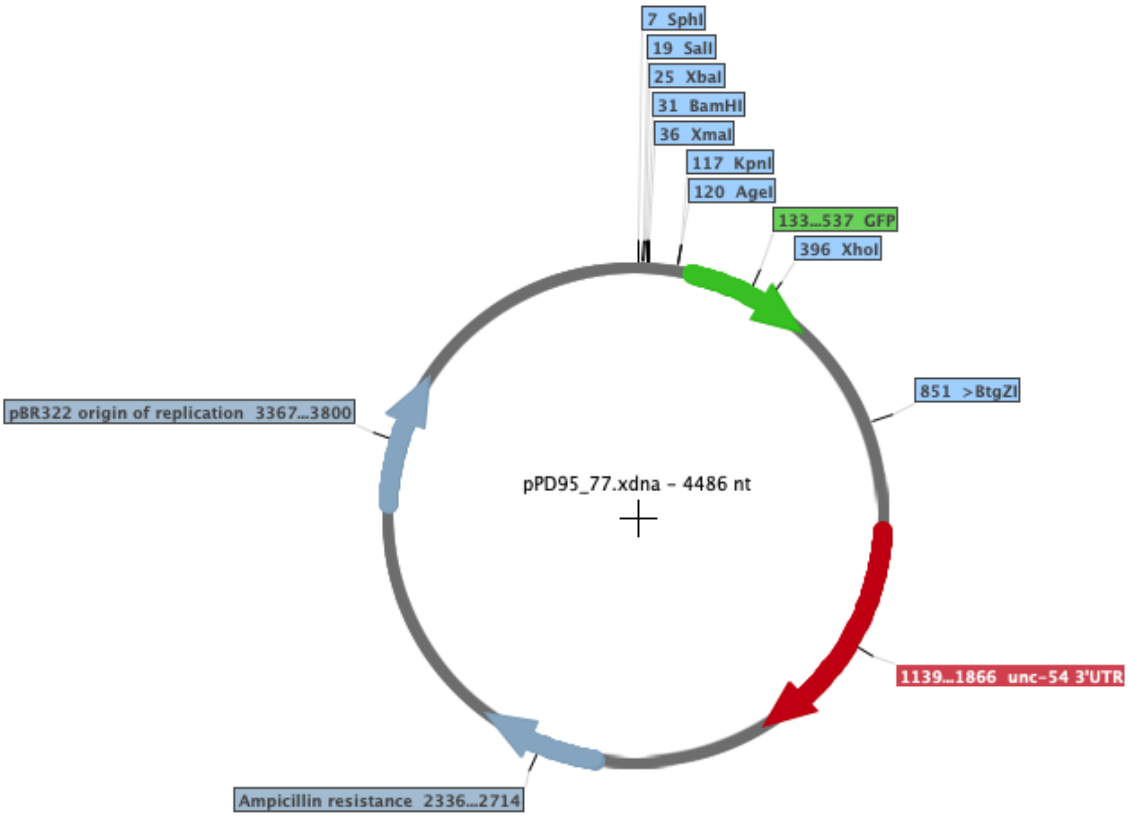

Supplementary Figure 13: Vector map of pPD95.77

A vector map of pPD95.77, used as a vehicle to enter transgenes into *C. elegans*. The CDS of GFP used for the generation of reporter strains (and sometimes replaced with wrmScarlet), is indicated, as are notable restriction sites used for molecular cloning of my constructs. The vector carries an ampicillin resistance gene.]

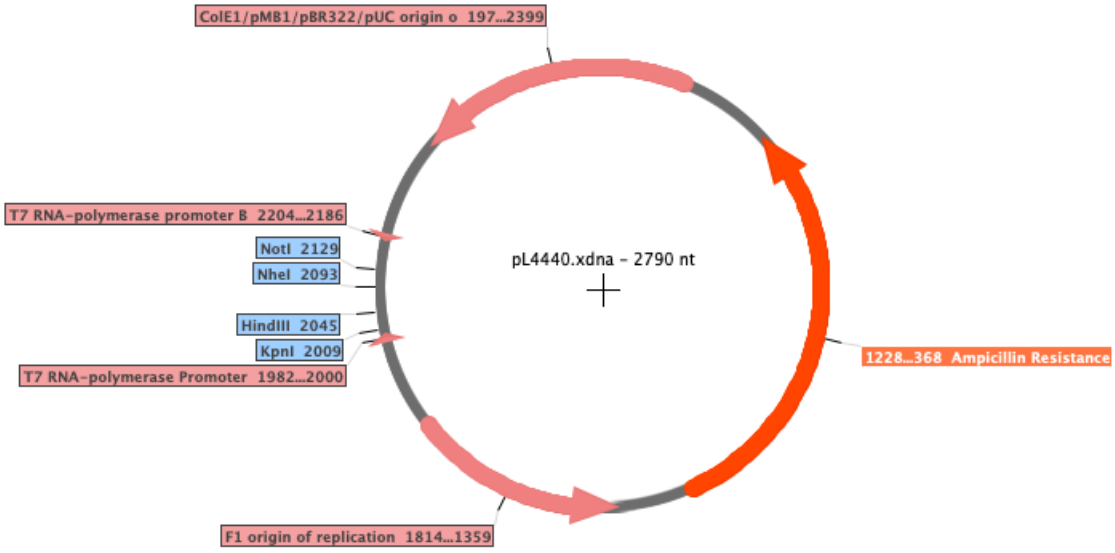

Supplementary Figure 14: Vector map of pL4440

A vector map of L4440, used to transform *E. coli* HT115 for RNAi-feeding in *C. elegans*. Notable restriction sites used for molecular cloning of my constructs are indicated, along with the T7 promoter sites used for transcription of dsRNA. The vector carries an ampicillin resistance gene.

9. List of abbreviations

Table 26: List of abbreviations

Abbreviation	Term
°C	Degree celsius
α-syn	α-synuclein
A	Amyloid beta
AbA	Antibody buffer A
ACD	α-crystallin domain (in sHsps)
ACN	Acetonitrile
AD	Alzheimer's disease
ADP	Adenosine diphosphate
AEC	Anion exchange chromatography
ALS	Amyotrophic lateral sclerosis

ANOVA	Analysis of variance
APP	Amyloid precursor protein
ASE neurons	Amphid neurons, single ciliated endings
ATP	Adenosine triphosphate
au	Arbitrary units
BCA	Bicinchoninic acid
BiP	Binding immunoglobulin protein, protein name
BLAST	Basic local alignment search tool
bp	Base pair
BSA	Bovine serum albumin
C. elegans	*Caenorhabditis elegans*
CAG	Cytosine adenine guanine codon
cDNA	Complementary DNA
CDS	Codon-determining sequence
CFP	Cyan fluorescent protein
CGC	*Caenorhabditis* genetics center
CLEM	Correlative light-electron microscopy
CS	Citrate synthase
CTD	C-terminal domain (in sHsps)
CV	Column volume(s)
Cy3	Cyanine dye 3
Cy5	Cyanine dye 5
C-terminal	Carboxy-terminal
DAPI	4’,6-Diamidin-2-phenylindol
DEG(-3)	Degeneration of certain neurons, protein name
DES(-2)	Degeneration suppressor, protein name
DMSO	Dimethyl sulfoxide
DNA	Deoxyribonucleic acid
DNase	Deoxyribonuclease
dNTP	Deoxynucleotide triphosphate
DTT	Dithiothreitol

E. coli	*Escherichia coli*
ECL	enhanced chemiluminescence
EDTA	Ethylenediaminetetraacetic acid
EM	Electron microscopy
ER	Endoplasmatic reticulum
FLIM	Fluorescence-lifetime imaging microscopy
Fn	Filial generation *n*
FastAP	Thermosensitive alkaline phosphatase
FDR	False discovery rate
FTD	Frontotemporal dementia
g (µg, mg)	gram (microgram, milligram)
GAPDH	Glyceraldehyde 3-phosphate dehydrogenase
GFP	Green fluorescent protein
GO	Gene ontology
GOI	Gene of interest
GST	Glutathione S-transferase
h	hour(s)
H_2O	Hydroxilic acid, used to refer to purified water
HD	Huntington's disease
HEPES	4-(2hydroxyethyl)-1-piperazineethanesulfonic acid
HS	Heat shock
hsp / HSP	Heat shock protein (gene / protein)
HSR	Heat shock response
Htt	Huntingtin
HttEx1	Huntingtin, first exon
ILS	Insulin-like signaling
IMAC	immobilized-metal affinity chromatography
IPTG	Isopropyl β-D-1-thiogalactopyranoside
IRES	Internal ribosomal entry site
kb	Kilobase
kDa	Kilodalton
L, (µl, ml)	Liter (microliter, milliliter)

L1-L4	Nematode larval stages 1 to 4
LB	Luria broth / Luria-Bertani media / lysogeny broth
LSM	Laser scanning microscope
m	muscular
M (pM, nM, µM, mM)	Molar (picomolar, nanomolar, micromolar, millimolar)
mA	Milliampere
MAPT	microtubule-associated protein Tau; “Tau-protein”
MDH	malic dehydrogenase
min	Minute(s)
mm (nm, µm, cm)	Millimeter (nanometer, micrometer, centimeter)
MWCO	Molecular weight cut-off
mRNA	Messenger ribonucleic acid
MS	Mass spectrometry
n	Neural
NCBI	National Center for Biotechnology Information
NEB	New England Biolabs
NEF	Nucleotide exchange factor
NGM	Nematode growth media
NHS	N-hydroxylsuccinimide
NP-40	4-Nonylphenyl poly(ethyleneglycol)
NPR(-1)	Natriuretic / neuropeptide receptor, protein name
NTD	N-terminal domain (in sHsps)
N-terminal	Amino-terminal
ORF	Open reading frame
PBS (T)	Phosphate buffered saline (with Tween 20)
PCC	Pearson’s correlation coefficient
PCR	Polymerase chain reaction
PD	Parkinson’s disease

PMSF	Phenylmethylsulfonyl fluoride
PN	Proteostasis network
POI	Protein of interest
PSEN	Presenilin
psi	“pound-force per square inch”
Proteostasis	Protein homeostasis
PVDF	Polyvinylidene fluoride
PVP	Polyvinylpyrrolidone
Q	Glutamine
QToF-MS	Quadrupole time-of-flight mass spectrometry
RIPA buffer	Radioimmunoprecipitation assay buffer
RME	Receptor-mediated endocytosis
RNA	Ribonucleic acid
RNAi	RNA interference
RNase	Ribonuclease
RT	Room temperature
SD	Standard deviation
SE	Sensitized emission
SEC	Size exclusion chromatography (gel filtration)
SEM	Standard error of means
SDS	Sodium dodecyl sulfate
SDS-PAGE	SDS-polyacrylamide gel electrophoresis
s	Second(s)
sHsp	Small heat shock protein
SRCC	Spearman’s rank correlation coefficient
TAE	Tris-acetate-EDTA
TBS (T)	Tris buffered saline (with Tween 20)
TCEP	Tris(2-carboxyethyl)phosphine
TEM	Transmission electron microscopy
Temed	Tetramethylethylenediamine
Tris	Tris(hydroxymethyl)aminomethane
UPR	Unfolded protein response

UV	Ultraviolet
V	Volt
v/v	Volume by volume
w/v	Weight per volume
WB	Western Blot
wt	Wild type
YFP	Yellow fluorescent protein

10. List of tables and Figures

10.1. List of tables

10.2. List of Figures

10.3. List of supplementary Figures

11. Data availability

11.1. Image data of translational *hsp-17* reporter strains

Z-stack images of the HSP-17 transgenic animals (*phsp-17::hsp-17::wrmScarlet*) have been deposited on the Zenodo platform to provide a comprehensive dataset on the expression of HSP-17 in the whole body, the head region and the tail. DOI: 10.5281/zenodo.3594412

11.2. Proteomics data generated from IP-MS/MS analysis of HSP-17

The mass spectrometry proteomics data have been deposited to the ProteomeXchange Consortium via the PRIDE (242) partner repository with the dataset identifier PXD016485. Supplementary table 1 (provided as digital content) contains a list of MS/MS experimental parameters, the peptides detected, the identified proteins and the evaluation thereof (by *Perseus*) as carried out by Heike Stephanowitz, modified for accessibility and a condensed list of resulting proteins, sorted by relative enrichment over control (proteins used for *DAVID* analysis marked in red). A complete list of GO terms identified by *DAVID* was also included.

11.3. Proteomics data generated from IP-MS/MS of mAβ & nAβ

The proteomics data generated by mass spectrometry have been deposited to the ProteomeXchange Consortium via the PRIDE (242) partner repository with the dataset identifier PXD017590 (mAβ) & PXD017591 (nAβ). Supplementary table 2 (provided as digital content) contains an exhaustive list of the experimental parameters of the MS/MS experiment, peptides detected, the identified proteins and the evaluation thereof (by *Perseus*) as carried out by Heike Stephanowitz and modified for accessibility. For mAβ, a complete list of GO terms identified by *DAVID* from significantly enriched hits was also included.

12. Affidavit

Hiermit erkläre ich an Eides statt, dass ich die zu Grunde liegende Promotionsordnung der Lebenswissenschaftlichen Fakultät vom 5. März 2015 zur Kenntnis genommen habe. Desweiteren habe ich nicht die Hilfe gewerblicher Promotionsberater in Anspruch genommen und die hier gezeigten Ergebnisse wurden nicht bei einer anderen wissenschaftlichen Einrichtung eingereicht, akzeptiert oder abgelehnt. Weder besitze ich einen anderen Doktorgrad, noch habe ich mich anderwärts um einen solchen beworben. Diese Dissertation habe ich mit der genannten Unterstützung und auf Grundlage der angegebenen Hilfsmittel gemäß § 6 (3) selbstständig angefertigt. Ich erkläre weiterhin, dass ich die Grundsätze zur Sicherung guter wissenschaftlicher Praxis der Humboldt-Universität zu Berlin eingehalten habe.

13. Danksagung & Acknowledgements

Abschließend möchte ich mich bei all den Personen bedanken, die mir auf dem Weg zu dieser Arbeit beigestanden haben und für ihre Vollendung unersetzlich waren.
Zunächst gilt mein Dank meiner Familie, mit der ich in einem Heim voller Bücher und Möglichkeiten aufwachsen durfte um schließlich meine Faszination zur Wissenschaft auszubilden und den Weg bis hierher zu finden.
Darauf möchte ich mich bei meiner Betreuerin Janine bedanken, die mir die Chance gegeben hat, in ihrer wundervollen Arbeitsgruppe als Doktorand zu Forschen und mir dabei auf jedem Schritt mit praktischer Hilfe und umfangreichem Rat beigestanden hat. Außerdem bedanke ich mich bei Prof. Adam Lange, der für mich die Betreuung als Professor an der Humboldt-Universität übernommen hat und bei den Mitgliedern meiner Promotionskommission für die fachkundige Begutachtung meiner Arbeit.
Für Jahre fachübergreifender und angenehmer Zusammenarbeit im Labor möchte ich mich bei Alice Baumann bedanken. Darüber hinaus gilt mein Dank den derzeitigen und ehemaligen Mitgliedern der AG Kirstein, die mir mit geduldiger Anleitung im Labor, produktiver Kooperation, Rat und Diskussion beigestanden und eine angenehme Arbeitsatmosphäre ermöglicht haben. Für tatkräftige Hilfe im

Laboralltag bin ich darüber hinaus allen Studenten dankbar, die ich während meiner Promotion betreut habe. Schließlich möchte ich auch meinen anderen Mitarbeitern am FMP danken, die mir mit Freundlichkeit und Hilfe zu einem erfolgreichen Arbeitsalltag verholfen haben.

Ich möchte mich außerdem bei den Mitarbeitern der *Core Facilities Mass Spectrometry* und *Cellular Imaging* am FMP bedanken, die mir mit Anleitung und fleißiger Arbeit ermöglicht haben, meine Forschung zu vervollständigen. Gleichermaßen bedanke ich mich bei Dr. Dmytro Puchkov und seinen Mitarbeitern für die kompetente Arbeit in der Elektronenmikroskopie und deren Auswertung für meine Forschung.

Für Proben des kleinen Hitzeschockproteins HSPB5 bedanke ich mich bei Anne Diehl und der AG Oschkinat. Für den *C. elegans* Stamm BJ49 bedanke ich mich bei der AG Leube, für die Stämme mQ_0 und iQ_{85} bei der AG Morimoto, für den Stamm DCD214 bei der AG David und für den Stamm RT2676 bei der AG Grant. Für weitere *C. elegans* Stämme bedanke ich mich beim *Caenorhabditis Genetics Center*. Für das Plasmid mit der Promotorsequenz von *klp-6* gilt mein Dank der AG Hobert und für die Sequenz des Fluorophors *wrmScarlet* der AG Boulin. Außerdem danke ich der *C. elegans* Internetplattform *WormBase*.

Zu guter Letzt möchte ich mich bei all meinen Freunden bedanken, die mir nicht nur geholfen haben, es bis zu dieser Stelle meiner Arbeit zu schaffen, sondern auch ein Leben außerhalb meiner Forschung ermöglichen.

Danke sehr!

14. List of publications resulting from this work

Publications (ORCID: https://orcid.org/0000-0002-1073-9023)

Iburg M, Puchkov D, Rosas-Brugada IU, Bergemann L, Rieprecht U, Kirstein J.: The non-canonical small heat shock protein HSP-17 from *C. elegans* is a selective protein aggregase.

J Biol Chem 2020 doi: 10.1074/jbc.RA119.011185

Pigazzini ML*, Gallrein C*, **Iburg M***, Kaminski Schierle G, Kirstein J: Characterisation of amyloid structures in aging C. elegans using fluorescence lifetime imaging.

JoVE 2020 doi: 10.3791/61004 *: equal contribution

Feleciano DR, Juenemann K, **Iburg M**, Bras I, Holmberg CI, Kirstein J: *Crosstalk between chaperone-mediated protein disaggregation and proteolytic pathways in aging and disease.*

Frontiers in Aging Neuroscience, 2019 Jan 29;11:9

Scior A, Arnsburg K, **Iburg M**, Juenemann K, Mlody B, Pigazzini ML, Buntru A, Puchkov D, Wanker EE, Prigione A, Priller J & Kirstein J: *Complete suppression of Htt aggregation and disaggregation of Htt fibrils by a specific trimeric chaperone complex*.

The EMBO Journal, 2018; 37(2)282-299

Gallrein C*, **Iburg M***, Michelberger T, Koçak A, Puchkov D, Liu F, Ayala Mariscal SA, Nayak T, Kaminski Schierle GS, Kirstein J: *Novel Amyloid-beta pathology C. elegans model reveals distinct neurons as seeds of pathogenicity*

Progress in Neurobiology 2020, in review *: co-first authors